CHARGE TRANSPORT IN ELECTROSTATIC RADIOGRAPHY

by

B. Gino Fallone

A Thesis Submitted to the

Faculty of Graduate Studies and Research

in Partial Fulfillment

of the Requirements for the Degree of

Doctor of Philosophy

Department of Physics

McGill University, Montreal

June , 1983

ai miei genitori

ABSTRACT

The charging characteristics of ionographic latent images are discussed in terms of saturation characteristics of ionographic chambers. Latent images are essentially foil electrets with surface charge densities proportional to the x-ray transmission through the object. A hyperbolic expression is developed which accurately describes the full saturation curve for x-rays and cobalt-60 gamma rays of parallel-plate ionization chambers filled with air, or with high atomic number gases at elevated pressures. Foil electrets with surface charge densities of up to 10^{-6} C/cm^2 and ionographic latent images are formed by blocking the collecting electrode of the chamber with a polymer. The hyperbolic expression is utilized to derive an accurate representation of the charging and discharging dynamics of the latent image. The theory of linear systems is used to derive the electric field and potential inside the electret chamber, and the solutions are equal to those obtained from Gauss' law at the surface of the electret, and to those obtained from a dipole layer model at large distances from the surface. An analog radiographic image subtraction technique based on the charging characteristics of ionographic latent images, formed either with a solid photoconductor or with a gas as the radiation sensitive medium, is described.

RÉSUMÉ

La formation de l'image latente ionographique est traitée en termes de phénomène de saturation des chambres ionographiques. L'image latente est constituée par la densité de charge à la surface d'électrets minces. La densité de charge est reliée à la transmission des rayons X par l'objet étudié. Une expression de forme hyperbolique décrit entièrement la courbe de saturation des chambres d'ionisation à électrodes parallèles, irradiées par rayons X ou par photons de cobalt-60. Elles peuvent être emplies d'air, ou de gaz de numéro atomique élevé à haute pression. Des électrets minces, de densité de charge atteignant le microcoulomb par centimètre carré, sont réalisés en interceptant sur un polymère les charges attirées par une des électrodes. L'expression hyperbolique permet une représentation fidèle de la charge et de la décharge de l'électret. La théorie des systèmes linéaires fournit le champ et le potentiel à l'intérieur de la chambre d'ionisation à électret. Les mêmes résultats sont obtenus soit par l'application de la loi de Gauss à la surface de l'électret, soit par le calcul à grande distance d'un feuillet dipolaire. On décrit aussi une technique de soustraction analogique basée sur les caractéristiques de charge et de décharge des images latentes ionographiques. Le milieu sensible peut être un gaz ou un photoconducteur solide.

ORIGINAL CONTRIBUTION

A new analytical hyperbolic expression is presented to describe the full saturation curve of parallel-plate ionization chambers filled with air or with high atomic number gases at elevated pressures. In contrast to the presently known expressions, which hold only for the region near saturation, this expression is in excellent agreement with measurements in the whole collection efficiency range from 0 to 1 for continuous x-ray sources and cobalt-60 gamma rays. It is shown that all parameters of the saturation curve expression and thus the saturation curve itself, can be calculated from one single measurement of ionization current at a given electric field and air gap thickness.

Isothermal charge deposition on polymers to form stable foil electrets by using an apparatus resembling parallel-plate ionization chambers is reported. Charge carriers produced by irradiation of the sensitive air volume drift in the externally applied electric field and get trapped on the polymer surface to form electrets with maximum charge densities close to 10^{-6}C/cm^2. Charge density as a function of applied voltage follows the form typical of a Schottky or Poole-Frenkel process.

By using the hyperbolic dependence of the ionization chamber current density on effective electric field, the time dependence of the polarization and depolarization current densities, the effective electric field in the electret chamber, and the electret surface charge densities are presented for the radiation-induced foil electret and an excellent agreement is obtained with the measured electret data. Both the saturation current density and the extrapolated electric field parameter consist of a component which is linear with air gap thickness and is

produced by primary photon interactions in the chamber sensitive volume, and another component, which exhibits an exponential saturation and is attributed to photoelectrons backscattered from the polarizing electrode into the chamber sensitive volume.

The theory of linear systems is used to derive the electric field and potential in distance space in the electret chamber. On the axis, the solutions for the electret surface are equal to those obtained from Gauss' law, and at large distance from the surface to those obtained from a dipole layer model of the electret.

The charging characteristics of ionographic latent images, which are essentially foil electrets with surface charge densities modulated by the x-ray transmission through the object, are discussed in terms of saturation characteristics of ionographic chambers. Sensitivity of the ionographic chamber can be increased tenfold by changing the low atomic number polarizing electrode to lead. The minimum applied electric field needed for an optimized charge collection in the ionographic chamber is presented in terms of both the electret characteristics polarization time and the electret relaxation time. It is shown that exposures above an optimum one will degrade the image and for high enough exposures, eventually result in a uniform foil electret charged to its maximum theoretical value.

The feasibility of radiographic image subtraction based on electrostatic imaging techniques is demonstrated. Latent image charging at one polarity corresponding to the production of the primary image, and latent image discharging with the opposite chamber polarity, are used to create the final image representing the region of interest.

ACKNOWLEDGEMENT

The research described has been performed under the auspices of the McGill Physics Department, and has been carried out in the Medical Radiation Physics laboratory of the McGill Radiation Oncology Department situated at the Montreal General Hospital.

I am gratefully indebted to Prof. E.B. Podgorsak for his support, interest, stimulation, help and direction during the course of this work. Special thanks are due to his many recommendations and discussions not only related to the research project but also to many other areas. The three years spent under his directorship were, both scientifically and personally, very rewarding .

I would also like to acknowledge Dr. R. Heese for the many helpful discussions on this project. A particular word of thanks is given to Mr. L. Palotay for his aid in the mechanical fabrication and design of the experimental apparatus. Other memebers of the staff must also be mentionned. These include Messrs. P. Lefebvre and N. Sharoubim, B.Sc., for their technical aid and advice in the electrical apparatus, and Dr. C. Pla, for his help on some of the computer programming stages of the work. Conversations with some of the remaining members of the staff , i.e., S. Chenery, Ph.D., G. Durante, B. Eng., M. Gosselin, A.C.(T), and M. Pla, M.Sc., were also beneficial.

Professors R.E. Bell, M. Cohen and M. Zuckerman from the Physics Department and Dr. C. Freeman, Chairman of the Radiation Oncology Department are thanked for their interest in the project. I am very grateful to Prof. R.A. Béique of l'Hôpital Notre-Dame of Montreal and l'Université de Montréal for his help and encouragement

during my graduate career.

I thank Dr. A. Fenster and Prof. H.E. Johns of the University of Toronto for loaning us their electrostatic development powder box. The help given by the Audio-visual Department of the Montreal General Hospital is appreciated; and the excellent typing services of Ms. Betty Coletta and Ms. Francine Lecours (Chapter 3 and Chapter 6) is gratefully acknowledged.

The financial support of the Medical Research Council of Canada is also acknowledged.

TABLE OF CONTENTS

CHAPTER 1

INTRODUCTION

1.1 General Introduction

There have been attempts, in recent years, to replace photographic imaging techniques in radiography by electrostatic imaging methods. The two most promising methods of electrostatic imaging applied to radiography are xeroradiography and gas ionography. In these methods, x-ray photons transmitted through the object produce charge carriers in a radiation sensitive medium that drift in an electric field and are trapped on a blocking electrode. These charge carriers form a charged latent image which can be rendered visible by electrostatic powder.

We present, in this thesis, our investigations of the transport of charge carriers and of the electret properties of the charged latent image produced in gas ionography. We studied charge transport by determining an expression describing the full saturation curve of parallel-plate ionization chambers filled either with air or with high atomic number gases at elevated pressures. In contrast to presently known expressions, which hold only in a limited region near saturation, our expression is in excellent agreement with measurements in the entire collection efficiency range from 0 to 1 for x-ray photons with effective energies from 20 keV to 150 keV and for cobalt-60 gamma rays. We describe a new electret production technique based on radiation induced ionization of air and utilize the saturation curve expression in conjunction with Gauss' law to accurately represent our measured data of the charging and discharging dynamics of this radiation induced foil electret. We also present a more accurate calculation of the electric field and potential at any point inside the electret chamber by using the theory of linear optical systems to solve the Laplace's equation.

The ionographic latent image, which is essentially a foil electret with a surface charge density proportional to the x-ray photons transmitted through the object, is described in terms of the charging characteristics of the radiation induced foil electret. The sensitivity of gas ionography can be increased by an order of magnitude by changing the low atomic number polarizing electrode to lead. The minimum applied electric field needed for an optimized charge collection in the ionographic chamber is also discussed.

We apply the charging and discharging characteristics of ionographic latent images to present an analog radiographic image subtraction technique. Either a solid photoconductor or a gas can be used as radiation sensitive medium to achieve subtraction. At the moment, radiographic subtraction by computers is an extremely important technique in radiological diagnosis, and we present our analog electrostatic subtraction technique as a possible inexpensive alternative to the commercially available and expensive computer techniques.

1.2 THESIS ORGANIZATION

Chapter 2 gives a thorough review of the physics of radiographic imaging. In this review, we discuss photographic film because it is the most popular radiographic imaging technique. Electrostatic radiographic imaging, which includes xeroradiography and gas ionography, is also discussed in detail; this discussion represents the general introduction to our investigations of charge transport phenomena in electrostatic radiography. Radiographic subtraction techniques are briefly discussed at the end of the Chapter 2 so that one can appreciate the relevance of the

electrostatic radiographic subtraction techniques discussed in the final chapters of the thesis. In Chapter 3, we discuss the experimental apparatus and procedures that were used in our studies. The remaining chapters, which discuss the results of our own investigations, essentially represent various studies that were published,[1-3] have been accepted for publication,[4-6,8] or have been submitted recently for publication.[7,9,10]

Chapter 4 presents our analytical expression to describe the full saturation curve of parallel-plate ionization chambers.[1] In Chapter 5, we use the saturation curve expression *i*) to introduce a method for production of stable foil electrets by ionizing radiation in air,[2] *ii*) to describe the charging and discharging dynamics of this foil electret,[3] and *iii*) to thoroughly discuss its characteristics.[4,5] In Chapter 6, the theory of linear optical systems is used to solve the Laplace's equation so that the electric field and potential at any point inside the electret producing chamber is known.[6] Certain characteristics of ionographic latent images[7] are then discussed in Chapter 7 in terms of the radiation induced foil electret presented in previous chapters. In the two following chapters,[8] we study the feasibility of an analog radiographic image subtraction based on the charging and discharging properties of the ionographic latent image discussed in Chapter 7. We present two techniques: one, given in Chapter 8,[9] uses a gas as the radiation sensitive medium, and the other, given in Chapter 9,[10] uses a photoconductor. The final chapter gives a summary of our work and some suggestions for future research in the field presented here.

1.3 REFERENCES

[1] B.G. Fallone and E.B. Podgorsak, Med. Phys. 10, 191(1983).

[2] B.G. Fallone and E.B. Podgorsak, Phys. Rev. B, 27, 2615(1983).

[3] B.G. Fallone and E.B. Podgorsak, Phys. Rev. B, 27, 5062(1983).

[4] B.G. Fallone and E.B. Podgorsak, IEEE Trans. Electrical Insulation, (in press).

[5] B.G. Fallone and E.B. Podgorsak, Phys. Rev. B, (in press).

[6] B.G. Fallone and E.B. Podgorsak, J. Appl. Phys., scheduled for August 1983, (in press).

[7] B.G. Fallone and E.B. Podgorsak, submitted to Medical Physics in May, 1983.

[8] B.G. Fallone and E.B. Podgorsak, IEEE Trans. Electrical Insulation, (in press).

[9] B.G. Fallone and E.B. Podgorsak, submitted to Medical Physics in May, 1983.

[10] B.G. Fallone and E.B. Podgorsak, submitted to Medical Physics in May, 1983.

CHAPTER 2

A REVIEW OF THE PHYSICS OF RADIOGRAPHIC IMAGING

2.1 INTRODUCTION

In this chapter we introduce, as background information, those areas of physics of radiological imaging that are related to the electrostatic radiographic studies discussed in the thesis. In general, the final visible image is produced from the x-ray image through an intermediate step referred to as the latent image. The spatial distribution of x-ray photons transmitted through the object in a plane perpendicular to the emerging x-ray beam forms the x-ray image and may be expressed in terms of variations in photon fluence, energy fluence or exposure.

In *radiography*, the x-ray image is first converted by ionizations and excitations into a latent image. If a photographic film is used the latent image consists of silver atoms distributed in proportion to the x-ray image. These atoms will initiate the transformation of the silver bromide crystals, on which they reside, into metallic silver during the development process to produce a visible image of the distribution. The latent image in electrostatic radiography, on the other hand, consists of electrostatic charges distributed according to the x-ray image and is subsequently rendered visible by charged powder (toner) or charged liquids. In *fluoroscopy*, the x-ray image is converted directly into a visible one by a fluorescent screen or an image intensifier-TV camera system.

The conversion of the x-ray image into an optimized visible image with a minimal exposure to the object is the subject of considerable radiological physics research. Numerous texts describing the radiological image formation and its characteristics are available.[1-5]

The discussion of radiologic imaging characteristics presented in this chapter for both the photographic film, which is the most widely used imaging technique in radiology, and for the electrostatic radiography, will serve as an introduction to studies of charge transport in electrostatic radiography described in subsequent chapters. Modern digital subtraction fluoroscopy systems are introduced at the end of this chapter so that a comparison can be made with the analog electrostatic subtraction technique discussed in final chapters.

Imaging characteristics are usually described by three parameters: sensitivity, quantum detection efficiency and resolution. Sensitiviy, sometimes referred to as speed, is defined as the reciprocal of the exposure required to produce a given optical density (usually 1). Quantum detection efficiency is the ratio of the number of x-ray photons that interact with the radiation sensitive medium to the number of photons forming the x-ray image.

Some of the most commonly used definitions for resolution are : *i*) the minimum distance between two points that can be distinguished in the image, *ii*) the number of line pairs per mm (*lp*/mm) or cycles per mm in the image of the bar pattern that can just be resolved, *iii*) the full width at half maximum, in units of distance, of the response to a point or line x-ray source, or *iv*) the Modulation Transfer Function (MTF) as defined from the theory of linear systems.

2.2 FILM AND SCREEN-FILM COMBINATION

2.2.1 QUANTUM DETECTION EFFICIENCY

Photographic films consist of a plastic base which is coated with an emulsion made up of silver halide crystals suspended in gelatin.

Dixon and Ekstrand[6] give an excellent account of x-ray film characteristics by presenting a model of a photographic emulsion which illustrates the relationship between fundamental physical processes, emulsion parameters and film characteristics.

The emulsion is extremely sensitive to visible light,[7] but absorbs only a fraction of the incident x-ray energy. Since the quantum detection efficiency of the emulsion is only $\sim$ 2%, film is usually used in conjunction with x-ray intensifying screens, consisting of a high atomic number phosphor, which emits visible or near-visible light when irradiated by x-rays. This process provides about 1000 visible or near-visible photons per x-ray photon absorbed.

In general, a double emulsion film (the thickness of each emulsion is about 10 μm) is sandwiched between two screens and housed in a light tight cassette which maintains firm contact between film and screens. In some cases the back screen may be of increased thickness to compensate for the reduction of the x-ray intensity incident on it. The x-ray photons are absorbed in the phosphor layer primarily by photoelectric interactions. The absorbed energy is transferred to secondary electrons which in turn deposit their energy by ionization and excitation. About 5% to 20% of the absorbed energy is radiated as visible or near-visible light which is almost totally absorbed in the film emulsion. It is thus generally agreed[8-10,11-15] that the main advantage of screens is their high quantum detection efficiency.

All phosphors used in screens are inorganic with most of them requiring a small amount of an activator. A list of most commonly used phosphors with some of their physical properties, taken from Arnold,[15] is given in Table 2.1 .

Table 2.1 - Physical Properties of Some Inorganic Phosphors

PHOSPHOR	Z	K-edge Energy (keV)	DENSITY g/cc	η %	LIGHT EMISSION SPECTRUM RANGE (nm)
Calcium Tungstate	74	69.5	6.06	3.5	340-540
Gadolinium Oxysulfide	64	50.2	7.34	15	400-650
Lanthanum Oxysulfide	57	38.9		12	480-650
Yttrium Oxysulfide	39	17.0		18	370-630
Lanthanum Oxybromide	57	38.9	6.30	13	360-620
Barium Strontium Sulfate	56	37.4	4.00	6	330-430
Barium Fluorochloride	56	37.4	4.70	13	350-450
Zinc Cadium Sulfide	30/48	26.7/9.6	4.43	18	450-650
Cesium Iodide	55/53	36/33.2	4.50	10	White
Barium Lead Sulfate	82	37.4	4.50		300-500

Z = Atomic number of the heavy element or elements, K-Edge = K Absorption edge energy of the heavy elements, η = Conversion efficiency (emitted light energy to absorbed x-ray energy as a percent). Light emission spectrum = gives the range of wavelengths of light photons emitted.

Table 2.1 Physical Properties of Some Inorganic Phosphors.[15]

2.2.2 SCREEN-FILM COMBINATION

Manufacturers modify screen parameters to achieve an optimum screen for a given application. Optimum sensitivity is achieved by matching the spectral response of the film to the light emission spectrum of the screen. Several investigators have studied the sensitivity of the newer screen-film combinations.[16-21]

In Table 2.2, adapted from Taylor et al.,[19] we compare the relative sensitivities of various screen-film combinations. The values in the table correspond to the exposure in mR at the screen-film position (taken with 75 kVp x-rays) needed to produce an optical density of 1.0 on the film. The table refers to hi-contrast and latitude films. Hi-contrast films are manufactured specifically to produce sharper (or higher contrast) images, and latitude films are manufactured to achieve a larger latitude or range of exposures over which the film will respond (i.e., a larger range of optical density). It must be noted that there is very little variation of speed with variations of kVp in the range from 75 kVp to 90 kVp.[16] It is only below 70 kVp and above 120 kVp that changes in kVp produce significant changes in speed.

2.2.3 RESOLUTION OF SCREEN-FILM COMBINATION

Of the many definitions given for resolution the one utilizing the Modulation Transfer Function (MTF) is the most complete. The MTF is the calculated response function of an assumed linear imaging

TABLE 2.2 Comparison of Relative Speeds for Various Screen-Film Combinations.[19] The values represent the exposure (mR) needed to achieve 1.0 density. (C= Hi-Contrast, L= Latitude)

Screens \ Films		DUPONT		CRONEX		AGFA-GEVAERT		GAF	KODAK	
		C	L	CL	C	C(RPL)	C(HR4)	C(SR2)	C(XR)	C(XRP)
DUPONT										
$CaWO_4$	Hi-Plus	0.50	0.47	0.54	1.00	0.43	0.93	0.41	0.25	0.50
	Par	1.00	0.93	1.00	2.14	0.93	2.00	0.87	0.54	1.07
	SP	0.71	0.66	0.71	1.24	0.62	0.32	0.58	0.35	1.71
	Detail	3.72	3.48	3.72	7.48	3.48	6.96	3.04	1.86	3.76
$BaPbSO_4$	Hi Speed	0.71	0.66	0.71	1.42	0.62	1.32	0.58	0.35	0.71
$BaF:Cl$	Quanta II	0.25	0.23	0.27	0.50	0.22	0.47	0.30	0.13	0.25
$LaO:Br$	Quanta III	0.13	0.12	0.14	0.25	0.11	0.23	0.10	0.07	0.13
KODAK X-OMAT										
$BaPb\ SO_4$	Fine	4.30	4.00	4.60	8.56	3.72	8.00	3.48	2.15	4.30
$BaPb\ SO_4$	Regular	0.58	0.54	0.58	1.16	0.62	1.07	0.47	0.26	0.58
GAF										
$CaWO_4$	TA-3	1.00	0.93	1.00	2.14	0.93	2.00	0.87	0.54	1.07
$CaWO_4$	TF-3	0.47	0.43	0.50	0.93	0.41		0.38	0.23	0.47
$CaWO_4$	SF-3	0.35	0.34	0.36	0.76	0.31		0.29	0.35	0.31

system to a sinusoidal pattern. In radiology, the transmitted spatial x-ray distribution can be resolved into a series of sinusoidal components of varying spatial frequencies and amplitudes. It is therefore possible, by knowing the MTF of a system, to predict the system's response to any complex input signal.

If we consider a one dimensional sinusoidal input radiation signal $A_{in}(x)$ of amplitude A and frequency ν, represented by:[22]

$$A_{in}(x) = A + (\Delta A) \cos 2\pi\nu x, \tag{2.1}$$

the input exposure contrast is defined as:

$$\Delta A/A = (A_{max} - A_{min})/(A_{max} + A_{min}). \tag{2.2}$$

If the output signal is represented by:

$$A_{out}(x) = CA + C(\Delta A)M(\nu)\cos[2\pi\nu x - \phi(\nu)], \tag{2.3}$$

where C is a proportionality constant, and $\phi(\nu)/2\pi\nu$ is the linear phase displacement between the input and output signals, the output exposure contrast now becomes equal to $M(\nu)\ \Delta A/A$, where $M(\nu)$, the Modulation Transfer Factor, is the ratio of the output exposure contrast to the input exposure contrast for a given frequency ν. A plot of $M(\nu)$ gives the Modulation Transfer Function.

However, since sinusoidal test patterns are difficult to build in radiology, square patterns giving square wave input signals are normally used. The relation of the square wave response $S(\nu)$ to $M(\nu)$ is

given by:[23,24]

$$S(\nu) = 4/\pi \{M(\nu) - M(3\nu)/3 + M(5\nu)/5 - M(7\nu)/7 \ldots\},$$

and

$$M(\nu) = \pi/4 \{ S(\nu) + S(3\nu)/3 - S(5\nu)/5 + S(7\nu)/7 \ldots\}. \quad (2.4)$$

The preferred method for MTF calculation, however, is the determination of the sinusoidal response to the response of an infinitely narrow line signal. This is reasonable because any one dimensional sinusoidal test pattern can be represented by an infinite number of line elements. The response to a beam of x-rays passing through an infinitely narrow slit is referred to as the Line Spread Function [LSF (x)]. We can then express the MTF as:

$$MTF(\nu) = \sqrt{O(\nu)O^*(\nu)} \; / \; \sqrt{O(_0)O^*(_0)} \;, \quad (2.5)$$

where * above indicates the complex conjugate and the one-dimensional Optical Transfer Function $O(\nu)$ is the Fourier transform of the LSF(x):[25,26]

$$O(\nu) = \int_{-\infty}^{\infty} LSF(x)\, e^{-2\pi i \nu x}\, d\nu \;. \quad (2.6)$$

Thus, the MTF (ν) is itself the absolute value of the Fourier transform of the LSF(x) normalized to 1 at $\nu = 0$. The two dimensional MTF(ν_x, ν_y) can be similarly evaluated by using the response to an x-ray

beam passing through a pin-hole. The two dimensional response function that results is called the Point Spread Function PSF(x,y).

Numerous investigators have measured the modulation transfer function for various screen-film combinations,[18,27-30] and one has fitted some of the experimental data with an empirical equation of the form[31]:

$$MTF(\nu) = 0.5\ \mathrm{erfc}[\alpha\ \ell n\ (\nu/\nu_o)]\ , \tag{2.7}$$

where ν_o is the frequency at which the MTF is 0.5, and α is an adjustable parameter when the MTF curve is plotted on a logarithmic-probability graph paper.

In Fig. 2.1, we present some Modulation Transfer Functions for various screen-film combinations taken from Arnold et al.[29] As expected, the response decreases for increasing spatial frequencies.

Speed and resolution of screen-film combinations are inversely related. A mathematical relationship derived by Rao and Fatouros[32] predicts that the product of the equivalent pass band N_e and the square root of the speed is constant for a given phosphor material and a given film. N_e is expressed as:

$$N_e = 2\int_0^\infty |MTF(\nu_x)|^2\ d\nu_x = 2\int_0^\infty |MTF(\nu_y)|^2\ d\nu_y, \tag{2.8}$$

where the two dimensional MTF is separable into its x and y components and $|MTF|^2$ signifies the average of the squares of the MTF's of individual layers over the whole screen. This relationship is shown in Fig. 2.2 for various screen-film combinations.

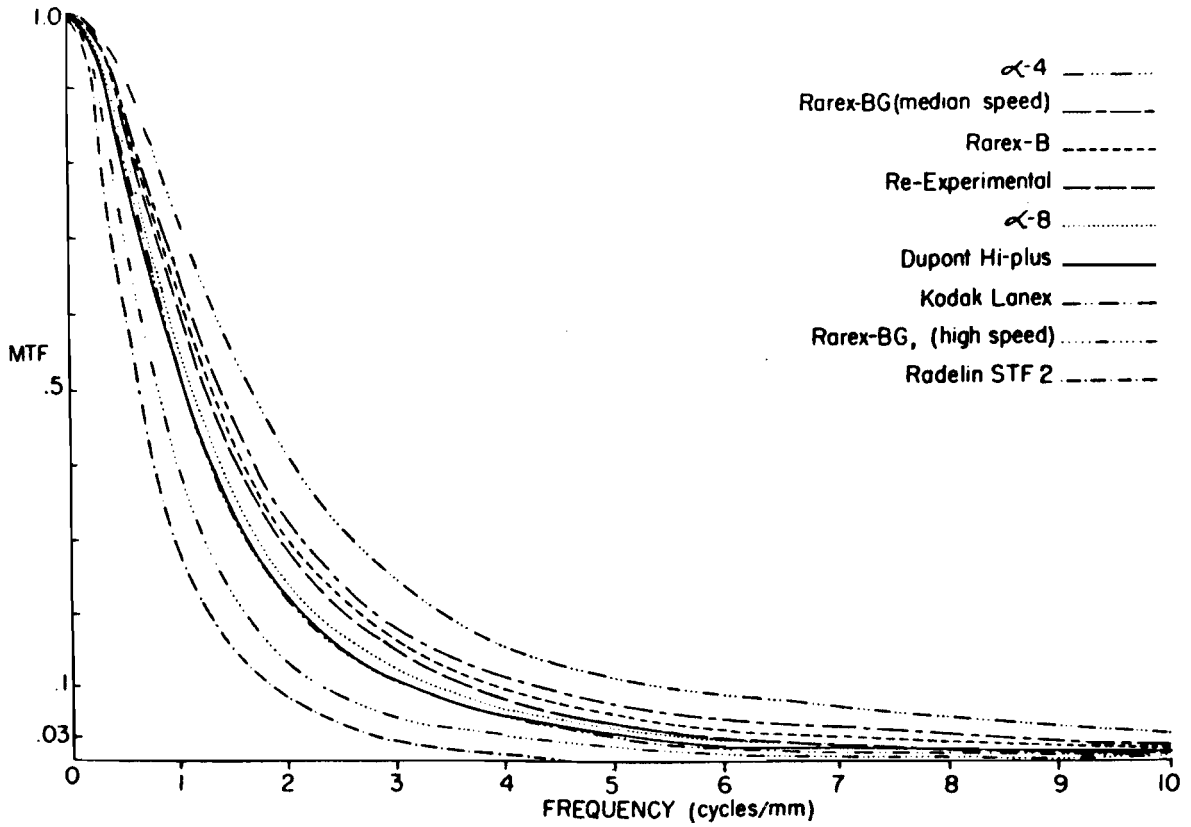

Figure 2.1 Modulation Transfer Functions (MTF) of several screen-film combinations.[29]

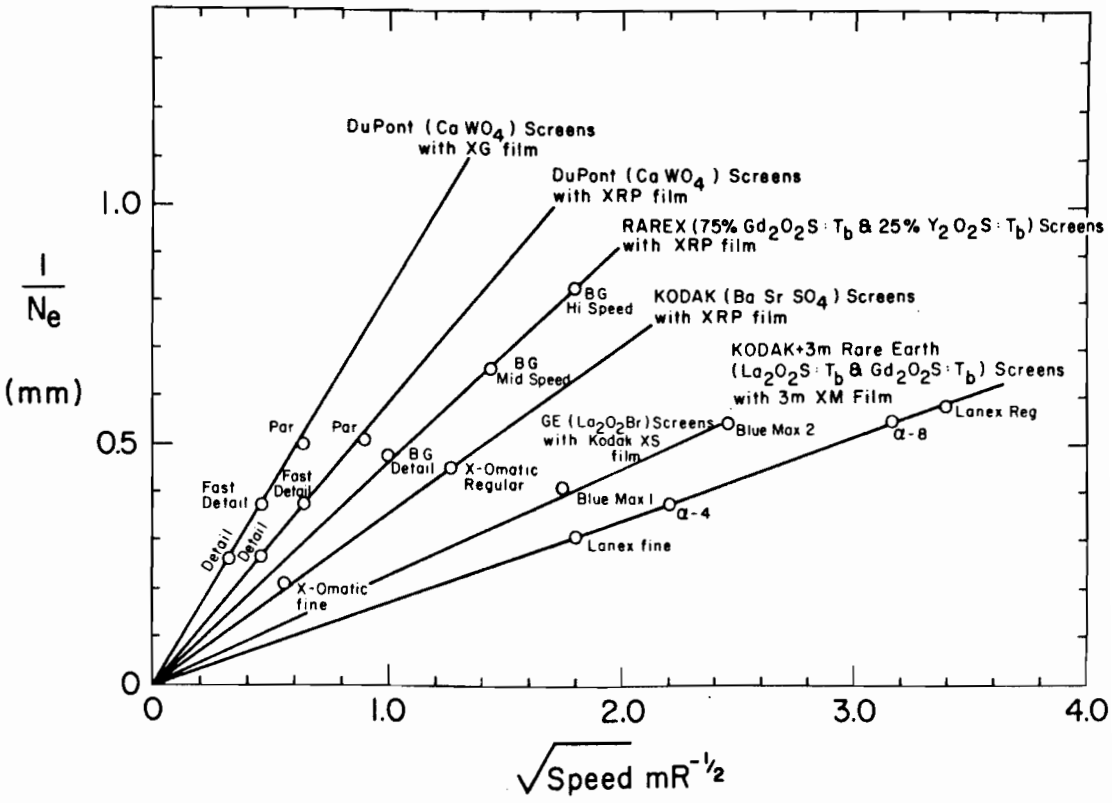

Figure 2.2 $(N_e)^{-1}$ plotted against $\sqrt{\text{Speed}}$ for different screen-film combinations.[32]

2.3 ELECTROSTATIC RADIOGRAPHY

2.3.1 BACKGROUND

Electrostatic radiography is an adaptation of the electrophotographic process [33] to diagnostic radiology. One of the electrostatic radiography techniques, xeroradiography,[34,35] has gained widespread use in mammography[36] and is commercially available from the Xerox Corporation. Although the imaging properties of the xeroradiographic technique have been studied in depth,[37-46] this technique has not yet replaced screen-film combinations in general radiography mainly because of its relatively low sensitivity.

New electrostatic techniques which achieve a high sensitivity have been suggested for possible use in general radiography. One of them is a technique which employs a high atomic number gas as the radiation sensitive medium at elevated pressures to generate free charge carriers through x-ray photon absorption and is referred to as Electron Radiography[47-49] or gas ionography.[50-53] This concept originated from a technique suggested much earlier, where the photoelectrons emitted from the electrodes by the radiation generated charge carriers in air.[50,51]

To improve the sensitivity of ionography an electrostatic system employing a high atomic number liquid has been built.[54] Recently, a solid state technique other than xeroradiography, relying mainly on high purity solid state absorbers has been studied.[55,56]

The production of the latent image in electrostatic systems proceeds as follows: *i*) the object of interest is exposed to x-ray photons, *ii*) free charge carriers, proportional to the photon energy

fluence transmitted through the object, are produced in the absorbing medium (e.g., gas, liquid or solid), *iii*) these free charge carriers drift in an effective electric field and are collected on a blocking electrode thereby forming a latent image with a surface charge distribution according to the x-ray fluence transmitted through the object; *iv*) the latent image is developed by powder aerosols or liquid colloids,[57] and v) the visible image is fixed with heat or chemical means.

2.3.2 PROPERTIES OF ELECTROSTATIC LATENT IMAGE

2.3.2.1 Gas Ionography

The sensitivity of gas ionography, using xenon or freon at elevated pressures, most nearly approximates that of screen-film systems and depends on chamber design, as well as on methods of image development. The charge collection efficiency, defined as the charge collected to charge produced in the radiation sensitive medium, has been studied for a wide range of applied voltages, pressures, chamber geometries and gas mixtures.[58,59]

A considerable increase in sensitivity can be achieved by adding special molecular gases to the freon or xenon used in high-pressure gas ionography. This technique gives images of unity optical density with as little as 10 or 100 μR exposures, but the image sharpness (i.e., resolution) and noise characteristics are adversely affected. There are, nevertheless, clinical situations such as pediatric studies, where lower resolution would be accepted to obtain higher sensitivity. The loss of resolution with amplification results from this technique being a pure electron

collection process accompanied by a large lateral particle diffusion, and from an increase in quantum noise due to low exposures. A one-hundred-fold increase in sensitivity will reduce the standard gas ionographic resolution of 15 $\ell p/mm$ to 1.4 $\ell p/mm$.[60]

It was observed that the image unsharpness (i.e., lack of resolution) in gas ionography is mainly due to the mobility of free electrons which is much larger than that of free ions. The Xonics Corporation has improved the resolution of their XERG system by using gaseous electron scavengers to collect negative charge in the form of ions.

The x-ray absorption efficiency in the gas is a function of beam quality, electrode separation, gas composition, as well as of pressure, and is considerably reduced by some of the absorbed energy emerging as fluorescent radiation.[52]

Because of the geometric lateral shift of x-ray path when photons travel the distance from tube focus to collecting surface, there will be a significant blur near the edge of the radiograph if the collecting electrode surface is flat. Some investigators have solved this problem by curving the electrode surface appropriately,[49,52] while others have deliberately distorted the collecting field of a planar electrode system.[37]

The design and manufacture of a practical gas ionography system involves considerable engineering difficulties. Because of the mechanical strength needed to withstand gas pressures of up to $\sim 10^3$ kPa ($\sim$10 atmospheres) the window material must be very strong and at the same time transparent to x-rays. The commercial XERG system achieves great strength in a thin assembly with minimum photon attenuation by the use of a new resin reinforced graphite. The imaging gas must be recycled

after x-ray exposure and the chamber properly flushed.

The latent image is formed on the blocking electrode consisting of a plastic insulator with conductive backing. The final image is obtained after the blocking electrode is put through the development and fixation processes.

2.3.2.2 Liquid electrostatic system (liquid ionography)

In principle, ions can be collected from any high resistivity (10^{15} Ohm-cm) liquid containing a high atomic number component. The two most commonly used liquids for ionography are: carbon tetrachloride ($CC\ell_4$) and tetra-methyl-tin [$Sn(CH_3)_4$]. This system resembles the gas ionographic unit, but operates at ordinary atmospheric pressure and employs an electrolytic purification chamber. The high density of the liquid leads to a significant increase of x-ray absorption efficiency, which should result in higher sensitivity. However, there is a tendency for charge recombination in liquids, resulting in a considerable dependence of collected charge on the applied electric field. Because of this, the sensitivity of the liquid chamber is only about 50% of that of an optimal gas ionographic chamber. The resolution of a liquid chamber was found to be similar to that of a gas chamber.

A sealed system for liquid ionography capable of producing a copy of the charged image with a varying degree of edge enhancement and sensitivity has been suggested.[61,62] Engineering difficulties have prevented further practical development of this technique.

2.3.2.3 Solid state radiography

Construction difficulties and relatively low sensitivities have stopped further development of liquid and gas ionography. The limited

success of gas and liquid ionographic techniques would suggest a study of ionic solids as the x-ray absorbing media in an ionographic device. Studies of thermoluminescence and thermally activated currents, however, showed that the charge carrier yield produced during an x-ray irradiation of an ionic solid is extremely low.[63] This would then preclude the use of ionic solids in ionographic devices. The recent advances in crystal growing techniques, however, allowed a high degree of control over the impurity concentrations in ionic solids and created a new interest in the charge transport phenomena in ionic solids. It has been found that the yield of charge carriers and their mobility during the irradiation is not an intrinsic property of the solid but rather is strongly dependent on the concentration of impurity and defect centers in the material.[64-66] Furthermore, it was observed that a decrease in impurity concentrations from 100 parts per million (ppm) to less than 10 ppm increased the radioconductivity of the ionic solid by a factor of 10^6, (from 10^{-16} Coulomb/cm^2-mR to 10^{-10} Coulomb/cm^2-mR), suggesting a possible use of this phenomenon in electrostatic radiography.[55,56]

The device used for solid state radiography resembles the gas and liquid ionographic systems but is much simpler because no high gas pressure or liquid containment is required. The absorbing medium is an ionic solid, preferably with a high effective atomic number to increase x-ray absorption. The material is juxtaposed with a plastic charge collection foil (Mylar) and this combination is inserted between two electrodes. The radiation transmitted through the object produces free charge carriers (i.e., electrons and holes) in the absorbing medium. These charge carriers migrate in the applied electric field ($\sim$ 1000 V/mm) until they are trapped at the interface with the collecting foil (blocking electrode) thereby

producing a latent image. The attempts using sapphire (Al_2O_3) as the absorbing medium were not successful,[55,56] however, and further work in this area was suspended.

Other investigators used photoconductors, PbO and CdS, as the radiation sensitive medium, and concluded that exposures greater than those used in pressurized gas ionography or screen-film combinations are necessary to achieve similar image qualities.[67,68]

2.3.3 DEVELOPMENT OF THE LATENT IMAGE

In the solid state electrostatic systems mentionned above the latent image is trapped at the interface between the absorber and the blocking electrode. The simplest way to transfer charges to the polymer of the blocking electrode is through a Paschen discharge by peeling the polymer foil from the absorber (see Sec. 3.6). For gas and liquid ionography , however, the free charge carriers forming the latent image actually reside on the polymer surface itself.

The charged polymer is then placed into a xerographic development apparatus where an air nebulizer injects a cloud of electrostatically charged powder particles which are separated by a high voltage grid of appropriate polarity to produce either a positive or negative visible image. The developed image can then be fixed by heat or by an exposure to trichloroethylene fumes. A more detailed discussion of the development process is given in Sec. 3.6.

2.3.4 XERORADIOGRAPHY

2.3.4.1 Latent image formation

The radiographic technique of xeroradiography is based on the dissipation of the surface charges on a photoconductive layer when irradiated with x-rays.[69] The technique has had partial success for general radiography and its main use has been in mammography.[36] We summarize in the following paragraphs accounts given by Schaffert,[70] Boag,[34] and Fatouros.[71]

The xeroradiographic plate consists of a photoconductive insulating layer of amorphous selenium on a metal base. A corona-charging unit is used to deposit a uniform density of positive (or of negative) charges on the selenium surface. Corona-charging will be further discussed with reference to electrets in Sec. 5.1.

The surface potential to which the plate is charged will depend upon the thickness of the selenium layer, and commercial plates of 130 μm are charged up to 1000 V - 1600 V (40 nC/cm^2 - 70 nC/cm^2). The selenium layer is both mechanically vulnerable and extremely light sensitive. Following the corona-charging, the selenium plate is exposed to the x-ray transmitted through the object being imaged. The x-rays absorbed in the selenium plate produce charge pairs which drift in the field produced by the initial surface charge layer to ultimately dissipate the layer in amounts proportional to the local incident radiation intensity. The residual voltage V after an x-ray exposure R has been found experimentally to follow an exponential relationship of the form.[38,48]

$$V = V_o e^{-R/R_o} \tag{2.9}$$

where V_o is the initial voltage on the selenium plate before

the exposure and R_o is a characteristic of a given plate related to sensitivity and beam quality. The resultant latent image on the surface of the selenium layer is rendered visible by depositing charged powder onto the layer and subsequently, transfering the powdered pattern onto a white paper. The plate is then cleaned and ready for further exposures.

In general, selenium plates are less sensitive than screen-films and the charge collection efficiency for xeroradiography is only 8%, compared to 20% to 30% for liquid ionography, and up to 50% for gas ionography. [40-44]

2.3.5 EDGE ENHANCEMENT

The measurement of resolution in electrostatic radiography is more complex than for screen-films. The problem originates from the edge contrast capabilities of electrostatic development procedures. In powder cloud development, for example, a powder line is drawn at boundaries between two areas of slightly different charge densities thereby enhancing the boundary. Edge enhancement arises from the fringing fields produced near a charge discontiunity.[72-75] These fields distort the trajectories of the charged powder drifting in an externally applied field ($\sim$500 V/cm) towards the latent image, as shown in Fig. 2.3.[75] The main distortion occurs 10 μm to 20 μm above the charge pattern in a region about 100 μm wide, giving rise to a depletion region where no powder can be deposited.[62] The powder is falling uniformly to about 20 μm above the charge pattern, where it is swept to the right to be deposited just inside the charge discontinuity thus enhancing the edge in the pattern. A further discussion of powder (toner) trajectories will be given in the section on experimental procedures (Sec. 3.6.3).

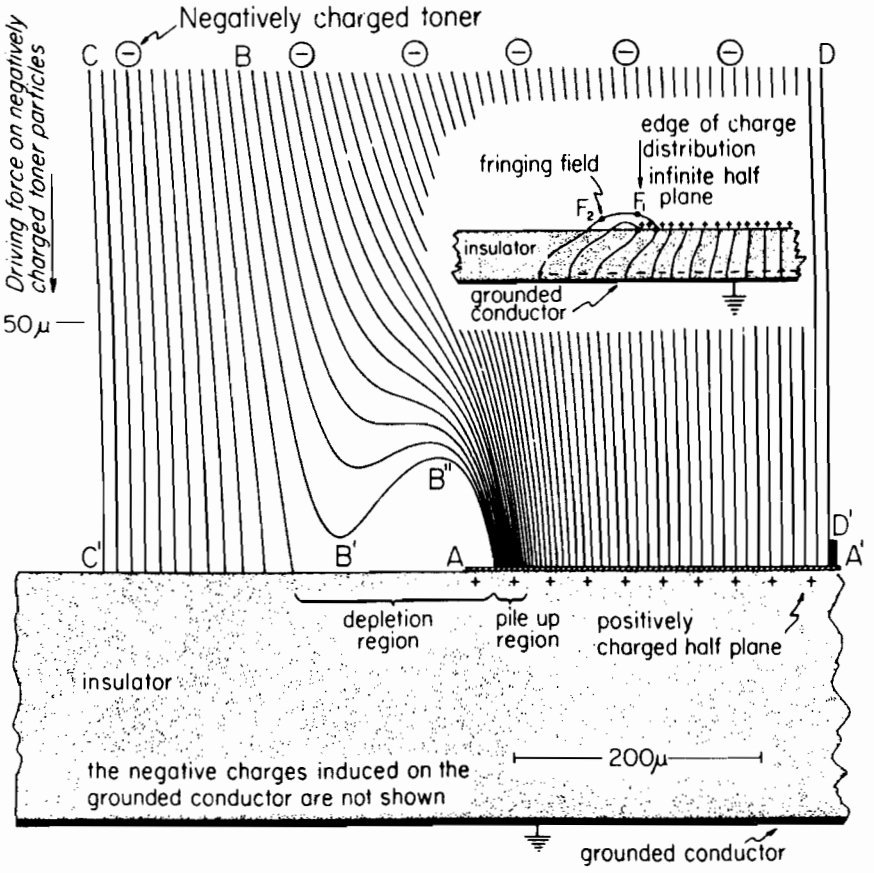

Figure 2.3 The trajectories of charged powder (toner) particles liberated at top of diagram and directed by an electric field towards the semi-infinite charge pattern to the right of A. The insert shows the nature of the fringing field at the edges of a charge pattern. The calculations were done assuming a toner diameter of 5 μm with a charge of 8×10^{-17}C per particle; viscosity of air 1.83×10^{-4} poise; driving uniform field of 500 V/cm downward; surface charge density 1.0 nC/cm^2 and dielectric constant of polymer 3.3.[75]

The Modulation Transfer Function (MTF) method of measuring the resolution is not very useful since the MTF does not represent the absolute magnitude of the response (i.e., MTF's are normalized to unity at zero frequency), and the function cannot be easily measured because of the very low mean level density differences across the charge discontinuity.[76] In photographic and optical imaging systems the response to a discontinuity is studied by scanning an edge to produce an Edge Response Function, differentiating it to obtain the Line Spread Function and finally taking the Fourier transform to obtain the Modulation Transfer Function. In electrostatic imaging systems, however, resolution is studied in absolute terms and is expressed as the Contrast Transfer Function CTF:[46,75]

$$CTF(\nu) = \gamma\, MTF(\nu), \tag{2.11}$$

where ν is the spatial frequency and γ is the slope of the D (optical density) versus $\log$ R (exposure) curve. Figure 2.4 shows xeroradiographic CTF's measured using knife-edge low contrast exposures at different mean density levels as indicated in the figure.[77] The contrast ($\Delta D/D$) in each case corresponds to a change of only 1 quantum/μm^2 across the edge. In contrast to screen-films where γ is a constant in the normal range of operation, γ for xeroradiography (and ionography) varies quite substantially. Although the zero frequency γ in Fig. 2.4 is less than 0.2 [$MTF(\nu = 0) \equiv 1$], γ may be as high as 10 units at ν = 1 cycle/mm [$MTF(\nu \neq 0) \leq 1$].

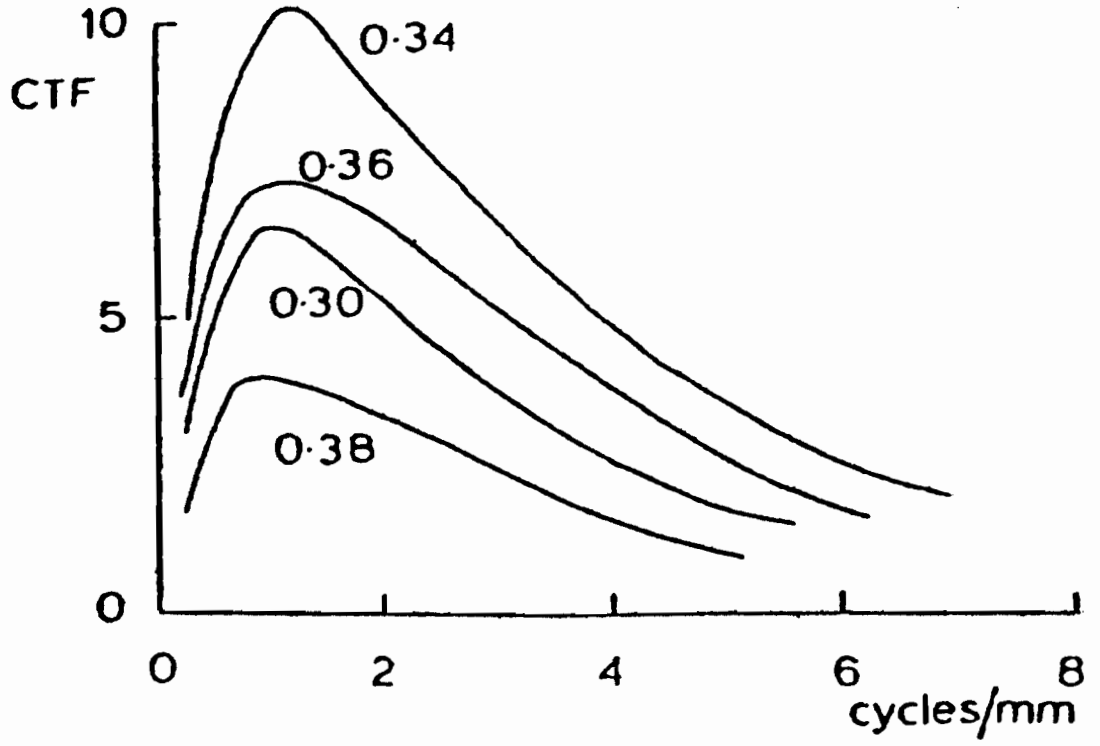

Figure 2.4 Contrast Transfer Function (CTF) for xeroradiography for a series of low contrast exposures taken at different mean exposure levels. The different mean density levels are indicated on each curve.[77]

2.4 Comparison Between The Photographic and the Electrostatic Radiography

Some of the advantages of screen-films over direct exposure films are *i*) lower radiation dose to patients, *ii*) higher film contrast at medium film density, and *iii*) high speed which allows the use of shorter exposure times, thereby minimizing blurring from motion. The disadvantages of screen-film compared to direct exposure film include *i*) lower resolution, *ii*) higher noise, and *iii*) artifacts from the screens. Lower resolution may not be a problem since motion blurring may be more significant.[78] A comparison of optical density against exposure is shown in Fig. 2.5(*b*) for type AA film[68,79] and for type Min-R screen-film,[80] respectively.

It is difficult to compare physical factors, such as resolution, contrast, and noise, for the xeroradiographic (or ionographic) system with those for screen-film systems.[42] The advantages of xeroradiography (ionography) include *i*) wide exposure latitude, *ii*) increased small-area contrast (as a result of the inherent edge-enhancement effect), and *iii*) visualization without a view box.[42,81] The disadvantages include *i*) low broad-area contrast, *ii*) higher radiation dose, *iii*) powder artifacts in the image, and *iv*) mechanical failure for xeroradiography.[81] Figure 2.6 shows characteristic curves for a mammographic screen-film combination and for xeroradiography.[71] The curves illustrate a much wider latitude but lower broad-area contrast for the xeroradiographic (or ionographic) systems. However, detail recognition in the electrostatic systems is achieved through edge enchancement arising from the charge gradients.

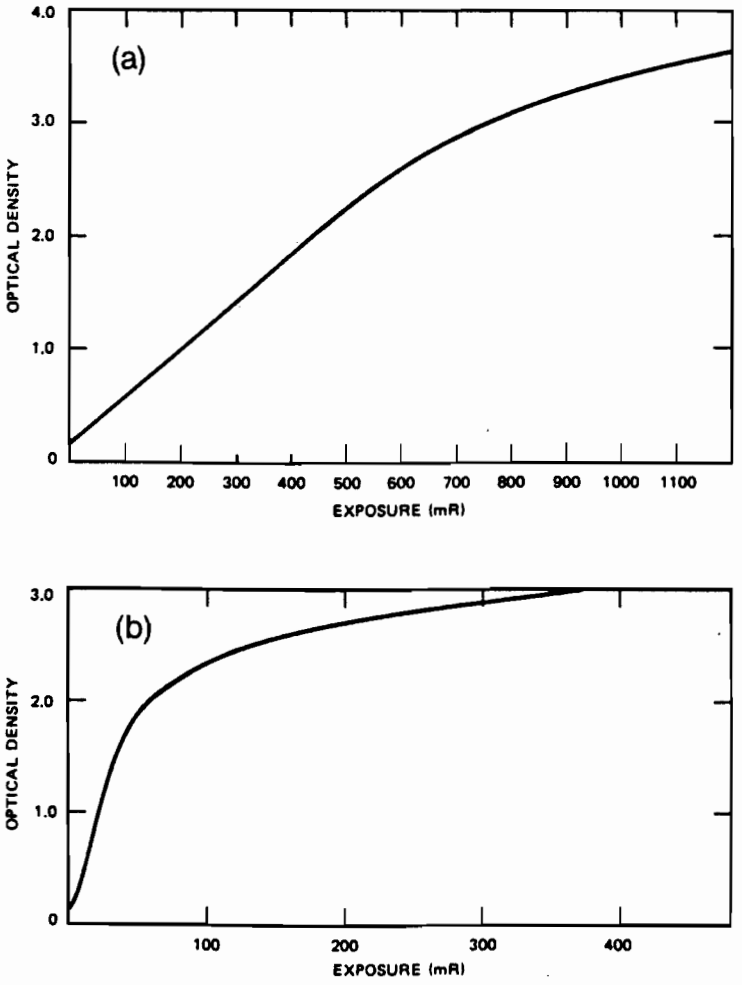

Figure 2.5 Optical density as a function of exposure for (*a*) type AA film using a 28 kVp beam ($\bar{E}$ = 18 keV) and a Mo filter,[68,79] (*b*) for type Min-R screen-film system using 28 kVp beam.[80]

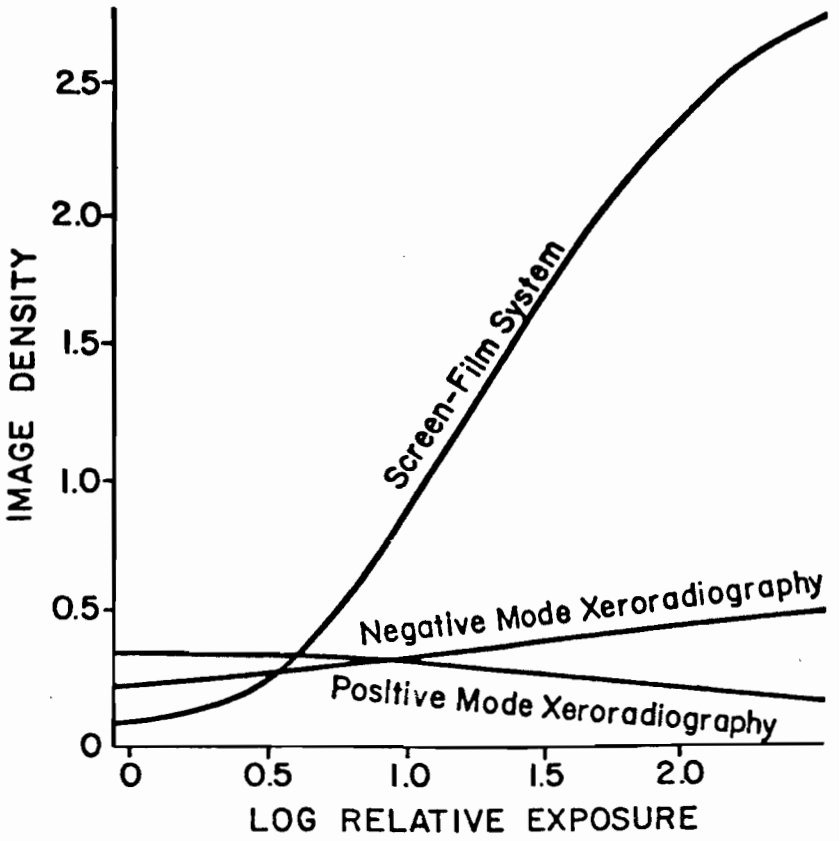

Figure 2.6 Optical image density against log relative exposure for screen-film system and xeroradiography.[71]

Brodie and Gutcheck have made an interesting theoretical estimate of the lowest exposure necessary to record the smallest feature of interest.[82] An example of their results is shown in Fig. 2.7, where the maximum exposure necessary for observing calcifications 150 μm in size with a probability of error of 1 in 10 is plotted as a function of average beam energy. We see that very small phenomena are more easily detected in xeroradiography. This is due to the edge enhancement properties of electrostatic development procedures.

In electrostatic radiography, ionography has been found to be more sensitive than xeroradiography.[45] We show in Table 2.3[45] the overall sensitivity in units of optical density (D) per exposure (mR) of xeroradiography and gas ionography for various x-ray beam qualities.

A good comparison between systems can be made in the radiology clinics themselves. In Table 2.4, we show a list of typical measured exposures in mammography[83] from various centres in Ontario for a number of different radiographic imaging modalities. In the table, the manufacturer Xerox refers to xeroradiography and Xonics to a gas ionographic system called Electron Radiography.

In general, screen-film combinations are more sensitive than xeroradiography and about as sensitive as the reported Electron Radiography technique. Screen-film combinations are preferred for general radiography while the electrostatic techniques are normally utilized for cases where very small low density lesions are to be detected.

Table 2.3 Comparative Imaging Sensitivity[45]

kVp	Xeroradiography (D/mR)	Gas Ionography (D/mR)
45	.066	.304
65	.097	.57
90	.11	.73
105	.12	.79

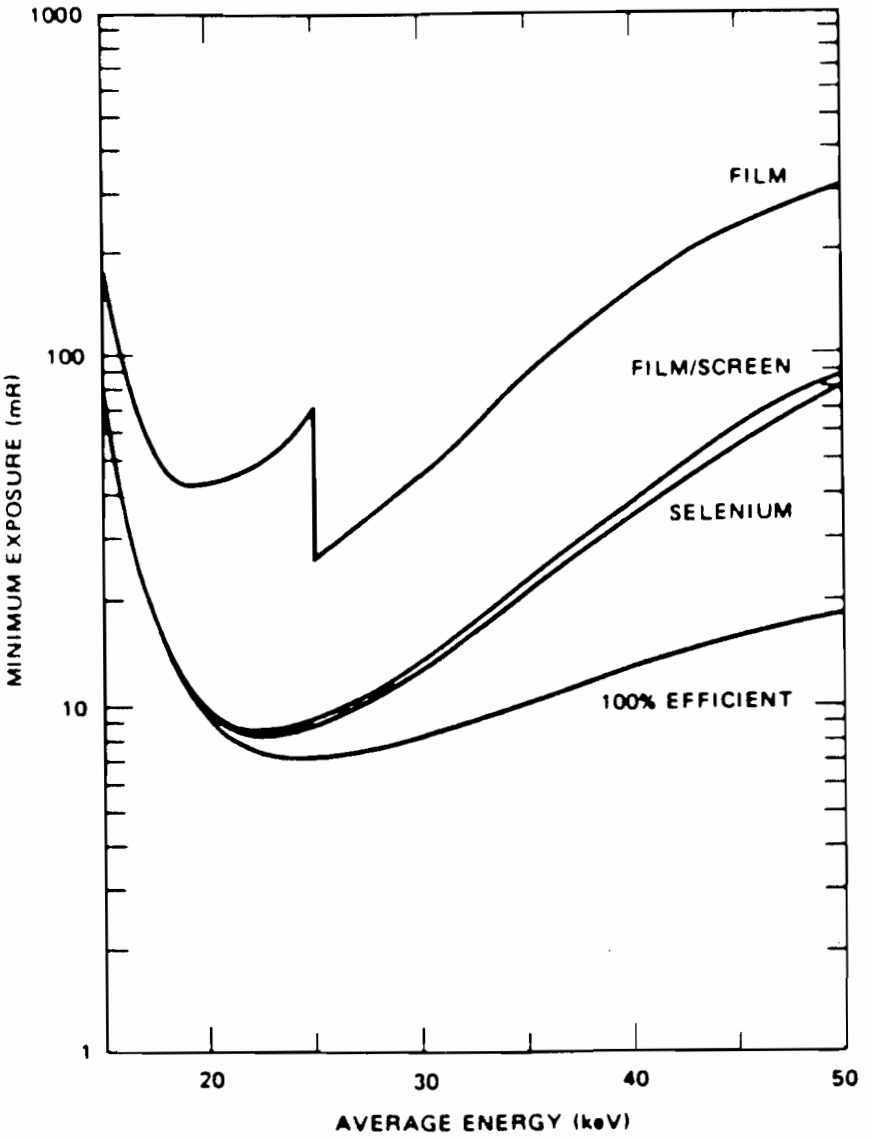

Figure 2.7 Minimum exposure necessary for viewing a 0.15 mm microcalcification in 5 cm of breast tissue, with a probability of error of 1 in 10, as a function of average x-ray beam energy for four detecting layers: film, screen-film, selenium plate, and a 100% efficient detector.[82]

TABLE 2.4
Measured Exposures in Mammography
(Typical Values in Ontario 1980)

(1) Manuf.	(2) Absorbing Material	(3) Imaging Material	(4) Anode	(5) Filter (mm)	(6) kV_p	(7) HVL mm Al	(8) Exposures Surface of Breast (R)	(9) Mean Dose in mGy per R to Surf.	(10) Mean Dose to Glandular Tissue (mGy)
Kodak	Film	AA film	Mo	.03 Mo	32	.37	20	1.0	20
Kodak	Film	No screen	Mo	.03 Mo	25	.30	4	.9	3.6
Dupont	Lo Dose screen	MRF-31	Mo	.06 Mo	33	.44	.9	1.3	1.2
Xerox	Selenium +ve mode	Selenium	W	2 Al	42	1.1	1.0	2.8	2.8
	−ve mode	Selenium	W	2 Al	42	1.1	.7	2.8	2.0
Kodak	Min R screen	Min R.	W	.5 Al	30	.37	.4	1.0	.4
Kodak	Min R screen	Min R.	Mo	.03 Mo	36	.39	.5	1.1	.5
Dupont	Lo Dose II screen	MRF-31	Mo	.03 Mo	29	.5	.24	1.4	.3
Dupont	Lo Dose II screen	Lo Dose	Mo	.03 Mo	30	.35	.5	1.0	.5
Xonics	Freon at 5 atmos.	Foil	W	.9 Al	36	.83	.2	2.2	.4

Table 2.4 List of typical exposures in mammography for a number of different radiographic imaging modalities.[83] Mean dose to glandular tissue of breast per R to the surface of breast is also corrected for backscatter.

2.5 DIGITAL SUBTRACTION ANGIOGRAPHY

2.5.1 SUBTRACTION RADIOGRAPHY

Very often in radiological procedures some type of contrast material, such as a radiopaque iodine compound, is introduced to facilitate the identification of low contrast interfaces or to accentuate the difference between two regions of similar radiopacity. Depending upon the region to be examined the introduction of the contrast material can be either a very simple or an extremely complicated procedure for both the examiner and the patient.[84]

Since des Plantes[85] first described a photographic subtraction technique in 1935 to suppress unwanted background information and to enhance the edges of the regions of interest, photographic subtraction methods have become increasingly popular as an adjunct to contrast procedures to suppress the appearance of structures overlying the regions of interest. In essence, the image of a patient taken after an injection of contrast material to delineate a region of interest is subtracted from one taken prior to the injection. Normally, the two photographic x-ray films would be subtracted by special darkroom techniques, the results of which however, are only fair.

Important procedures such as arteriograms using intravenous injections of radiographic contrast media and photographic film systems were reported as early as the 1940's.[86,87] The development of catheterization techniques for the arterial administration of contrast media soon led to the replacement of the intravenous approach with the much more invasive (i.e., more difficult for patient and examiner) intra-arterial procedures. The morbidity associated with these invasive catheterization

procedures was clearly outweighed by the improved resolution and contrast of the images relative to those obtained using intravenous methods. Subtraction of unprocessed information taken from the video output of fluoroscopic systems, adequate for augmentation of arterial injection techniques, was not sensitive enough to be used with intravenous injections of the contrast media. However, techniques capable of imaging the small contrast levels produced after an intravenous injection began to appear in the early seventies.[88-91] These techniques involved the use of time and K-edge energy subtraction methods for iodine imaging.

But it was only when digitized video images from an image intensifier T.V. camera system were introduced by Mistretta and colleagues at the University of Wisconsin[92-95] and a group at the University of Arizona[96-98] that intravenous digital subtraction angiography became, what many observers have stated,[99] perhaps the most significant innovation in diagnostic radiology, since the introduction of the CT (computerized tomography) scanner. Digital (computerized) subtraction techniques and computer processing may now make it possible to return to intravenous angiography while maintaining good image contrast and acceptable resolution.

It is important to understand that the computerization process does not improve the image. The analog photographic image is still far superior to the digitized computer image. However, it is in the resultant image after subtraction that the computer image is superior to the photographic one.

2.5.2 DIGITAL SUBTRACTION FLUOROSCOPY

In conventional fluoroscopy an x-ray image intensifier replaces the film as the primary image receptor. The x-ray image intensifier is a vacuum tube that contains an input screen that converts the x-ray pattern into an electron pattern, and an electro-optical system that accelerates and focuses the electrons into an output screen which finally converts the electron pattern into a high intensity visible one. The output screen is then optically coupled to a television camera (e.g., vidicon, orthicon or plumbicon) so that the images can be viewed on a video monitor or recorded on a video disc or tape.

Current digital radiography systems are divided into digital fluoroscopy systems and the much less common scan projection radiographic systems. In the latter systems collimated x-ray beams are used to scan the patient, either by moving the beam over the patient or by moving the patient through the beam. The detectors used are usually scintillators, photodiodes or high pressure xenon ionization chambers. In digital fluoroscopy, the main components of which are shown schematically in Fig. 2.8,[100] the video signals are digitized and stored in a computer memory for future use. In general, the vidicon camera is replaced by a 1000: 1 signal-to-noise ratio plumbicon camera, and a logarithmic amplifier may be inserted between the video output and the analog-to-digital converters (ADC) to compensate for the exponential attenuation of x-rays in the patient. Subtraction of stored images is then easily achieved through computer manipulation. The complexity of the system can be better appreciated by showing in Fig. 2.9 a block schematic of a digital fluoroscopy unit as developed by the University of Arizona.[101] In subsequent chapters, (i.e., chapters 8 and 9) we will present analog radiographic subtraction techniques utilizing electrostatic imaging principles.

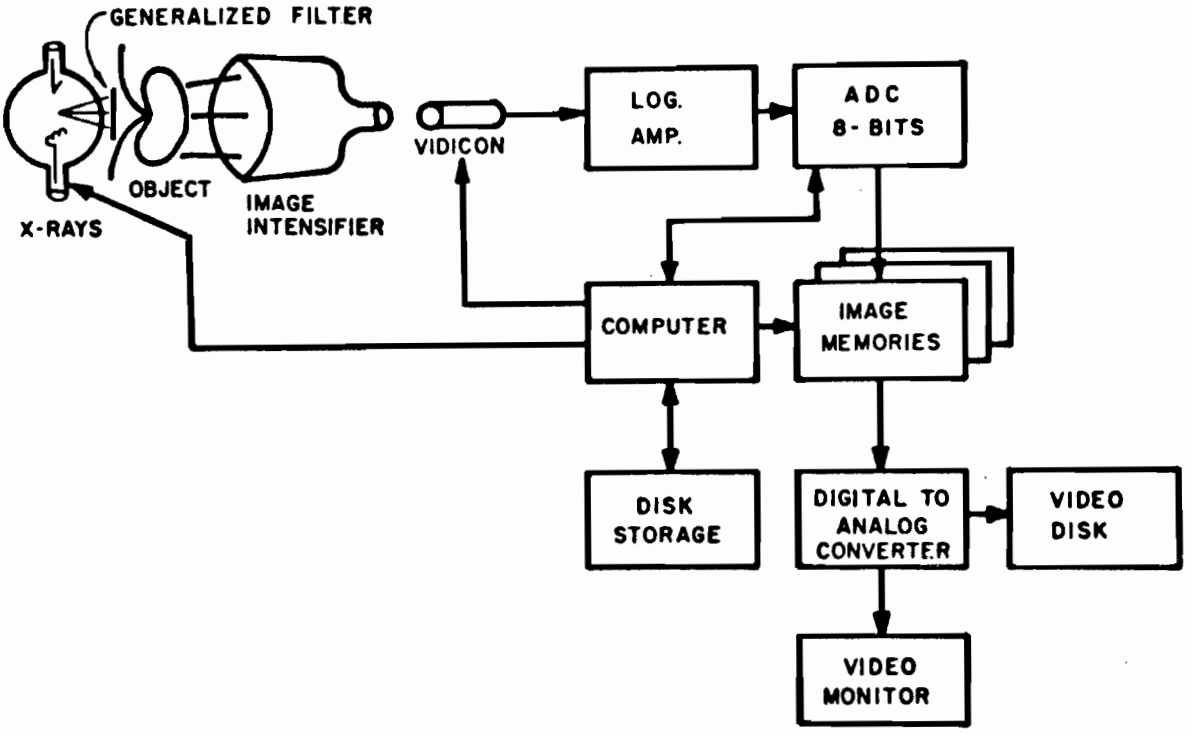

Figure 2.8 The primary components of a digital fluoroscopy system are the x-ray tube, image intensifier, a low noise video camera (lead-oxide vidicon or plumbicon), a logarithmic video amplifier, a high speed ADC, image memories, large disc, digital to analog converter (DAC) for video display of images and tape for storage of images.[100]

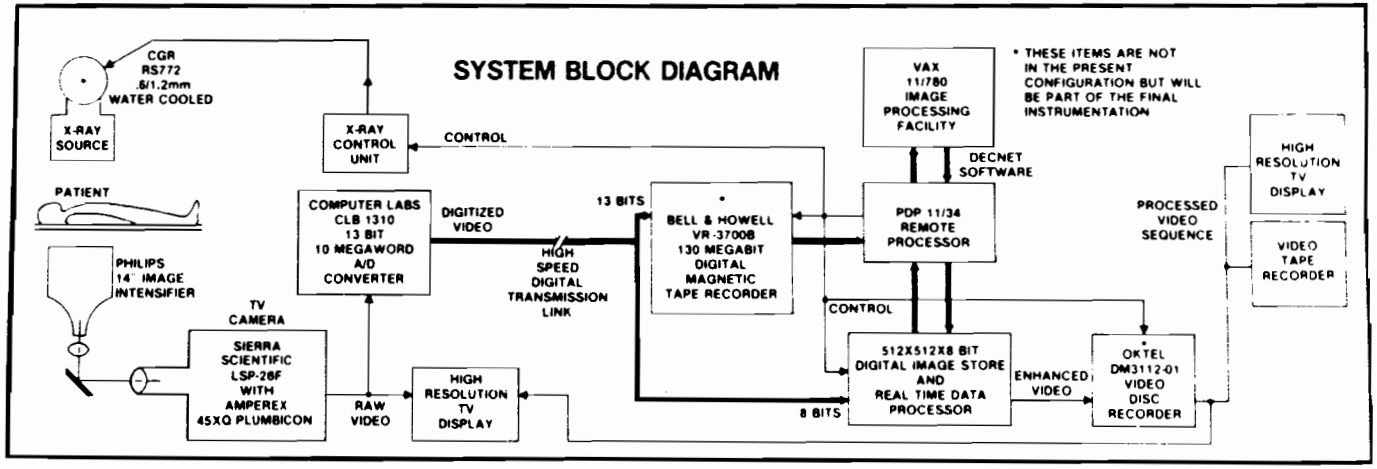

Figure 2.9 Block diagram of a realistic digital fluoroscopy system developed by the University of Arizona.[101]

2.6 SUMMARY AND CONCLUSION

An introduction to basic characteristics of photographic and electrostatic radiography has been given. In the photographic film, exposed silver bromide crystals in the emulsion are transformed into metallic silver to render the x-ray image visible. In electrostatic imaging, on the other hand, the exposure produces charge carriers that drift in an effective electric field and get trapped on a blocking electrode to form a charge layer distribution proportional to the exposure, which is rendered visible by electrostatic powder (toner) or electrostatic colloids.

Important imaging parameters, such as sensitivity, spatial resolution, and quantum detector efficiency have been defined and the various methods used to improve these parameters for the different radiographic techniques have been discussed. An intensifying screen has been added to the photographic film while various studies have been performed for the electrostatic absorbing medium (e.g., high atomic number gases at elevated pressures, high atomic number liquids, solid state ionic crystals and photoconductor materials), to increase the sensitivity and quantum detector efficiency. The various imaging parameters were compared for the different techniques. In general, although the sensitivity of screen-film radiography is superior to that of electrostatic radiography, the property of edge enhancement and independence of silver are interesting advantages of electrostatic systems over screen-film combinations. Moreover, edge enhancement permits the visualization of lesions that are smaller than those that can be detected by screen-film combinations.

The technique of subtracting a radiograph taken before, from one taken after the injection of a contrast medium (e.g., an iodine solution), to delineate certain regions of interest was introduced. Because of the importance of this technique to clinical diagnosis, conventional fluoroscopy was briefly described to explain the modern digital subtraction fluoroscopic systems where the video output of the TV camera is digitized and entered into a computer for the subsequent subtraction procedures.

The chapter serves as an introduction to the discussion of our investigation of the charging characteristics of the electrostatic latent image. This image is essentially a foil electret with a surface charge distribution modulated by the photons transmitted through the object. This discussion will include the determination of an expression representing parallel-plate ionization chambers filled either with air or with high atomic number gas at elevated pressures, so that the charging and discharging properties of the electret production technique can be studied. The results of this study will then be applied to improve the understanding of the physical properties of the ionographic latent image. The results will also be used to demonstrate the feasibility of radiographic image subtraction based on electrostatic techniques with either a gas or a solid as the radiation sensitive medium which could eventually be developed into an inexpensive alternative to complex digital subtraction systems.

REFERENCES

1 H.E. Johns and J.R. Cunningham, The Physics of Radiology (C.C. Thomas, Springfield, 1983).

2 M.M. Ter-Pogossian, The Physical Aspects of Diagnostic Radiology (Harper and Row, New York, 1967).

3 The Physics of Medical Imaging: Recording System Measurements and Techniques, edited by A.G. Haus (Am. Inst. Phys., New York 1979).

4 W.R. Hendee, Medical Radiation Physics (Year Book, Chicago,1970).

5 W.J. Meredith and J.B. Massey, Fundamental Physics of Radiology (John Wright and Sons, Bristol, 1972).

6 R.L. Dixon and K.E. Ekstrand, Med. Phys. 3, 340(1976).

7 A.N. Stevels, Medica Mundi 20, 12(1975).

8 J.F. Hamilton and B. Bayer, J. Opt. Soc. Amer. 55, 528(1965).

9 G.R. Biad, R.C. Jones and A.E. Ames, Appl. Opt. 8, 2389(1969).

10 H.M. Cleare, in Med. X-Ray Photo-Opt. Sys. Eval. edited by Weaver, Wagner and Goodenough (Dept. of HEW, 1975), p. 184.

11 M.M. Ter-Pogossian, in The Physical Aspects of Diagnostic Radiology, (Harper and Row, New York, 1967), p. 203.

12 B. Arnold, in The Physics of Medical Imaging: Recording System, Measurements and Techniques, edited by A.G. Haus (Am.Inst.Phys. New York, 1979).

13 T.R. Fewell and K.E. Weaver, in Med. X-Ray Photo-Opt.Syst. Eval., edited by Weaver, Wagner and Goodenough, (Dept. of HEW, 1975).

14 B. Arnold, in The Physics of Medical Imaging, edited by A.G. Haus, (Am.Inst.Phys., New York, 1979), p.35.

[15] B. Arnold, in The Physics of Medical Imaging, edited by A.G. Haus (Am.Inst.Phys., New York, 1979), p.39.

[16] G.V. Rao, P,P. Fatouros and A.E. James, Invest. Radiol. 13, 460(1978).

[17] R. Wagner and K.E. Weaver, Radiology 118, 183(1976).

[18] B.A. Arnold, E.W. Webster and L. Kalisher, Radiology 129, 179(1978).

[19] K.W. Taylor, B.P. McLeish, B.B. Hobbs and I.J. Hughes, Proc.Soc. Photo-Optical Instrumentation Engineers 173, 306(1979).

[20] J.G. Pearce, G.D. Gillan, W.W. Roeck and E. Milne, Proc.Soc. Photo-Optical Instrumentation Engineers 173, 105(1979).

[21] R.P. Rossi, W.R. Hendee and C.R. Ahrens, Radiology 121, 465(1976).

[22] H.E. Johns and J.R. Cunningham, in The Physics of Radiology, (C.C. Thomas, Springfield, 1983), p. 599.

[23] J.W. Coltman, J. Opt. Soc. Amer. 44, 468(1954).

[24] G.U.V. Rao, Amer. J. Roentgenol. 111, 628(1971).

[25] K. Rossman, Radiology 93, 257(1969).

[26] G.K. Sanerson, in The Physics of Medical Imaging:Recording System, Measurements and Techniques, edited by A.G. Haus (Am.Inst.Phys., N.Y. 1979), p. 133.

[27] B.A. Arnold and B.E. Bjarngard, Med. Phys. 6, 500(1969).

[28] D.J. Lawrence, Med. Radiography and Photo. 53, 2(1977).

[29] B.A. Arnold, H. Eisenberg and B.E. Bjarngard, Radiology 121, 473(1976).

[30] K. Doi and K. Rossman, Proc. Soc. Photo-Optical Instrumentation Engineers 56, 45(1975).

[31] A.E. Burgess, Med. Phys. 5, 199(1978).

[32] G.U.V. Rao and P. Fatouros, Med. Phys. 5, 205(1978).

[33] R.M. Schaffert, Electrophotography, Focal Press, London 1975.

[34] J.W. Boag, Xeroradiography, Phys. Med. Biol. 8, 3(1973).

[35] R.E. Hayford, The Principles of Xeroradiograhic Process, (Xerox, Pasadena, Calif.,1971).

[36] J.N. Wolfe, Xeroradiography of the Breast, (C.C. Thomas, Springfield, 1972).

[37] E.P. Muntz, J. Lewis, T. Azzarelli, M. Welkowsky, A.L. Morsell, E. Kaegi and C. Jacobson, Proc. Soc. Photo-Optical Instrumentation Engineers 56, 208(1975).

[38] G.H. Zeman, G.U.V. Rao and F.A. Osterman, Radiology 119, 689(1976).

[39] S.S. Jaeger, R.K. Cacak, J.E. Barnes and W.R. Hendee, Radiology 128, 212(1978).

[40] P.P. Fatourous and G.U.V. Rao, Med. Phys. 6, 1(1979).

[41] R. Shaw, in The Physics of Medical Imaging: Recording System and Measurement and Techniques, edited by A.G. Haus (Am.Inst.Phys., N.Y., 1979), p. 233.

[42] P.P. Fatourous, in The Physics of Medical Imaging: Recording System, Measurements and Techniques,

[43] L. Stanton, in The Physics of Medical Imaging: Recording System, Measurements and Techniques, edited by A.G. Haus (Am.Inst.Phys., N.Y. 1979), p. 288.

[44] L. Stanton, T. Villafana, J.L. Day, D.A. Lightfoot and R.E. Stanton, Radiology 132, 455(1979).

[45] D. Plewes and H.E. Johns, Med. Phys. 7, 315(1980).

[46] P.P. Fatouros, G.U.V. Rao and C.C. Kao, Med. Phys. 7, 331(1980).

[47] E.P. Muntz, A. Proudian and P.B. Scott, US Patent Number 3 774 029(1973).

[48] A. Proudian, R.L. Carangi, G. Jacobson and E.P. Muntz, Radiology 110, 667(1974).

[49] E.P. Muntz, H. Meyers, E. Wilkinson and G. Jacobson, Radiology 125, 517(1977).

[50] K.H. Reiss, Z. Angew, Phys. 19, 1(1965).

[51] K.H. Reiss and G. Lange, Phys. Med. Biol. 18, 695(1973).

[52] H.E. Johns, A. Fenster, D. Plewes, J.W. Boag and P.N. Jeffery, Br. J. Rad. 47, 519(1974).

[53] A. Fenster, D. Plewes and H.E. Johns, Med. Phys. 1, 1 (1974).

[54] A. Fenster and H.E. Johns, Med. Phys. 1, 262(1974).

[55] L.A. DeWerd and P.R. Moran, Soc. Photo-Optical Instrumentation Engineers 96, 158(1976).

[56] L.A. DeWerd and P.R. Moran, Med. Phys. 5, 23(1978).

[57] R.M. Schaffert, in Electrophotography (Focal Press, London, 1975), p. 557.

[58] J.W. Boag, R. J. Barish and W.W. Seelentag, Med. Phys. 2, 245(1975).

[59] W.W. Seelentag, J.W. Boag and R.J. Barish, Med. Phys. 3, 384(1976).

[60] K.R. Peschmann and G. Grosche, Med. Phys. 1, 202(1977).

[61] A. Fenster and H.E. Johns, Med. Phys. 1, 262(1974).

[62] D. Plewes and H.E. Johns, Phys. Med. Biol. 23, 1000(1978).

[63] D.J. Huntley and J.R. Andrews, Can. J. Phys. 46, 147(1968).

[64] E.P. Podgorsak, Radiation and Impurity Induced Thermally Activated Charge Transport in Calcium Fluoride, Ph. D. thesis, University of Wisconsin (1973).

[65] E.P. Podgorsak and P.R. Moran, Science 179, 380(1973).

[66] E.P. Podgorsak and P.R. Moran, Phys. Rev. B 8, 3405(1973).

[67] I. Brodie and J.B. Mooney, Annual Meeting of IEEE Industrial Applications Society, Toronto, Canada (1978).

[68] I. Brodie, R.A. Gutchek and J.B. Mooney, Proc.Soc. Photo-Optical Instrumentation Engineers, 233, 65(1980).

[69] R.M. Schaffert, R.M. McMaster and W.E. Bixky, U.S. Patent 2 666 144(1954).

[70] R.M. Schaffert, in Electrophotography (Focal Press, London, 1975), p. 191.

[71] P.P. Fatouros, Med. Phys. 9, 819(1982).

[72] N.E.J. Neugebauer, Appl. Opt. 3, 385(1964).

[73] N.E.J. Neugebauer, Appl. Opt. 4, 453(1965).

[74] N.E.J. Neugebauer, Appl. Opt. 6, 943(1967).

[75] H.E. Johns and J.R. Cunningham, in The Physics of Radiology (C.C. Thomas, Springfield, 1983), p. 627.

[76] R. Shaw, in The Physics of Medical Imaging: Recording System, Measurements and Techniques, edited by A.G. Haus, (Am.Inst.Phys., N.Y.), p. 234.

[77] R. Shaw, Proc.Soc.Photo-Opt. Instrumentation Engineers 70,359(1975).

[78] A.G. Hays, R.W. Cowart, R.W. Dodd and J. Bencomo, Radiology 128, 775(1978).

[79] A.G. Haus, G. D. Dodd and R.D. Paulus, Proc.Soc.Photo-Opt. Instrumentation Engineers 173, 120(1979).

[80] R.F. Wagner and E.P. Muntz, Proc.Soc.Photo-Opt. Instrumentation Engineers 173, 162(1979).

[81] G.D. Dodd, Cancer 47, 1766(1981).

[82] I. Brodie and R.A. Gutchek, Med. Phys. 9, 79(1982).

[83] H.E. Johns and J.R. Cunningham, The Physics of Radiology (C.C. Thomas, Springfield, 1983), p. 647.

[84] C.A. Mistretta, M.G. Ort, J.R. Cameron, A.B. Crummy and P.R.Moran, Invest. Radiol. 8, 43(1973).

85 R.G. des Plantes, Fortsch. Geb. Roentgenstr. 52,69(1935).

86 A. Castellanos, R. Pereiras and A. Garcia, Arch. Soc. Estud. Clin. (Habana) 31, 523(1937).

87 G.P. Robb and I Steinberg, AJR 41, 1(1939).

88 C.A. Mistretta, M.G. Ort, J.R. Cameron et al., Invest.Radio. 8, 43(1973).

89 M.G. Ort, C.A. Mistretta and F. Kelcz, Opt. Eng. 12, 169(1973).

90 C.A. Mistretta, M.G. Ort, F. Kelcz, et al., Invest. Radiol. 8, 402(1973).

91 F. Kelcz, Med. Phys. 3, 159(1976).

92 C.A. Mistretta and A.B. Crummy, in Physical Basis of Medical Imaging, edited by C.M. Coulam, J.J. Erickson, F.D. Rollo and A.E. James (Appleton-Century-Crofts, New York, 1981), p. 107.

93 R. Kruger, C. Mistretta, T. Honk, et al., Radiology 130, 49(1979).

94 R. Kruger, C. Mistretta, T. Honk, et al., Invest. Radiol. 14, 279(1979).

95 C.A. Mistretta, A.B. Crummy and C.M. Strother, Radiology 139, 273(1981).

96 S. Nudelman, M.P. Capp, H.D. Fisher, et al., Proc.Soc.Photo-Opt. Instrumentation Engineers 164, 138(1978).

97 T.W. Ovitt, M.P. Capp, H.D. Fisher, et al., Proc.Soc.Photo-Opt. Instrumentation Engineers 167, 61(1978).

98 P.C. Christenson, T.W. Ovitt, H.D. Fisher, et al., AJR 135, 1145(1980).

99 R.R. Price, F.D. Rollo, W.G. Monahan and A.E. James Jr., in Digital Radiography: A Focus on Clinical Utility, edited by R.R. Price, F.D. Rollo, W.G. Monahan and A.E. James Jr., (Grune and Stratton, New York, 1982), p.1.

[100] R.R. Price, F.D. Rollo, W.G. Monahan and A.E. James Jr., in Digital Radiography: A Focus on Clinical Utility, edited by R.R. Price, F.D. Rollo, W.G. Monahan and A.E. James Jr., (Grune and Stratton, New York, 1982), p. 8.

[101] B.J. Hillman, T. W. Ovitt, S. Nudelman, et al., Radiology 139, 277(1981).

CHAPTER 3

EXPERIMENTAL APPARATUS AND PROCEDURES

3.1 INTRODUCTION

In this chapter we discuss the experimental apparatus and techniques used in our study of charge transport in electrostatic radiography. The main components of the apparatus are: *i*) an x-ray tube as the source of ionizing radiation, *ii*) a 5 cm diameter air-filled ionization chamber used in the air saturation and the electret studies, *iii*) a 20 cm diameter air-filled ionization chamber used in ionographic imaging, *iv*) an evacuated chamber or cassette built for solid state electrostatic radiography, *v*) a powder toner box for development of electrostatic images, and *vi*) an assortment of high quality electronic equipment such as electrometers, a plotter, high voltage power supplies, and a roughing vacuum pump. A more detailed description of the components and techniques is given below.

3.2 X-RAY SOURCE

In most of our experiments the x-rays were generated by a constant potential therapy unit[1] enclosed in a lead-lined box as shown schematically in Fig. 3.1 . The unit was used with a potential of 100 kVp and a current of 3 mA corresponding to an x-ray beam with a half-value layer of 2.2 mm of aluminum or an effective x-ray beam energy of 28 keV.[2] The polarizing electrodes of the air and solid state chambers were at a distance of 50 cm from the x-ray focal spot irrespective of air gap thickness. The exposure rate at this distance was 150 mR/s. In some of the measurements discussed in Chapter 4, various x-ray beams with effective energies up to 150 keV [3] and cobalt-60 gamma rays[4] were used.

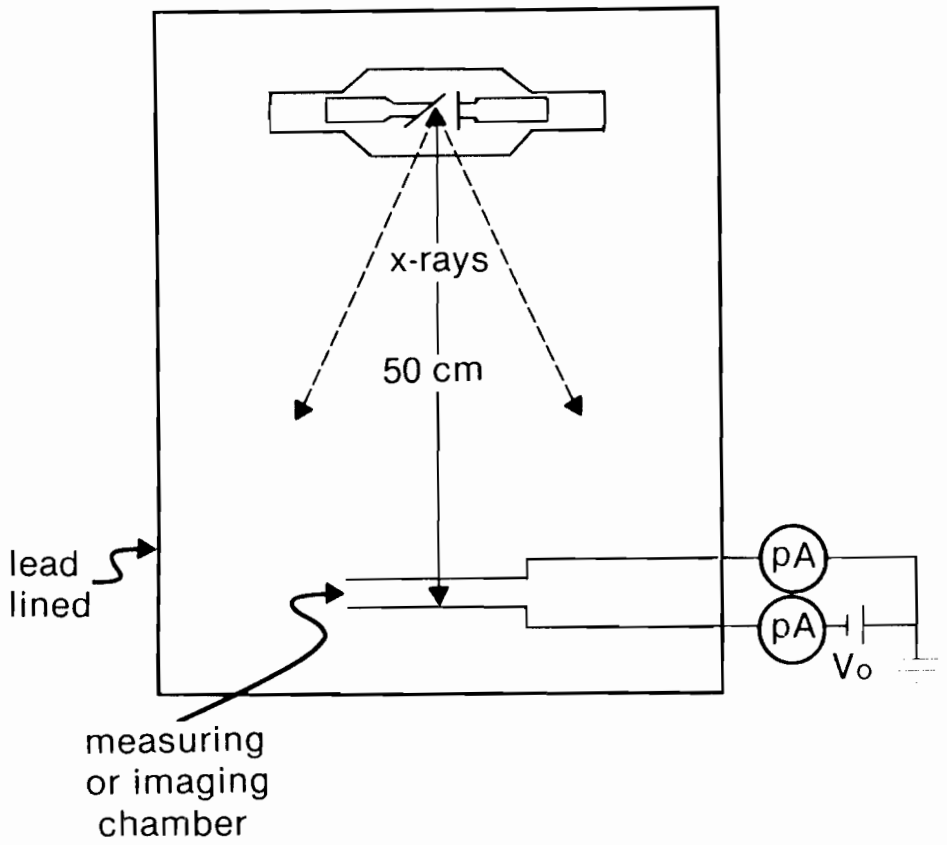

Figure 3.1 Schematic of the lead-lined box containing the x-ray source and the measuring (or imaging) chamber with polarizing electrode 50 cm from the source.

3.3 AIR-FILLED IONIZATION CHAMBER

The ionization chamber used in our measurements of the saturation curve is shown schematically in Fig. 3.2 . The measuring electrode is a 20 μm thin foil of aluminized Mylar, reinforced with a 5 mm thick lucite plate, and grounded through an electrometer.[5] The ionization current measurements were performed at room temperature and ambient pressure. The polarizing electrode is also made of aluminum (2 mm thick) and is connected to a variable power supply.[6] The measuring electrode is circular with a diameter of 5 cm and is surrounded by a 1 cm wide guard ring which is grounded directly. The guard ring defines the chamber sensitive volume and minimizes the leakage currents measured by the electrometer. The chamber sensitive air volume is defined by the product of the measuring electrode area A and the air gap thickness a. The saturation curves were studied with air gaps ranging from 0.2 to 6 cm.

3.4 ELECTRET CHAMBER

The electret forming chamber resembles the standard parallel-plate ionization chamber discussed above and is shown schematically in Fig. 3.3 . The measuring electrode is blocked and the electret state is produced on a polyethylene terephthalate foil (PET-Mylar), which is aluminized on the side facing the x-ray source and has a thickness p on the order of 100 μm. The aluminum on the polymer is used as the measuring electrode grounded through an electrometer.[5] The polymer is facing the polarizing electrode over a variable air gap ranging from a few mm to a few cm. The polarizing electrode is connected to a power supply V_o through

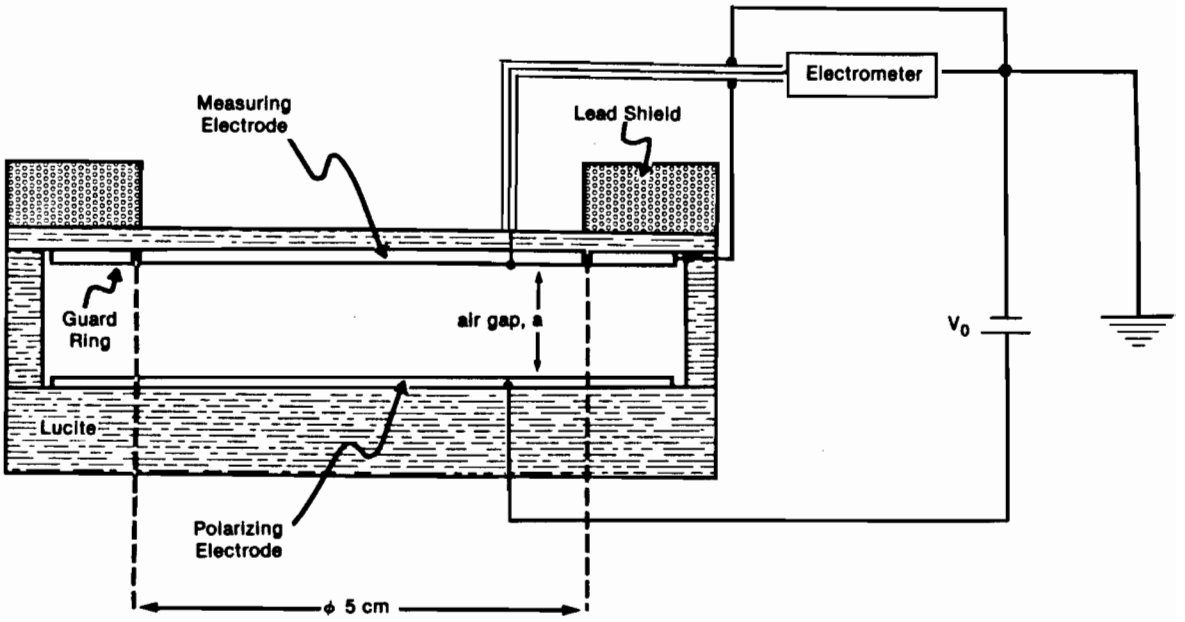

Figure 3.2 Schematic representation of the ionization chamber used in the measurement of saturation curves.

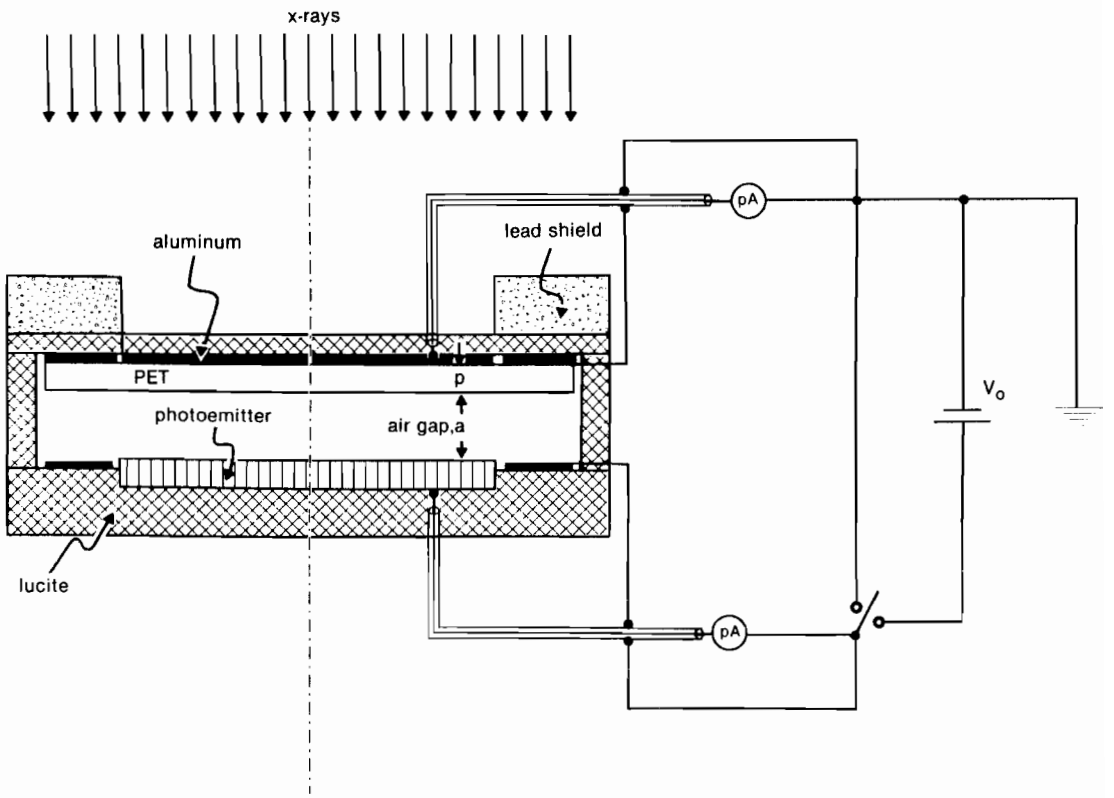

Figure 3.3 Schematic diagram of the electret chamber.

an electrometer and consists of a photoemittive metal with a thickness larger than the range of photoelectrons produced in the material by the x-rays. The switch in the high voltage circuit enables us to connect the polarizing electrode either to the power supply in the electret charging studies or to ground in the electret discharging studies.

Both electrodes are circular with a diameter of 5 cm and are surrounded by a 1 cm wide guard ring. The ring around the foil electrode is grounded directly while that around the polarizing electrode is connected to the switch thus bypassing the electrometer in the high voltage circuit. The guard rings allow us to define the chamber sensitive volume as the product of the electrode area A and the air gap thickness a, and they also minimize the leakage currents measured by the electrometers during the electret formation and decay studies. The current and charge measurements were performed at room temperature with digital electrometers[5] connected to a recorder.[7] The characteristics of the foil electret state, representing the latent ionographic image, were studied for various air gaps ranging from a fraction of a mm to a few cm, for various photoemitting polarizing electrodes ranging from low atomic number carbon to high atomic number lead, and for various thicknesses of the polymer dielectric.

3.5 AIR-FILLED IONOGRAPHIC CHAMBER

The air-filled ionographic chamber is essentially identical to the electret chamber discussed above except that the electrode diameter was enlarged to 20 cm to accomodate imaging of larger objects. The chamber is placed behind the object to be examined and is shown schematically in Fig. 3.4 . The polymer foil containing the latent image can be removed

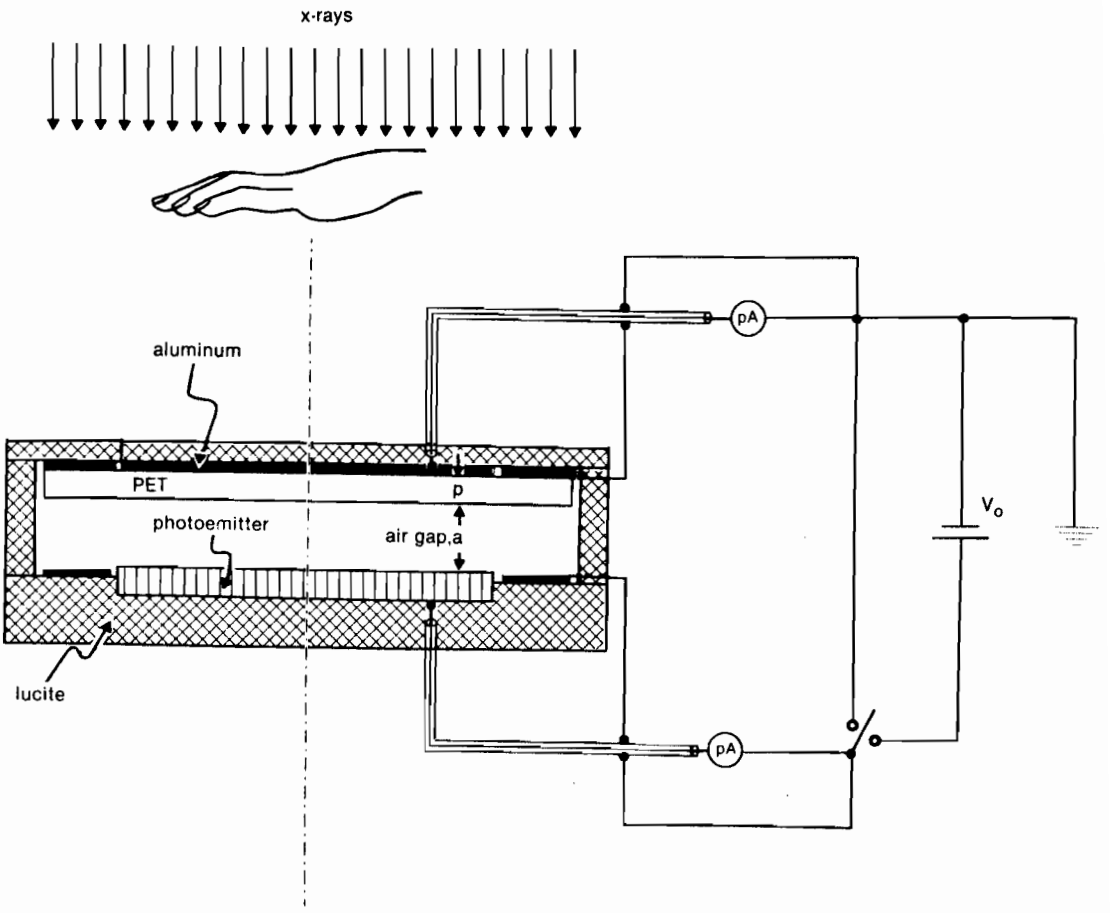

Figure 3.4 Schematic diagram of the ionographic chamber which is placed behind the object.

and inserted into a powder toner development system for visualization of the image. To achieve the optimum sensitivity and resolution in the latent image, a lead polarizing electrode and an air gap of 2 mm to 8 mm was used in this chamber. Different types of polymers were examined and we found that white metalized polypropylene films formed a very good contrast background against the developed black image.

3.6 SOLID STATE ELECTROSTATIC IMAGING

3.6.1 SOLID STATE ELECTROSTATIC CASSETTE

In Fig. 3.5 we show a schematic of the electrostatic imaging cassette. A photoconductor is placed in contact with a dielectric paper or foil, the other side of which is conductive, x-ray transparent and used as the grounded electrode. The metal substrate upon which the photoconductor has been placed is used as the polarizing electrode. The two electrodes are connected to an external power supply[6] during the x-ray irradiation of the object. The potential that can be applied across the photoconductor-dielectric paper combination is limited by breakdown to about 1500 V. A rough vacuum[8] of about 94.4 kPa (~ 710 mm Hg) is used to press the dielectric paper uniformly over the photoconductor. The rough vacuum is also used to keep the dielectric paper in contact with the photoconductor when the polarity of the electrodes is changed during image subtraction procedures.

The photoconductor consists of a 130 μm thick selenium coating upon an aluminum substrate available commercially.[9] The dielectric paper has a conductive backing and is commercially available as electrographic paper.[10] The latent image residing at the interface between the photoconductor and the dielectric paper can be transferred to the paper

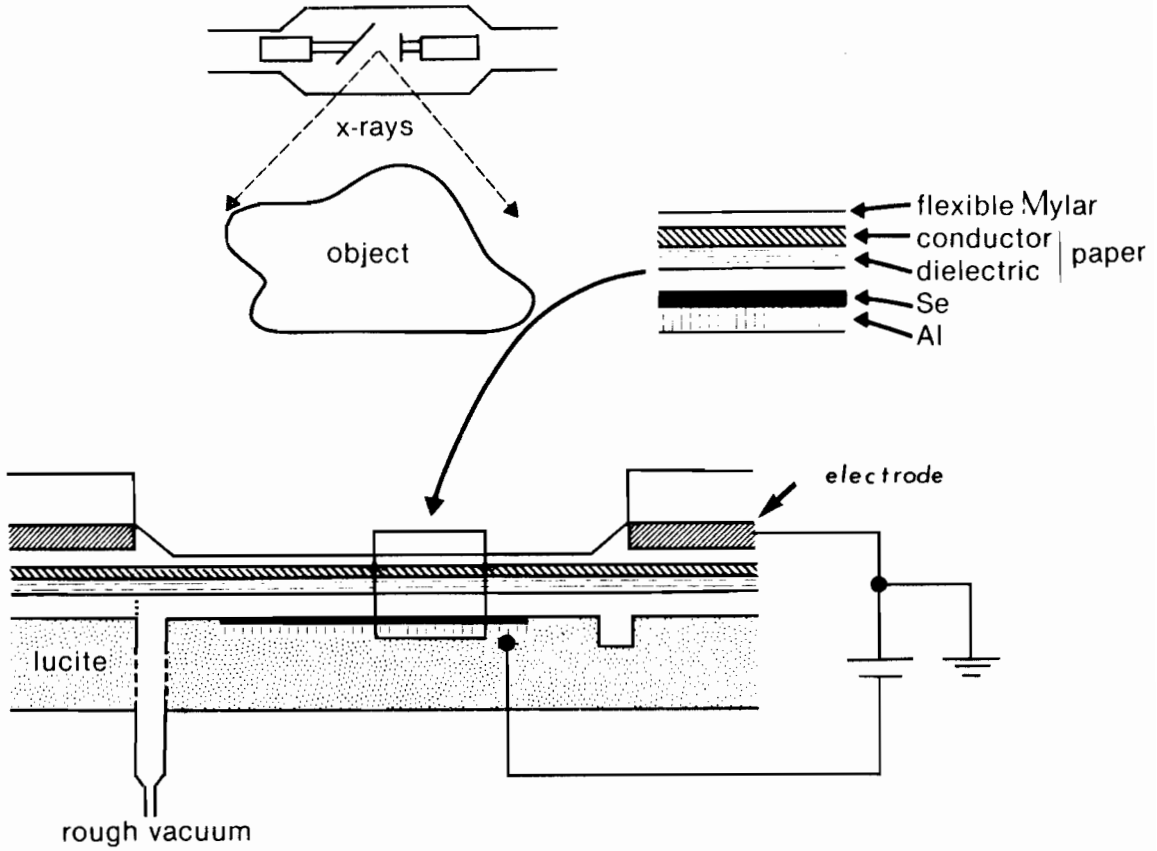

Figure 3.5 Schematic of the solid state electrostatic imaging cassette. The rough vacuum presses the dielectric paper uniformly over the selenium (Se) layer, and the imaging electrode onto the conductive backing of the dielectric paper.

through a Paschen discharge mechanism in air by peeling the paper from the photoconductor. The charged image on the paper is then visualized by dry electrographic techniques in the toner developer with powder used in commercial photocopiers.[11]

3.6.2 CHARGE TRANSFER MECHANISM

We will follow a treatment given by Schaffert[12] to explain the charge transfer mechanism involved in our solid state electrostatic cassette. The transfer of charges from the photoconductor onto the dielectric paper in the solid state electrostatic cassette requires the movement of electrical charges through the air gap separating the two surfaces. For gaps greater than 8 μm the charge transfer mechanism is explained on the basis of gaseous discharge phenomena using the Paschen discharge curve. For gaps of a few microns which exist when two surfaces are in virtual contact a modified form of the Paschen curve is used.

Following Paschen's law for breakdown of a gas in an electric field, the breakdown voltage is a linear function of the product of the gas pressure p_o and the separation d between the electrodes. As shown in Fig. 3.6, this law holds only for $p_o d \gtrsim 0.7$ mm x kPa(~5 mm x mm Hg); for $p_o d$ values below this limit, there is a sharp upturn in the Paschen curve.[13] The minimum breakdown voltage for air is about 350 volts.

The Paschen curve in Fig. 3.6 can be calculated for air at atmospheric pressure and is represented as breakdown voltage versus air gap (solid curve)[14] in Fig. 3.7 . The voltage across the air gap d separating the selenium film of thickness s from the dielectric of thickness p, can be represented as:

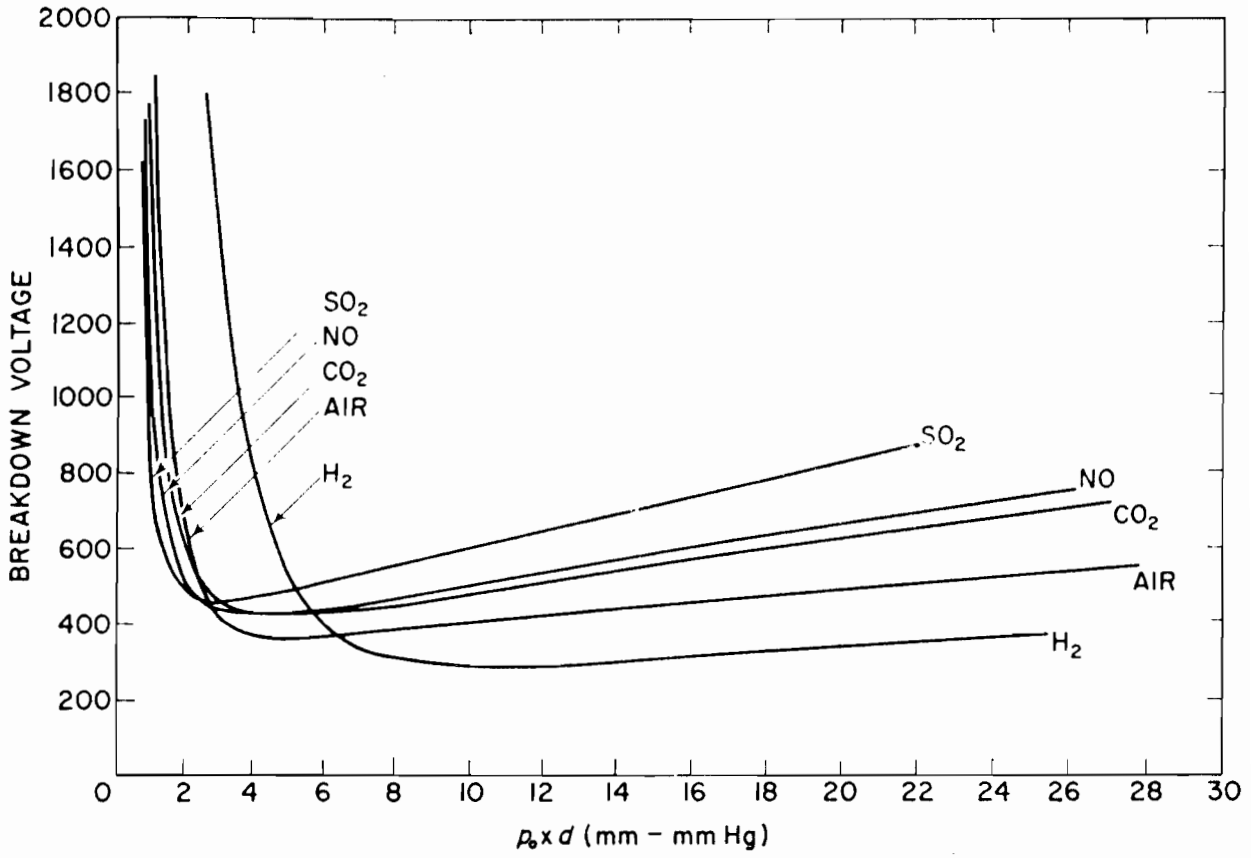

Figure 3.6 Paschen curves for several gases.[13]

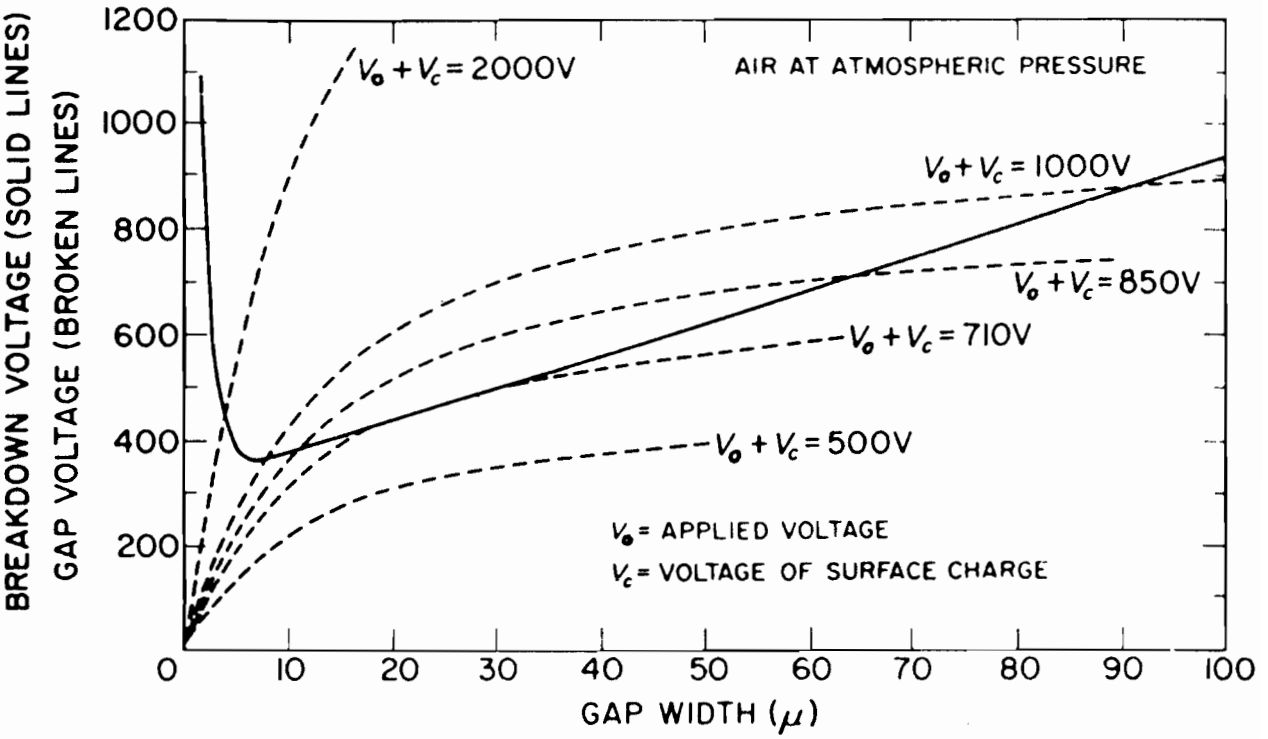

Figure 3.7 Normal Paschen curve (solid) and typical (i.e., for illustrative purposes) gap voltages V_d [Eq. (3.1)] for the indicated (V_o+V_c) versus gap width d (dashed).[14]

$$V_d = \frac{(V_o + V_c)\, d}{s/\varepsilon_s + p/\varepsilon_p + d}\,, \tag{3.1}$$

where ε_s and ε_p are the dielectric constants of the photoconductor and insulator, respectively, $V_c = \sigma s/\varepsilon_s\varepsilon_o$ is the potential produced by the surface charge density σ which resides on the surface of the photoconductor and V_o is the externally applied potential. The air gap voltage V_d is plotted as a function of gap width d (dashed curves) in Fig. 3.7 for various values of $(V_o + V_c)$. Charge transfer occurs only for points where the curves representing V_d cross the Paschen curve. In cases where the intersection occurs at two points, charge transfer will be initiated at the point reached first, i.e., at the smaller gap width when the surfaces are being separated and at the larger gap when the surfaces are brought together.

Although the behaviour of particular gases in the range of $p_o d$ greater than the Paschen minimum is well known and follows the Paschen law, the behaviour in the range smaller than this minimum will follow the law only at low pressures. No steep rising curve has been observed for gaps smaller than that at the Paschen minimum which is 8 μm for air at atmospheric pressure. It seems that the high fields in these small gaps initiate field emission current which predominate over those generated by the Townsend avalanche mechanism.[13] The Paschen curves obtained at atmospheric pressure (i.e., modified Paschen curves) for various gases are shown in Fig. 3.8, and exhibit a plateau extending to the left of the Paschen minimum indicated as V_s in the figure, and a steep line the slope of which is independent of the type of gas. This line runs to the origin and is attributed to field emission. The beginning of the normal Paschen breakdown is just the line to the right of the plateau.

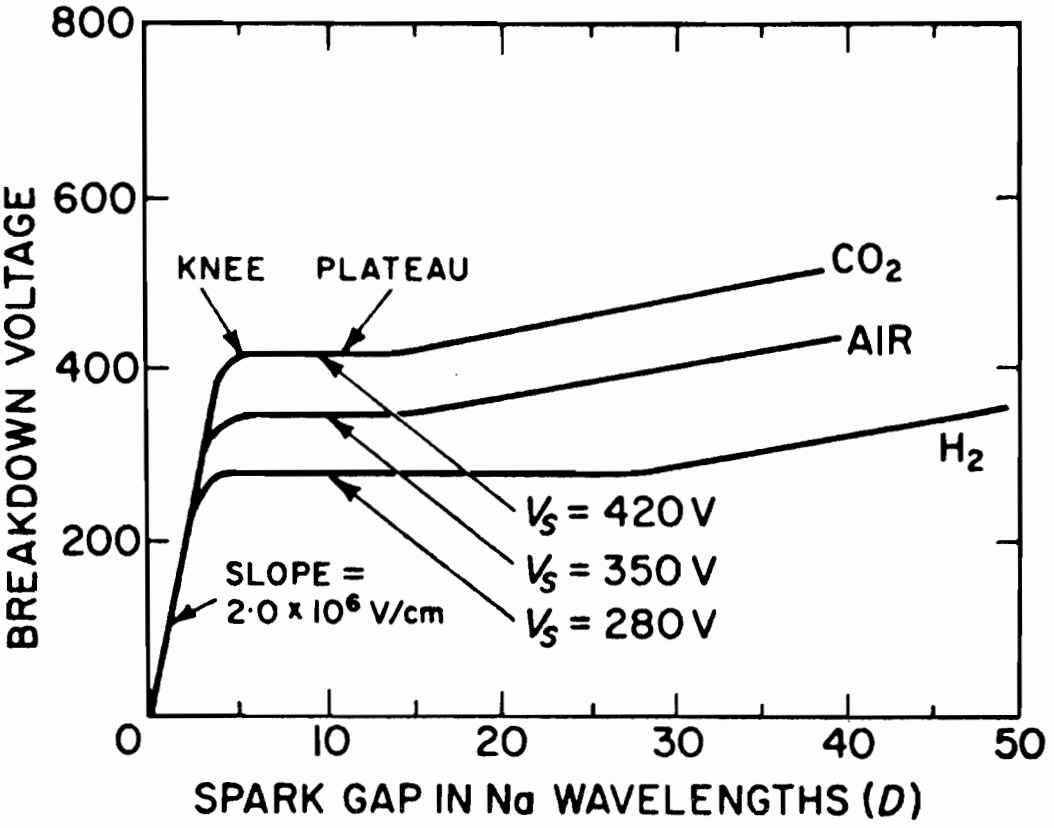

Figure 3.8 Representative plot of breakdown voltage versus electrode distance for small gaps near the $p_o d$ minimum at normal pressure. The Na wavelength D is 0.59 μm.[12,13]

In our solid state electrostatic radiographic cassette the dielectric paper and photoconductor surface are at first in virtual contact ($d \simeq 1$ μm). This is achieved through the rough vacuum as described in the previous section. Charge transfer from the photoconductor to the dielectric insulator is accomplished in a series of incremental steps as the surfaces are separated. The step-wise transfer can be illustrated for a purely hypothetical case. This is represented in Fig. 3.9 where *A* is the modified Paschen curve and *B* is a curve assumed to be the gap voltage after each incremental charge transfer, as a function of gap width. With the initial voltage across the air gap, $V_{d0} = (V_o + V_c)$, the initial discharge takes place at a point a in the figure in the field emission region. The discharge reduces the gap voltage to the point a' in the figure, and reduces the effective applied voltage across the gap, which can be expressed as:

$$V_{d1} = V_{d0} - \Delta_1\sigma_t \, (s/\varepsilon_s + p/\varepsilon_p)/\varepsilon_o \, , \tag{3.2}$$

where $\Delta_1\sigma_t$ is the charge density transferred to the dielectric. As the surfaces are separated, the second discharge will occur at b and stop at b' reducing the effective potential to V_{d2}. This process continues until V_d has been reduced below the minimum for air breakdown. It can be shown that the total amount of charge transferred during the separation of the two surfaces can be approximated by:

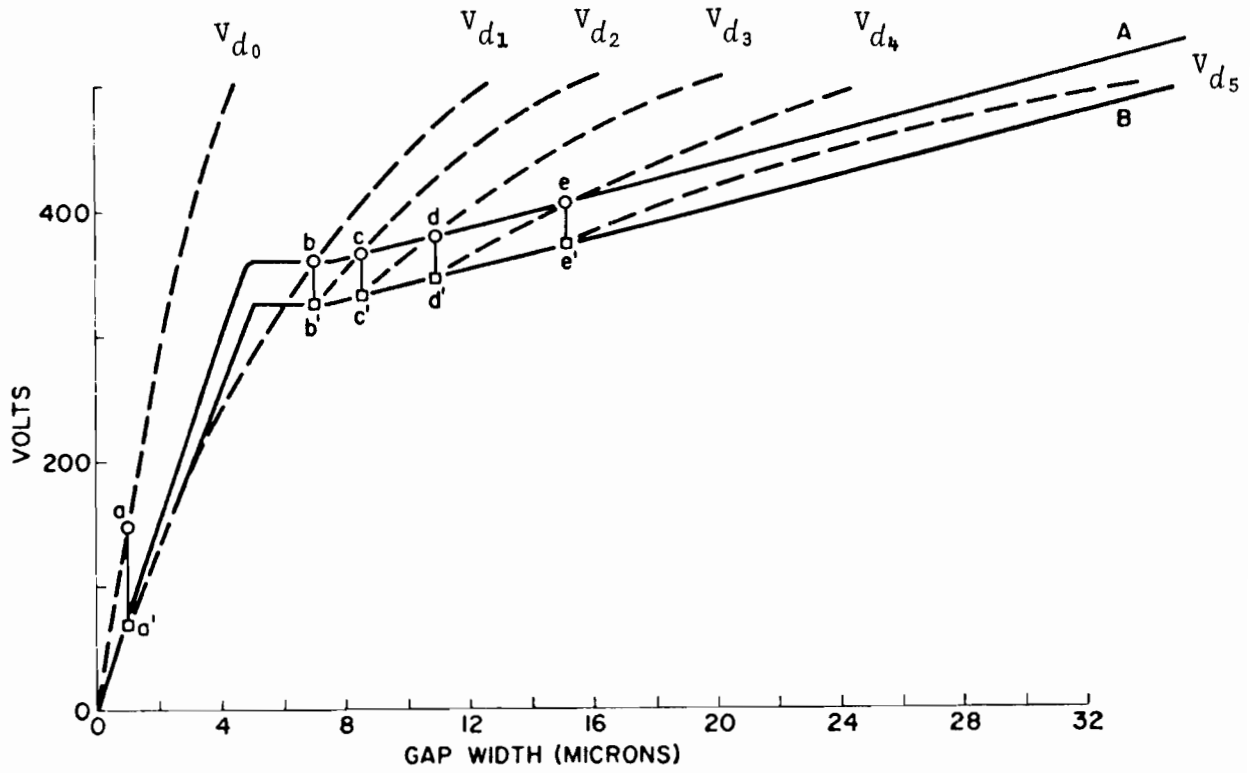

Figure 3.9 Hypothetical stepwise discharge along the Paschen curve during separation of the dielectric paper from the selenium.[12]

$$\sigma_t = \sum_{i=1}^{n} \Delta_i \sigma_t \cong \varepsilon_o/\varepsilon_s \, [V_c + V_o - (\sqrt{u\varepsilon_c} + v\varepsilon_c + w)]$$

$$\cong \varepsilon_o/\varepsilon_s \left[\frac{\sigma s}{\varepsilon_s \varepsilon_o} + V_o - (\sqrt{u\varepsilon_c} + v\varepsilon_c + w) \right] , \qquad (3.3)$$

where u, v, and w are constants that equal to 7737.6 $V^2/\mu m$, 6.2 $V/\mu m$ and 312 V, respectively; and ε_c equals to $(s/\varepsilon_s + p/\varepsilon_p)$ in μm.

If the values for the various parameters used in our electrostatic solid state cassette, i.e., s = 130 μm, p = 4 μm, ε_s = 6, ε_p = 3, and V_o = 0 volts during the peeling operation, are inserted into Eq. (3.3), σ_t is approximately equal to σ indicating that most of the charges are transferred to the dielectric. However, if a much thicker p is used, say 200 μm, most of the charges remain on the selenium and the latent image on the dielectric cannot be visualized through powder techniques. This has been verified in our laboratory and is the reason why dielectric paper is preferred over Mylar in this cassette. Mylar with a thickness of 3 μm to 5 μm is difficult to acquire and impossible to work with. The dielectric paper is made up of a paper base acting as a support layer followed by a conductive substrate of resistivity 10^5 to 10^8 ohm/cm² immediately under a 3 to 5 μm thick vinylchloride-vinylacetate copolymer dielectric.[14] The thickness of the dielectric is suitable to transfer a reasonable amount of charge from the photoconductor to the dielectric.

3.7 DEVELOPMENT OF LATENT IMAGES

3.7.1 POWDER BOX

The charged latent image can be developed by dry powder or liquid colloids. The development system we used is very similar in basic design to the Xerox 125 system and is shown schematically in Fig. 3.10 . An aerosol of fine powder particles can be produced by spraying powder[11] through a fine nozzle or toner gun using compressed nitrogen as carrier gas. The gas is forced through the gun in short puffs of about a second, every few seconds. At the same instant puffs of nitrogen are directed in the opposite direction from a balancing nozzle to force the toner particles sidewise around the middle of the baffle. The powder particles are charged either positively or negatively by triboelectric effect[15] due to collisions of the powder particles with each other or with the metal walls. The Mylar foil, polypropylene film or dielectric paper, is placed on top of the box with the latent image side facing the powder cloud. The conductive side is connected to ground. The sign of the powder reaching the latent image can be selected by a biasing grid connected to a potential of about 5000 V of appropriate polarity held about 10 cm below the surface of the latent image.

3.7.2 POWDER MOTION

The various forces acting on a spherical powder particle of radius r, density ρ, charge Q and dielectric constant ε_Q, when moving with a velocity v through a gas of viscosity η under the influence of an electric field E_b, are as follows:

i) gravitational force

$$F_g = 4/3\ \pi r^3 \rho g\ , \tag{3.4}$$

ii) electric force due to free charge

$$F_{\not b} = QE_b\ , \tag{3.5}$$

and

iii) frictional force due to motion through the gas expressed by Stokes' law

$$F_s = 6\ \pi r \eta v\ , \tag{3.6}$$

where η is 1.9×10^{-5} N-s/m² for air at 20°C.

Typical values for variables used in electrostatic imaging[16] are shown in Table 3.1, and the corresponding maximum and minimum forces shown in Table 3.2 .

In our powder box shown in Fig. 3.10 particles enter the chamber under the baffle and travel in a turbulent stream of air at about 10^2 cm/s . The stream of air then carries the powder around the baffle and up through the biasing grid below the latent image foil and the particles now have speeds of a few centimetres per second. In this region, $F_{\not b}$ is greater than F_s, and $\vec{F}_{\not b}$ selects out those toner particles of appropriate signs to drive them towards the latent image surface. Close to the surface of latent image the motion of the powder is primarily dictated by electrostatic forces and the effect of air currents is comparatively small. Investigations have shown that at this point[15] the influence of air motion on the developed image is not of primary importance. Once the powder is very close to the latent image the very strong

Table 3.1 Typical ranges in powder cloud development[16]

	Radius r(μm)	Density ρ(g/cm³)	Charge Q(C)	Velocity v(cm/s)	Electric Field E_b(V/μm)
MINIMUM	0.2	1	5×10^{-19}	0.1	0.1
MAXIMUM	5	10	5×10^{-17}	10	10

Table 3.2 Extreme values for different forces on powder particle[16]

	F_g(N)	F_ℓ(N)	F_s(N)
MINIMUM	3×10^{-16}	5×10^{-14}	7×10^{-13}
MAXIMUM	5×10^{-11}	5×10^{-10}	1.8×10^{-10}

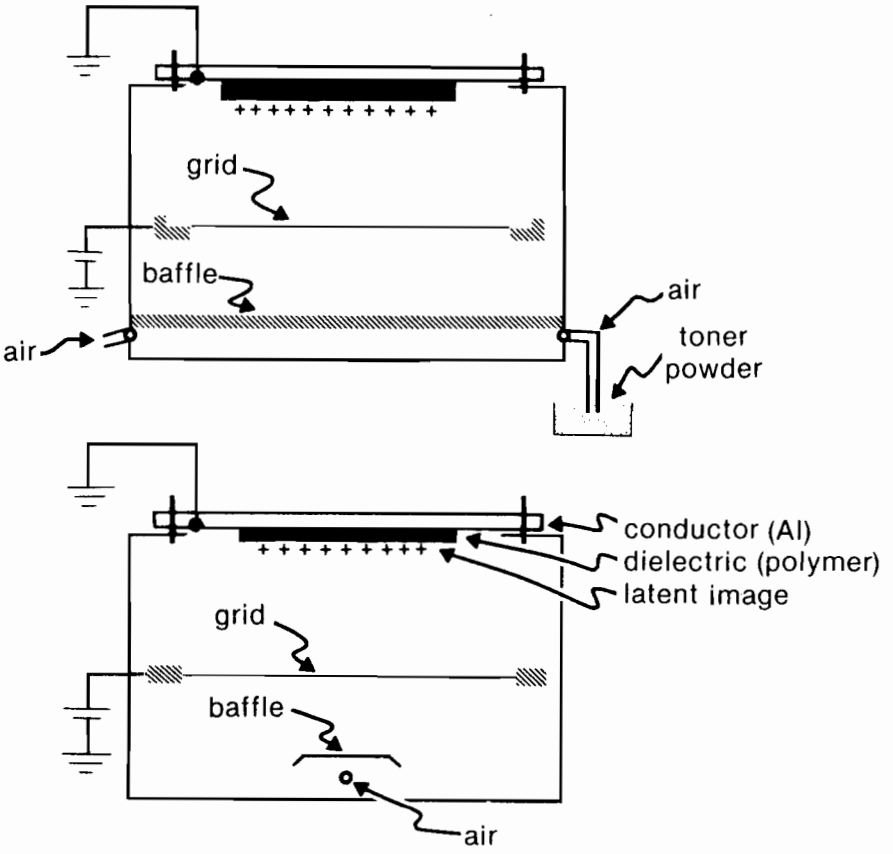

Figure 3.10 Diagram of the powder (toner) cloud development box used to render the electrostatic latent images visible. The dimensions of this box are 43 cm × 43 cm by 17 cm deep.

electric fields close to the surface produced by the latent image compel the powder particles to follow the appropriate path in the electric field towards the surface of the dielectric and to stick there by friction.

3.7.3 SPECIFIC POWDER TRAJECTORIES

It may be of interest to briefly discuss the possible trajectories of powder towards the charged dielectric. A good illustration has been given by Lewis and Stark,[17] and in a more detailed form by Fenster et al.[18] from where Fig. 3.11 has been adapted.

In Fig. 3.11(*a*) a negatively charged half-plane is powdered with a bias field E_b of 0.4 kV/cm which selects negative powder particles. Particles outside the charge pattern will follow nearly straight lines to deposit in region 'c'. Those near the charge edge will follow complicated trajectories and pile up just outside the charge edge in region 'p'. If the bias field E_b is stronger than the vertical component of the field due to the charge pattern, a few trajectories such as 'B' can deposit negative toner inside the charge pattern. Such depositions occur in region 'a' remote from the edge with no powder near the edge. There is also the possibility that through air turbulence, some positive toner may reach region Q above the foil inside the arching electric field near the edge of the charge pattern. Then these would drift to 'e' in Fig. 3.11(*b*) . The expected powder distribution is shown in Fig. 3.11(*c*) . Normally, if air turbulence is minimal no powder would be deposited between 'a' and 'f'. This region has been called the depletion or forbidden region by Stark and Lewis.[17] Even if air turbulence is important there still remains a strip 'f' between 'e'

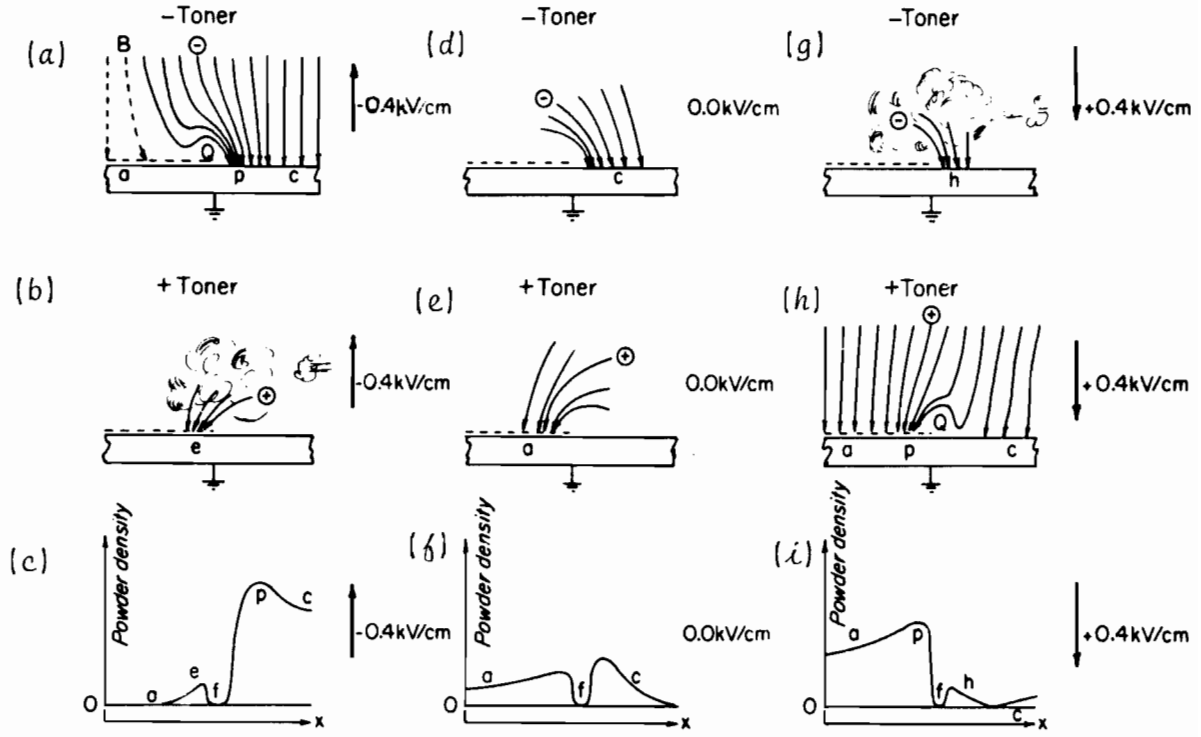

Figure 3.11 Schematic diagrams of the trajectories of positive and negative powder (toner) particles when a negative charge pattern is developed with a biasing field E_b of (a) - (c) -0.4 kV/cm, (d) - (f) 0.0 kV/cm, and (g) - (i) +0.4 kV/cm. The expected powder distributions for each of the -0.4, 0.0 and + 0.4 kV/cm development conditions are shown in (c), (f) and (i), respectively.[18]

and 'p' into which powder is not deposited. Its width would depend on E_b, the size of the surface charge density discontinuity and, of course, on air turbulence.

If the charge pattern is powdered with no biasing field, there is no selection of toner charge, and powder is transported with air turbulence alone as shown in Figs. 3.11(*d*) and 3.11(*e*) . In these figures negative toner is deposited near the edge and outside the charge pattern in region 'c' while positive toner is deposited inside the charge pattern in region 'a', leaving behind a narrow powderless gap 'f' between them as shown in Fig. 3.11(*f*).

If the bias field, E_b is + 0.4 kV/cm, positive toner is selected. The positive particle will follow the trajectories as shown in Fig. 3.11(*h*) leading to a pile up at 'p' and somewhat less powder in region 'a'. Outside the charged region positive toner will be deposited away from the charge edge in region 'c'. If air turbulence forces negative toner to reach Q in Fig. 3.11(*g*) it will give rise to a peak at 'h'. The expected powder density distribution is shown in Fig. 3.11(*i*).

It is interesting to note that selection of charged powder permits positive or negative pictures as expected. However, we do not get a uniform powdered distribution when $E_b = 0$. As shown in Fig. 3.11(*f*) there remains a distinct unpowdered region on the edge of the charge pattern.

In Fig. 3.12 we show images we have taken with the solid state cassette and developed with different bias field polarities [Figs. 3.12(*a*) and 3.12(*b*)] and with no bias field [Fig. 3.12(c)] to substantiate what was discussed above.

For good image contrast it is evident that the bias grid must be kept at a potential to select toner particles and periodically cleaned

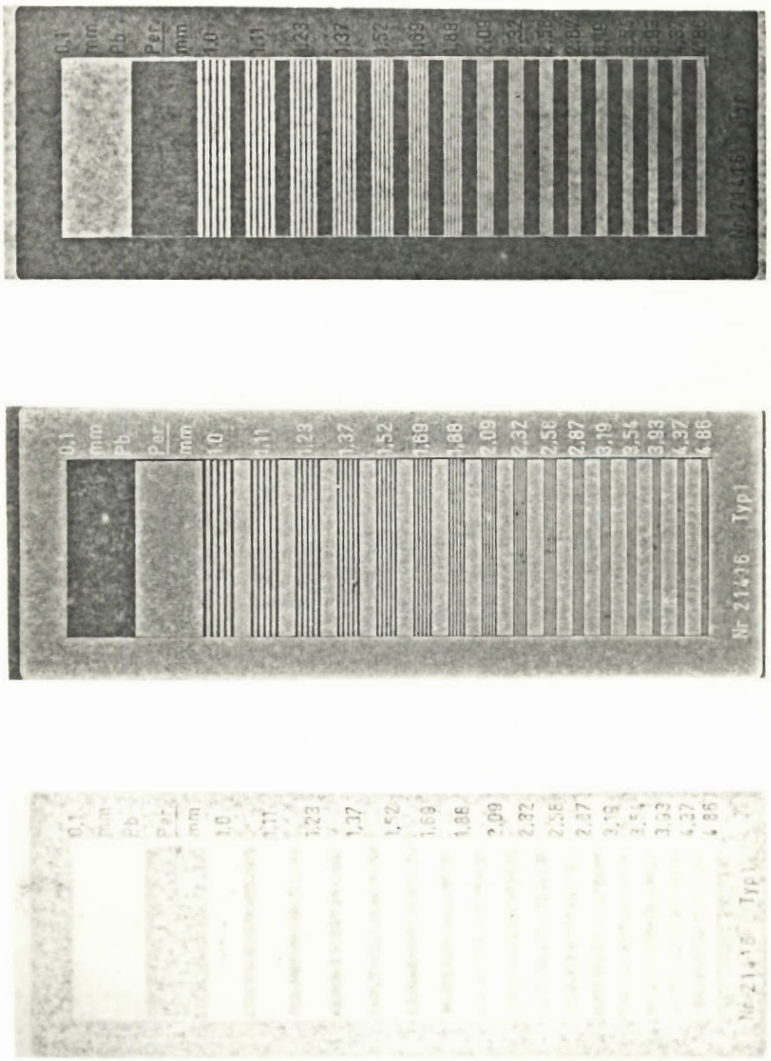

Figure 3.12 Electrostatic radiographs taken with our solid-state electrostatic cassette (Fig. 3.5) and developed with biasing fields E_b of different polarities [(*a*) and (*b*)], and with no biasing fields (*c*).

to prevent the build-up of charge powder that would effectively reduce the bias potential. In addition, air turbulence should be kept to a minimum to prevent the small accumulation of powder shown as peaks 'e' and 'h' in Figs. 3.11(c) and 3.11(i), respectively.

3.8 FIXING THE POWDERED IMAGE

After the charged latent image has been discharged through the electrographer powder and becomes visible, the powdered image is fixed either by exposing it to trichloroethylene fumes or by baking it for a few seconds at ~140°C. The resultant visible image is durable and will not fade away in time.

3.9 SUMMARY

The main components of our apparatus from x-ray source to imaging chambers were described. Charge carriers produced in the parallel-plate ionization chamber by the x-ray irradiation drift in the externally applied electric field towards the appropriate electrodes. If the measuring electrode is ohmic,the chamber is a standard ionization chamber used for dosimetry; if it is blocking the charges are trapped on the polymer surface of the blocking electrode to form an electret with either a uniform surface charge distribution or a distribution modulated by transmission through an object (i.e., the charged latent image of an object). Charge carriers produced in the solid state electrostatic cassette, however, remain on the surface of the photoconductor to form the latent image, and are transferred to the dielectric paper by Paschen discharge when the dielectric paper is peeled from the photoconductor.

The latent images formed by either technique are visualized by an electrostatic powder cloud development system which selects the sign of the powder particles to form either a negative or positive visual image. Certain particularities of this development process were discussed and simple methods of fixing the powdered image were described.

3.10 REFERENCES

1 General Electric, Maximar 100 .

2 H.E. Johns and J.R. Cunningham, The Physics of Radiology, (C.C. Thomas, Springfield, 1983), p. 278 .

3 Siemens, Stabilipan II .

4 Atomic Energy of Canada, Theratron-780.

5 Keithley, 616 Digital Electrometer.

6 Bertan Associates, Model 205A 50 P and/or Keithley, 245 H.V. Supply.

7 Hewlett-Packard, 700 4B x-y Recorder

8 Direct Torr Vacuum Pump

9 Xerox, Xeroradiographic plate.

10 Versatec, Electrographic paper.

11 Xerox, 6R49 powder.

12 R.M. Schaffert, in Electrophotography (Focal Press, London, 1975), p. 512.

13 L.B. Loeb, in Basic Processes of Gaseous Electronics (Univ. of Calif. Press, Berkeley, 1955), p. 813.

14 K. Takagi, K. Tasai and K. Tsukatani, Fujitsu Sci. Tech. J., 1, 227 (1965).

15 R.M. Schaffert in Electrophotography (Focal Press, London, 1975), p. 557 .

16 J.W. Boag, Phys. Med. Biol., 18, 3 (1973).

17 R.B. Lewis and H.M. Stark, in Current Problems in Electrophotography edited by W.F. Berg and K. Hauffe (de Gruyter, Berlin, 1972), p. 332.

18 A. Fenster, D. Ostler and H.E. Johns, J. Appl. Photo. Engineering, 3, 18 (1977).

CHAPTER 4

SATURATION CURVES OF PARALLEL-PLATE IONIZATION CHAMBERS

4.1 INTRODUCTION

In this chapter we will discuss saturation curves of parallel-plate ionization chambers. First, we will summarize the work of previous investigators on this subject and then develop an empirical expression which is a better representation of experimental data and will be used in subsequent chapters to describe the charging and discharging dynamics of the radiation-induced foil electret and to explain the charging characteristics of the ionographic latent image.

When the voltage applied to the polarizing electrode of an ionization chamber exposed to radiation is increased from zero to a high value, the current collected on the measuring electrode increases, at first linearly with voltage, then more slowly, until it finally approaches asymptotically the saturation current for the given radiation intensity. The saturation current is attained at relatively high voltages where all ion-pairs produced by radiation in the sensitive chamber volume are collected. The curve relating the measured ionization current to the applied voltage or electric field is called the saturation curve. At lower voltages the lack of saturation may be due to *i*) diffusion loss caused by the diffusion of ions into the measuring electrodes against electric field; *ii*) initial recombination, when positive and negative charge carriers formed in the track of a single ionizing particle meet and recombine, and *iii*) general (volume) recombination, when recombination occurs between charge carriers produced by different ionizing particles.

Various authors have shown that charge collection defects due to initial recombination and diffusion loss depend on 1/E, while the defect due to the general recombination depends on $1/E^2$, where E is the electric field produced by the applied voltage in the chamber sensitive volume. Since present analytical expressions for the saturation curve were primarly developed for the near saturation region, there is a considerable discrepancy between measured and calculated values when the rest of the saturation curve is considered. The situation is quite adequate when one studies the ion collection efficiencies for chambers used in radiation dosimetry, because the chambers are always employed in the saturation region or at least very close to it. In our studies of polarization and depolarization phenomena on radiation induced foil electrets, however, a reasonably accurate knowledge of the full ionization chamber saturation curve is required. Since the presently available analytical expressions were not suitable, a new empirical expression which covers the whole saturation curve was developed. The purpose of this chapter is to present and discuss this new expression, to show its general application to any parallel-plate ionization chamber and to compare it with the presently known models. This expression will also be used to derive the full saturation curve from one single measurement of chamber current at a given electric field.

4.1.1. Charge Collection Efficiency and the Saturation Curve

A typical parallel-plate ionization chamber was shown schematically in Fig. 3.2. The charge collection efficiency f is defined as the ratio of the rate of charge collection on the measuring electrode to the rate of charge production in the sensitive volume. It may

also be expressed as the ratio of the measured current density j to the saturation current density j_{sat}:

$$f = \text{charge collected/charge produced} = j/j_{sat} \tag{4.1}$$

The saturation characteristics of parallel-plate ionization chambers were first considered by Thomson and Rutherford[1] and later by Mie[2] and Townsend[3]. Boag[4] and Wilson[5] performed an extensive theoretical and experimental study of the saturation curve, the results of which have been the basis of saturation curve studies. The results of their work are summarized here.

In the near saturation region, the space charge field due to the ions can be neglected, in comparison with the collecting field, $E=V_o/a$. The positive and negative ions with mobilities k_1 and k_2, respectively, will then drift with constant velocities k_1E and k_1E from their point of origin towards the appropriate electrodes. If recombination is assumed very small, the rate of recombination of charge per unit volume at a plane x parallel to the electrodes can be represented as:

$$(\alpha/e)\rho_1(x) = (\alpha/e)[(qa^2)^2/k_1k_2V_o^2](x/a) \times (1 - x/a), \tag{4.2}$$

and the total recombination R between electrodes in charge per unit area per unit time is:

$$R = \int_0^a (\alpha/e)\rho_1\rho_2 dx = a(\alpha/e)(q^2a^4/6k_1k_2V_o), \qquad (4.3)$$

where $\rho_1(x)$ is the charge density of positive ions at a distance from the positive electrode, $\rho_1(x)$ is the charge density of negative ions at x, q is the ionization rate (charge per unit volume per unit time), e the charge per ion and a recombination coefficient. Boag defines the collection efficiency δ near the saturation region as $1-R/qa$. Since the saturation current j_{sat} is equal to the charge liberated per unit area per unit time qa, the collection efficiency is then given by:

$$\begin{aligned} \delta &= 1-R/j_{sat} \\ &= 1-(a/6k_1k_2) \\ &= 1-\zeta^2/6, \end{aligned} \qquad (4.4)$$

where ζ is defined as $m\sqrt{aj_{sat}/E^2}$ and m, which is equal to $\sqrt{a/ek_1k_2}$, is a characteristic of the gas at a given temperature and pressure.

Since the above solution for δ overestimates recombination, the investigators have replaced the ideal charge densities at the electrodes j_{sat}/k_1V_o and j_{sat}/k_2V_o by $\delta j_{sat}/k_1V_o$ and $\delta j_{sat}/k_2V_o$, respectively. The expression for δ then becomes:

$$\delta = 1-\delta^2\zeta^2/6, \qquad (4.5)$$

which now underestimates recombination. Finally, a compromise was made such that:

$$\eta \cong 1-\eta\zeta^2/6. \tag{4.6}$$

Manipulating Eq. (4.1) with the above equation we arrive at a more convenient expression of the form:

$$\eta=(1+n^2 a j_{sat}/E^2)^{-1} \tag{4.7}$$

where n^2 is simply $m^2/6$.

The collection efficiency is actually a product of three factors: η_v, η_i and η_d referring to volume recombination,[2,6] initial recombination[7] and diffusion loss[8], respectively; and Böhm[9] proposed the following analytical expression for η:

$$\eta = \eta_v\eta_i\eta_d = [1-(\Gamma_o^2 a j/E^2)]\times[1-(E_1/E)]\times[1-2kT/eaE] \quad , \tag{4.8}$$

where Γ_o is a parameter similar to n in Eq. (4.7) incorporating the recombination coefficient, and mobilities of positive and negative carriers; E_1 is a constant with dimensions of electric field; $kT \cong 0.025$ eV at room temperature and e is the elementary charge.

If diffusion loss is neglected and if $(1-\eta_v)<<1$ and $(1-\eta_i)<<1$ one gets a simplified version of Eq. (4.8) as follows:

$$\eta \cong 1-(\Gamma_o^2 a\eta/E^2)-(E_1/E). \tag{4.9}$$

A further simplification is obtained when the contribution of initial recombination is neglected. Equation (4.7) then transforms into:

$$f \cong 1-(\Gamma_o^2 aj/E^2), \tag{4.10}$$

which is similar to Eq. (4.7).

Pulsed radiation beams pose some unique problems as far as collection efficiencies are concerned, because of high dosage per pulse; and Boag[10] derived the following formula for collection efficiency, again valid for the near saturation region only:

$$f = u^{-1} \ln(1+u), \tag{4.11}$$

where $u=t\times r/V$, t is a parameter similar to n in Eq. (4.7), V is the collection voltage and r is the charge liberated per unit volume per pulse.

The analytical expressions for f given above all contain semi-empirical constants and may only be applied for values of f down to 0.9; below 0.9 there is a considerable discrepancy between theory and measurement. It appears that these analytical functions, describing the regions of interest in f from 0.9 to 1 were satisfactory because, for the chambers used in radiation dosimetry, the applied electric field is always large enough to ensure a collection efficiency close to 1.

In our study of polarization and depolarization of radiation induced foil electrets, which will be discussed in Chapter 5, however, an exact knowledge of the full saturation curve is required. The charge

deposition on the foil during the electret formation decreases the effective electric field in the electret chamber, and the displacement current measured on the measuring electrode exhibits saturation characteristics similar to those obtained by varying the externally applied field on a conventional ionization chamber. The dynamics of electret charge polarization can only be described by an accurate knowledge of the full electret chamber saturation curve and we therefore derived a new analytical expression for collection efficiency, as discussed below.

4.2 COLLECTION EFFICIENCY FOR LOW ENERGY X-RAYS AND CO-60

In Fig. 4.1 we show two typical examples of collection efficiencies as a function of electric field, measured with our ionization chamber shown schematically in Fig. 3.2. One is for a 100 kVp x-ray beam (effective energy 30 keV) and the other is for a cobalt-60 gamma ray beam (energy 1.25 MeV). The measured data are compared with values calculated from Eq. (4.7) using the air gap, a=1.68 cm, the appropriate value for j_{sat} and two extreme values for n, low of 29 and high of 44 in units of $(3\times10^9\ V^2/A\text{-cm})^{\frac{1}{2}}$, as quoted in the literature.[4,5,11] The shaded areas represent the loci of curves which would be obtained by values of n between the two extremes.

It is immediately obvious that, as stated above, the theory, even once the appropriate value for n is chosen, conforms with the measured data reasonably well only for $0.9<f\leq1$. In this region and for our particular configuration, it appears that the best value for n is 29; f is then overestimated in the region of f between 0.5 and 0.9 and is underestimated for values of f below 0.5. The discrepancy is particularly

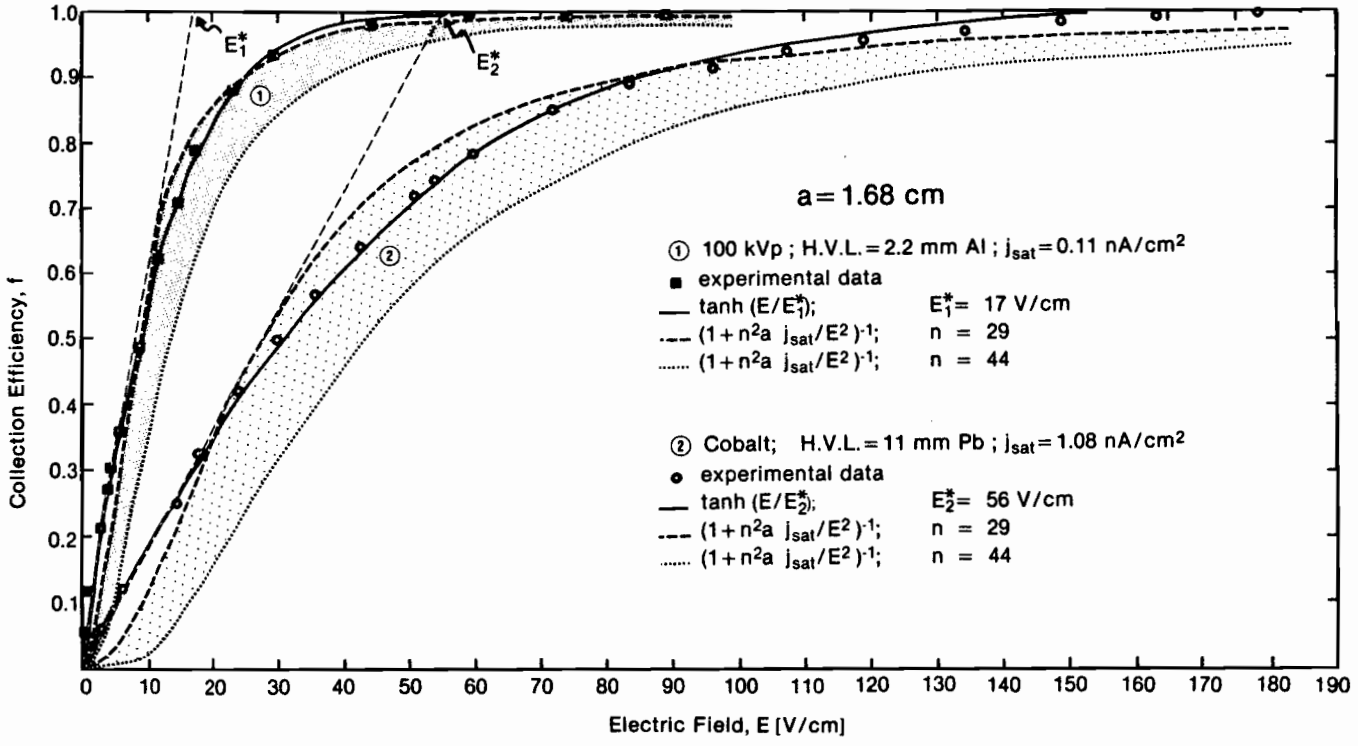

Figure 4.1 Measured and calculated collection efficiencies f as a function of electric field E for air gap thickness a of 1.68 cm, and for: (1) 100 kVp X-ray beam with half value layer of 2.2 mm Al, and (2) Cobalt-60 gamma rays. The solid line represents a plot of Eq. (4.12) with the appropriate E^* and the dashed curves represent loci of curves obtained for n in units of $(3\times10^9\ V^2/A\ cm)^{\frac{1}{2}}$ between the two extreme values of 29 and 44.

pronounced for values of η below 0.2, where the theory predicts a quadratic relationship between η and E, while the measurements clearly indicate a linear relationship.

The measured collection efficiencies, as shown in Fig. 4.1, rise linearly with electric field for small fields, then they rise progressively slower at intermediate fields, until a saturation value of unity is reached at high electric fields. We found that a hyperbolic function, of the form given below, describes the full measured saturation curve much better than Eq. (4.7). The collection efficiency η is thus given by:

$$\eta = \tanh(E/E^*). \tag{4.12}$$

where E^*, the extrapolated electric field, is the field at which the collection efficiency would equal unity if the initial linear relationship between η and E, exhibited at small fields, held for all electric fields E.

As shown in Fig. 4.1, the agreement between the two measured and calculated saturation curves is excellent, when the extrapolated fields, E^* of 17 and 56 V/cm respectively, are used in Eq. (4.12). The hyperbolic function of Eq. (4.12) exhibits behavior identical to that of the measured saturation curves: linearity at small fields, where $\tanh(E/E^*) \cong E/E^*$ and saturation for fields larger than 3 E^*.

4.3 COLLECTION EFFICIENCY AS A FUNCTION OF AIR GAP

Figure 4.2 shows a set of measured and calculated saturation curves for various air gap thicknesses a. The effective beam energy

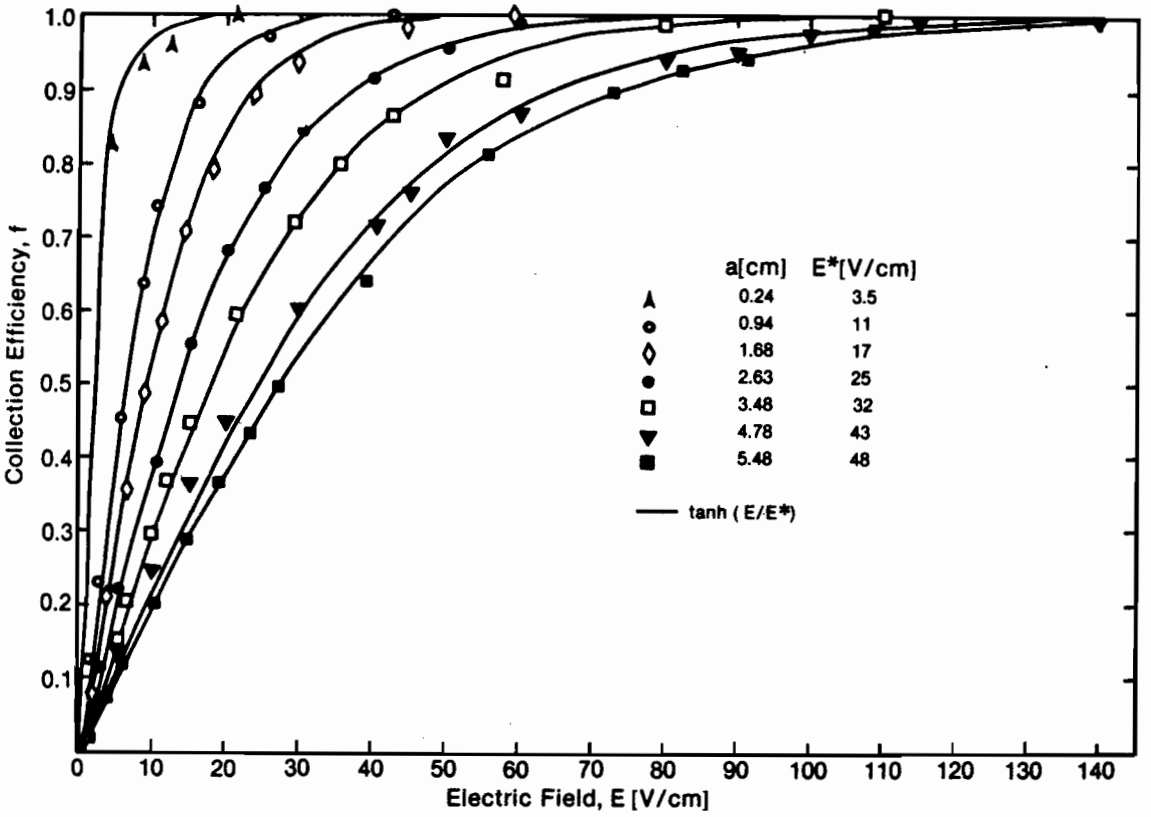

Figure 4.2 Measured and calculated collection efficiencies f as a function of electric field E for various air gap thicknesses a. X-ray beam : 100 kVp, with H.V.L. 2.2 mm Al and exposure rate 9.4 R/min. Extrapolated field E^* is obtained by extrapolating the initial slope of the saturation curve to $f = 1$. Solid curves represent a plot of Eq. (4.12) with the appropriate E^*.

was 30 keV and the exposure rate at the centre of the chamber sensitive volume 50 cm from the target was kept constant at 9 R/min. The extrapolated fields E^* were obtained from the initial slope of the saturation curves; the solid line represents a plot of Eq. (4.12) with the appropriate E^*. The agreement between the measured and calculated saturation curves is again excellent. We also notice that the extrapolated field depends on the air gap thickness. For the same exposure rate, the larger the gap, the larger is the extrapolated field. The exact functional relationship between E^* and a will be discussed later.

We found similar agreement between saturation curves calculated with Eq. (4.12) and measured, for air gaps ranging from few millimeters to few centimeters, for exposure rates between 1 R/min to 500 R/min, for x-ray beams of low and intermediate effective energies and for cobalt beams.

We conclude that Eq. (4.12) describes the saturation curve of any ionization chamber exposed to continuous radiation, once the appropriate extrapolated field E^* is found. In the remaining sections of this chapter we will discuss the extrapolated field in detail, show that it is a function of the air gap and exposure rate, but is independent of beam energy. We will also show that there is a unique relationship between E^* and the saturation current density j_{sat}, independent of beam quality and that both E^* and j_{sat} can be calculated from a single measurement of current density j at a given electric field E anywhere on the saturation curve.

4.4 SATURATION CURRENT DENSITY

The data of Fig. 4.2 are plotted in Fig. 4.3 in the form of unnormalized curves; the current density j is plotted as a function of electric field E for various air gap thicknesses a. The dashed curves represent the saturation curves calculated from a modified Eq. (4.12):

$$j = j_{sat}\delta = j_{sat} \tanh (E/E^*), \tag{4.13}$$

with extrapolated fields E^* obtained from Fig. 4.2 by extrapolating the initial rise of the saturation curve to $\delta = 1$.

All curves, irrespective of the air gap thickness a, start with the same initial slope and eventually asymptotically reach the saturation current density j_{sat}. The larger the air gap, the larger is the saturation current, since j_{sat} is directly proportional to the sensitive chamber volume for a constant exposure rate.

It is interesting to note that when the saturation current densities of Fig. 4.3 are plotted as a function of the air gap thickness a, the relationship is not strictly linear. As shown in Fig. 4.4, the slope of the j_{sat} versus a curve decreases with increase in a from 0 to 1 cm until it finally remains constant for a larger than 1 cm. If we were dealing only with primary ionization in air then the relationship between j_{sat} and a should be linear; the shape of the curve in Fig. 4.4 indicates that there is an external contribution to the ionization of air in the sensitive volume. Since j_{sat} versus a eventually settles into a linear relationship, this external contribution to ionization must exhibit a saturation behaviour.

The external contribution to air ionization is caused by photoelectrons backscattered into the sensitive volume from the aluminum

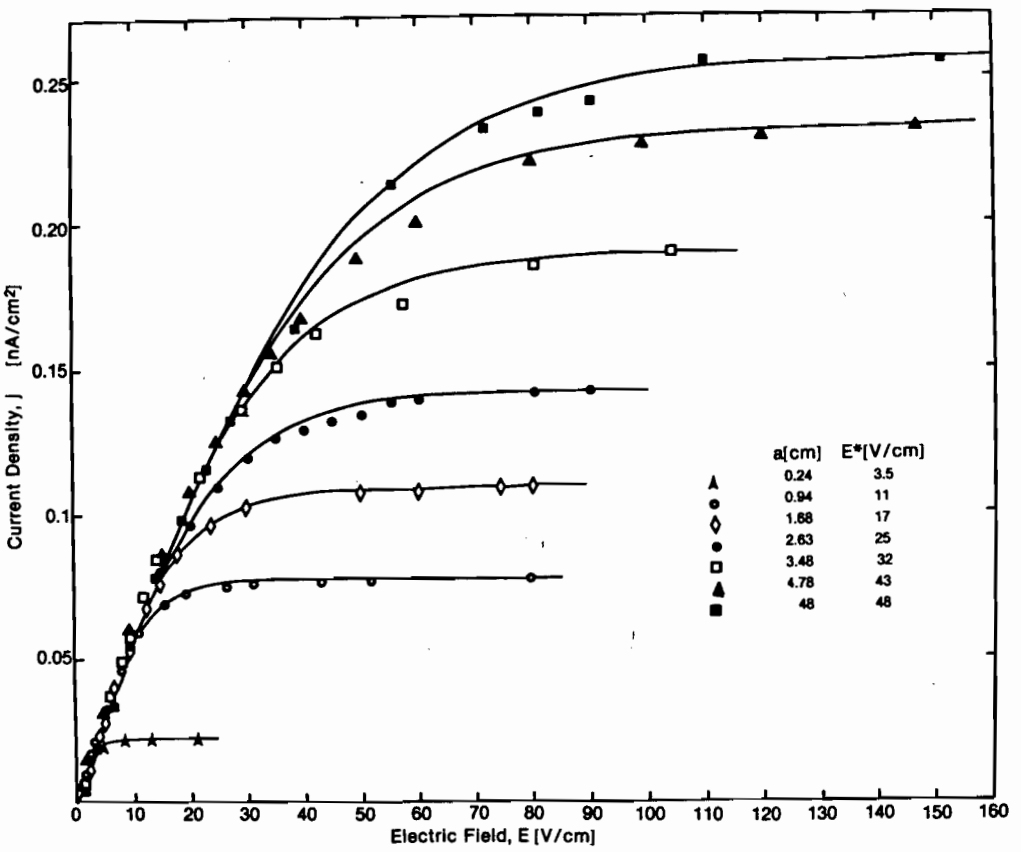

Figure 4.3 Measured and calculated current densities j as a function of electric field E for various air gap thicknesses a and same x-ray beam parameters as in Fig. 4.2; solid curves represent a plot of Eq. (4.11) with the appropriate E*.

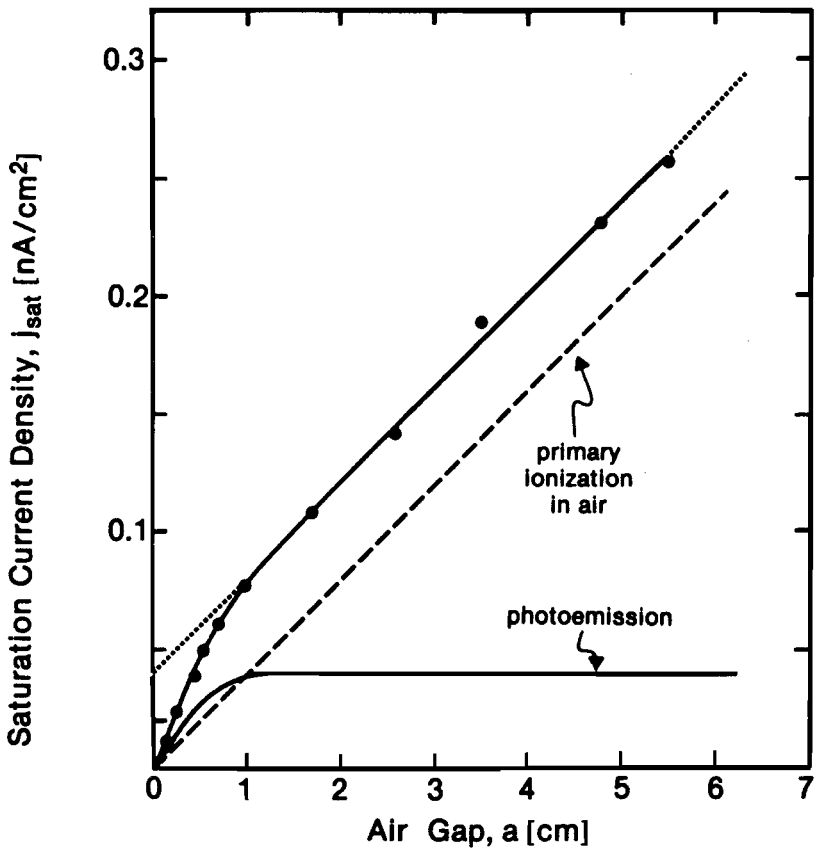

Figure 4.4 Saturation current density j_{sat} as a function of air gap thickness a for a 100 kVp x-ray beam with a H.V.L. of 2.2 mm Al and an exposure rate of 9.4 R/min.

polarizing electrode. These photoelectrons have a range of ≅ 1 cm for our x-ray parameters[12-14] and thus ionize air up to a distance of 1 cm from the bottom electrode. For gaps larger than 1 cm the contribution to air ionization by the photoelectrons is thus constant, for gaps smaller than 1 cm the contribution depends on the gap thickness since some of the photoelectrons cross the gap and impinge onto the measuring electrode before they expend all of their energy through ionization. The measured saturation density j_{sat} is thus the sum of the current density produced by the primary ionization in air and the current density produced by the backscattered photoelectrons. For our particular example, as shown in Fig. 4.4, the two components are equal when the range of photoelectrons in air equals the air gap thickness (1 cm). The primary ionization component increases linearly with a, as shown with the dashed line in Fig. 4.4. For air gaps smaller than 1 cm the photoemission component is larger than that of the primary ionization, while for gaps larger than 1 cm the photoemission component remains constant. The photoelectron component depends strongly on the bottom electrode effective atomic number and will not be as pronounced in a conventional ionization chamber, where the bottom electrode is usually carbon (Aquadag). The distinction between the two components, of course, is important only when an ionization chamber is used for absolute measurements. In this case only the primary air ionization should be measured and the contribution of the photoelectrons to the saturation current density should be subtracted from the total, as shown in Fig. 4.4.

As the photon energy is increased the photoelectron contribution to the saturation current diminishes and becomes negligible for cobalt beams, as shown in Fig. 4.5. The saturation current density is

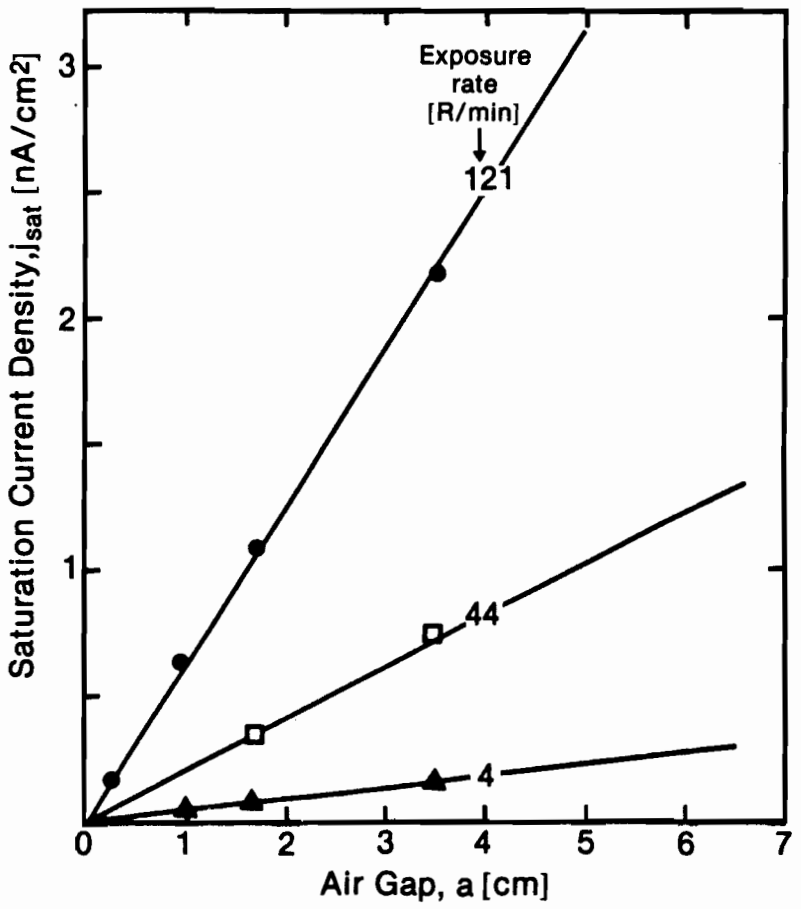

Figure 4.5 Saturation current density j_{sat} as a function of air gap a for various exposure rates of a cobalt-60 beam.

plotted as a function of the air gap for three exposure rates with the chamber centre at 80 cm from the source. Since the relationship between j_{sat} and a is linear we conclude that only primary air ionization is contributing to j_{sat} and the photoelectron backscatter from the bottom electrode is negligible.

4.5 EXTRAPOLATED FIELD

We have seen in Fig. 4.2 that the value of the extrapolated field E^* increases with an increase in the air gap thickness a. When E^* is plotted as a function of a for a constant exposure rate and beam energy, a straight line results. This implies a direct proportionality between E^* and a. In Fig. 4.6, two families of the E^* versus a relationship are shown. The solid lines represent an irradiation for various exposure rates with a 100 kVp beam (E_{eff}=30keV) and the dashed lines represent various exposure rates of a 50 kVp beam (E_{eff}=20keV). The slope of the linear relationship between E^* and a increases with an increase in exposure rate for same beam energy. The relationship between E^* and a may thus be expressed as follows:

$$E^* = \delta a, \tag{4.14}$$

where δ, the slope on the E^* versus a plot, is a function of the exposure rate and may also be a function of beam energy.

Figure 4.7 where E^* versus a is plotted for various exposure rates of cobalt irradiation, shows that Eq. (4.14) also holds for high energy photon beams. The possible dependence of δ on beam energy can be

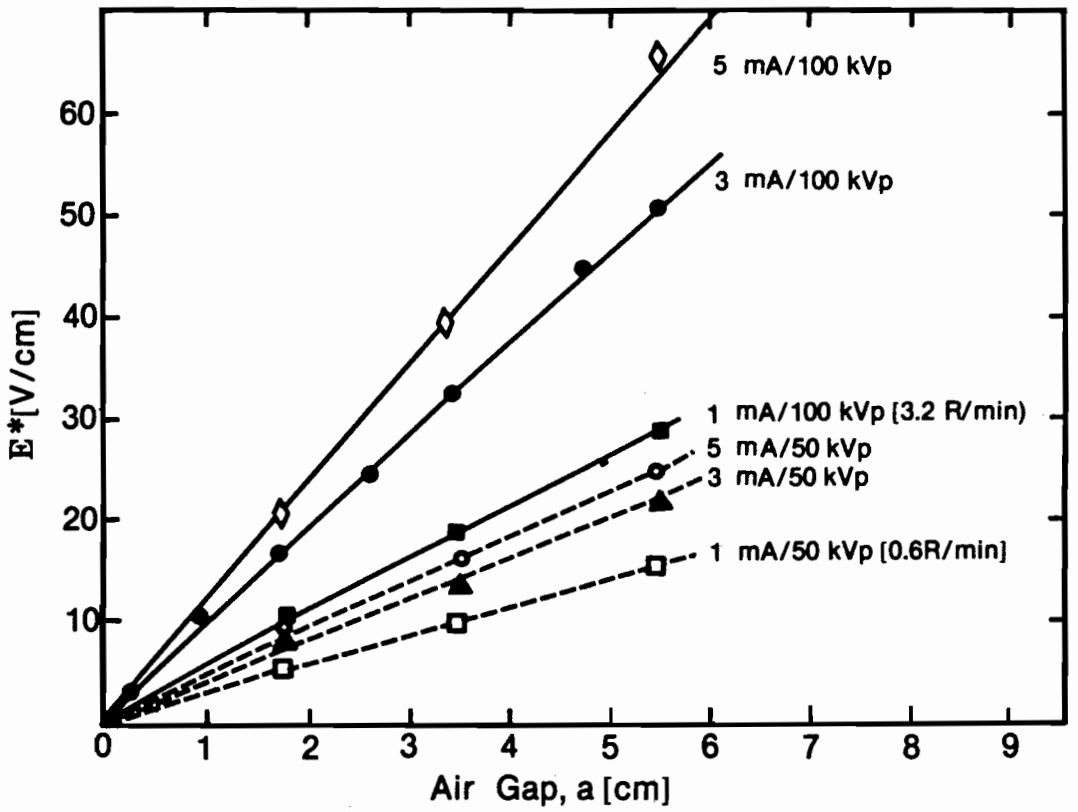

Figure 4.6 Measured extrapolated electric field E^* as a function of air gap thickness a for various exposure rates of a 50 kVp(1.0 mm Aℓ) and a 100 kVp (2.2 mm Aℓ) x-ray beam.

tested by comparing values of δ for different beam energies at similar exposure rates. The data presented in Figs. 4.6 and 4.7 indicate that the values of δ are similar for similar exposure rates, eventhough the agreement is not perfect. The saturation current density j_{sat} for our chamber is not exactly proportional to the exposure rate for low energy photon beams, because of the photoemission contribution to air ionization, as shown in Fig. 4.4. Thus, at low energies, j_{sat} indicates an exagerated exposure rate and therefore the extrapolated field and δ are also different from values that would be obtained if only primary ionization were considered. A correction to the full low energy saturation curve yields values for E^* and δ identical to those for cobalt irradiation for same exposure rates. We thus conclude that δ is independent of beam energy, but is a function of exposure rate $\dot{x}$. To avoid problems with photoemission contribution to j_{sat}, reference will be given to the parameter (j_{sat}/a) rather than the exposure rate. It should be noted, however, that under ideal conditions (j_{sat}/a) is directly proportional to the exposure rate.

4.6 IONIZATION CHAMBER CONSTANT

To investigate the relationship between δ and exposure rate, δ is plotted in Figs. 4.8 and 4.9 as a function of j_{sat}/a for photon beams of various energies. Figure 4.8 represents a plot on a linear scale and we note that all points irrespective of beam energy fall on one curve, going through the origin and resembling a power function of the type:

$$\delta = k\ (j_{sat}/a)^m, \tag{4.15}$$

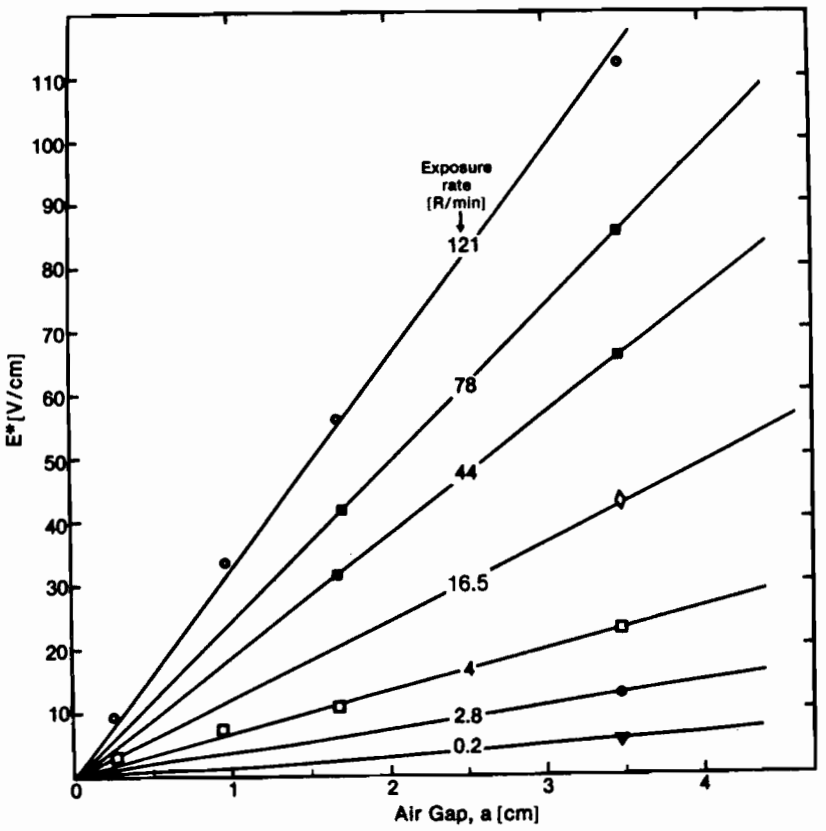

Figure 4.7 Measured extrapolated electric field E* as a function of air gap thickness a for various exposure rates of a cobalt-60 beam.

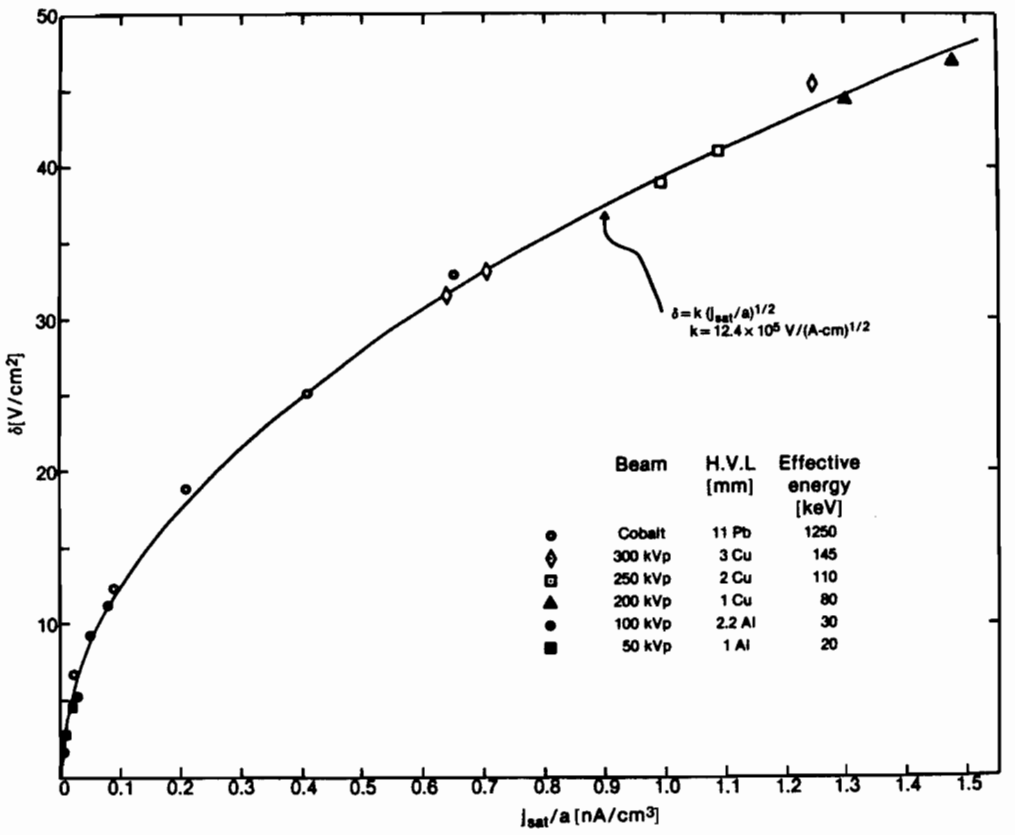

Figure 4.8 Function $\delta\ (j_{sat}/a)$ for various effective beam energies, exposure rates and air gap thicknesses a. The solid line represents a plot of Eq. (4.15) with $k=12.4\times10^5$ V/(A-cm)$^{\frac{1}{2}}$ and $m=0.5$.

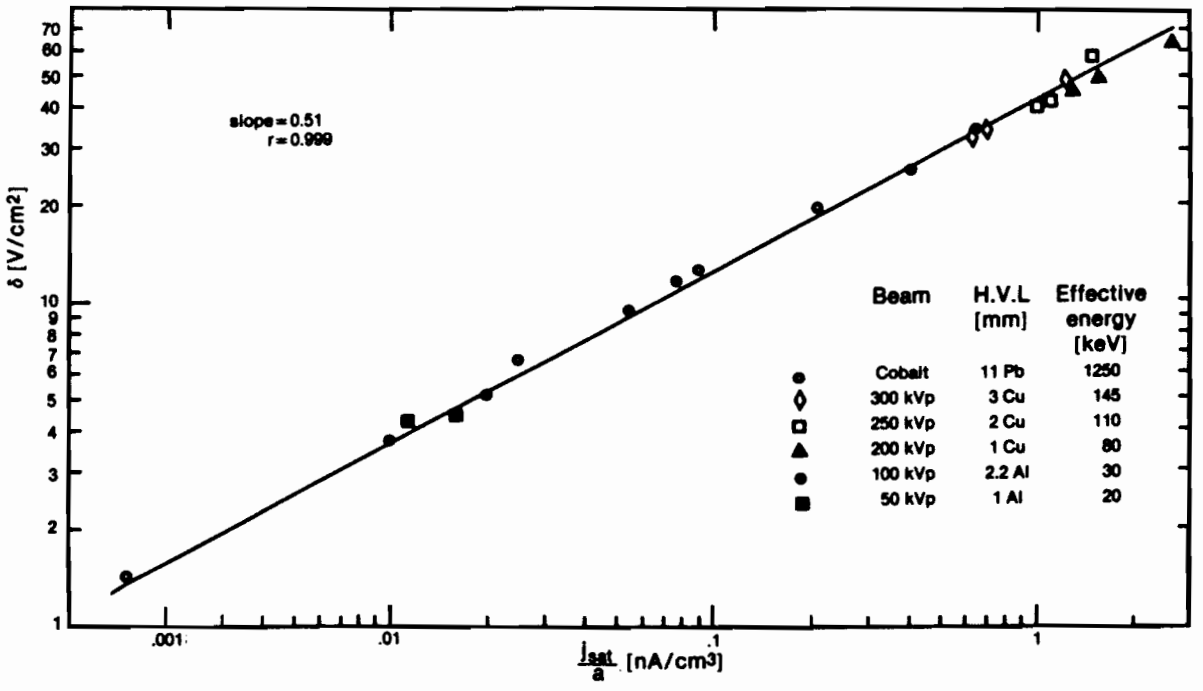

Figure 4.9 Function δ versus (j_{sat}/a) for various effective beam energies, exposure rates and air gap thicknesses a.

where k is a constant of proportionality and m the power.

When the data of Fig. 4.8 are replotted on a log-log scale, a straight line results as shown in Fig. 4.9. Least square fit calculation gives a slope of 0.51 with a correlation coefficient r = 0.999. The power m of Eq. (4.15) is thus equal to $1/2$ and the relationship between δ and j_{sat}/a may be expressed as follows:

$$\delta = k\ (j_{sat}/a)^{\frac{1}{2}} \tag{4.17}$$

Equation (4.17) indicates that E^* can be calculated for any ionization chamber when the air gap a and the saturation current density j_{sat} are known. The assumption is made, however, that k is a universal ionization chamber constant. To test this hypothesis, the measured extrapolated electric field E^* was plotted against $(aj_{sat})^{\frac{1}{2}}$ for various air gaps, photon beam energies and exposure rates. Figure 4.10 shows that the plot is linear for a photon energy range from 20 keV to 1.25 MeV with exposure rates from 1 R/min to 500 R/min. The least square fit to measured data yields a value of 12.4×10^5 V/(A-cm)$^{\frac{1}{2}}$ for the ionization chamber constant k with a correlation coefficient of r=0.998. Referring back to Fig. 4.9, we observe an excellent agreement between experimental data and the dashed line representing Eq. (4.15) with values for the parameters k and m equal to 12.4×10^5 V/(A-cm)$^{\frac{1}{2}}$ and 0.5, respectively.

Equation (4.17) gives a general relationship for a parallel-plate ionization chamber. The extrapolated field E^*, which is used in Eq. (4.13) to obtain the full saturation curve, is calculated from the measured saturation current density and the known air gap thickness. As shown before, of course, E^* can also be obtained from a measured saturation

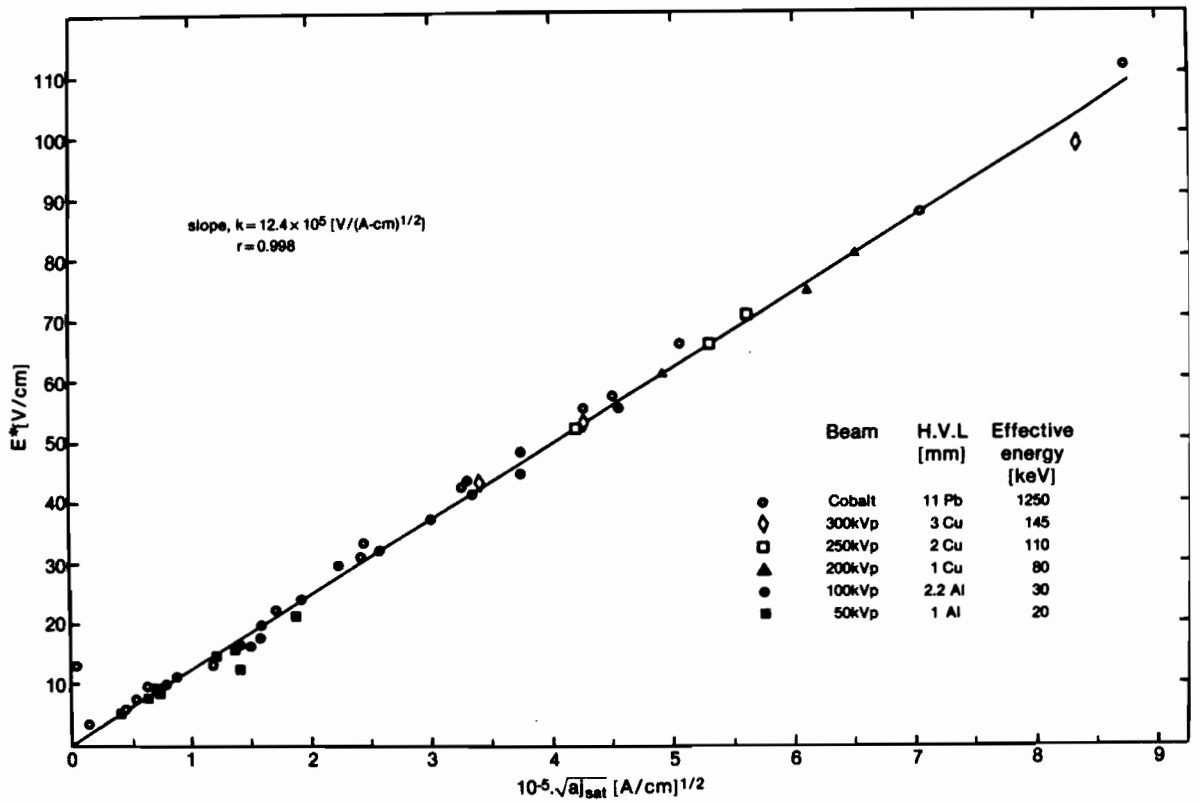

Figure 4.10 Extrapolated field $\overset{*}{E}$ as a function of $(aj_{sat})^{\frac{1}{2}}$ for various effective beam energies, exposure rates and air gap thicknesses a. j_{sat} is the saturation current density.

curve, extrapolating the initial slope to the value of 1 for the collection efficiency. Since (j_{sat}/a) is proportional to the irradiation exposure rate $\dot{x}$, one should note that E^* is proprotional to $a^2(\dot{x})^{\frac{1}{2}}$ (ignoring the photoemission from bottom electrode at low energies).

Combining Eqs. (4.13) and (4.17), the saturation curve can now be expressed, depending either on E^* or j_{sat} as parameter, as follows:

$$j = (E^{*2}/ak^2)\ tanh(E/E^*), \tag{4.18}$$

or

$$j = j_{sat} tanh[E/k(aj_{sat})^{\frac{1}{2}}], \tag{4.19}$$

where k is the universal parallel-plate ionization chamber constant given above.

It is interesting to note from Eq. (4.19) that the initial ionization current for small electric fields is given by:

$$j \cong k^{-1}(j_{sat}/a)^{\frac{1}{2}} E \propto k^{-1}(\dot{x})^{\frac{1}{2}} E, \tag{4.20}$$

which indicates that, initially, the current is proportional to the square-root of the exposure.

4.7 CALULATION OF SATURATION CURVE

Equation (4.18) gives a relatively simple relationship between the measured ionization current j and chamber electric field E.

The question of calculating the full saturation curve from one pair of measured (j,E) values now arises. The procedure would be as follows: take the pair of measured (j,E) values, use Eq. (4.18) to calculate the extrapolated field E^*, next use Eq. (4.17) to calculate the saturation current density j_{sat} and finally use Eq. (4.13) to get the full saturation curve.

The process sounds simple; the problem, unfortunately, is that Eq. (4.18) cannot be solved analytically for E^*. It may, however, be solved graphically as shown in Fig. 4.11 for a specific measured pair (j,E) of (0.063 nA/cm^2, 10.7 V/cm), an air gap a of 1.68 cm and the 100 kVp (E_{eff}=30keV) beam. Equation (4.18) can be written as:

$$Y = (E^{*2}/jak^2) = [\tanh(E/E^*)]^{-1} , \qquad (4.21)$$

with E^* being the independent variable, labelled X in Fig. 4.11. The left and right-hand sides of Eq. (4.21) are plotted as two separate functions with X the independent and Y the dependent variable. The point of intersection of the two functions represent the extrapolated field E^* and is thus the unique solution to Eq. (4.18), as shown in Fig. 4.11 for our particular example E^* = 17 V/cm. This agrees very well with the value obtained through the extrapolation of the initial slope on the saturation curve (Fig. 4.2, 17 V/cm) or with the value of 16.8 V/cm obtained from Eq. (4.17) with the appropriate measured saturation current density.

It is thus possible, as shown by the example above, to calculate the extrapolated field E^*, the saturation current density j_{sat}, and the full saturation curve from a single measurement of chamber

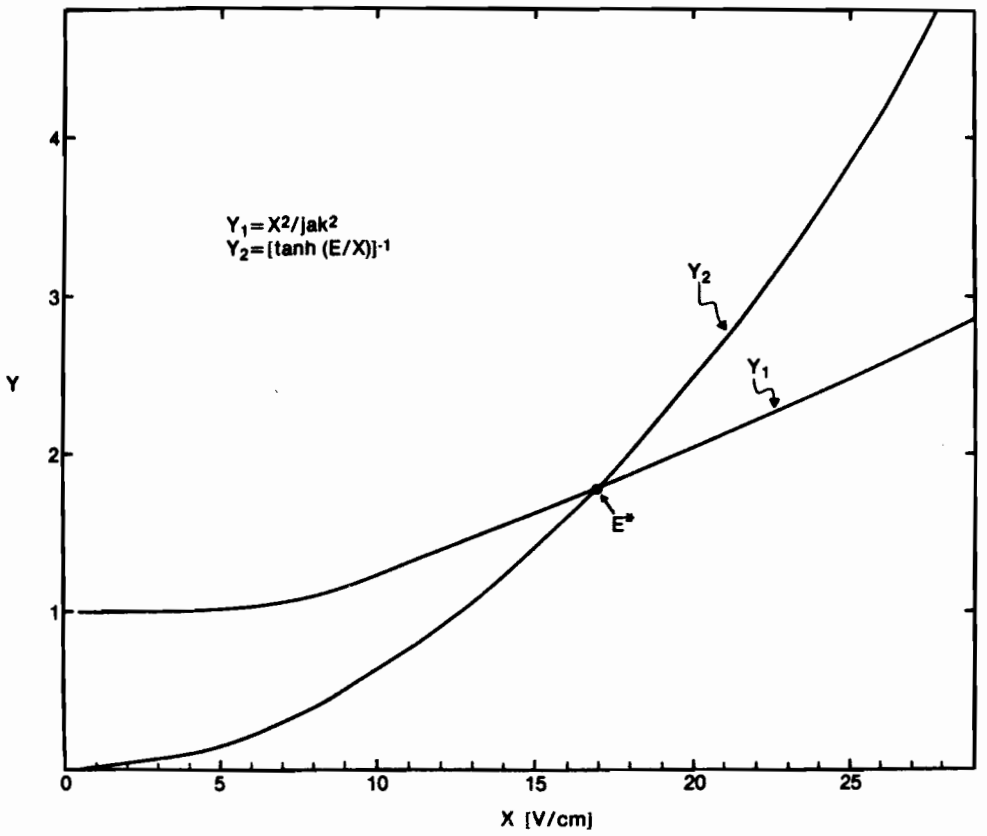

Figure 4.11 A graphic solution to Eq. (4.16) for a measured current density j, electric field E pair of (0.063 nA/cm^2, 10.7 V/cm) with an air gap thickness a of 1.68 cm and a 100 kVp (2.2 mm Aℓ) beam.

current j at a given electric field E. The chamber air gap thickness, of course, has to be known, and the value for the universal ionization chamber constant k is 12.4×10^5 V/(A-cm)$^{\frac{1}{2}}$, as shown above.

It should be noted that for large electric fields E where $E \geq 3\ E^*$ and the current density j reaches its saturation value j_{sat}, Eq. (4.18) transforms into Eq. (4.17) because $\tanh(E/E^*) = 1$ for $E \geq 3\ E^*$. The extrapolated field can then be calculated directly from Eq. (4.17) as discussed above. Equation (4.18) thus holds for all electric fields from 0 where $j = 0$ to ∞ where $j = j_{sat}$.

4.8 SUMMARY AND CONCLUSION

A new analytical expression has been presented to describe the full saturation curve of parallel-plate ionization chambers. The full saturation curve, i.e., plot of collection efficiency f versus electric field E of a parallel-plate ionization chamber, can be expressed as $f = \tanh(E/E^*)$, where E^* is the extrapolated electric field. This field, which is independent of beam energy but is a function of both exposure rate $\dot{x}$ and air gap thickness a, may be obtained from i) the measured saturation curve by extrapolating the initial slope of $f = 1$, ii) the known air gap a and saturation current density j_{sat} by multiplying our experimentally determined ionization chamber constant $k = 12.4\times10^5$ V/(A-cm)$^{\frac{1}{2}}$ with $(aj_{sat})^{\frac{1}{2}}$, and iii) from a single current density j measurement for a given electric field E and air gap a by graphically finding the intercept of two functions $Y_1 = (E^{*2}/jak^2)$ and $Y_2 = [\tanh(E/E^*)]^{-1}$.

The latter method is obviously the most useful since all of the parameters of the saturation curve equation and thus the saturation

curve itself can be calculated from one single measurement of ionization current at a given electric field and air gap thickness.

In contrast to the currently known expressions, which hold only in the near saturation region (i.e., $0.9 \leq f \leq 1$ and require at least two measurements in this region), the $f = \tanh(E/E^*)$ relationship is in excellent agreement with measurements in the whole collection efficiency range from 0 to 1 for x-ray sources with effective energies from 20 to 150 keV and cobalt-60 gamma rays.

Because this expression represents the full saturation curve, it will be used in subsequent chapters to describe the full charging and discharging dynamics of the radiation induced foil electret and to explain the charging characteristics of the ionographic latent image.

4.9 REFERENCES

1 J.J. Thomson and E. Rutherford, Philos. Mag. 42, 392(1896).

2 G. Mie, Ann. Phys. 13, 857(1904).

3 J.S. Townsend, Electricity in Gases (Oxford University Press, London,1915).

4 J.W. Boag, "Ionization Chambers", in Radiation Dosimetry,edited by F.H. Attix and W.C. Roesch (Academic Press, New York, 1966), Vol. 2.

5 J.W. Boag and T. Wilson, Br. J. Appl. Phys. 3, 222(1952).

6 Y. Moriuchi, Res. Electrotechn. Lab No. 736 (Tokyo,Japan,1973)

7 E. Kara-Michailova and D.E. Lea, Proc. Cambridge Philos. Soc. 36, 101(1940).

8 P. Langevin, Le Radium(Paris) 10, 113(1913).

9 J. Böhm, Phys. Med. Biol. 21, 754(1976).

10 J.W. Boag, Br. J. Radiology 23, 601(1950).

11 J.R. Greening, Phys. Med. Biol. 9, 143(1964).

12 K.W. Dolan, J. Appl. Phys. 46, 2456(1975).

13 C.A. Aeby and G.A. Whan, IEEE Transactions on Nuclear Science, NS-28, 4177(1981).

14 A.T. Nelms, Nat. Bur. Stand. (U.S.),Circ. 577,(1956).

CHAPTER 5

CHARACTERISTICS OF A RADIATION INDUCED FOIL ELECTRET

5.1 INTRODUCTION

As discussed before, the electrostatic latent image is essentially a foil electret with surface charge density modulated by the photon transmission through the object. In this chapter we discuss the characteristics of foil electrets with a uniformly distributed charge density. The results will be used in Chapter 7 to describe the properties of electrostatic latent images. The expression we had developed in the previous chapter for the saturation curves of parallel-plate ionization chambers will be used to describe the characteristics of the foil electret. The electret production technique is simple, the charge deposition extremely well controllable and the surface charge density, which easily reaches the theoretical limit, is uniform. The existence of electrets has been known for quite some time but it is only in the last decade that electrets have gained prominence because of numerous practical applications found for them in science and industry (e.g., microphones, electrostatic recording, air filters, motors and generators, dosimeters, piezoelectric polymer transducers and devices, artificial arteries, etc.). An excellent treatment of electrets is given in a recent book edited by G.M. Sessler.[1]

An electret is a dielectric material exhibiting a quasi-permanent electrical charge. The electret charge may consist of surface charge layers (space charges) or polarization charges or a combination of both. The real charges comprise layers of trapped positive and negative carriers often positioned at or near the two surfaces of the dielectric while true polarization is usually a frozen-in alignment of dipoles. On certain metallized electrets, a compensation charge may

reside on the electrode unable to cross the energy barrier between the metal and dielectric. It is important to note that the net charge on an electret is zero or close to zero and the fields produced by the electrets are attributed to charge separation and not to net charge.

An electret is in many ways the electrostatic analogue of a permanent magnet, with the difference that electret properties are due to either dipolar or monopolar charges which may actually attract charged particles from the surrounding medium to compensate the charges on the electret surface. The electret merely provides an electric field; it is not a source of energy.

Eguchi[2] in 1922 performed the first systematic research into electrets when he discovered that when a certain liquid dielectric mixture (e.g., carnauba wax) was allowed to solidify in an external electric field, and the electric field subsequently removed, the solid exhibited electric polarization which was retained for a long time. This type of electret is now called a thermoelectret because it is formed by the simultaneous action of an electric field and heat. Although thermal techniques have been used to produce classical electrets in carnauba wax or similar substances,they have also been applied to other solids, such as naphthalene[3] and ionic crystals[4]. Nadjakov[5] in 1937 discovered what is now called the photoelectret[6] where polarization is produced by simultaneous action of electric field and light.

Modern electret research has shifted to thin polymer films because of numerous practical applications of foil electrets. Standard polymer film thermoelectrets[7] are formed in relatively low electric fields (10-50 kV/cm) at temperatures of 100-200°C, while piezoelectric

polymer films are obtained by application of fields of up to 800 kV/cm applied to the electrodes evaporated onto the polymer surfaces at elevated temperatures, or by fields of 4 MV/cm at room temperature. Piezoelectric and pyroelectric electrets are of interest in industrial research because of their potential value as thermoelectric and electromechanical transducers.

Isothermal charge deposition methods have recently gained importance because of the ease and speed with which they allow polymer films to be charged. Some isothermal techniques are based on spark discharge[9], liquid contact[10], injection of monoenergetic particle beams[11,12] of range smaller than the thickness of the dielectric, or carrier displacement by large doses of x-rays or gamma rays (radioelectrets).[13] The most widely used is the corona charging technique where an inhomogenous field, generated by a voltage between a point shaped electrode (at a few kV) placed above the dielectric and a planar back electrode on the other side of the dielectric, produces a discharge in the air at atmospheric pressure. Corona currents are controlled by the flow of ions in the space-charge field between the corona emitter (i.e., point shaped electrode) and the dielectric surface. When the emitter is negative the ions carry negative charges, and when it is positive the ions have positive charges. The ions are generated by collisions of electrons and ions with molecules in the highly accelerating electric field[15].

The deposition of charge has been studied by investigators involved with xerography and it has been found that a voltage grid must be inserted into the system to improve the uniformity of the surface charge distribution. The best arrangement is to place a wire

grid at a potential of a few hundred volts between the corona point and the dielectric.

In Fig. 5.1, taken from Schaffert[15], we show tranverse charge distribution with various voltages Vg of the grid placed at various positions between the corona point and dielectric. It is assumed that the eventual distribution is "generally" uniform if the charging is carried to the point where the entire sample surface has assumed a saturation potential which equals the grid potential.

In this chapter we report a new isothermal technique for accurate deposition of uniform and stable charge densities close to 10^{-6} C/cm^2 on polymers to form an electret.[16-18] The electret is produced in a chamber resembling a parallel-plate ionization chamber used in radiation dosimetry. The chamber shown schematically in Fig. 3.4. is placed into a radiation field and the charge carriers produced by photon interactions in the sensitive chamber air volume drift in the effective electric field towards the appropriate electrode. The polarizing electrode is a standard conductive electrode; the measuring electrode, however, is blocking and is covered by a thin polymer foil. The charge carriers drifting towards the measuring electrode get trapped on the polymer surface thereby forming a stable foil electret. The polarity of the electret depends on the direction of the externally applied electric field. The initial electret charging current is proportional to the sensitive air volume and to the x-ray exposure rate. It also depends strongly on the atomic number of the polarizing electrode reflecting the photoemission contribution to the air ionization in the electret chamber sensitive volume.

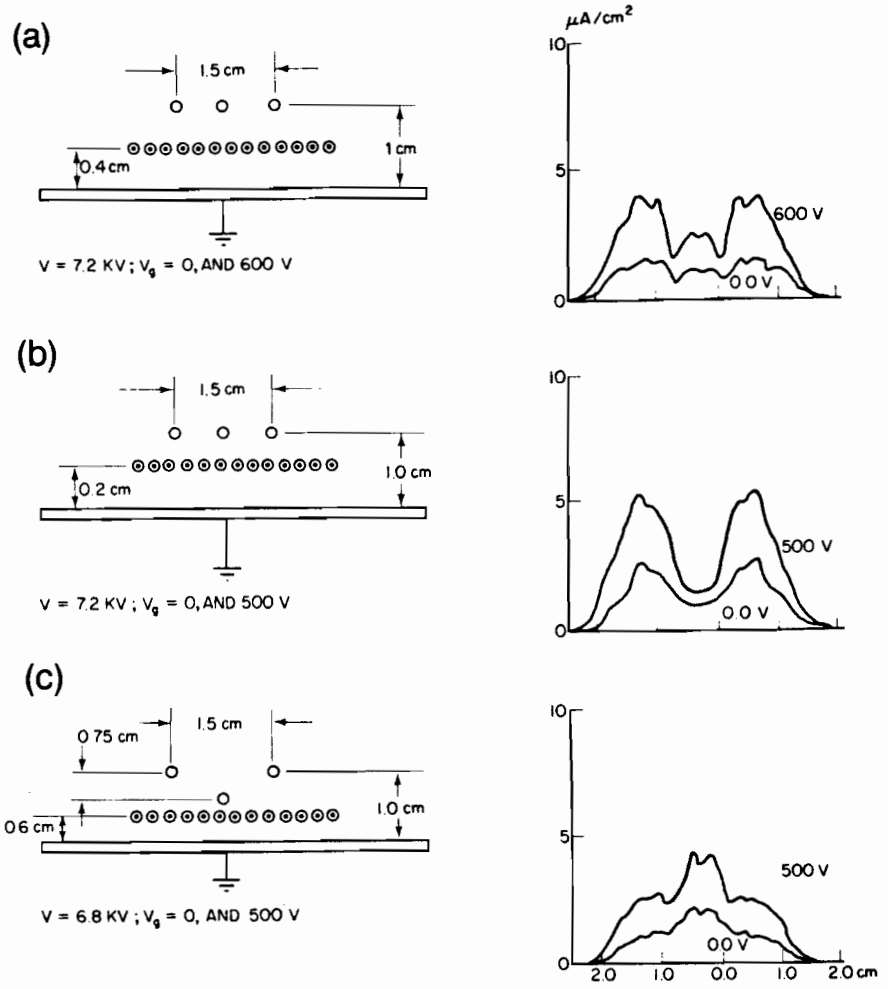

Figure 5.1 Transverse distribution of wire-to-plate currents for 3 wire corona arrangement with intervening grid. (*a*),(*b*) Effect of grid-to-plate spacing; (c) effect of moving centre of corona wire closer to plate.[15] Vg = grid voltage.

Studies of the production of the radiation induced foil electret state described here are relevant for two reasons: first, at high exposures, the technique is a new and simple isothermal method for production of stable, uniform and strong foil electrets, and second, at low exposures, the technique has been used for years in electrostatic radiographic imaging[19-20] without a realization that the latent image was actually a weak nonuniform foil electret. An understanding of the electret charging and discharging dynamics will thus also improve our understanding of imaging properties in electrostatic imaging, where the electret charging corresponds to the production of the latent image and the electret discharging corresponds to the development of the radiographic image.

In the following sections, the experimental technique for production of radiation induced foil electrets is explained in detail, the maximum surface charge densities achieved experimentally reported and the dynamics of the electret charging and discharging process examined theoretically and experimentally. The influence of the externally applied electric field and chamber parameters (e.g., polymer and air gap thickness, polymer and polarizing electrode material) on the chamber saturation current density, on the extrapolated electric field and on the electret characteristic polarization or depolarization time is discussed.

5.2 PRODUCTION OF RADIATION INDUCED FOIL ELECTRETS

The air in the chamber sensitive volume is ionized by electrons produced by the direct interactions of photons with air molecules and by photoelectrons which are produced by x-rays in the polarizing electrode and backscattered into the chamber sensitive volume. The free charge carriers drift in the chamber effective electric field towards the appropriate electrode. In contrast to a standard ionization chamber, where the charges impinge directly onto the electrodes, in the electret chamber the charges moving in the direction of the measuring electrode get stopped and trapped on or near the polymer surface to form a stable foil electret. The current measured in the external circuit is due to compensation charges moving onto the measuring electrode from the power supply.

As shown schematically in Fig. 5.2 (a-c) the effective electric field in the air gap $\vec{E}_{eff}(t)$ is, for the electret charging process, equal to the vector sum of the field $\vec{E}_a(0)$ produced in the air gap by the external power supply V_o and the time dependent field $\vec{E}_\sigma(t)$ produced by the electret charges accumulated on the foil:

$$\vec{E}_{eff}(t) = \vec{E}_a(0) + \vec{E}_\sigma(t). \tag{5.1}$$

$E_a(0)$, the magnitude of $\vec{E}_a(0)$, may be written in terms of the external power supply V_o, air gap a, polymer thickness p, and the dielectric constants ε_a and ε_p for air and polymer respectively as:

$$E_a(0) = V_o \varepsilon_p / (p\varepsilon_a + a\varepsilon_p). \tag{5.2}$$

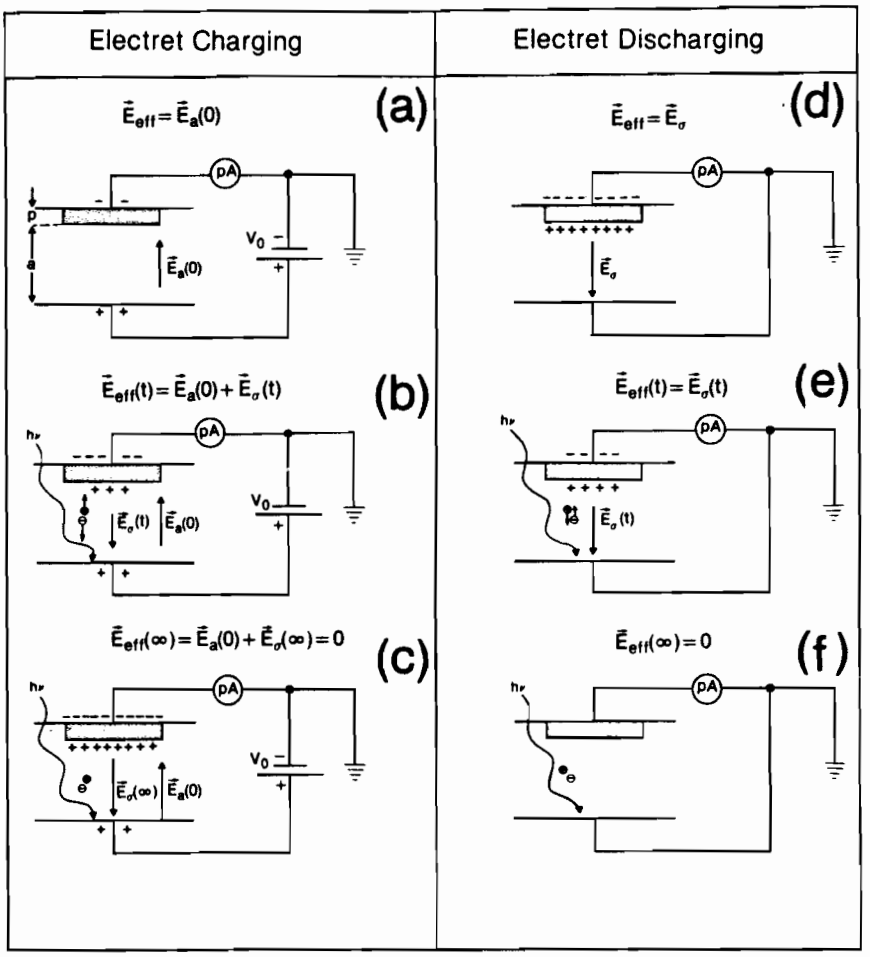

Figure 5.2 Schematic representation of the electret charging (a)-(c), and electret discharging (d)-(f) process. $\vec{E}_a(0)$ is the externally applied electric field in the air gap a, $\vec{E}_\sigma(t)$ the electric field produced by the electret, and $\vec{E}_{eff}(t)$ the effective electric field in the air gap.

$\vec{E}_\sigma(t)$ is pointing in the opposite direction to $\vec{E}_a(0)$ so that the magnitude of $\vec{E}_{eff}(t)$ ranges from $E_a(0)$ at the beginning of the electret charging process, where $E_\sigma(0) = 0$, to 0 when the electret is fully charged and $E_\sigma(\infty) = E_a(0)$.

Using Gauss's law:

$$\varepsilon_p E'_{eff}(t) - \varepsilon_a E_{eff}(t) = \sigma(t)/\varepsilon_o , \tag{5.3}$$

and Kirchoff's law:

$$V_o = aE_{eff} + pE'_{eff} , \tag{5.4}$$

where E'_{eff} is the magnitude of the effective electric field in the polymer, and $\sigma(t)$ is the electret surface charge density, we can express $E_{eff}(t)$, the magnitude of the effective field in the air gap, as:

$$E_{eff}(t) = E_a(0) - E_\sigma(t) = \frac{V_o\varepsilon_p - p\sigma(t)/\varepsilon_o}{p\varepsilon_a + a\varepsilon_p} \tag{5.5}$$

The electret discharging process, which is used in studies of the electret state dynamics, is shown schematically in Fig. 5.2 (d-f). The chamber polarizing and measuring electrodes are shorted through an electrometer as shown in Fig. 5.2(d). Since the externally applied electric field $\vec{E}_a(0)$ is now equal to zero, the effective field in the chamber sensitive volume $\vec{E}_{eff}(t)$ is equal to the field $\vec{E}_\sigma(t)$ produced by the electret charge layer. This field is opposite in sign but initially equal in magnitude to the original field $E_a(0)$ applied during the

electret charging process. The charge carriers produced by radiation are thus moving in directions opposite to directions in the charging process, causing the depletion of the electret charge layer through annihilation of opposite charge carriers on the polymer surface [Fig.5.2 (e)]. Consequently, the effective electric field in the air gap is steadily decreasing in time and it reaches zero when the electret is completely discharged as shown in Fig. 5.2 (f). A similar electret discharging process has recently been proposed as a radiation dosimetry technique.[21]

5.3 MAXIMUM ELECTRET POLARIZATION

When the two opposing fields, $\vec{E}_a(0)$ and $\vec{E}_\sigma(t)$ become equal in magnitude during the electret charging process, the ion pairs produced by radiation no longer drift in an electric field and no additional charge deposition onto the polymer surface is possible. The electret surface charge density $\sigma(t)$ has reached its maximum possible value, which is from Eq.(5.5), with $E_{eff}(t) = 0$, expressed as:

$$\sigma_{max} = \varepsilon_o \varepsilon_p V_o/p = C_e V_o \ . \tag{5.6}$$

This relationship is equal to the basic expression giving the maximum charge density on a parallel plate dielectric capacitor of a specific capacitance C_e with V_o across the dielectric of thickness p. At this maximum the electret charge density σ_{max} is larger than the original charge densities on the plates of the capacitor, defined by measuring and polarizing electrodes of the electret chamber, by a factor approximately equal to $(a\varepsilon_p/p)$ which is typically

equal to 10^3.

The maximum electret surface charge density σ_{max} is, at high applied voltages V_o, limited by the dielectric strength of the foil material. For Mylar the dielectric strength is equal to 2.8 MV/cm.[9] In Fig. 5.3, we show the measured σ_{max} as a function of potential difference V_o for two thicknesses of Mylar (0.05 mm and 0.175 mm). σ_{max} was determined either by measuring the compensation charge collected on the measuring electrode during the electret charging process or by measuring the charge leaking off the measuring electrode during the electret discharging process. Both techniques give same charge magnitudes but opposite polarities.

For applied voltages below 1000 V there is a perfect agreement between Eq.(5.6) and experiment. For voltages above 1000 V but below the dielectric strength limit, however, the measured charge densities become progressively lower than values calculated from Eq. (5.6). Empirically, we find that σ_{max} depends upon the polarizing voltage V_o according to an expression resembling a Schottky[22,23] or Poole-Frenkel[23] process:

$$\sigma_{max} = 2C_e v_B^{\frac{1}{2}} \left[(V_o + v_B)^{\frac{1}{2}} - v_B^{\frac{1}{2}} \right] , \qquad (5.7)$$

where C_e is the electret specific capacitance obtained from Eq. (5.6) and v_B the breakpoint voltage between the low voltage linear ($\sigma_{max} \propto V_o$) region described by Eq. (5.6) and high voltage quadratic ($\sigma_{max}^2 \propto V_o$) region. The solid lines in Fig. 5.3 are plotted for two polymer thicknesses using Eq.(5.7) with appropriate values for C_e and a value of 2500 V for v_B. The agreement between Eq. (5.7) and the

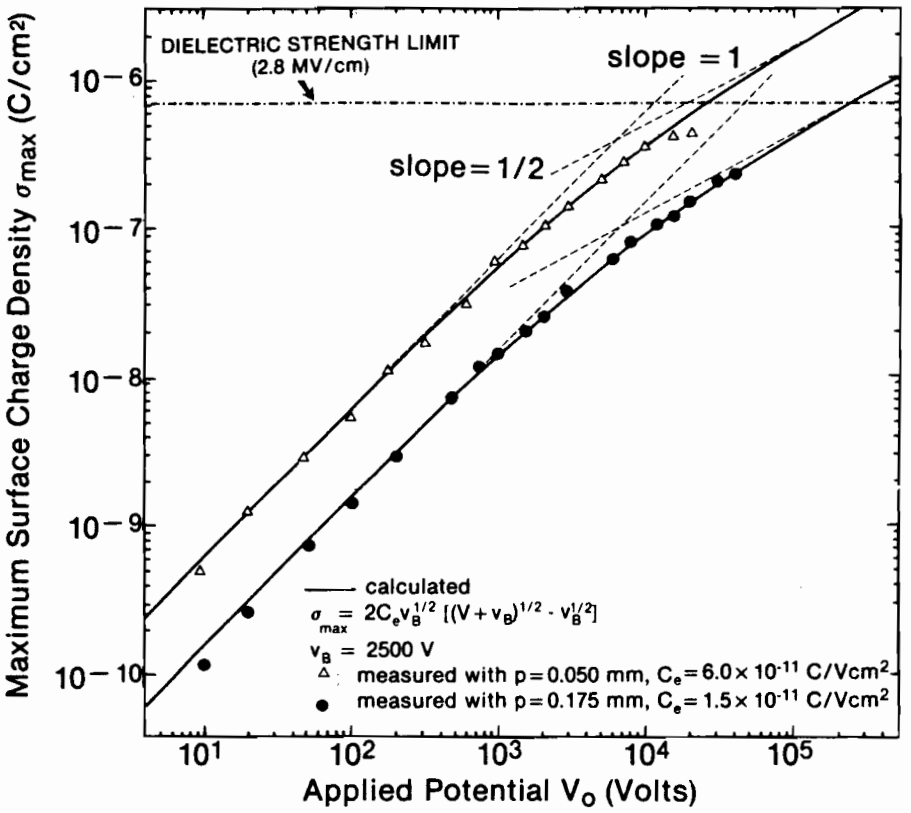

Figure 5.3 Dependence of the maximum electret surface charge density σ_{max} upon the externally applied voltage V_o for two thicknesses of Mylar.

experimental values is excellent in the whole practical range of voltages. It can be shown that Eq.(5.7) transforms into Eq. (5.6) for $V_o \ll v_B$. Similar $V_o^{\frac{1}{2}}$ dependence was observed at high voltages for ionic space charge thermoelectrets,[4] and electret states in naphtalene crystals[3].

As shown in Fig. 5.3,electrets with surface charge densities close to 10^{-6} C/cm^2 can be produced by our new isothermal charging technique. Either positive or negative charge carriers can be trapped on the polymer surface depending on the polarity of the external power supply. Any desired surface charge density can be achieved, since the charging process follows Eq. (5.7) perfectly. The limitation, of course, is the dielectric strength of the electret material.

5.4 DYNAMICS OF ELECTRET CHARGING AND DISCHARGING

In Fig. 5.4,we show schematically for a typical electret charging discharging cycle (*a*) the experimental configuration and (*b*) the electret charging and discharging current density as a function of time. The electret polarization (charging) process begins at a time $t = 0$. In practice this is achieved either by switching the x-rays on at $t < 0$ and the external field at $t = 0$, or by switching the external field on at $t < 0$ and the x-rays at $t = 0$. The electret depolarization (discharging) process also, for calculation purposes, begins at $t = 0$. The x-rays are switched on at $t = 0$ and the electrodes shorted at $t = 0$, or the electrodes are shorted at $t < 0$ and the x-rays switched on at $t = 0$.

Initially the charging current is constant and equal to a standard ionization chamber current under same conditions, provided

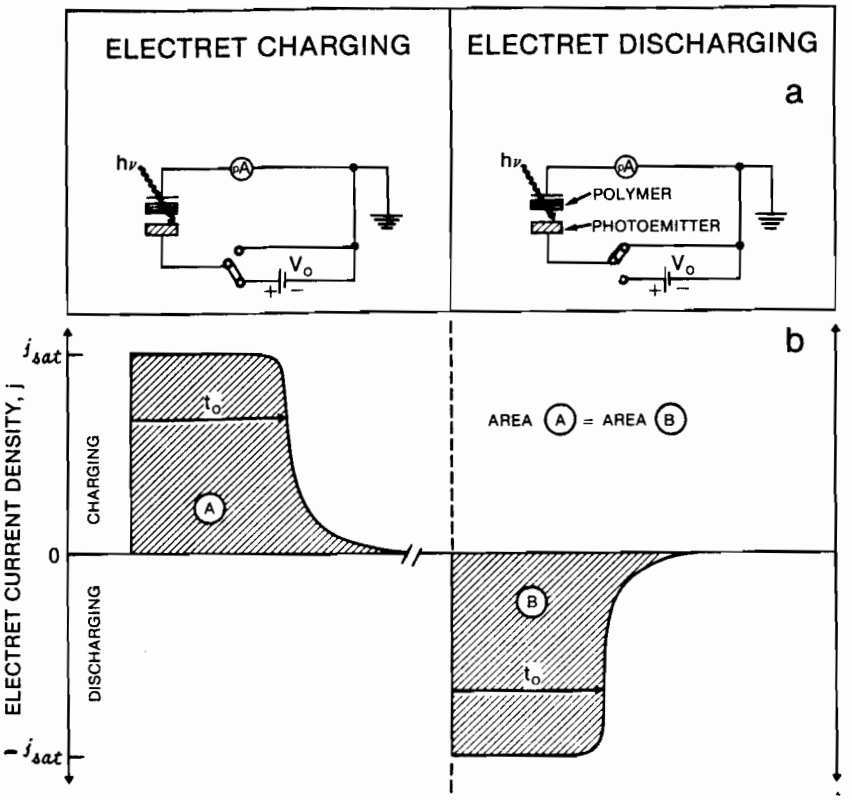

Figure 5.4 Time dependence for a typical electret polarization (charging) depolarization (discharging) cycle: (*a*) schematics of experimental configuration, and (*b*) electret polarization and depolarization current density. t_o is characteristic electret polarization or depolarization time.

that V_o, the externally applied voltage, is high enough to produce saturation conditions in the electret chamber. After a characteristic time t_o, dependent on V_o, the charging current drops to zero exponentially as shown in Fig. 5.4 (*b*) and the result is a foil electret charged to its limit as determined by Eq. (5.7). For a typical exposure rate of 9 R/min, t_o varies from a few seconds to a few minutes, depending on the electret chamber parameters. As discussed above the electret can be discharged by shorting the two chamber electrodes in the x-ray field resulting in a discharging current profile equal in magnitude but opposite in sign to that of the charing current. The charge conservation is thus preserved since the areas under the charging and discharging current profiles are equal.

In general the electret surface charge density $\sigma(t)$ may, from Eq. (5.5), be written as:

$$\sigma(t) = \sigma_{max} - \beta E_{eff}(t) \ , \tag{5.8}$$

where σ_{max} is given by Eq. (5.7) and β is a parameter defined as:

$$\beta = \varepsilon_o (a\varepsilon_p + p\varepsilon_a) / p \ . \tag{5.9}$$

The electret charging or discharging current density j may be expressed by differentiating Eq. (5.8) to obtain:

$$j = d\sigma / dt = - \beta dE_{eff}(t)/dt \ . \tag{5.10}$$

We have shown in Chapter 4 that the full saturation curve i.e., a plot of the collection efficiency f versus the applied electric field E, of a parallel-plate ionization chamber can be expressed as:

$$f = j/j_{sat} = \tanh (E/E^*) , \qquad (5.11)$$

where f is defined as the ratio of ion pairs collected to ion pairs produced, j is the measured current density as a function of the applied electric field E in the chamber sensitive volume, and j_{sat} is the saturation current density attained when all ion pairs produced in the chamber sensitive volume are collected. The hyperbolic function of Eq. (5.11) exhibits a form identical to that of measured saturation curves: linearity at small fields, where $\tanh(E/E^*) \sim E/E^*$, and saturation for fields larger than $3E^*$, where $\tanh (E/E^*) \sim 1$. The extrapolated electric field E^* is the field at which the collection efficiency would equal unity if the initial linear relationship between f and E, exhibited at small fields, held for all electric fields. It is a function of the x-ray exposure rate, the polarizing electrode material as well as the air gap thickness and will be discussed in detail in Sec. 5.6 . The saturation curve calculated from Eq.(5.11) is in excellent agreement with measurements in the whole collection efficiency range from 0 to 1 for x-ray sources with effective energies from 20 to 300 keV and for cobalt-60 gamma sources.

Figure 5.5 (*a*) shows a typical saturation curve calculated (solid line) from Eq. (5.11) and measured (experimental points) for our electret chamber converted into a standard ionization chamber by

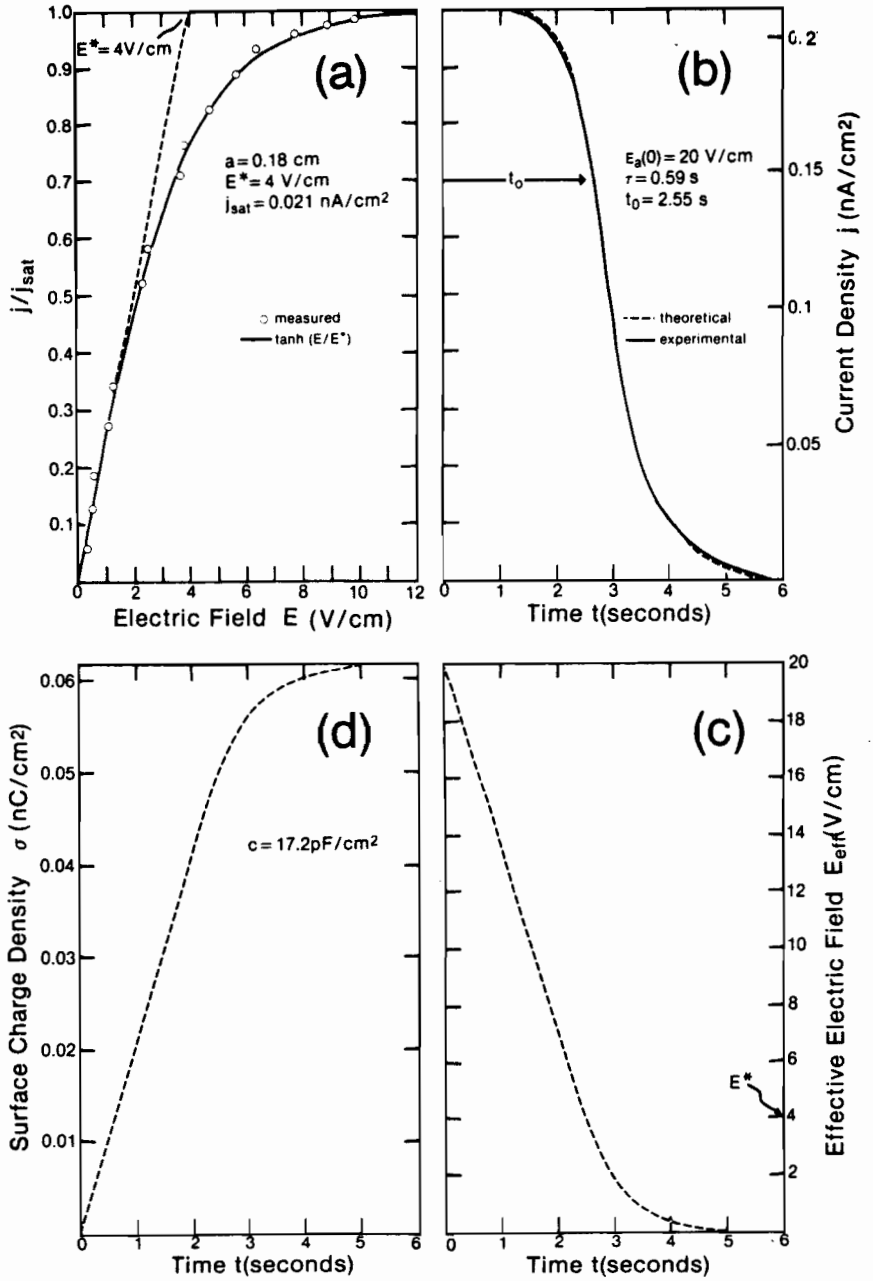

Figure 5.5 (a) Measured and calculated ion collection efficiency for a parallel-plate ionization chamber with an air gap a of 0.18 cm and an aluminum polarizing electrode, (b) measured [solid curve] and calculated [dashed curve] polarization current density j as a function of time t for an air gap of 0.18 cm, polymer thickness p of 0.018 cm, polymer dielectric constant ε_p of 3.5 and an applied voltage V_o of 3.7 Volts, (c) calculated effective field E_{eff} as a function of time t for same parameters as in (b), and (d) calculated electret surface charge density σ as a function of time t for same parameters as in (b).

removing the thin polymer coating from the measuring electrode. The agreement between measured and calculated data is excellent. For an air gap a of 0.18 cm, an aluminum polarizing electrode, and an exposure rate of 9 R/min, the extrapolated electric field E^*, obtained by extrapolating the initial linear relationship between δ and E to $\delta = 1$, is 4 V/cm.

Since the electret chamber closely resembles a standard ionization chamber, Eq. (5.11) may be used to describe the electret polarization or depolarization current density j, noting of course that the applied field E in Eq. (5.11) is now the effective field $E_{eff}(t)$ in the air gap as given by Eq. (5.5):

$$j = j_{sat} \tanh[E_{eff}(t)/E^*] \ . \tag{5.12}$$

Combining Eqs. (5.10) and (5.12) we get the following expression relating $E_{eff}(t)$ with t :

$$\int_{E_a(0)}^{E_{eff}} \coth[E_{eff}(t)/E^*]\, dE_{eff} = -\,(j_{sat}/\beta) \int_0^t dt \ , \tag{5.13}$$

and after solving for t :

$$t = t_\sigma - \tau \ln \sinh[E_{eff}(t)/E^*], \tag{5.14}$$

where τ , the electret relaxation time, and t_σ, the electret characteristic polarization or depolarization time are given below:

$$\tau = \beta E^{*}/j_{sat} \,, \tag{5.15}$$

and

$$t_o = \tau \, \ell n \, sinh[E_a(0)/E^{*}], \tag{5.16}$$

with $E_a(0)$ and β defined by Eqs. (5.2) and (5.9), respectively.

Equations (5.13) through (5.16) are valid for both the electret polarization and the depolarization process. One should note, however, that $E_a(0)$, the externally applied field, which was used to charge the electret is equal to zero in the depolarization process. It is replaced in Eqs.(5.13) and (5.16) by $E_\sigma(0)$, the field produced by the initial electret charge layer. As discussed in Sec. 5.2, the fields $E_a(0)$ and $E_\sigma(0)$ are equal in magnitude but opposite in sign. The depolarization current profile is thus equal in shape but opposite in sign to the polarization current profile, as indicated in Fig. 5.4 (b).

Employing Eq. (5.12) in conjunction with Eq. (5.14) we can now express the electret polarization or depolarization current density as a function of time as :

$$j(t) = j_{sat}\, e^{(t_o - t)/\tau} \{1 + e^{2(t_o - t)/\tau}\}^{-\frac{1}{2}} \,, \tag{5.17}$$

where t_o and τ were defined above.

Since in the saturation region $E_a(0) > 3E^{*}$ then $t_o > \tau$ and $j(t)$ will exhibit the following behavior: at $t = 0$ it will be equal to j_{sat} and remain equal to j_{sat} until the effective field in the air gap $E_{eff}(t)$ falls below $3E^{*}$. Then j begins to decrease, becomes

equal to $(1/\sqrt{2})j_{sat}$ at $t = t_o$ and exponentially approaches zero as t increases further.

A plot of an electret polarization current density $j(t)$ measured (solid line) and calculated from Eq. (5.17) (dashed line) is shown in Fig. 5.5 (b). The electret chamber parameters were identical to those of Fig. 5.5(a), i.e., $E^* = 4$ V/cm, an aluminum polarizing electrode and an exposure rate of 9 R/min. The chamber was initially in the saturation region since the externally applied field E_a (0) was 20 V/cm, i.e., $E_a(0) = 5\ E^*$. τ and t_o were calculated with Eqs. (5.15) and (5.16) as 0.59 s and 2.55 s respectively, in excellent agreement with experimental data.

The effective electret field $E_{eff}(t)$ in the air gap, which was defined by Eq. (5.5), may now be rewritten from Eq. (5.14) as:

$$E_{eff}(t) = E^* \operatorname{arc\,sinh} [e^{(t_o - t)/\tau}], \tag{5.18}$$

and is plotted in Fig. 5.5 (c) for our particular example ($t_o = 2.55$ s and $\tau = 0.59$ s). As expected, E_{eff} initially linearly decreases with time to compensate for the linear increase in $E_\sigma(t)$ resulting from a constant initial polarization current density j equal to j_{sat}. As t increases, however, the decrease in E_{eff} becomes progressively slower to reflect the hyperbolic behavior of j [(Eq. (5.12)] for effective fields smaller than $3\ E^*$.

The electret surface charge density $\sigma(t)$, which may be written combining Eqs. (5.8) and (5.18) as:

$$\sigma(t) = \sigma_{max} - \beta E^* \operatorname{arc\,sinh} [e^{(t_o - t)/\tau}], \tag{5.19}$$

is plotted in Fig. 5.5 (*d*) for our particular example. The time dependence is identical to that of $E_{eff}(t)$, plotted in Fig. 5.5 (c), except that here the function is subtracted from σ_{max}, giving a zero value for $\sigma(t)$ at $t = 0$, a linear rise for small t and an asymptotic approach to σ_{max} for large t . The electret charging process is terminated when $E_{\sigma}(t)$ becomes equal to $E_a(0)$ and the electret charge density $\sigma(t)$ reaches its maximum value σ_{max} defined by Eq. (5.7).

Radiation induced currents in the polymer could conceivably interfere with the measurements of electret polarization or depolarization current profiles. As shown in Fig. 5.5 (*b*), typical saturation current densities are on the order of 0.2 nA/cm^2. The maximum radiation induced current density in the polymer is estimated as less than 10^{-2} nA/cm^2 for a carrier production rate in Mylar[25] of $10^{-11}cm^{-3}s^{-1}$ per cGy/s assuming that all charge carriers produced in the polymer by radiation contribute to the current. The actual radiation induced currents are much smaller than the above estimate as we measure current densities much lower than 10^{-11} A/cm^2 with fully charged electrets during the electret charging process as well as with fully discharged electrets during the discharging process.

From Eq. (5.15) we determine that the electret relaxation time τ is a function of both the electret chamber characteristics (air gap and polymer thickness, polymer type, polarizing electrode material) and the exposure rate of the x-ray beam. It does not, however, depend on the magnitude of the externally applied electric field $E_a(0)$. From Eq. (5.16) we find that the electret characteristic polarization or depolarization time t_o is directly proportional to τ but it also

depends in a seemingly complicated manner on $E_a(0)$. For experiments in the saturation region, where $E_a(0) > 3\ E^*$, however, we may approximate Eq. (5.16) by:

$$\frac{t_o}{\tau} = \frac{E_a(0)}{E^*} - \ell n\ 2, \tag{5.20}$$

which suggests that t_o/τ is linearly proportional to the applied field $E_a(0)$. In Fig. 5.6 we plot experimentally determined values of t_o/τ as a function of $E_a(0)/E^*$ for various polarizing electrode materials. The solid line represents a plot of Eq. (5.16) in excellent agreement with experimental data. The t_o/τ curve intercepts the abscissa at $E_a(0)/E^* = 0.88$ which corresponds to $t_o = 0$. The electret polarization current density is, from Eq. (5.17), for $t_o = 0$, written as :

$$j = j_{sat}\ e^{-t/\tau}[1 + e^{-2t/\tau}]^{-\frac{1}{2}}, \tag{5.21}$$

which exhibits a typical exponential decay starting at $j = (1/\sqrt{2})j_{sat}$ for $t = 0$. The electret characteristic polarization or depolarization time t_o is thus a linear function of the applied field $E_a(0)$ for $E_a(0)/E^* > 3$ where saturation condition prevails, and the initial electret polarization or depolarization current density $j(t=0)$ is equal to j_{sat}. In the region $0.88 \leq E_a(0)/E^* < 3$ the initial $j(0)$ is between j_{sat} and $(1/\sqrt{2})j_{sat}$, j exponentially decays to zero and t_o is still defined by Eq. (5.16) as that time during the electret polarization or depolarization process in which the current drops to $(1/\sqrt{2})j_{sat}$. For $0 < E_a(0)/E^* < 0.88$ the initial $j(0)$ is smaller

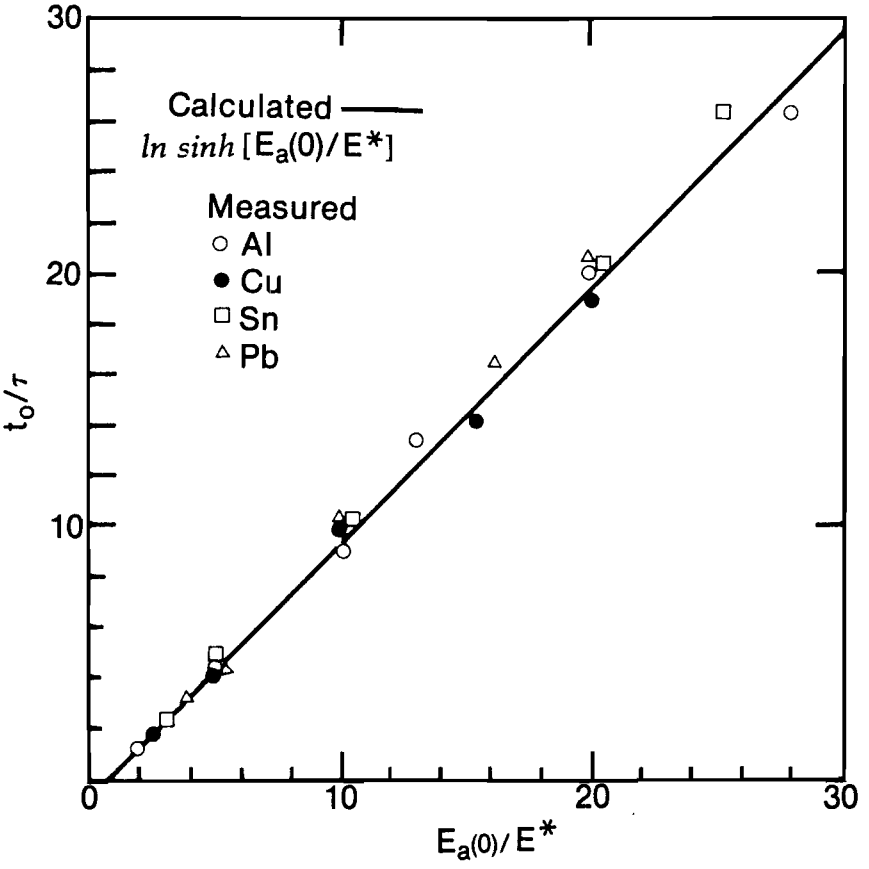

Figure 5.6 Measured and calculated values for t_σ/τ as a function of $E_a(0)/E^*$.

than $(1/\sqrt{2})j_{sat}$, $t_o < 0$ and $j(t)$ rapidly decays to zero. In Fig. 5.7 we show examples of polarization current densities calculated from Eq. (5.17) for various values of $E_a(0)/E^*$.

5.5 SATURATION CURVES OF ELECTRET CHAMBERS

The charge carriers in the electret chamber sensitive volume are produced by electrons originating through direct interactions of photons with air molecules and by photoelectrons produced in the polarizing electrode and backscattered into the chamber sensitive volume. The efficiency for photoelectron production depends on the exposure rate and energy of photons as well as on the atomic number of the polarizing electrode. The range of photoelectrons in air depends on photon energy only.

In order to study the efficiency for charge carrier production, which of course influences the electret polarization and depolarization process, the electret chamber was converted into a standard parallel-plate ionization chamber and saturation curves for various polarizing electrode materials ranging from carbon to lead were measured. In Fig. 5.8 we show saturation curves obtained with an exposure rate of 9 R/min and an air gap of 3.48 cm. The saturation current, which is reached when all charge carriers produced in the sensitive volume are also collected, obviously depends strongly on the atomic number of the polarizing electrode, as there is almost a five fold increase in j_{sat} when going from carbon to lead for the same exposure rate. The dashed lines in Fig. 5.8 represent collection efficiencies (*a*) and current densities (*b*) calculated from Eq. (5.11) using experimentally determined values for the extrapolated field E^*, given in

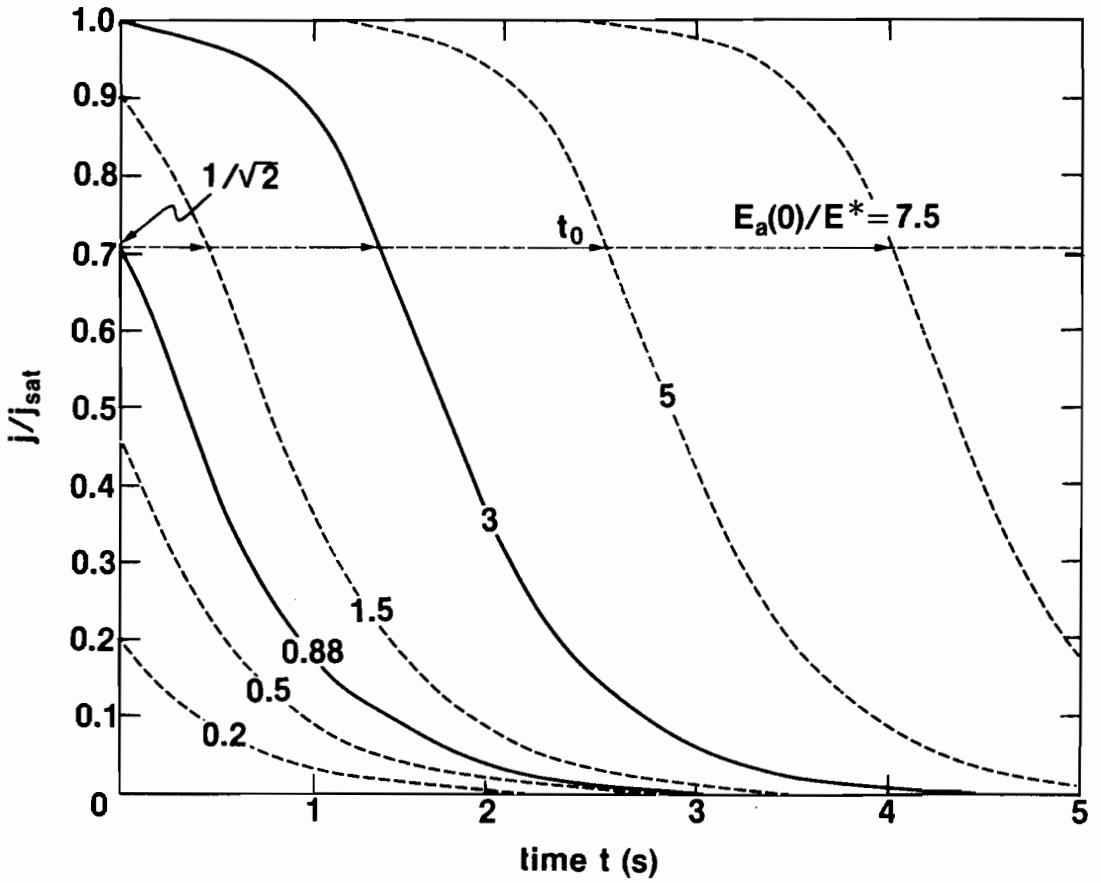

Figure 5.7 Calculated polarization or depolarization current density j normalized to j_{sat} for various $E_a(0)/E^*$ ranging from 0.2 to 7.5 (τ = 0.59 s).

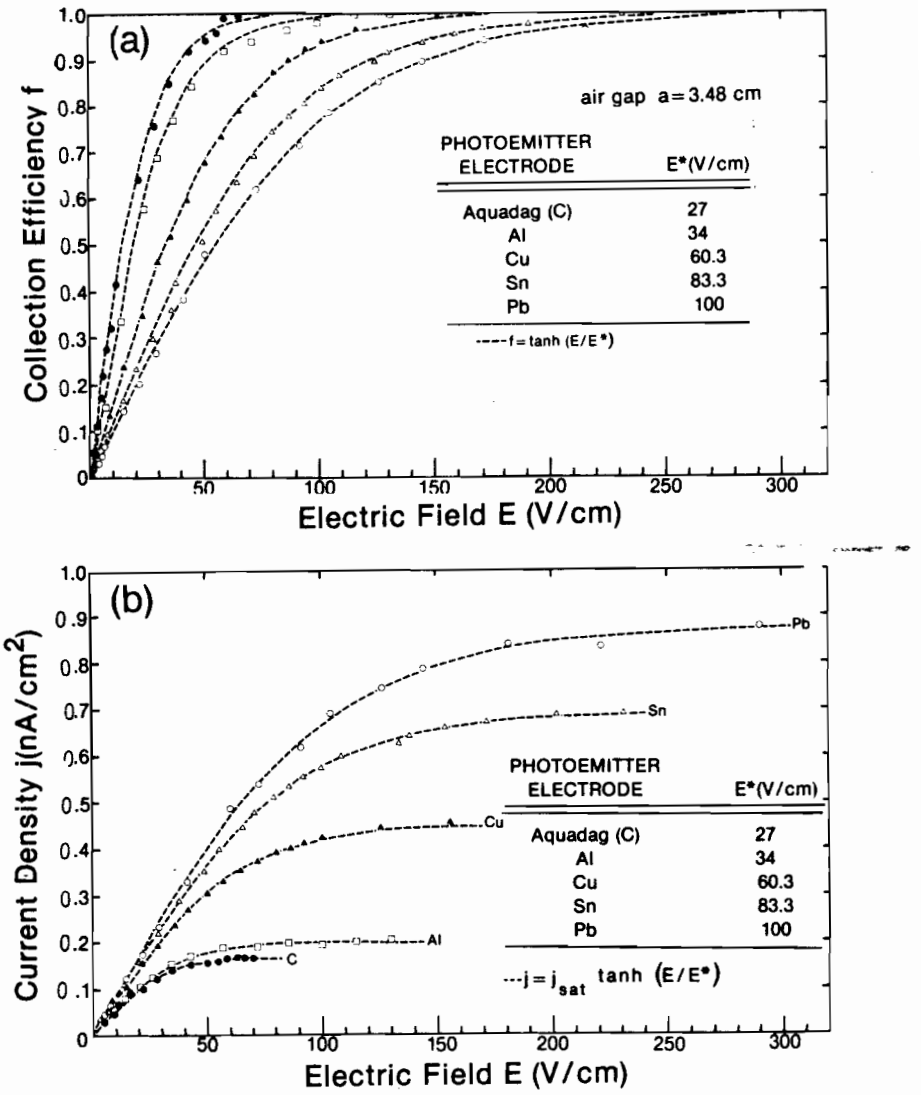

Figure 5.8 (a) Collection efficiency f and (b) current density j as a function of the applied electret field E in an ionization chamber with an air gap a of 3.48 cm for various polarizing electrode materials. Exposure rate : 9 R/min. The extrapolated field E^* is obtained by extrapolating the initial slope of the saturation curve to $f = 1$. The dashed curves represent plots of Eq. (5.11) with the appropriate E^*.

the insert to Fig. 5.8 (a). The excellent agreement between the experimental and calculated current densities indicates that Eq. (5.11) is not affected by the polarizing electrode material, as long as the appropriate E^*, which strongly depends on electrode material, is used.

Both saturation current density j_{sat} and the extrapolated field E^* are proportional to the x-ray exposure rate, to the air gap thickness a and to the atomic number Z of the polarizing electrode. The E^* dependence on the x-ray exposure rate was discussed previously[24] in Sec. 4.5; its dependence on a and Z will be discussed in the next section. In Fig. 5.9 we plot the saturation current densities j_{sat} (solid curves) as a function of a for various polarizing electrode materials. We have already seen in Fig. 5.8 that for equal air gaps (3.48 cm) and equal exposure rates the larger the electrode atomic number Z the larger is j_{sat}. From Fig.5.9 we conclude that for a given material j_{sat} increases linearly with a for large a; for small a, however, the linearity breaks down. The j_{sat} vs a curve may be separated into two components, a linear function j_{sat}^{air} and an exponential function j_{sat}^{p}, both starting at the origin. The saturation current density $j_{sat}(a)$ may thus be written as :

$$j_{sat}(a) = j_{sat}^{air}(a) + j_{sat}^{p}(a) \quad . \tag{5.22}$$

The linear function j_{sat}^{air} is the component of j_{sat} produced by the charge carriers originating from electrons released in the chamber sensitive volume by direct interactions of photons with air molecules. It is independent of electrode material and linearly dependent upon air gap thickness a. It may be written as :

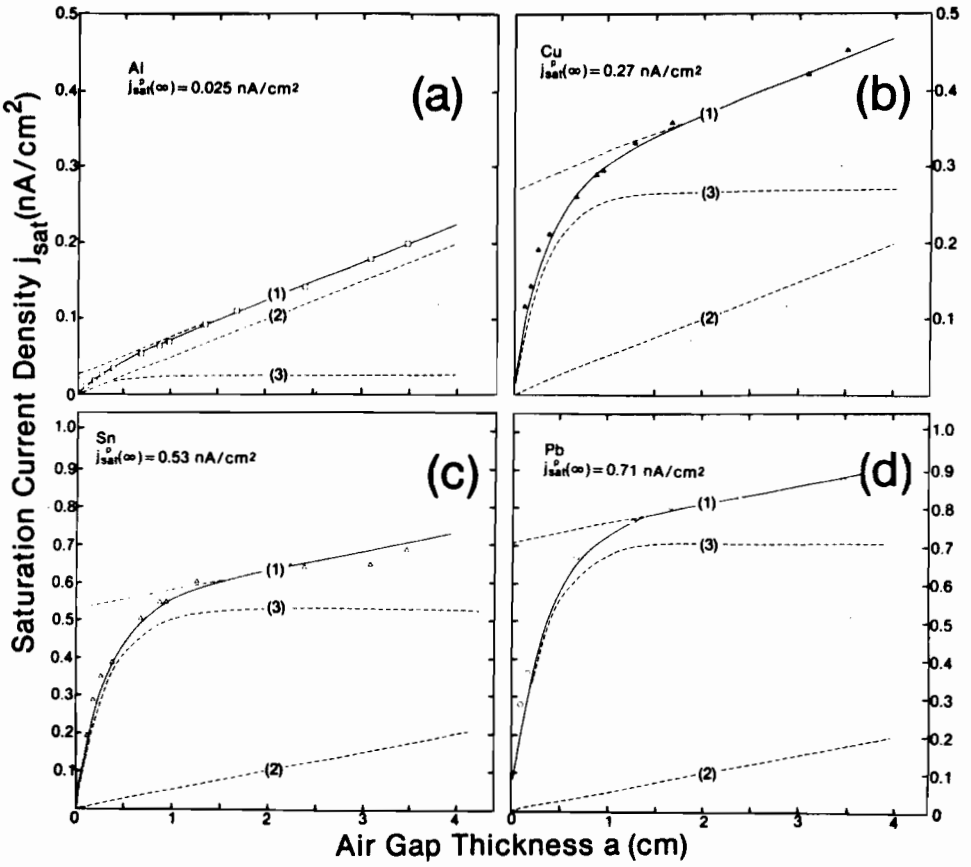

Figure 5.9 Saturation current density j_{sat} as a function of air gap a for various electrode materials. Exposure rate : 9 R/min. Curves (1) represent a plot of Eq. (5.27), curves (2) represent Eq. (5.2) and curves (3) represent Eq. (5.24).

$$j_{sat}^{air} = \kappa a \dot{x} \ , \qquad (5.23)$$

where $\dot{x}$ is the exposure rate, a the air gap thickness and κ the usual proportionality constant 3.33×10^{-10} (As/cm^3R). Equation 5.23 is plotted in Fig. 5.9 as dashed lines (2) for an exposure rate of 9 R/min. Note that j_{sat}^{air} is identical for all electrode materials.

The current density j_{sat}^{p} which is the exponential component of j_{sat}, is the contribution of charge carriers produced by photoelectrons backscattered into the chamber sensitive volume from the polarizing electrode. These photoelectrons have a range[26] of $\simeq$ 1 cm for our x-ray photon energies. For air gaps larger than 1 cm the contribution to air ionization by the photoelectrons is thus constant, for gaps smaller than 1 cm the contribution depends on the gap thickness since some of the photoelectrons cross the gap and impinge onto the measuring electrode before they expend all their energy through ionization. The extrapolation of the linear portion of the j_{sat} vs a curve back to $a = 0$ gives the saturation value for j_{sat}^{p}, which is strongly dependent on Z of the polarizing electrode as indicated in Fig. 5.9 where the saturation value for j_{sat}^{p} is labelled as $j_{sat}^{p}(\infty)$. Subtracting the linear $j_{sat}^{air}(a)$ from the measured $j_{sat}(a)$, we get j_{sat}^{p} as a function of a shown in Fig. 5.9 as curve (3) for the four electrode materials. For the aluminum electrode, which has a Z relatively close to the effective Z of air[27] (7.64), most of the chamber current is contributed by normal air ionization current, while with lead most of the measured current is contributed by photoemission. Copper and tin are between the two extremes. It should be pointed out that ionization chambers used in radiation dosimetry employ electrodes with effective atomic numbers close to air so

that the photoemission contribution is negligible and Eq.(5.23) is used directly for exposure determination from the measured ionization current. In our chamber, however, it is possible to increase the ionization currents by a factor of 10 with high atomic number electrodes. Empirically, we find that $j^p_{sat}(a)$ may be expressed with the following exponential expression:

$$j^p_{sat}(a) = j^p_{sat}(\infty)[1 - e^{-3a/a_r}] , \qquad (5.24)$$

represented as curves (3) in Fig. 5.9, with a_r = 1 cm, the range of photoelectrons for our experimental conditions and $j^p_{sat}(\infty)$, the photoemission saturation current density, for $a > a_r$, obtained, as discussed above, by extrapolating the measured linear portion of $j_{sat}(a)$ towards $a = 0$.

The relationship between $j^p_{sat}(\infty)$ and the efficiency for production of backscattered electrons ε is investigated in Fig. 5.10 for an exposure rate of 9 R/min. The values for the efficiency ε, which is defined as the number of backscattered electrons per incident photon, were taken from Dolan[26] who had performed an extensive study of the x-ray induced electron emission from metals with a lithium-drifted silicon detector. Both $j^p_{sat}(\infty)$ and ε are plotted as a function of Z in Fig. 5.10. The insert shows a plot of $j^p_{sat}(\infty)$ vs ε for the four electrode materials used in our experiments. Since the slope of the relationship is equal to 1, we conclude that $j^p_{sat}(\infty)$ is directly proportional to ε,i.e.,:

$$j^p_{sat}(\infty) = \lambda\varepsilon , \qquad (5.25)$$

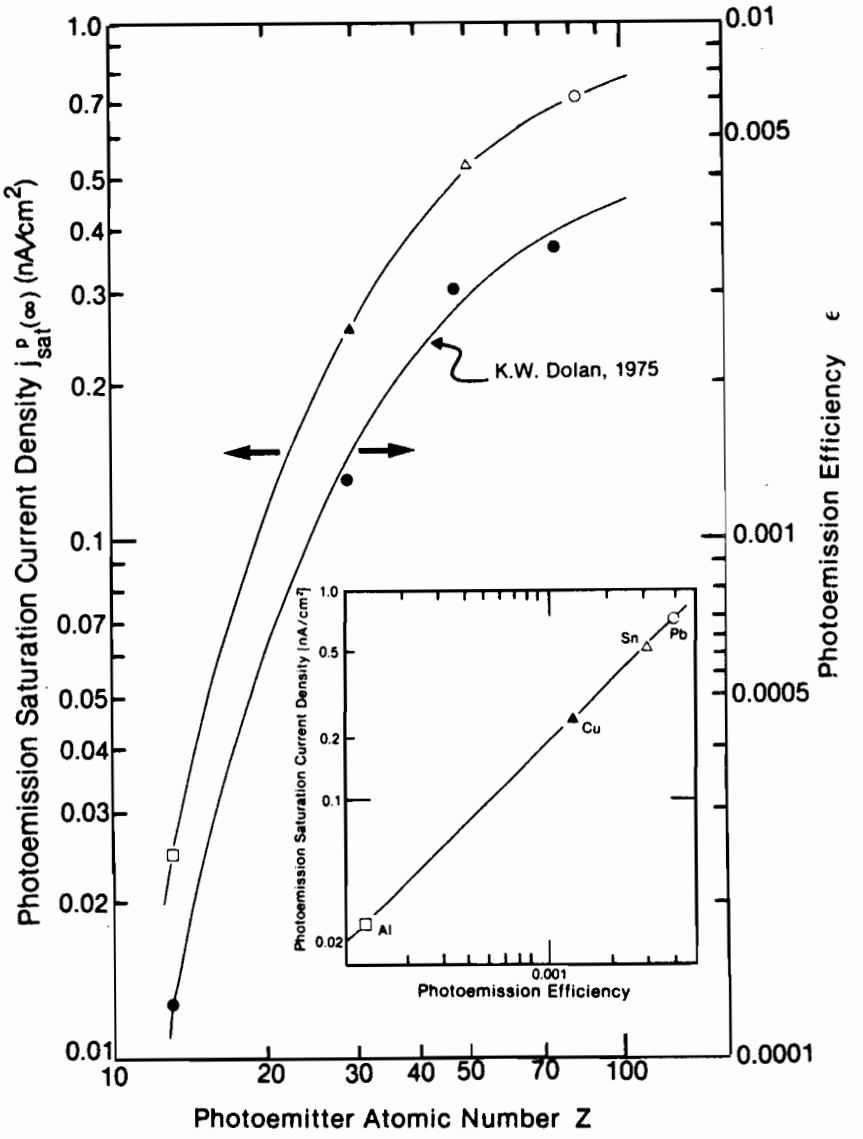

Figure 5.10 Photoemission Saturation Current Density $j^p_{sat}(\infty)$ and photoemission efficiency ε (ref. 26) as a function of polarizing electrode atomic number. The insert shows direct proportionality between $j^p_{sat}(\infty)$ and ε.

with λ the proportionality constant equal to 200 nA cm^{-2} $(\text{electrons/photon})^{-1}$ for our particular exposure rate.

In general, $j^{p}_{sat}(\infty)$, which is a function of exposure rate $\dot{x}$ and energy E_ν of the x-ray beam as well as of the effective atomic number Z of the polarizing electrode, may be written as:

$$j^{p}_{sat}(\infty) = \lambda' \dot{x} \varepsilon(Z, E_\nu), \tag{5.26}$$

where λ' is now the proportionality constant independent of the exposure rate and equal to 1.33×10^{-6} (C/R cm^2) $(\text{electrons / photon})^{-1}$.

The ionization chamber saturation current density j_{sat} as a function of air gap a may thus be expressed as:

$$j_{sat}(a, Z) = \dot{x} \{\kappa a + \lambda' \varepsilon(Z, E_\nu)[1 - e^{-3a/a_r(E_\nu)}]\}, \tag{5.27}$$

where κ and λ' are constants given above, $\varepsilon(Z, E_\nu)$ is the efficiency for production of backscattered photoelectrons and $a_r(E_\nu)$ is the range of photoelectrons in air at normal temperature and pressure.

In standard ionization chambers, where low atomic number materials are used as the polarizing electrode, $\varepsilon(Z, E_\nu)$ is so small that the photoemission term of j_{sat} is negligible in comparison with primary air ionization. With lead as polarizing electrode material, on the other hand, the main contribution to j_{sat} comes from the photoemission term because of the large value of $\varepsilon(Z, E_\nu)$ for lead.

5.6 EXTRAPOLATED ELECTRIC FIELD

The extrapolated electric field E^* was introduced and briefly discussed in Sec. 5.4. As shown by Eq. (5.11) it is a parameter in the saturation curve expression, depending on the configuration of the parallel-plate ionization chamber and the x-ray exposure rate. A typical fit of Eq. (5.11) to measured data was shown in Fig. 5.5 (a). In Fig. 5.11 we show E^* as a function of air gap thickness a for various polarizing electrode materials. We notice that, similarly to $j_{sat}(a)$, discussed in the previous section, $E^*(a)$ is linear with a for large a; the linearity breaks down, however, for small a. $E^*(a)$ also has two components, both starting at 0 for $a = 0$; one, $E^*_{air}(a)$, is linear for all a and again attributed to primary ionization in air, and the other $E^*_p(a)$ exhibits an exponential saturation behavior at approximately 3 a_r and is attributed to the photoemission from the polarizing electrode. The saturation value, $E^*_p(\infty)$, is obtained by extrapolating the linear portion of the E^* vs a curve to $a = 0$ as shown in Fig. 11. We have shown[24] in Sec. 4.5 that $E^*_{air}(a)$ may be expressed as:

$$E^*_{air}(a) = k(a j^{air}_{sat})^{\frac{1}{2}} , \qquad (5.28)$$

where j^{air}_{sat} is the contribution to j_{sat} by primary ionization in air, as discussed in the previous section, and k is a universal parallel-plate ionization chamber constant equal to 12.4×10^5 V/(A-cm)$^{\frac{1}{2}}$. Inserting Eq. (5.23) into Eq. (5.28) we find:

$$E^*_{air}(a) = k\sqrt{\kappa}\, a\dot{x}^{\frac{1}{2}} , \qquad (5.29)$$

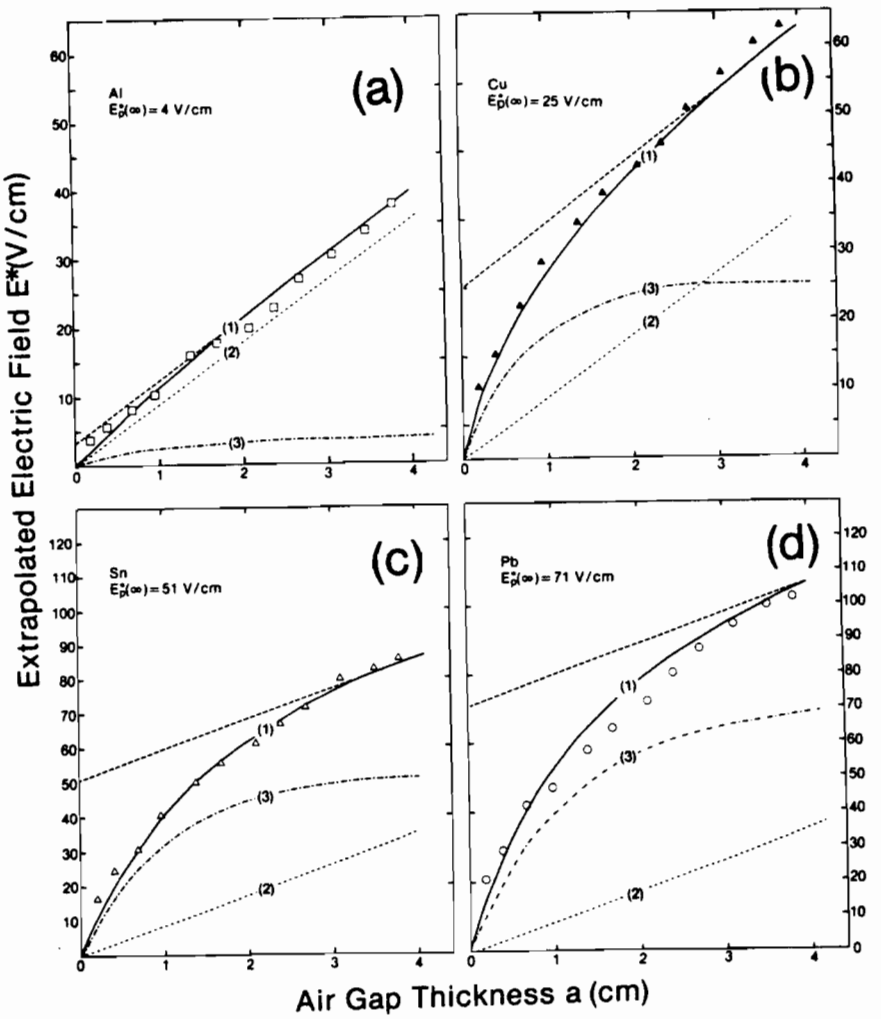

Figure 5.11 Extrapolated electric field E^* as a function of air gap a for various polarizing electrode materials. Exposure rate: 9 R/min. Curves (1) represent Eq. (5.32), curves (2) Eq. (5.28) and curves (3) represent Eq. (5.30).

which suggests that E^*_{air} is linearly dependent on the air gap thickness a and on the square root of the exposure rate. The linear $E^*_{air}(a)$ is represented in Fig. 5.11 by curves (2) and is independent of the polarizing electrode material. Its subtraction from $E^*(a)$ yields $E^*_p(a)$ shown as curves (3). Empirically we find that $E^*_p(a)$ may be expressed, similarly to $j^p_{sat}(a)$, by an exponential expression:

$$E^*_p(a) = E^*_p(\infty)[1 - e^{-a/a_r}] , \tag{5.30}$$

where $E^*_p(\infty)$ was defined above and a_r, the range[26] of photoelectrons in air, is equal to ~ 1 cm under our experimental conditions.

In Fig. 5.12 we plot $E^*_p(\infty)$ for various photoemitter materials as a function of (a) photoemitter atomic number Z, showing a strong Z dependence of $E^*_p(\infty)$, (b) photoemission saturation current density $j^p_{sat}(\infty)$, showing direct proportionality between $E^*_p(\infty)$ and $j^p_{sat}(\infty)$, and (c) photoemission efficiency ε, showing a linear relationship between $E^*_p(\infty)$ and ε.

In general, $E^*_p(\infty)$ may be expressed incorporating Eq (5.26) as:

$$E^*_p(\infty) = m j^p_{sat}(\infty) = m\lambda'\dot{x}\varepsilon(Z,E_\nu) , \tag{5.31}$$

where m is the slope from Fig. 5.9 (b) and λ' was defined in the previous section.

The general relationship for $E^*(a,Z)$ is now given by:

$$E^*(a,Z) = k'a\dot{x}^{\frac{1}{2}} + m'\varepsilon(Z,E_\nu)\dot{x}\,[1 - e^{-a/a_r(E_\nu)}] , \tag{5.32}$$

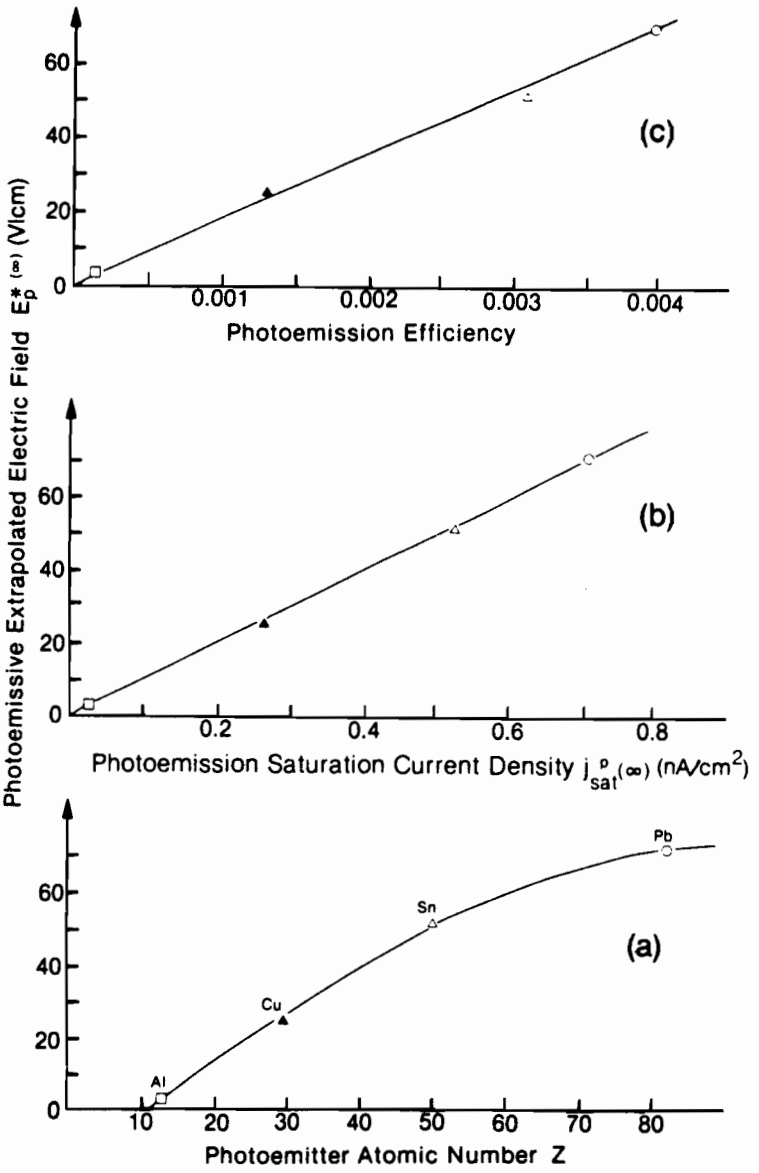

Figure 5.12 Photoemission Extrapolated Electret field $E_p^*(\infty)$ as a function of (*a*) polarizing electrode atomic number Z, (*b*) photoemission saturation current density $j_{sat}^{p}(\infty)$, and (c) photoemission efficiency.

where $m' = m\lambda' = 1.33\times10^{5}$ V cm^{-1}(R/s)$^{-1}$(electrons/photon)$^{-1}$ and $k' = k\sqrt{\kappa} = 22.6$ V cm^{-2}(R/s)$^{-\frac{1}{2}}$.

The extraplolated field E^* thus consists of two terms; one, determined by the primary ionization in air is dominant for chambers with low atomic number electrodes, and the other, determined by photoemission from the polarizing electrode is dominant at high atomic number polarizing electrodes.

5.7 POLARIZATION CURRENT DENSITY PROFILES

The time dependence of the electret polarization current density during the electret charging process was described by Eq. (5.17) and a typical example was shown in Fig. 5.6 (*b*). In this section we discuss the general properties of polarization current density profiles based on the saturation current density j_{sat} and extrapolated field E^*. In Figs. 5.13 and 5.14 we show various calculated polarization current density profiles obtained in the electret chamber with a lead polarizing electrode and various air gaps a ranging from 0.18 cm to 3.48 cm for an applied field $E_a(0)$ equal to 5 E^* (Fig. 5.13) and a constant applied voltage V_o of 500 Volts (Fig. 5.14). The inserts to both figures give relevant parameters, such as E^*, $E_a(0)$ and j_{sat} as a function of a. The extrapolated fields E^* were obtained from measured saturation curves for various air gaps and agree well with data calculated from Eq. (5.32). The electret relaxation time τ and characteristic polarization time t_o were calculated from Eqs. (5.15) and (5.16) respectively.

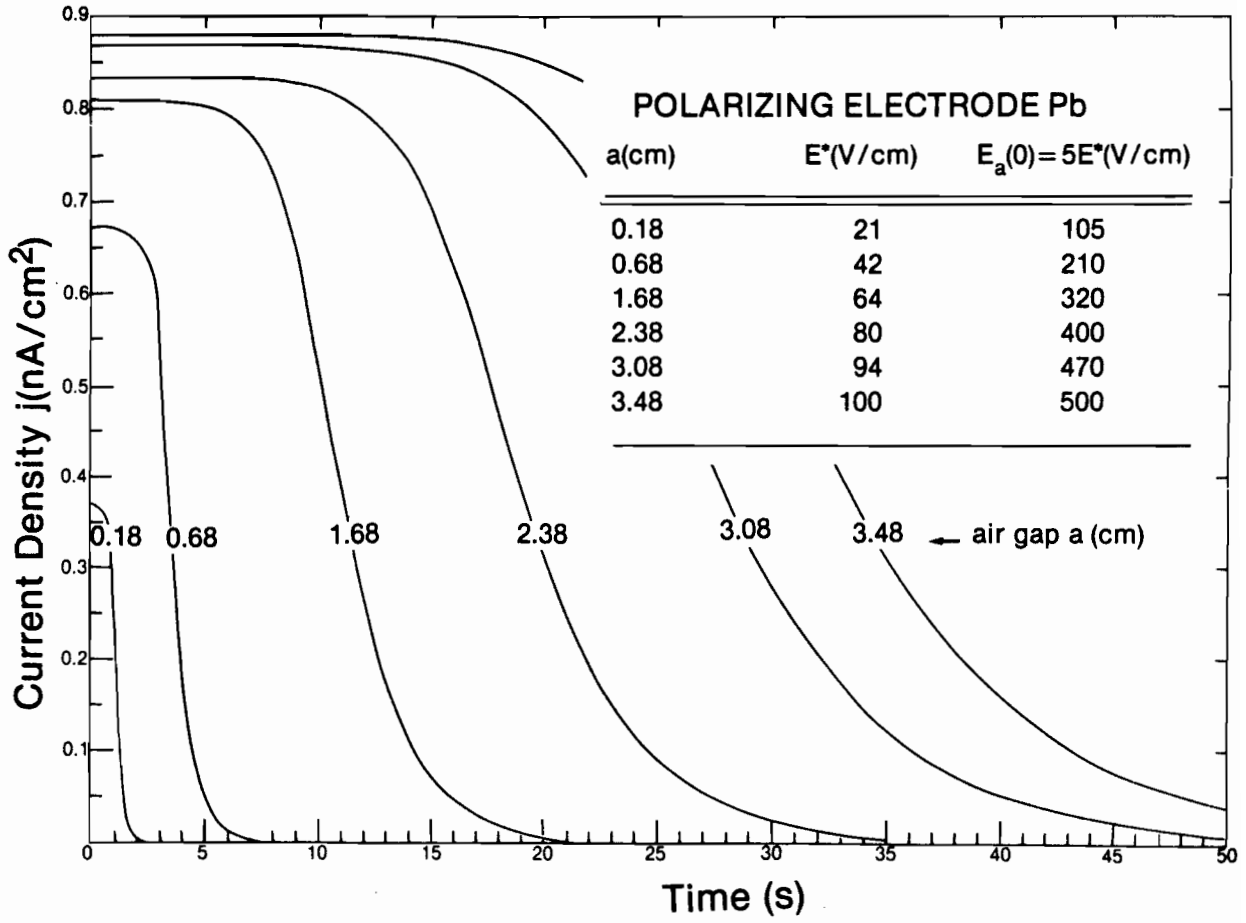

Figure 5.13 Calculated time dependence of the electret charging or discharging current j for a lead polarizing electrode with various air gaps a. The electret chamber was initially under saturation conditions since $E_a(0) = 5\ E^*$ for all a.

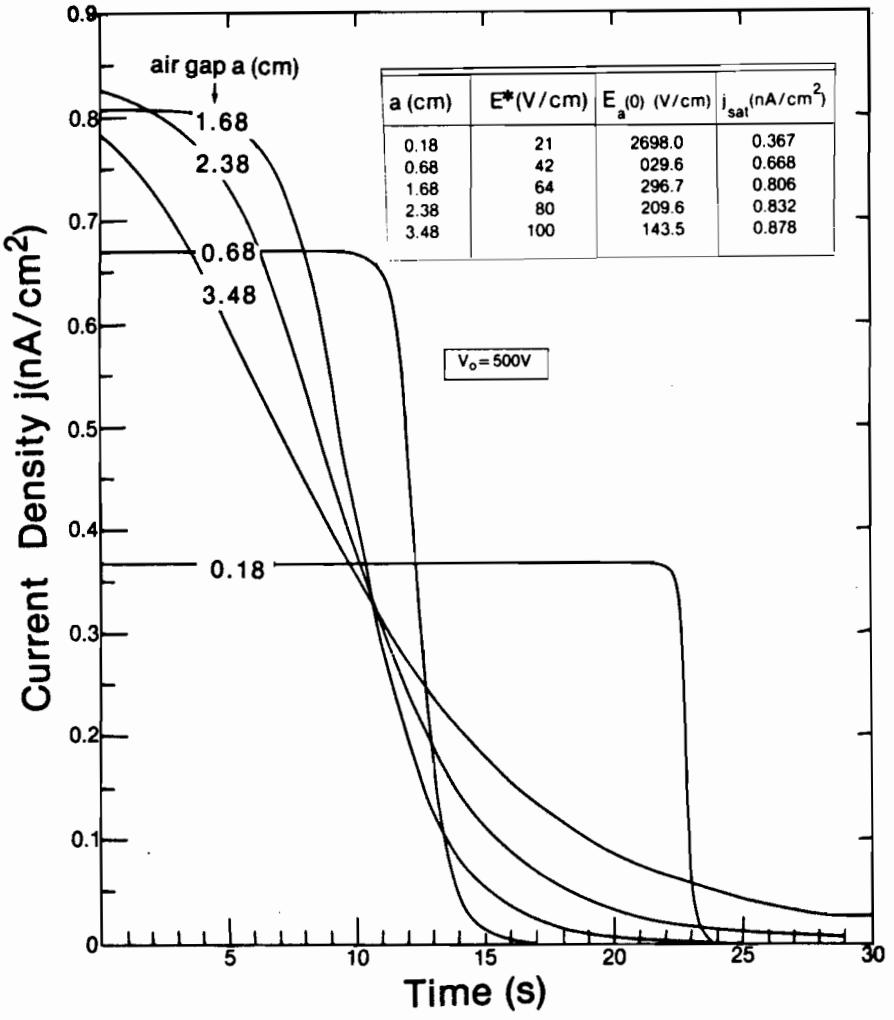

a (cm)	E*(V/cm)	$E_a(0)$ (V/cm)	j_{sat}(nA/cm^2)
0.18	21	2698.0	0.367
0.68	42	029.6	0.668
1.68	64	296.7	0.806
2.38	80	209.6	0.832
3.48	100	143.5	0.878

Figure 5.14 Calculated time dependence of the electret charging or discharging current j for a lead polarizing electrode with various air gaps a. The externally applied voltage V_o was 500 Volts for all air gaps a.

The condition $E_a(0) = 5\ E^*$ in Fig. 5.13 ensures that the electret chamber is initially in the saturation region for all air gaps and the initial polarization current density is equal to the standard saturation current density j_{sat}. A plot of measured $j_{sat}(a)$ for a lead electrode was shown in Fig. 5.9 (*d*) in excellent agreement with data calculated from Eq. (5.27). Combining Eqs. (5.20), (5.15) and (5.9) we get:

$$t_o = 4.31 \frac{\varepsilon_o (a\varepsilon_p + p\varepsilon_a) E^*}{p j_{sat}} \quad , \tag{5.33}$$

the characteristic electret polarization time, which at least for small air gaps gives a fairly good indication of the time needed to charge the electret to σ_{max} given by Eq. (5.7). At larger gaps, however, the current profile becomes less and less steep and the time needed to fully charge the electret is much longer than t_o ,which is still defined as the time where $j = (1/\sqrt{2})j_{sat}$.

Figure 5.14 shows polarization current density profiles for a constant external voltage V_o of 500 Volts applied across air gaps of various thicknesses. The chamber is in the saturation region for the three small air gaps since for them $E_a(0) > 3E^*$. The current profiles start at j_{sat}, remain constant for a while depending on t_o and then exponentially drop to zero. The areas under all three profiles are identical and equal to σ_{max} as given by Eq. (5.7). For the air gaps of 2.38 cm and 3.48 cm the chamber is not in the saturation region, the initial current density is lower than j_{sat} and starts an immediate decay towards zero. The areas under the current profiles, however, are also equal to σ_{max}, indicating that the electret becomes fully

charged even in situations where saturation conditions do not prevail in the electret chamber. It is evident from Fig. 5.14 that the time required to fully charge the electret under these conditions can become quite large.

In Fig. 5.15 we compare the calculated Eq.(5.7) and measured polarization current profiles for various polarization electrode materials, an air gap of 0.18 cm and for three applied fields $E_a(0)$ equal to approximately 5 E^*, 10 E^* and 20 E^*. We notice that for $E(0) \sim 5\ E^*$ the agreement between calculated and measured profiles is excellent; for large applied fields, however, the calculated curve is considerably steeper than the measured one. This discrepancy may be attributed either to the electret chamber, where a breakdown in saturation characteristics may occur at very high voltages, or to the electret charging characteristics which may depend on charge densities already trapped on the polymer surface.

5.8 SUMMARY AND CONCLUSION

The new isothermal technique for production of stable foil electrets in apparatuses closely resembling standard parallel-plate ionization chambers offers several advantages over the presently employed electret production methods. It is very simple, the charge deposition onto the dielectric foil is easily controlled and the exact surface charge density to be deposited is predetermined by chosing the appropriate externally applied voltage and electret chamber parameters.

The maximum electret surface charge density first rises linearly with polarizing voltage and then for voltages greater than the

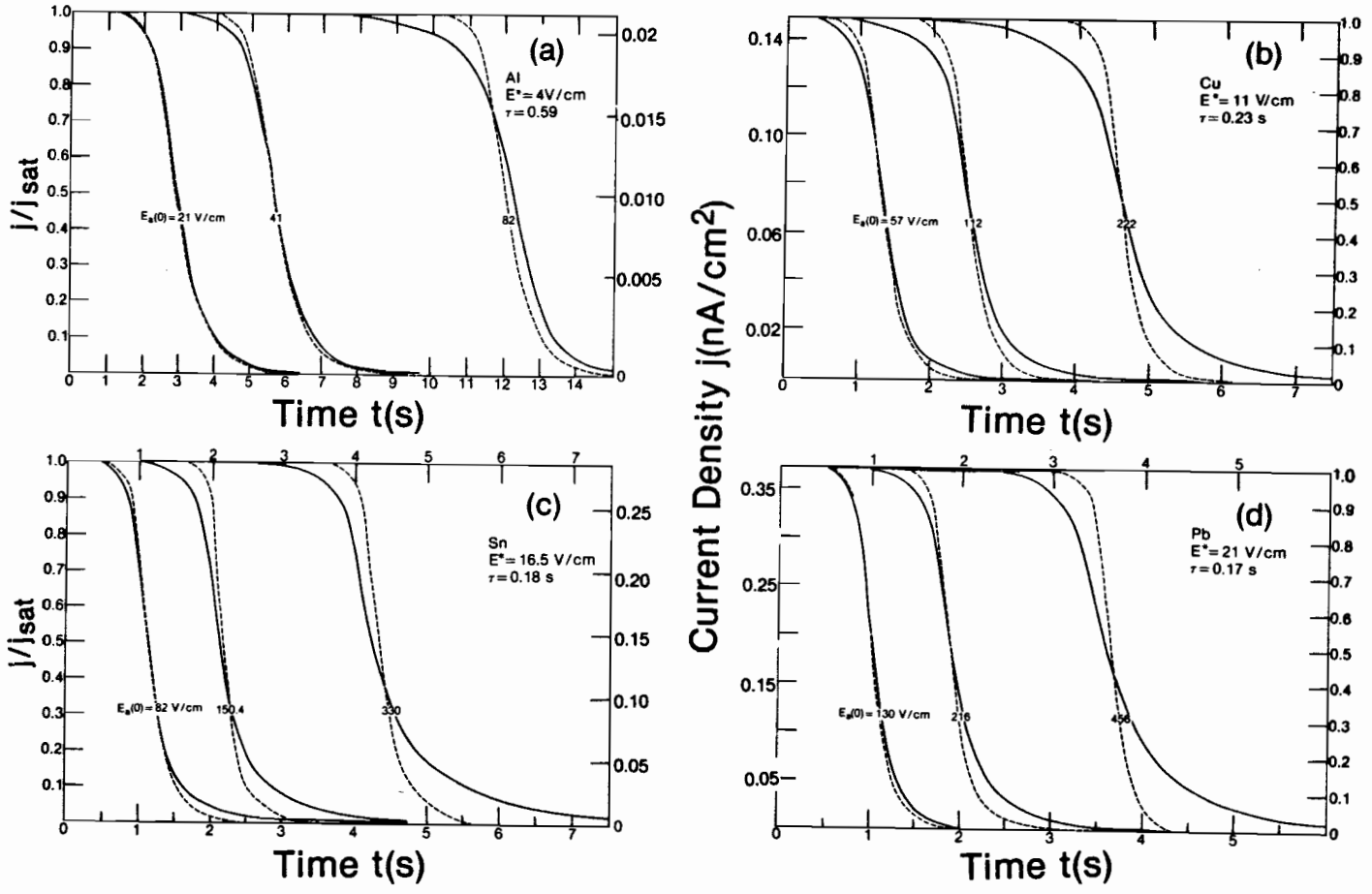

Figure 5.15 Theoretical (dashed) vs measured (solid) polarization current densities as a function of time for various polarizing electrode materials and externally applied fields $E_a(0)$. The air gap thickness a was 0.18 cm; exposure rate 9 R/min.

breakpoint voltage (~ 2 500 V for Mylar) follows a $V^{\frac{1}{2}}$ dependence. Electret surface charge densities close to 10^{-6} C/cm^2 are attained with an applied potential of a few kV and a dielectric foil thickness of typically 100 μm. The surface charge distribution is determined by the spatial distribution of the x-ray beam intensity.

Any desired surface charge density can be achieved; the limitation, of course, is the dielectric strength of the electret material. The electret thus produced is extremely stable and no charge loss was observed when a sample charge was read out four months after the electret state was produced in the sample.

The free charge carriers, produced in the chamber sensitive volume by primary photon interactions with air molecules and by photoelectrons backscattered from the polarizing electrode, drift in the effective electric field towards the dielectric foil. The effective electric field is the vector sum of the externally applied field and the opposing time dependent field produced by the electret surface charge density.

The time dependence of the electret charging and discharging current density, as well as of the effective electric field and of the surface charge density, is calculated using the hyperbolic relationship between the chamber ion collection efficiency and the effective electric field. The characteristic electret polarization and depolarization time ranges from a few seconds to a few minutes depending on the x-ray exposure rate, the externally applied voltage and the electret chamber parameters. In the saturation region the characteristic time is linearly proportional to the applied electric field and inversely proportional to the extrapolated electric field.

The electret charging and discharging properties strongly depend on the saturation current density and on the extrapolated electric field in the electret chamber. Both have two components. One, which is linearly dependent on the air gap thickness, is attributed to the contribution of primary ionizations in the chamber sensitive volume, and the other, which exhibits an exponential saturation, is attributed to ionizations produced by photoelectrons emanating from the polarizing electrode. The photoelectron contribution to saturation current density and to the extrapolated electric field is directly proportional to the efficiency for photoemission production, almost negligible, in comparison with primary air ionizations, for low atomic number polarizing electrodes but dominant for high atomic number electrodes.

We feel that the isothermal method described here offers certain advantages over the existing techniques and should be considered as a simple and practical new method for production of stable high surface charge density foil electrets. Furthermore, the results of the electret studies discussed here will be used in subsequent chapters to describe some interesting charging characteristics of ionographic latent images which are in effect electrets with surface charge distributions modulated by the photon transmission through an object.

5.9 REFERENCES

1 *ELECTRETS*, Topics in Applied Physics, Vol. 33, edited by G.M. Sessler (Springer-Verlag, Berlin, 1980).

2 M. Eguchi, Philos. Mag. 49, 179(1925).

3 M. Campos, S. Mascarenhas and G.L. Ferreira, Phys. Rev. Lett. 27, 14 2(1971).

4 E.B. Podgorsak and P.R. Moran, Phys. Rev. B: 8, 3405(1973).

5 G. Nadjakov, Compt. Rend. 204, 1865(1937).

6 V.M. Fridkin and I.S. Zheludev, in Photoelectrets and the Electrophotographic Process (Consultants Bureau, New York, 1960).

7 Y. Asano and T. Suzuki: Jpn. J. Appl. Phys. 2, 1139(1972).

8 M.G. Broadhurst and G.I. Davis, Piezo-and Pyroelectric Properties in *ELECTRETS*, Topics of Applied Physics Vol 33, edited by G.M. Sessler (Springer-Verlag, Berlin, 1980), p.285.

9 G.M. Sessler and J.E. West, J. Appl. Phys. 43, 922(1972).

10 P.W. Chudleigh, J. Appl. Phys. 47, 4475(1976).

11 B. Gross, G.M. Sessler and J.E. West, J. Appl. Phys. 45, 111(1975).

12 G.M. Sessler and J.E. West, J. Electrostatics 1, 111(1975).

11 B. Gross, G.M. Sessler and J.E. West, J. Appl. Phys. 47, 968(1976).

14 C.F. Carlson, U.S. Patent No. 2 588 699 (1952).

15 R.M. Schaffert, Electrophotography, (Focal Press, London, 1975), p.441.

16 B.G. Fallone and E.B. Podgorsak, Phys. Rev. B: 27, 2615(1983).

17 B.G. Fallone and E.B. Podgorsak, Phys. Rev. B: 27, 5062(1983).

18 B.G. Fallone and E.B. Podgorsak, Phys. Rev. B: in press(1983).

19 D. Plewes and H.E. Johns, Med. Phys. 7, 15(1980).

[20] A.P. Proudian, R.L. Carangi, G. Jacobson and E.P. Muntz, Radiology 110, 667(1974).

[21] H. Bauser and W. Ronge, Health Phys. 34, 97(1978).

[22] H.K. Henisch, in Rectifying Semi-conductor Contacts (Oxford U.P., New York, 1957), p. 214.

[23] C.M. Vodenicharovaand M.B. Vodenicharova, Phys. Stat. Sol. (a) 57, 48 (1980).

[24] B.G. Fallone and E.B. Podgorsak, Med. Phys. 10, 191(1983).

[25] B. Gross, in *ELECTRETS*, Topics in Applied Physics, Vol. 33, edited by G.M. Sessler (Springer-Verlag,Berlin,1980), p. 221.

[26] K.W. Dolan, J. Appl. Phys. 46, 2455(1975).

[27] H.E. Johns and J.B. Cunningham, The Physics of Radiology, (C.C. Thomas, Springfield, 1977), p.145.

CHAPTER 6

ELECTROSTATIC FIELDS IN THE IONIZATION CHAMBER ELECTRET

6.1 INTRODUCTION

In the previous chapter, Gauss' law, which holds at the polymer-air interface, was used to approximate the electric field in the electret ionization chamber; in this chapter the electrostatic fields and potentials will be calculated by solving Laplace's equation inside the chamber.

Since the discovery of the electret,[1] numerous techniques for the formation of polymer foil electrets have been developed. Originally, the foil electret was produced through thermal[2] (thermoelectret) or optical[3] (photoelectret) charge deposition methods. Recently, however, isothermal charge deposition techniques have been favored, because of the ease and speed at which they allow dielectric polymer films to be charged. The most widely used isothermal technique is corona-charging,[4,5] which utilizes a discharge in air with an inhomogeneous electric field. Other techniques are based on spark discharge,[6] liquid contact,[7] injection of monoenergetic particle beams (electrons or ions)[8,9] of range smaller than the thickness of the dielectric, or carrier displacement by large doses of x-rays or γ-rays (radioelectrets).[10]

In the previous chapter we reported an isothermal charge deposition method[11] of ionizing radiation in air to produce stable foil electrets with maximum charge densities close to 10^{-6} C/cm^2 in an apparatus resembling parallel-plate ionization chambers. The charge carriers produced by radiation in the sensitive air volume between two parallel electrodes drift in an externally applied electric field and get trapped on a polymer (Mylar) surface attached to the grounded collecting

electrode. The polymer faces a polarizing electrode across an air gap. The electret can be depolarized by shorting the electrodes during irradiation thus causing charge carriers of opposite sign to drift, in the electric field produced by the surface charge on the foil, towards the polymer surface where they neutralize the original electret charges. The dynamics of the polarization and depolarization process for this radiation induced foil electret[12-14] was also discussed in the previous chapter. Other groups[15,16] have utilized high pressure gas instead of air in a similar polarizing process to form latent electrostatic images (discussed in Section 2.3) without investigating the electret properties of such images. The electret depolarization by ionizing radiation was recently proposed as a radiation dosimetry technique.[17]

The purpose of this chapter is to present a mathematical analysis of potentials and electric fields produced in the electret chamber by the surface charge distribution on the polymer. Various methods have been proposed to study electric fields produced under similar conditions. Schaffert[18] summarized the mathematical treatment of electrostatic fields above an infinitely large sinusoidal charge distribution at the interface of a photoconductor and a dielectric film, while Neugebauer[19] solved a simpler two-layer model without the film for some special charge distributions using the method of virtual images. Other investigators used the latter technique for a number of different ground configurations,[20] and for the study of electrostatic fields in xeroradiography.[21]

Schaffert,[18] Neugebauer,[22,23] and Kao[24] introduced the theory of linear optical systems to study the electrostatic fields produced by charge distributions on a photoconductor. In this theory, the electric field and the charge distribution on the surface of the dielectric can be related by a spread function (i.e., the Green's function of the

electric field due to a delta point charge), or by its Fourier transform, the transfer function. The Green's function is referred to as the spread function in distance space or the transfer function in frequency space. In principle, the electric field is obtained either by a convolution of the charge distribution of interest with the spread function or by first multiplying the Fourier transform of the same charge distribution with the transfer function and then taking the inverse Fourier transform of the product.

Because of computational difficulties no successful convolution calculations for electrostatic fields have been reported. Furthermore, although the transfer function has been used to determine the electrostatic fields in frequency space for various studies,[24-27] there have been no communications concerning the inverse Fourier transform of the product to arrive at a general analytic solution for the electric field in distance space. In this chapter we use the theory of linear optical systems to calculate analytically the electric field and potential in distance space by taking the inverse Fourier transform of results in frequency space for sizes of surface charge distributions typical of electret foils and for configurations appropriate to the electrets produced by ionization in air. The general solution thus calculated is in excellent agreement with results obtained on chamber central axis either with a dipole layer model for points far from the surface charge density or with Kirchoff's and Gauss' laws for points on the surface.

6.2 POTENTIAL AND ELECTRIC FIELD IN FREQUENCY SPACE

Figure 6.1 shows schematically the electret polarization and depolarization configuration. The externally applied electric potential is denoted by V_o, the polymer thickness (typically few μm) by p and the air gap (typically few cm) by a. The chamber is cylindrical and the radius of the x-ray aperture, which determines the circle of charge distribution, is denoted by R. The surface charge density $\sigma(x,y)$ is trapped on the polymer surface at $z = 0$. The point of interest $P(x,y,z)$ may be written in terms of two coordinates, r and z, because of the chamber cylindrical symmetry, with $r = \sqrt{x^2 + y^2}$.

The electrostatic potential, $V(x,y,z)$ at the point $P(x,y,z)$ satisfies the Laplace's equation:

$$\left(\frac{\partial^2}{\partial x^2} + \frac{\partial^2}{\partial y^2} + \frac{\partial^2}{\partial z^2} \right) V(x,y,z) = 0 . \tag{6.1}$$

The Fourier transform, $\overline{V}(\omega_x,\omega_y,z)$ of $V(x,y,z)$ with respect to x and y is defined as:

$$\overline{V}(\omega_x,\omega_y,z) = \int_{-\infty}^{\infty}\int_{-\infty}^{\infty} \overline{V}(x,y,z) e^{-i(x\omega_x+y\omega_y)} dxdy , \tag{6.2}$$

while the inverse Fourier transform is given by:

$$V(x,y,z) = \frac{1}{(2\pi)^2} \int_{-\infty}^{\infty}\int_{-\infty}^{\infty} \overline{V}(\omega_x,\omega_y,z) e^{i(x\omega_x+y\omega_y)} d\omega_x d\omega_y. \tag{6.3}$$

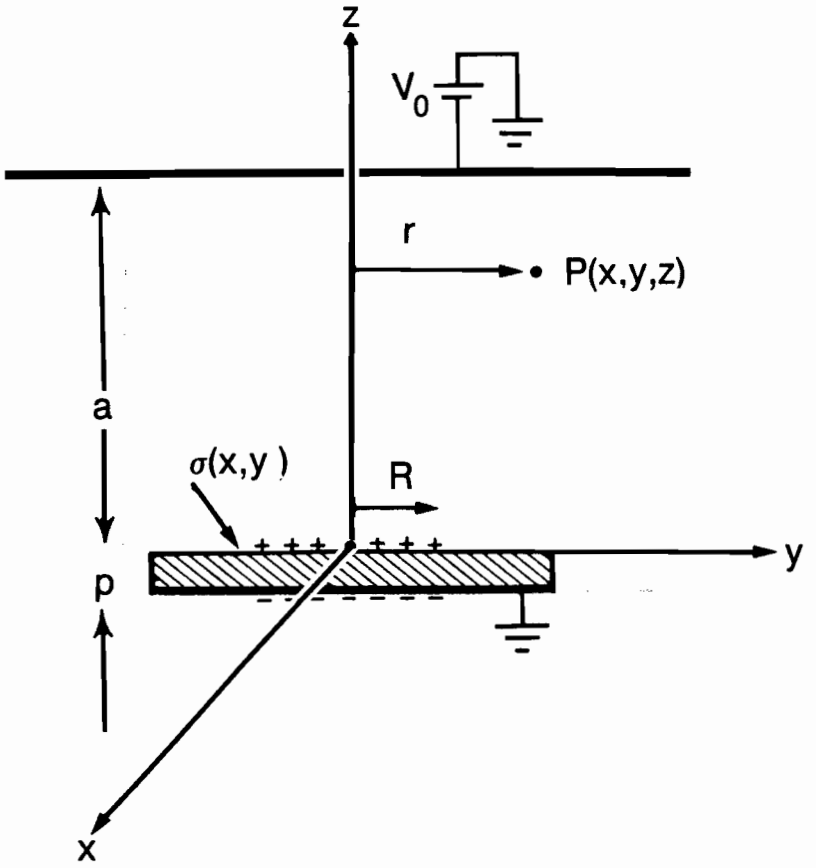

Figure 6.1 Schematic diagram of the electret chamber with a and p, the thickness of the air gap and the polymer, respectively. R is the radius of the circular charge distribution on the electret foil, $\sigma(x,y)$ the charge density and V_o the externally applied potential.

We use the relationship $\partial^2/\partial x^2 = -\omega_x^2$ and $\partial^2/\partial y^2 = -\omega_y^2$ with Eqs. (6.1) and (6.2) to get the following expression for the Laplace's equation in the frequency space:

$$\left(\frac{\partial^2}{\partial z^2} - \omega^2 \right) \overline{V} (\omega_x, \omega_y, z) = 0 , \tag{6.4}$$

where $\omega = (\omega_x^2 + \omega_y^2)^{\frac{1}{2}}$.

Equation (6.4) is the Helmholtz partial differential equation and its solution for $\omega^2 > 0$ has the form:

$$\overline{V}_i(\omega_x, \omega_y, z) = A_i e^{\omega z} + B_i e^{-\omega z} , \tag{6.5}$$

where i stands for either a or p denoting the potential in the air gap or in the polymer, respectively, and the constants A_i and B_i are functions of ω, determined by the boundary conditions.

Consequently, the Fourier transform of the normal component of the electric field is given by:

$$\overline{E} (\omega_x, \omega_y, z) = - \frac{\partial \overline{V}_i}{\partial z} = -\omega (A_i e^{\omega z} - B_i e^{-\omega z}) . \tag{6.6}$$

The boundary conditions for our chamber configuration (Fig. 6.1) and with the externally applied electric potential V_o, are in distance space:

$$V_p(x, y, z = -p) = 0 ; \tag{6.7}$$

$$V_a(x,y,z=a) = V_o \ ; \tag{6.8}$$

$$V_a(x,y,z=0) = V_p(x,y,z=0) \ ; \tag{6.9}$$

$$-\varepsilon_o\varepsilon_p \left.\frac{\partial V_p}{\partial z}\right|_{z=0} + \varepsilon_o\varepsilon_a \left.\frac{\partial V_a}{\partial z}\right|_{z=0} = \sigma(x,y) \ ; \tag{6.10}$$

and in frequency space:

$$A_p e^{-\omega p} + B_p e^{\omega p} = 0 \ ; \tag{6.11}$$

$$A_a e^{\omega a} + B_a e^{-\omega a} = 4\pi^2 V_o \delta(\omega_x)\delta(\omega_z) \ ; \tag{6.12}$$

$$A_a + B_a = A_p + B_p \ ; \tag{6.13}$$

$$\varepsilon_o\varepsilon_p\omega(A_p - B_p) - \varepsilon_o\varepsilon_a\omega(A_a - B_a) = \bar{\sigma}(\omega) \ , \tag{6.14}$$

where δ is the delta function and $\bar{\sigma}(\omega)$, the Fourier transform of the spatial charge distribution, is defined as :

$$\bar{\sigma}(\omega) = \bar{\sigma}(\omega_x,\omega_y) = \int_{-\infty}^{\infty}\int_{-\infty}^{\infty} \sigma(x,y) e^{-i(x\omega_x + y\omega_y)} dxdy \ . \tag{6.15}$$

After some manipulation of the boundary conditions given by Eqs. (6.11) to (6.14) the constants B_a and B_p are expressed as :

$$B_a = \frac{\bar{\sigma}(\omega) + 4\pi^2 V_o \delta(\omega_x)\delta(\omega_y)\varepsilon_o\omega[\varepsilon_p \coth(-\omega p) - \varepsilon_a] e^{-\omega a}}{\varepsilon_o\varepsilon_a\omega[1+e^{-2\omega a}][1+(\varepsilon_p/\varepsilon_a)\coth(\omega p)\tanh(\omega a)]} \ , \tag{6.16}$$

and

$$B_p = \frac{-\bar{\sigma}(\omega)-4\pi^2 V_o \delta(\omega_x)\delta(\omega_y)\varepsilon_o\varepsilon_a\omega[\coth(\omega a)+1]e^{-\omega a}}{\varepsilon_o\varepsilon_p\omega[1+e^{2\omega p}][1+(\varepsilon_a/\varepsilon_p)\coth(\omega a)\tanh(\omega p)]} \quad . \tag{6.17}$$

Combining Eqs. (6.5) and (6.6) with the boundary conditions in frequency space we get the following expressions for the Fourier transform of the potential $\bar{V}_p(\omega,z)$ and electric field $\bar{E}_p(\omega,z)$ in the polymer:

$$\bar{V}_p(\omega,z) = B_p[e^{-\omega z} - e^{\omega(2p+z)}] \quad , \tag{6.18}$$

and

$$\bar{E}_p(\omega,z) = B_p\omega[e^{-\omega z} + e^{\omega(2p+z)}] \quad . \tag{6.19}$$

The Fourier transforms of the potential $\bar{V}_a(\omega,z)$ and electric field $\bar{E}_a(\omega,z)$ in the air gap are similarly derived as:

$$\begin{aligned}\bar{V}_a(\omega,z) &= 4\pi^2 V_o \delta(\omega_x)\delta(\omega_y)e^{-\omega(a-z)} + B_a[e^{-\omega z} - e^{-\omega(2a-z)}] \\ &= 4\pi^2 V_o \delta(\omega_x)\delta(\omega_y) + \bar{\sigma}(\omega)\,\bar{F}_V(\omega) \quad ,\end{aligned} \tag{6.20}$$

and

$$\overline{E}_a(\omega,z) = -4\pi^2\omega V_o\delta(\omega_x)\delta(\omega_y)e^{-\omega(a-z)} + B_a\omega[e^{-\omega z}+e^{-\omega(2a-z)}]$$

$$= \frac{-4\pi^2 V_o\delta(\omega_x)\delta(\omega_y)\varepsilon_p}{p\varepsilon_a + a\varepsilon_p} + \bar{\sigma}(\omega)\,\overline{F}_E(\omega) \quad , \tag{6.21}$$

where $\overline{F}_V(\omega)$ and $\overline{F}_E(\omega)$, the transfer functions relating the charge distributions $\bar{\sigma}(\omega)$ with the potential $\overline{V}_a(\omega,z)$ and electric field $\overline{E}_a(\omega,z)$ respectively, are given below:

$$\overline{F}_V(\omega) = \frac{e^{-\omega z} - e^{-\omega(2a-z)}}{\omega\varepsilon_o\varepsilon_a[1+e^{-2\omega a}][1+(\varepsilon_p/\varepsilon_a)\coth(\omega p)\tanh(\omega a)]} \quad , \tag{6.22}$$

and

$$\overline{F}_E(\omega) = \frac{e^{-\omega z} + e^{-\omega(2a-z)}}{\varepsilon_o\varepsilon_a[1+e^{-2\omega a}][1+(\varepsilon_p/\varepsilon_a)\coth(\omega p)\tanh(\omega a)]} \quad . \tag{6.23}$$

The electric field [Eq. (6.21)] at the polymer-air interface for small a and p must be equivalent to that calculated from Gauss' and Kirchoff's laws expressed in distance space as:

$$E = \frac{-\varepsilon_p V_o + p\sigma/\varepsilon_o}{p\varepsilon_a + a\varepsilon_p} \quad . \tag{6.24}$$

This is verified by replacing the hyperbolic and exponential functions in $\overline{F}_E(\omega)$ with their small argument expansions, $\tanh(\omega a) \sim \omega a$, $\coth(\omega p) \sim 1/\omega p$, and $e^{-2\omega a} \sim 1 - 2\omega a$, so that at $z = 0$:

$$\bar{E}\ (\omega,0) = \frac{-4\pi^2 V_o \delta(\omega_x)\delta(\omega_y)\varepsilon_p + p\bar{\sigma}(\omega)/\varepsilon_o}{p\varepsilon_a + a\varepsilon_p}\ , \tag{6.25}$$

the inverse Fourier transform of which equals Eq. (6.24).

To simplify the general calculations for any point P in the air gap we assume that the electret surface charge density $\sigma(x,y)$ is uniform in the distance space. Furthermore, since our electret chamber is cylindrically symmetric, as shown in Fig. 6.1 , $\sigma(x,y)$ is expressed as:

$$\sigma(x,y) = \sigma(r) = \begin{cases} \sigma_o & \text{for } r \leqq R \\ 0 & \text{for } r > R \end{cases}\ , \tag{6.26}$$

where $r^2 = x^2 + y^2$, R is the radius of the charge distribution and σ_o the surface charge density.

The Fourier transform of $\sigma(x,y)$ was given in Eq. (6.15) and may in cylindrical coordinates be expressed as:

$$\bar{\sigma}(\omega) = \int_0^{\infty}\int_0^{2\pi} \sigma(r) e^{-ir\omega\ cos(\theta-\phi)} r\,dr\,d\theta\ , \tag{6.27}$$

where $x = r\ sin\theta$, $y = r\ cos\theta$, $\omega_x = \omega\ sin\phi$ and $\omega_y = \omega\ cos\phi$.

Equation (6.27) is actually a Hankel transform and can be written in a Bessel function form after incorporating Eq. (6.26) as follows:[28]

$$\bar{\sigma}(\omega) = 2\pi \int_0^{\infty} \sigma(r) J_o(\omega r) r dr$$

$$= 2\pi\sigma_o \int_0^{R} r\, J_o(\omega r) dr = \frac{2\pi R\sigma_o}{\omega} J_1(\omega R). \qquad (6.28)$$

The potential, electric field and surface charge density presented in this section were calculated in the frequency space following a method proposed by Kao,[24] who, however, left his results in the frequency space. In the following sections we discuss our method for calculating the electric field and potential in distance space from the given expressions in frequency space.

6.3 POTENTIAL AND ELECTRIC FIELD IN DISTANCE SPACE

To be of practical value in our study, the electret chamber electric field and potential should be given in distance space. In principle one obtains these parameters by applying the inverse Fourier transformation to the expressions for these parameters in the frequency space. Thus, the potential $V_a(r,z)$ in cylindrical coordinates is given by:

$$V_a(r,z) = \frac{1}{2\pi} \int_0^{\infty} \bar{V}_a(\omega,z) \left\{ \int_0^{2\pi} e^{ir\omega \cos(\theta-\phi)} d\phi \right\} \omega d\omega$$

$$= \frac{1}{2\pi} \int_0^{\infty} \bar{V}_a(\omega,z)\, J_o(\omega r)\, \omega d\omega\,, \qquad (6.29)$$

where $\bar{V}_a(\omega,z)$ was given in Eq. (6.20), with $\bar{\sigma}(\omega)$ given in Eq. (6.28).

Inserting Eqs. (6.20) and (6.28) into Eq. (6.29) we get:

$$V_a(r,z) = V_o + \sigma_o R \int_0^\infty \bar{F}_V(\omega)\, J_o(\omega r)\, J_1(\omega R)\, d\omega, \qquad (6.30)$$

with $\bar{F}_V(\omega)$ given by Eq. (6.22).

Similarly, the electric field $E_a(r,z)$ is given by:

$$E_a(r,z) = \frac{-V_o \varepsilon_p}{p\varepsilon_a + a\varepsilon_p} + \sigma_o R \int_0^\infty \bar{F}_E(\omega)\, J_o(\omega r)\, J_1(\omega R)\, d\omega, \qquad (6.31)$$

where $\bar{F}_E(\omega)$ is the transfer function given by Eq. (6.23) .

It is very difficult to evaluate the integrals in Eq. (6.30) and Eq. (6.31) analytically; we can, however, make some approximations in the transfer functions, $\bar{F}_V(\omega)$ and $\bar{F}_E(\omega)$, and thus obtain a solvable integral. For $\omega a \geq 3$ and $\omega p \leq 0.2$, which corresponds to a frequency range $3/a \leq \omega \leq 0.2/p$ and which stipulates that $a > 15\ p$, the following approximations are valid: $\tanh(\omega a) \approx 1$, $\coth(\omega p) \approx 1/\omega p$, and $1 + e^{-2\omega a} \approx 1$. $\bar{F}_V(\omega)$ from Eq. (6.22) is then given by:

$$\bar{F}_V(\omega) \approx p\,[\, e^{-\omega z} - e^{-\omega(2a-z)}\,]\,/\varepsilon_o \varepsilon_p\ , \qquad (6.32)$$

and the potential $V_a(r,z)$ given by Eq. (6.30) may now be expressed as:

$$V_a(r,z) = V_o + \frac{\sigma_o p R}{\varepsilon_o \varepsilon_p} \int_0^\infty [e^{-\omega z} - e^{-\omega(2a-z)}] J_o(\omega r) J_1(\omega R) d\omega. \qquad (6.33)$$

The transfer function $\overline{F}_E(\omega)$, given by Eq. (6.23), may now be approximated by:

$$\overline{F}_E(\omega) \approx \omega p \, [e^{-\omega z} + e^{-\omega(2a-z)}] / \varepsilon_o \varepsilon_p \, , \tag{6.34}$$

and the electric field $E_a(r,z)$ using Eq. (6.31) may be expressed as:

$$E_a(r,z) = \frac{-V_o \varepsilon_p}{p\varepsilon_a + a\varepsilon_p} + \frac{\sigma_o p R}{\varepsilon_o \varepsilon_p} \int_0^\infty [e^{-\omega z} + e^{-\omega(2a-z)}]$$

$$\times J_o(\omega r) \, J_1(\omega R) \, \omega d\omega \, . \tag{6.35}$$

To test the validity of the approximations to transfer functions, we show in Fig. 6.2 a comparison between the exact transfer functions $\overline{F}_V(\omega)$ and $\overline{F}_E(\omega)$ (solid lines) given by Eqs. (6.22) and (6.23) respectively and the approximations (dashed lines) given by Eqs. (6.32) and (6.34) respectively, for several combinations of air gap thickness a and axial distance z. The agreement between the transfer functions and their approximations is excellent for relatively large ω; it breaks down, however, for $0 \leq \omega \leq 3/a$, where for $\omega \to 0$ the approximations go towards zero in contrast to transfer functions, which have a large finite value at $\omega \to 0$. It is easy to show that $\varepsilon_o \overline{F}_V(0)$ equals to $(a-z)/(\varepsilon_a + \varepsilon_p a/p)$ while $\varepsilon_o \overline{F}_E(0)$ is equal to $(\varepsilon_a + \varepsilon_p a/p)^{-1}$. The discrepancy at small ω between the transfer functions and their approximations would at first glance suggest that the approximations are invalid. As shown in Eqs. (6.30) and (6.31), however, in the calculation of the potential and the electric field, the transfer function is multiplied by two Bessel

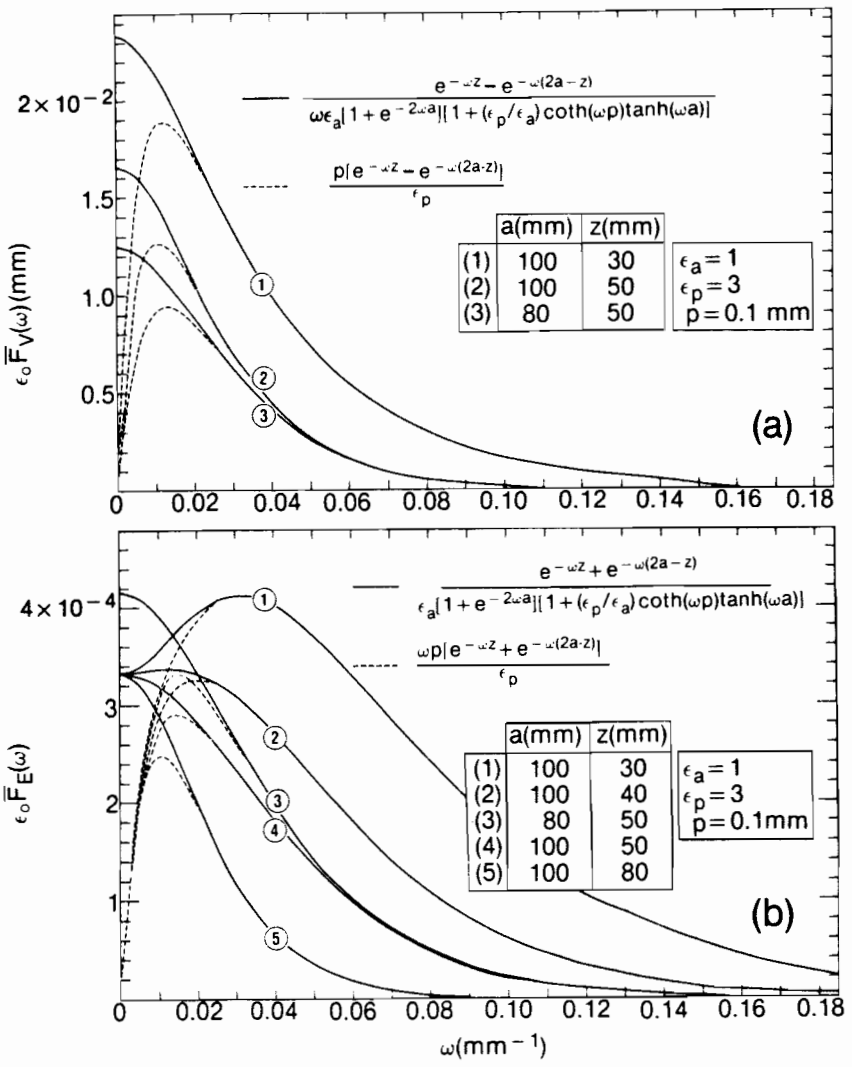

Figure 6.2 Transfer functions $\bar{F}_V(\omega)$ in (*a*) and $\bar{F}_E(\omega)$ in (*b*) as given by Eqs. (6.22) and (6.23) respectively (solid lines), and their approximations as given by Eqs. (6.32) and 6.34) respectively (dashed lines) for various air gap thicknesses a and axial distances z.

functions, $J_o(\omega r)$ and $J_1(\omega R)$ and subsequently integrated with respect to ω from 0 to ∞. For $\omega \to 0$, $J_o(\omega r) \to 1$ and $J_1(\omega R) \to 0$, and the integrand in Eqs. (6.30) and (6.31) is determined mainly by the value of $J_1(\omega R)$, irrespective of the values for the transfer functions. This is substantiated in Fig. 6.3, where in part (a) we show the Bessel function $J_1(\omega R)$ vs ω for various values of the charge distribution radius R, and in part (b) we plot the function $\overline{F}_V(\omega)\, J_1(\omega R)$ with the exact $\overline{F}_V(\omega)$ (solid lines), and its approximation (dashed lines), again for various values of R. In contrast to Fig. 6.2(a), both the solid and dashed curves are now very close in the whole frequency range from 0 to ∞, even though the approximation is rigorously correct only for $3/a \leqq \omega \leqq 0.2/p$, which for our specific example corresponds to 0.03 line pairs/mm $\leqq \omega \leqq$ 2 line pairs/mm. The areas under the solid curves, representing the integrand of Eq. (6.30) with the exact $\overline{F}_V(\omega)$, are almost identical to the areas under the dashed curves, representing the integrand of Eq. (6.33), and even for the worst example shown in Fig. 6.3(b), with R = 50 mm, the two areas are equal to within a few %. It is evident that the error becomes larger as R is increased; we can conclude, however, that for $R \leqq a$ the approximations to transfer functions give reasonably accurate results in calculations of the potential and the electric field. Since $\overline{F}_E = -\partial \overline{F}_V / \partial_Z$, it can be shown that the function $\overline{F}_E(\omega)\, J_1(\omega R)$ behaves similarly to the function $\overline{F}_V(\omega)\, J_1(\omega R)$ shown in Fig. 6.3(b).

The potential and electric field are calculated in the frequency range from 0 to ∞ and the approximations to transfer functions are rigorously correct only for $3/a \leqq \omega \leqq 0.2/p$. We can nevertheless apply the integration from 0 to ∞ and still use the approximations to $\overline{F}_V(\omega)$ and $\overline{F}_E(\omega)$, because in the range $0 \leqq \omega \leqq 3/a$ the Bessel function

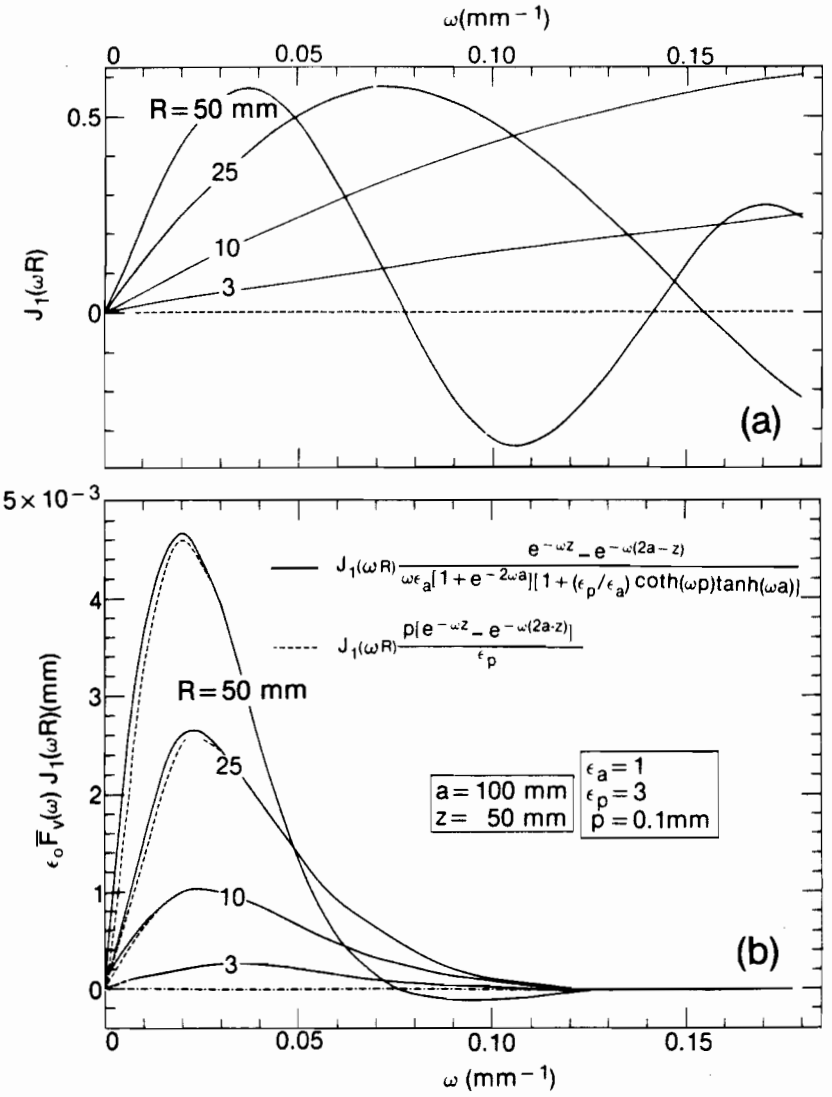

Figure 6. 3 (*a*) $J_1(\omega R)$ vs ω for various radii R, and (*b*) the function $\varepsilon_\sigma \bar{F}_V(\omega)\ J_1(\omega R)$ vs ω for various R with the solid line representing the calculation with the exact $\bar{F}_V(\omega)$ as given by Eq. (6.22) and the dashed line representing the calculation with the approximation to $\bar{F}_V(\omega)$ as given by Eq. (6.32).

$J_1(\omega R)$ is the determining factor in the integrand of Eqs. (6.30) and (6.31), and in the range $0.2/p \leqq \omega \leqq \infty$ the transfer functions $\overline{F}_V(\omega)$ and $\overline{F}_E(\omega)$ as well as their approximations are very close to 0 and therefore make a negligible contribution to the integrals. The latter situation will certainly be true for reasonably large z; for small z, however, it can happen that both the transfer function and its approximation do not have a negligible value at $\omega \geqq 0.2/p$. Integration of Eqs. (6.33) and (6.35) in the region from $0.2/p$ to ∞ will then give incorrect contributions to the potential and electric field. We estimate this limitation on z accepting all z which are large enough to yield values for the $\varepsilon_o \overline{F}_V(\omega)$ at $\omega = 0.2/p$ such that $\overline{F}_V(0.2/p) \leqq 10^{-2}\ \overline{F}_V(0)$ and get: $exp(-0.2\ z/p) \leqq 10^{-2}$, or: $z \geqq 23\ p$. Similarly, for $\overline{F}_E(0.2/p) \leqq 10^{-2}\overline{F}_E(0)$ we get $exp(-0.2\ z/p) \leqq 5 \times 10^{-2}\ p/a$ which for the example in Fig. 6.2(b) corresponds to $z \geqq 50\ p$.

The useful range for the approximations to $\overline{F}_V(\omega)$ and $\overline{F}_E(\omega)$ has thus been extended from $3/a \leqq \omega \leqq 0.2/p$ to the full frequency range $0 \leqq \omega \leqq \infty$ under the conditions discussed above: $a > 15\ p$, $R \leqq a$, and $z > 23\ p$.

In the following sections the approximations to transfer functions $\overline{F}_V(\omega)$ and $\overline{F}_E(\omega)$ given by Eqs. (6.32) and (6.34) respectively will be used to calculate analytically in distance space the potential and electric field in our electret chamber for both the points on the chamber central axis and for off-axis points.

The integrals in Eqs. (6.33) and (6.35) are solved using the following general relationship,[29] which is valid under the conditions that $Re[\lambda+\mu+\nu] > 0$ and $Re[\alpha \pm i\beta \pm i\gamma] > 0$:

$$\int_0^\infty x^{\lambda-1}\, e^{-\alpha x}\, J_\mu(\beta x) J_\nu(\gamma x)\, dx = \frac{\beta^\mu \gamma^\nu}{\Gamma(\nu+1)}\, 2^{-\nu-\mu}\, \alpha^{-\lambda-\mu-\nu}$$

$$\times \sum_{m=0}^{\infty} \frac{\Gamma(\lambda+\mu+\nu+2m)}{m!\,\Gamma(\mu+m+1)}\, F\left(-m,\ -\mu-m;\ \nu+1;\ \frac{\gamma^2}{\beta^2}\right), \qquad (6.36)$$

where F is the hypergeometric function.

It is obvious that there are, for each pair of (r,z) two solutions for $V_a(r,z)$ and $E_a(r,z)$. Both give identical values for $r > 0$; one of them, however, exhibits a singularity at $r = 0$. We thus take the solution which is finite for $r = 0$ and express the potential $V_a(r,z)$ in the air gap as follows:

$$V_a(r,z) = V_o + \frac{\sigma_o p R^2}{2\varepsilon_o \varepsilon_p} \left\{ \sum_{m=0}^{\infty} \frac{(-1)^m (2m+1)!}{m!\,(m+1)!} \sum_{n=0}^{m} \frac{(-m)_n (-1-m)_n}{n!\,n!} \right.$$

$$\left. \times \left(\frac{r^2}{R^2}\right)^n \left[\left(\frac{R^2}{4z^2}\right)^m \frac{1}{z^2} - \left(\frac{R^2}{4(2a-z)^2}\right)^m \frac{1}{(2a-z)^2} \right] \right\}, \qquad (6.37)$$

and the electric field $E_a(r,z)$ as:

$$E_a(r,z) = -\frac{V_o \varepsilon_p}{p\varepsilon_a + a\varepsilon_p}$$

$$+ \frac{\sigma_o p R^2}{2\varepsilon_o \varepsilon_p} \left\{ \sum_{m=0}^{\infty} \frac{(-1)^m (2m+2)!}{m!\,(m+1)!} \sum_{n=0}^{m} \frac{(-m)_n (-1-m)_n}{n!\,n!} \right.$$

$$\left. \times \left(\frac{r^2}{R^2}\right)^n \left[\left(\frac{R^2}{4z^2}\right)^m \frac{1}{z^3} + \left(\frac{R^2}{4(2a-z)^2}\right)^m \frac{1}{(2a-z)^3} \right] \right\}, \qquad (6.38)$$

where the gamma functions of Eq. (6.36) have been replaced by their factorial form and the hypergeometric function by an equivalent expression[30]:

$$F(-m,\ -1-m;\ 1;\ \frac{r^2}{R^2}) = \sum_{n=0}^{m} \frac{(-m)_n(-1-m)_n}{n!n!} \left(\frac{r^2}{R^2}\right)^n$$

$$= 1 + \frac{-m(-1-m)}{1.1}\left(\frac{r^2}{R^2}\right)$$

$$+ \frac{-m(-m+1)(-1-m)(-1-m+1)}{1.2.1.2}\left(\frac{r^2}{R^2}\right)^2$$

$$+ \ldots. \qquad (6.39)$$

6.4 AXIAL POTENTIAL AND ELECTRIC FIELD IN DISTANCE SPACE

Equations (6.37) and (6.38), which give general solutions for the potential and electric field in the air gap for the electret chamber configurations shown in Fig. 6.1 , can be handled by computer techniques. A listing of the programs used is given in the Appendix. First we consider the potential and electric field on the chamber axis where $r = 0$. With $V_o = 0$, Eqs. (6.37) and (6.38) become somewhat simpler:

$$V_a(0,z) = \frac{\sigma_o p R^2}{2\varepsilon_o \varepsilon_p}\left\{\sum_{m=0}^{\infty} \frac{(-1)^m(2m+1)!}{m!(m+1)!}\left[\left(\frac{R^2}{4z^2}\right)^m \frac{1}{z^2}\right.\right.$$

$$\left.\left. - \left(\frac{R^2}{4(2a-z)^2}\right)^m \frac{1}{(2a-z)^3}\right]\right\}, \qquad (6.40)$$

and

$$E_a(0,z) = \frac{\sigma_o p R^2}{2\varepsilon_o \varepsilon_p} \left\{ \sum_{m=0}^{\infty} \frac{(-1)^m (2m+2)!}{m!\ (m+1)!} \left[\left(\frac{R^2}{4z^2}\right)^m \frac{1}{z^3} \right.\right.$$

$$\left.\left. + \left(\frac{R^2}{4(2a-z)^2}\right)^m \frac{1}{(2a-z)^3} \right]\right\}, \qquad (6.41)$$

but will exhibit divergence for small z compared to R and the value for z = 0 is not defined. It will be shown later that converging solutions can be obtained only for z > R.

To investigate the region on the chamber axis for $0 \leqq z \leqq R$, we turn back to Eqs. (6.33) and (6.35), seth both V_o and κ equal to 0, and get the following relationship for $V_a(0,z)$ and $E_a(0,z)$:

$$V_a(0,z) = \frac{\sigma_o p R}{\varepsilon_o \varepsilon_p} \int_0^{\infty} \left[e^{-\omega z} - e^{-\omega(2a-z)} \right] J_1(\omega R)\ d\omega$$

$$= \frac{\sigma_o p}{\varepsilon_o \varepsilon_p} \left\{ \frac{\sqrt{R^2+z^2}-z}{\sqrt{R^2+z^2}} - \frac{\sqrt{R^2+(2a-z)^2}-(2a-z)}{\sqrt{R^2+(2a-z)^2}} \right\}, \qquad (6.42)$$

and

$$E_a(0,z) = \frac{\sigma_o p R}{\varepsilon_o \varepsilon_p} \int_0^{\infty} \left[e^{-\omega z} + e^{-\omega(2a-z)} \right] J_1(\omega R)\, \omega d\omega$$

$$= \frac{\sigma_o p R^2}{\varepsilon_o \varepsilon_p} \left\{ \frac{1}{[R^2+z^2]^{\frac{3}{2}}} + \frac{1}{[R^2+(2a-z)^2]^{\frac{3}{2}}} \right\}. \qquad (6.43)$$

$E_a(0,z)$ is thus described either by Eq. (6.41) which converges for $z > R$ or by Eq. (6.43), which is much simpler and valid for the whole range of z from 0 to ∞.

Similarly, $V_a(0,z)$ is described either by Eq. (6.40) or a much simpler Eq. (6.42). It is given below for the point at the center of the charge distribution, i.e., $z = 0$ and $r = 0$ as:

$$V_a(0,0) = \frac{\sigma_o p}{\varepsilon_o \varepsilon_p} \left[1 + \left(\frac{R}{2a}\right)^2\right]^{-\frac{1}{2}} , \tag{6.44}$$

which is equal to:

$$V_a(0,0) = \frac{\sigma_o p}{\varepsilon_o \varepsilon_p} = const. \text{ for } R < a = \infty , \tag{6.45}$$

and may be approximated by:

$$V_a(0,0) \sim \frac{\sigma_o p}{\varepsilon_o \varepsilon_p} = const. \text{ for } 2R < a < \infty , \tag{6.46}$$

and

$$V_a(0,0) \sim \frac{\sigma_o p}{\varepsilon_o \varepsilon_p} \left(\frac{2a}{R}\right) \text{ for } a \ll R . \tag{6.47}$$

$V_a(0,z)$ is plotted in Fig. 6.4 for air gap $a \to \infty$, with various charge distribution radii, R. The dashed lines represent Eq. (6.42) with the overlapping solid line representing Eq. (6.40) in its region of con-

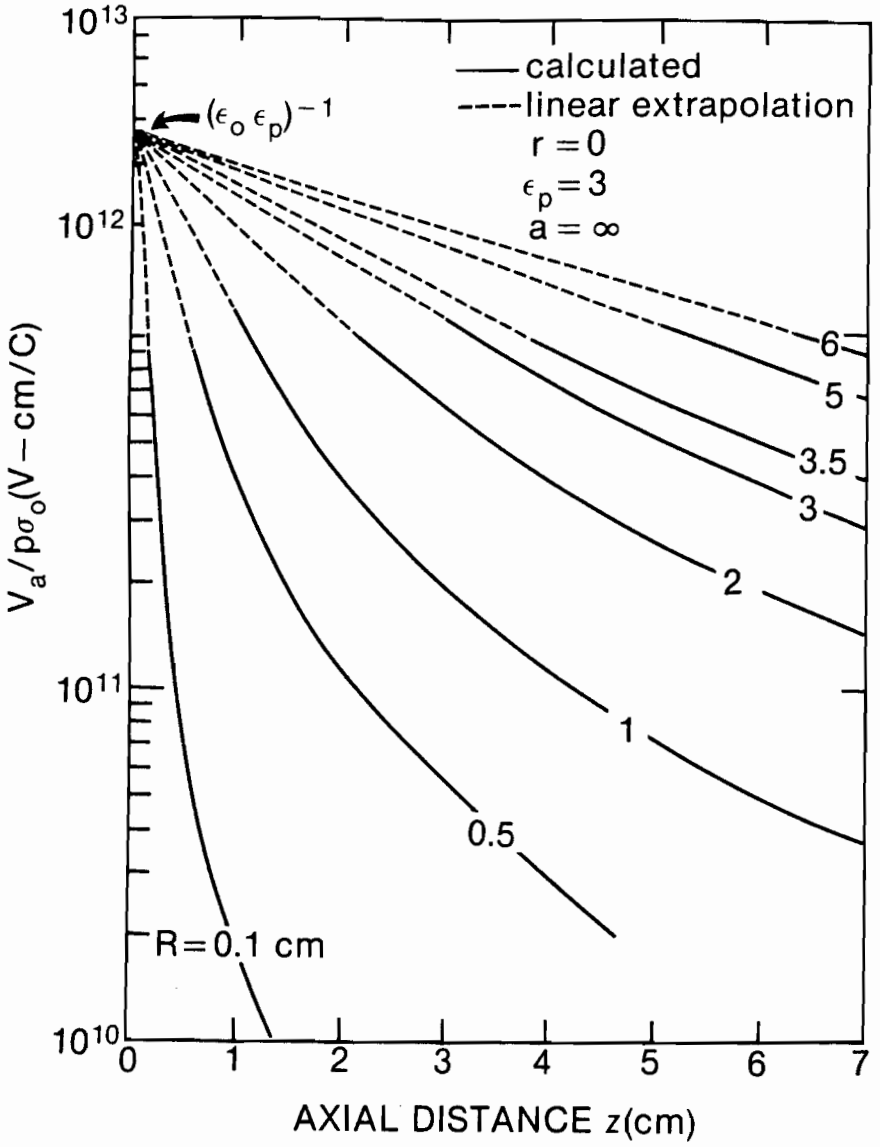

Figure 6.4 A semilogarthmic plot of $V_a(0,z)/p\sigma_o$ as a function of axial distance z for various charge distribution radii R. with an infinite air gap a. The dashed curves represent Eq. (6.42) and the overlapping solid curves represent Eq. (6.40) in its region of convergence (z > R).

vergence ($z > R$). As shown by Eq. (6.45) the potential at $z = 0$ is equal to $\sigma_o p/\varepsilon_o \varepsilon_p$ and is independent of R.

In Fig. 6.5, $V_a(0,z)$ is plotted for an air gap a of 10 cm with various radii R in the range from 0.01 cm to 5 cm. Again the dashed line represents Eq. (6.42) and the solid line Eq. (6.40). Since the limiting case of Eq. (6.46) now prevails, $V_a(0,0)$ is again equal to the constant $\sigma_o p/\varepsilon_o \varepsilon_p$. The axial potential $V_a(0,z)$ for $z = a$ is generally equal to V_o as required by boundary conditions [Eq. (6.8)]. We, however, subsequently set $V_o = 0$ and Eq. (6.43) thus yields a value of 0 for $z = a$.

Figure 6.6 shows a comparison of axial potentials, $V_a(0,z)$, obtained for two radii, 0.1 cm and 3.5 cm, with various air gaps. Because $2R < a$, $V_a(0,0)$ again is equal to $\sigma_o p/\varepsilon_o \varepsilon_p$ for all curves displayed.

We now show that by using a dipole layer model for our charge distribution, $\sigma(x,y)$, and with an air gap, $a \to \infty$, we obtain for z large compared to R, an expression for the potential identical to Eqs. (6.40) and (6.42).

Implementing the dipole layer definition given by Jackson[31] we get the following expression for $V_a(0,z)$:

$$V_a(0,z) = -\int_S D(z) \frac{d\alpha}{z^2} , \tag{6.48}$$

where S is the area of dipole layer distribution, $d\alpha$ the area element of $\sigma(x,y)$, and D(z) the dipole layer moment defined as:

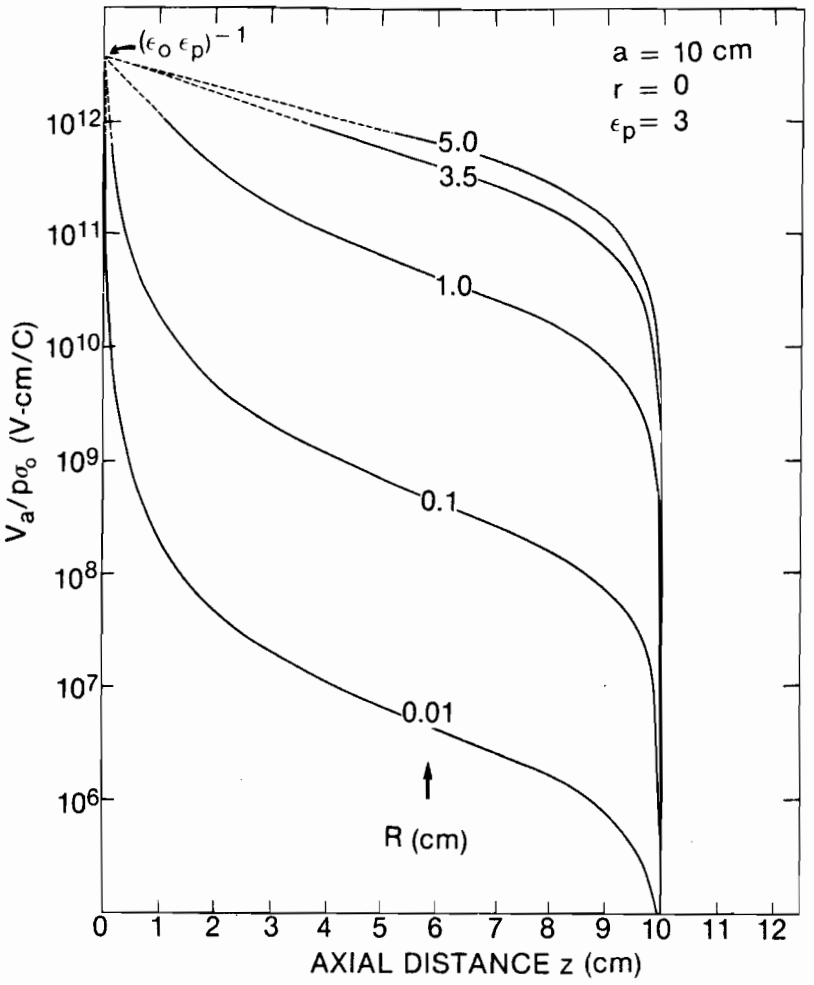

Figure 6.5 $V_a(0,z)/p\sigma_o$ is plotted as a function of axial distance z for an air gap of 10 cm with various charge distribution radii R, in the range from 0.01 cm-5 cm. The dashed curves represent Eq. (6.42) with the overlapping solid curves representing Eq. (6.40) in its region of convergence (z > R).

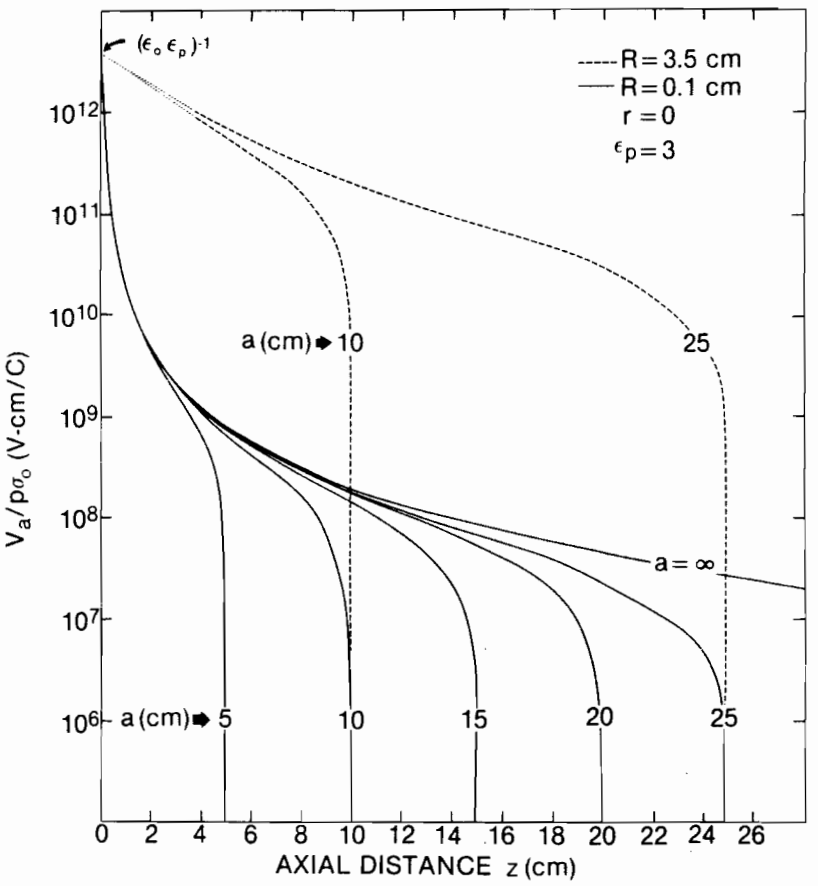

Figure 6.6 A plot of $V_a(0,z)/p\sigma_o$ for two charge distribution radii R (0.1 cm and 3.5 cm) for various air gaps a. The dotted curves represent Eq. (6.42) with overlapping solid and dashed curves representing Eq. (6.40) in its region of convergence

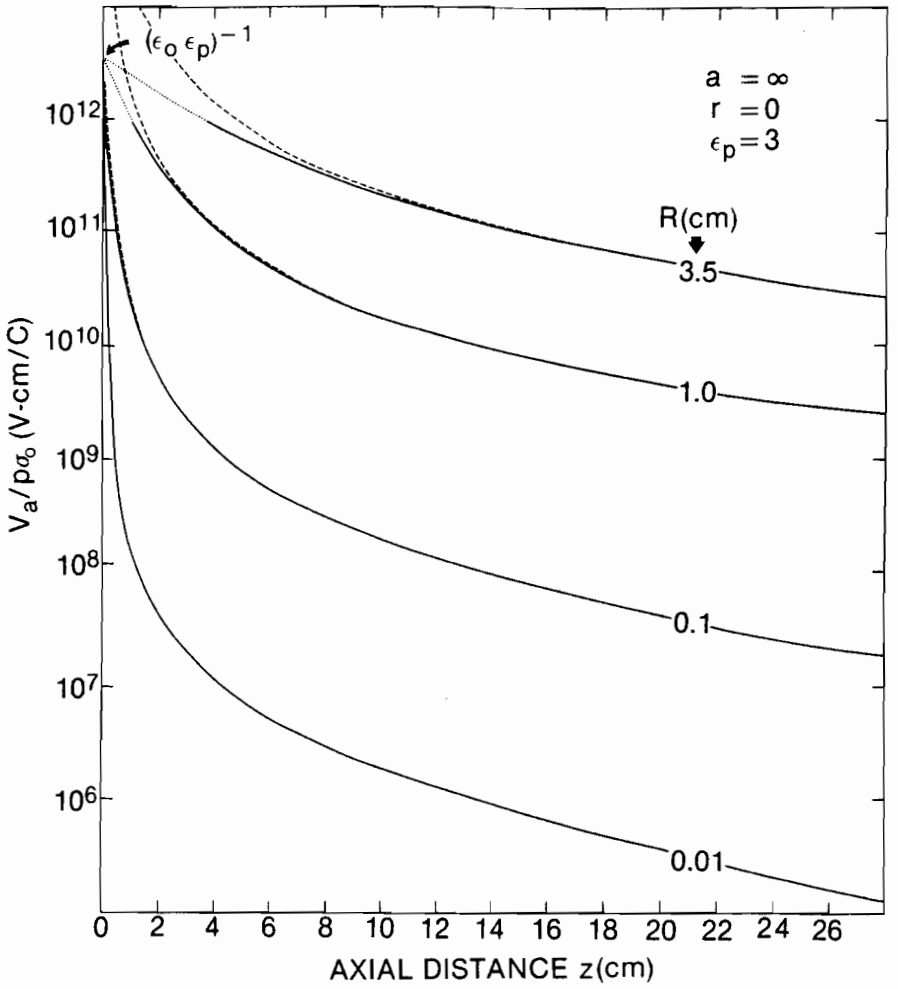

Figure 6.7 $V_a(0,z)p\sigma_o$ is shown for various charge distribution radii R for an infinite air gap a. The dashed curves represent the calculation from the dipole layer model, Eq. (6.50). The dotted curves represent Eq. (6.42) with the overlapping solid curves representing Eq. (6.40) in its region of convergence.

$$D(z) = -\frac{1}{4\pi\varepsilon_o\varepsilon_p}\lim_{p\to 0}\sigma_o(2p) = -\frac{p\sigma_o}{2\pi\varepsilon_o\varepsilon_p}\,. \tag{6.49}$$

Inserting Eq. (6.49) into Eq. (6.48) we get:

$$V_a(0,z) = \frac{p\sigma_o}{\varepsilon_o\varepsilon_p}\,\frac{R^2}{2z^2}\,. \tag{6.50}$$

This solution is now compared to Eqs. (6.40) and (6.42) which seemingly describe the axial potential under conditions identical to those in the dipole layer mode. Equation (6.40) actually transforms into Eq. (6.50) for $m = 0$. The number of terms in the summation required for convergence of Eq. (6.40) decreases with decreasing R/z until finally for sufficiently small R/z the sum converges for $m = 0$. It is clear that this happens when $z \gg R$ and this agrees well with Eq. (6.50) which also holds only in the regions far from the dipole layer charge distribution.

We next show that Eq. (6.42) in the far region also transforms into Eq. (6.50). Inserting $a = \infty$ and $z \gg R$ into Eq. (6.42) we get:

$$V_a(0,z) = \frac{\sigma_o p}{\varepsilon_o\varepsilon_p}\left\{1 - \frac{1}{(1+R^2/z^2)^{\frac{1}{2}}}\right\} \sim \frac{\sigma_o p}{\varepsilon_o\varepsilon_p}\,\frac{R^2}{2z^2} \tag{6.51}$$

A comparison of the three equations describing $V_a(0,z)$ is shown in Fig. 6.7, for various R from 0.01 cm to 3.5 cm. As discussed above the dipole layer equation applies well in the far region where $z \gg R$, but exhibits a singularity at $z = 0$. Equation (6.40) is valid for both the far and the intermediate regions ($z \gtrsim R$), but exhibits divergence for $z < R$. Equation (6.42), however, covers the whole region of interest, from $z = 0$ where $V_a(0,0) = \sigma_o p/\varepsilon_o\varepsilon_p$ to $z \to \infty$.

A plot of Eqs. (6.41) and (6.43) which describe the axial electric field $E_a(0,z)$ in the electret chamber is shown in Fig. 6.8 for various radii R and air gaps a. Equation (6.41) is only defined for $R > z$, while Eq. (6.43) covers the whole range in z from 0 to ∞. Similarly to the discussion of the axial potential, we compare Eqs. (6.41) and (6.43) for $a \to \infty$ and $z \gg R$ with the far field approximation of a dipole layer obtained from Eq. (6.50) as follows:

$$E_a(0,z) = -\frac{\partial V_a}{\partial z}\bigg|_{(z,0)} = \frac{\sigma_o p R^2}{\varepsilon_o \varepsilon_p z^3} \quad . \tag{6.52}$$

Both Eq. (6.41) with $m = 0$ and Eq. (6.43) with $z \gg R$ give expressions identical to Eq. (6.52). The far field of the dipole layer can thus be described by any of the three equations, (6.41), (6.43) or (6.52), the intermediate region by either Eq. (6.41) or Eq. (6.43), while the near field can only be expressed by Eq. (6.43).

Several approximations can be made to Eq. (6.43) depending on relative values of a, R and z; they are, however, all trivial and will not be discussed. It is interesting to note that Eq. (6.43) predicts an inverse proportionality between $E_a(0,0)$ and R for $a \to \infty$, as expected. The field calculated beyond the grounded electrode ($z > a$) is symmetrical with the fields before it. This indicates that the dipole layer-grounded plane configuration separated by a distance a, can be represented by two identical dipole layers a distance $2a$ apart with the electrode at a, acting as a mirror plane. This representation is similar to the well known point charge-ground plane situation.

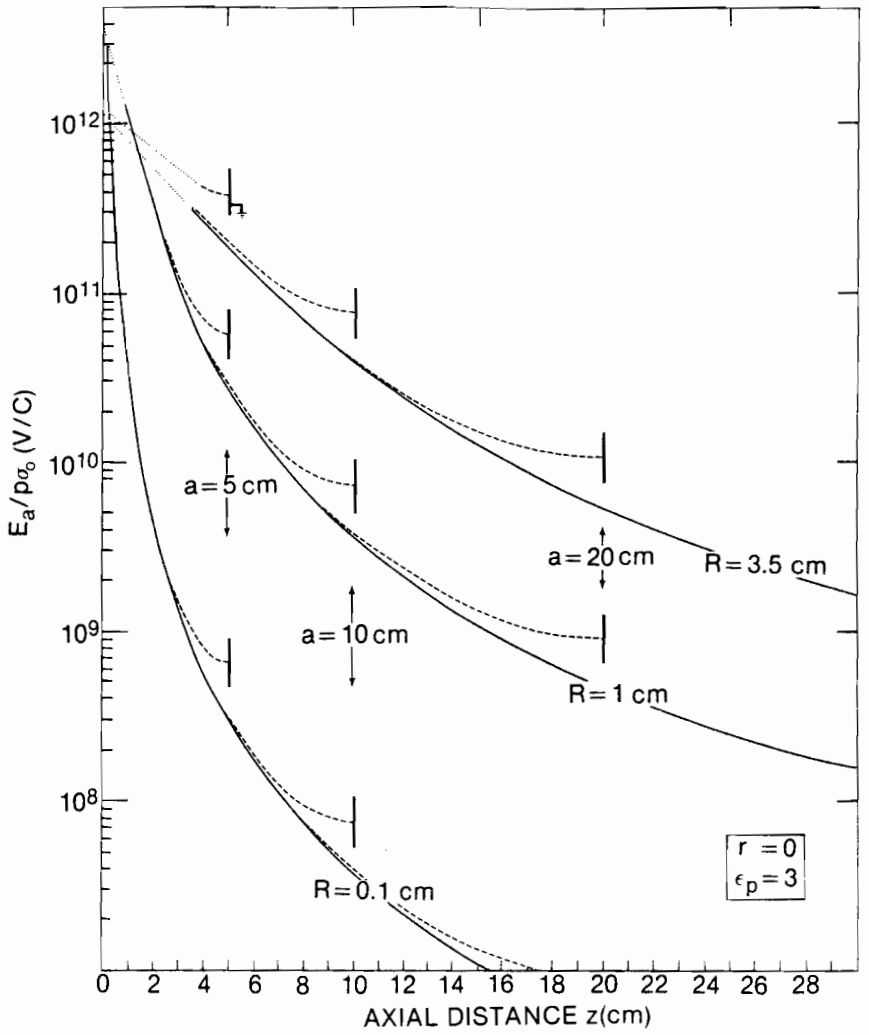

Figure 6.8 $E_a(0,z)/p\sigma_o$ is plotted as a function of axial distance z for various radii R and air gaps a. The dotted curves represent Eq. (6.43) with the overlapping solid curves representing Eq. (6.41) for an infinite air gap a, and the dashed curves representing Eq. (6.41) for various air gaps, a.

6.5 OFF-AXIS POTENTIAL AND ELECTRIC FIELD

The potential and the electric field in the air gap of the electret chamber were given by solutions to Eqs. (6.33) and (6.35), respectively. In the previous section we discussed the axial potential and electric field. We now discuss the general solutions to Eqs. (6.33) and (6.35) given by Eqs. (6.37) and (6.38) for $r \geq 0$. These solutions describe the potential and electric field for off-axis points in the electret chamber; they do not, however, converge for all combinations of z, r and R.

We study the convergence limits for the case of an electret in air for $a = \infty$ and $V_o = 0$. Conclusions reached with this example can then be generalized to a finite air gap a and to electric fields. Equation (6.37) becomes:

$$V_a(r,z)\Big|_{a\to\infty} = \frac{\sigma_o R^2}{2z^2\varepsilon_o\varepsilon_p}\left\{\sum_{m=0}^{\infty}\frac{(-1)^m(2m+1)!}{m!\,(m+1)!}\left(\frac{R^2}{4z^2}\right)^m\right.$$

$$\left.\times\sum_{n=0}^{m}\frac{(-m)_n(-1-m)_n}{n!n!}\left(\frac{r^2}{R^2}\right)^n\right\}. \qquad (6.53)$$

To determine the convergence limits of the equation above we plot in Fig. 6.9 for a typical value of R = 3.5 cm and various values of z and r the term $T = \frac{(2m+1)!}{m!\,(m+1)!}\left(\frac{R^2}{4z^2}\right)^m$, and the hypergeometric series $F = \sum_{n=0}^{m}\frac{(-m)_n(-1-m)_n}{n!n!}\left(\frac{r^2}{R^2}\right)^n$, as a function of integer m for $0 \leq m \leq 60$.

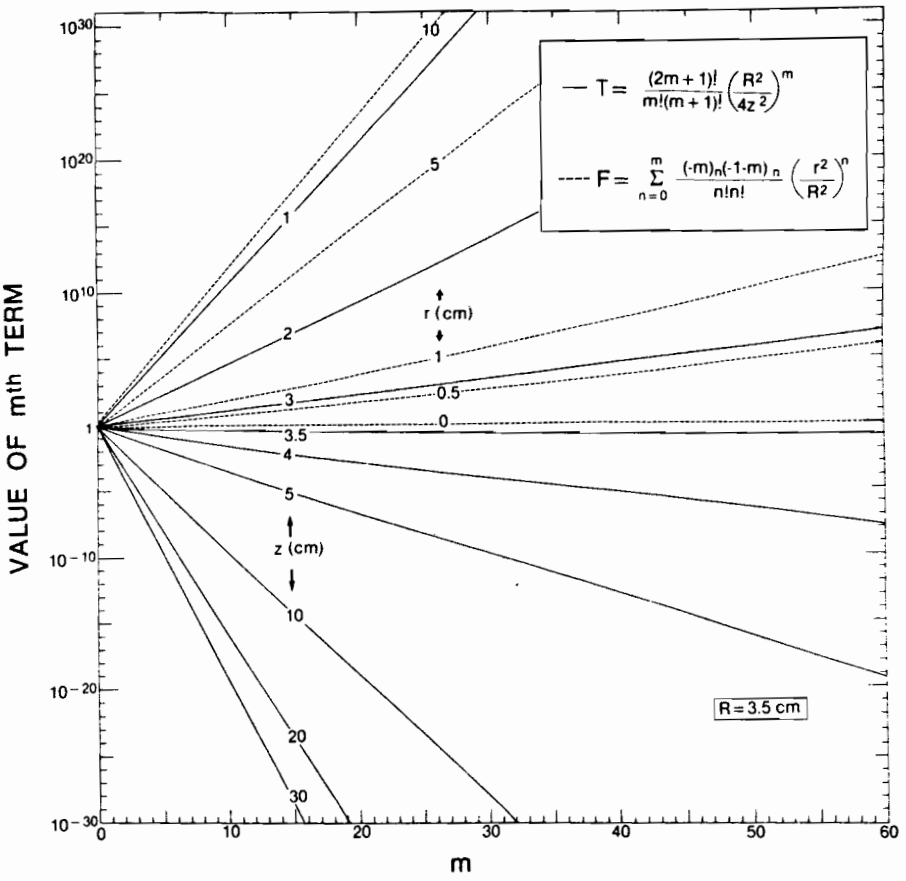

Figure 6.9 The term T (solid curves) and the hypergeometric function F (dashed) are plotted for a charge distribution radius R of 3.5 cm as a function of integer m for various axial distances z and radial distances r respectively.

Both T and F are equal to 1 for $m = 0$. Furthermore, F remains equal to 1 for all axial calculations ($r = 0$) irrespective of m. For $r > 0$, however, the value of F almost linearly increases with m on a semilogarithmic plot, the slope of which increases with an increasing r. T, on the other hand, decreases almost linearly with increasing m for $z \geq R$, and increases linearly with m for $z < R$. Equation (6.53) does not converge for those values of z and r for which both T and F increase with increasing m. It does converge, however, for combinations of z and r, where, for increasing m, T approaches zero faster than F increases to ∞.

T and F may be approximated by exponential functions:

$$T \sim e^{\delta_T m}, \tag{6.54}$$

and

$$F \sim e^{\delta_F m}, \tag{6.55}$$

where δ_T and δ_F are the slopes of T and F respectively obtained from Fig. 6.9 . Therefore, for large m, the potential in Eq. (6.53) is:

$$V_a(r,z)\Big|_{a\to\infty} = \frac{\sigma_o p R^2}{2\varepsilon_o \varepsilon_p}\ \frac{1}{z^2} \sum_{m=0}^{\infty} e^{m(\delta_T+\delta_F)}, \tag{6.56}$$

and it converges for $\delta_T+\delta_F \leq 0$. In Fig. 6.10(a) we plot the convergence parameters δ_T and δ_F as a function of z and r respectively for R = 3.5 cm. Parameters δ_T and δ_F are also plotted as a function of

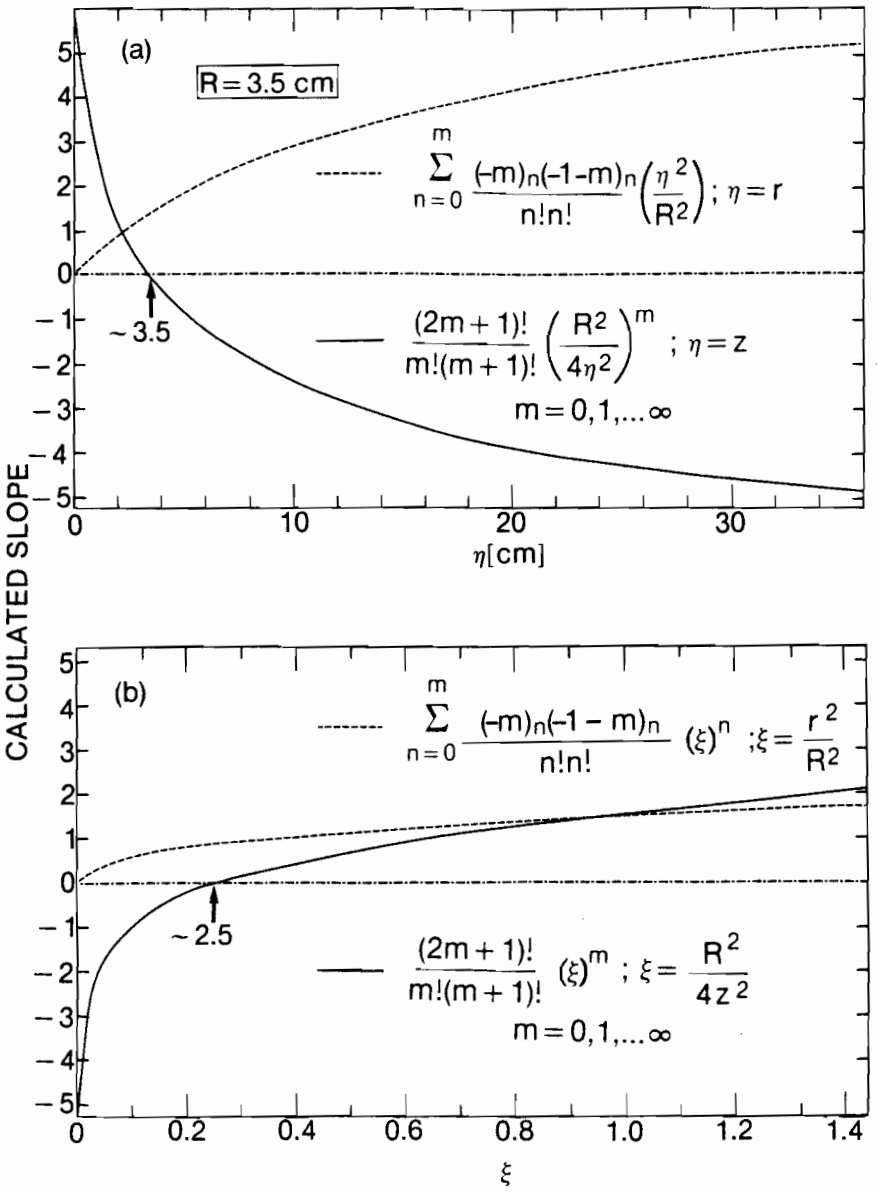

Figure 6.10 The convergence parameters δ_T(solid curves) and δ_F (dashed) are plotted as a function of (*a*) z and r, respectively with R = 3.5 cm, and (*b*) $R^2/4z^2$ and r^2/R^2, respectively.

$R^2/4z^2$ and r^2/R^2 respectively in Fig. 6.10(*b*) to show the effects of varying R. Since $\delta_F \geq 0$ for all r, the convergence condition will be satisfied only when $\delta_T \leq 0$ and $|\delta_T| \geq \delta_F$. The solid curve in Fig. 6.10(*a*) shows that $\delta_T \leq 0$ for $z \geq R = 3.5$ cm, and in Fig. 6.10(*b*) that $\delta_T \leq 0$ for $R^2/4z^2 \leq 0.25$, i.e., $z \geq R$.

Therefore, on the axis of the chamber where $\delta_F = r = 0$, Eq. (6.56) converges for $z \geq R$. For points off axis the domain of convergence is more restricted and is determined by noting δ_T from Fig. 6.10(*b*), and then finding the largest (r^2/R^2) for which $\delta_T+\delta_F \leq 0$. This procedure determines the maximum radial distance for which Eq. (6.56) converges at a given R and z. The region of convergence has a conical shape with the tip on chamber central axis at $z = R$ and an increasing radius of convergence with an increasing z.

We thus conclude that Eqs. (6.37) and (6.38) describe the potential and electric field in our electret chamber; they are, however, useful only in a well determined region of convergence, which is valid for $z \geq R$ at $r = 0$, and then expands to larger r with increasing z.

Figure 6.11 shows typical electric fields (*a*) and potentials (*b*) as a function of radial distance r calculated from Eqs. (6.38) and (6.37) normalized to 1.00 on the central axis. The plots are given for two values of air gap a (15 cm and ∞) and two values of charge distribution radius R (0.1 cm and 3.5 cm) at an axial distance z of 10 cm.

In Fig. 6.12, we show equipotential surfaces for our electret chamber configuration with the radius of charge distribution, R = 1 cm, and the externally applied potential $V_o = 0$. The left side represents an infinite air gap, the right side is for an air gap of 3 cm. The axial potential was calculated from Eq. (6.42), the off-axis points were

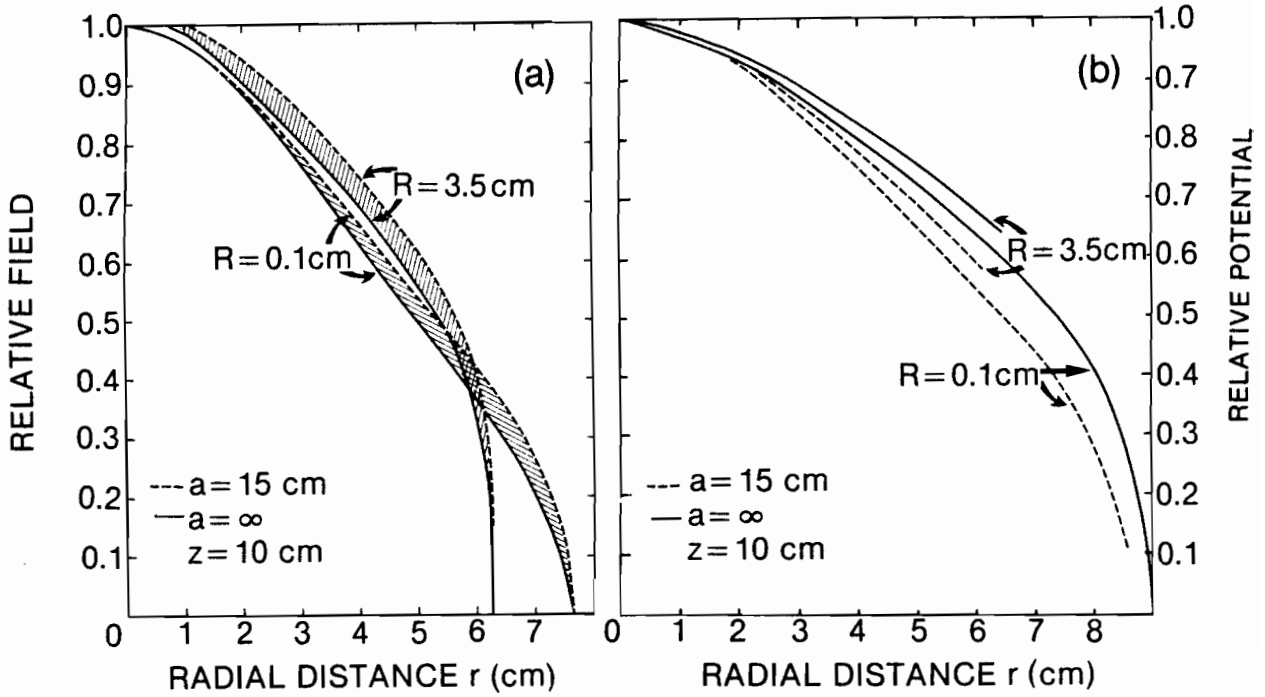

Figure 6.11 Calculated (a) electric fields from Eq. (6.38) and (b) potentials from Eq. (6.37) as a function of radial distance r for two air gaps a (15 cm and ∞) and two charge distribution radii R (0.1 cm and 3.5 cm) at an axial distance z of 10 cm.

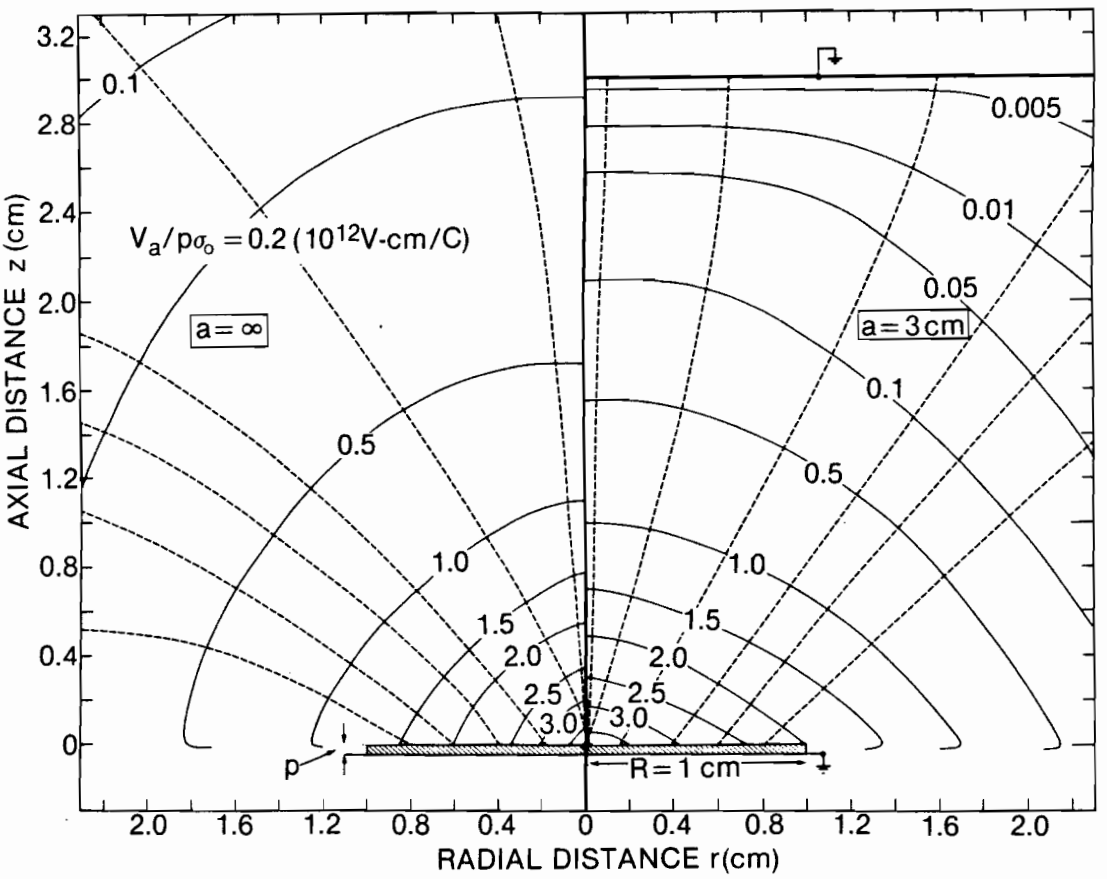

Figure 6.12 Lines of constant potential equipotential surfaces and electric displacement (dashed) for a *1* cm radius circular electret charged to a surface charge density σ_o and of thickness p for an infinite air gap (left) and an air gap a of 3 cm (right).

obtained either from Eq. (6.37) for points inside the region of convergence or through a linear extrapolation, similar to the extrapolation exhibited for axial potentials in Figs. 6.4 and 6.5 for points outside the region of convergence. The effect of the grounded electrode above the electret surface is to progressively flatten the equipotential surfaces as the air gap a decreases, to make them virtually parallel with the electret surface for very small a.

6.6 SUMMARY

Laplace's equation is used in conjunction with the theory of linear systems to calculate the potential and electric field in distance space for a cylindrical polarization/depolarization electret chamber. To calculate the inverse Fourier transformation analytically the transfer functions are simplified through the assumption that the air gap a separating the electret from the polarizing electrode in the chamber is much larger than the thickness p of the electret, which corresponds to a frequency range of $3/a \leq \omega \leq 10$ line pairs/mm . We show, however, that this approximation is valid to within a few %, in the whole frequency range from 0 to ∞. General solutions are given for the near, intermediate and far regions, and the domain of convergence for off-axis solutions is discussed. On the chamber axis the potentials calculated near the electret surface are equal to those obtained from Gauss' and Kirchoff's laws. With the electrode removed, i.e., $a = \infty$, the axial solutions for large distances from the electret surface are equal to those calculated from a dipole layer model of the electret.

6.7 REFERENCES

1 M. Eguchi, Philos. Mag. 49, 179 (1925).

2 ELECTRETS, Topics in Applied Physics, Vol. 33, edited by G.M. Sessler (Springer-Verlag, Berlin, 1980).

3 V.M. Fridkin and I.S. Zheludev, in Photoelectrets and the Electrophotographic Process (Consultants Bureau, New York, 1960).

4 C.F. Carlson, U.S. Patent No. 2 588 699 (1952).

5 R.M. Schaffert, Electrophotography, (Focal Press, London, 1975).

6 G.M. Sessler and J.E. West, J. Appl. Phys. 43, 922 (1972).

7 P.W. Chudleigh, J. Appl. Phys. 47, 4475 (1976).

8 B. Gross, G.M. Sessler and J.E. West, J. Appl. Phys. 45, 111 (1975).

9 G.M. Sessler and J.E. West, J. Electrostatics 1, 111 (1975).

10 B. Gross, G.M. Sessler and J.E. West, J. Appl. Phys. 47, 968 (1976).

11 B.G. Fallone and E.B. Podgorsak, Phys. Rev. B 27, 2615 (1983).

12 B.G. Fallone and E.B. Podgorsak, Med. Phys. 10, 191 (1983).

13 B.G. Fallone and E.B. Podgorsak, Phys. Rev. B 27, 5062 (1983).

14 B.G. Fallone and E.B. Podgorsak, Phys. Rev. B (in press).

15 D. Plewes and H.E. Johns, Med. Phys. 7, 315 (1980).

16 A.P. Proudian, R.L. Carangi, G. Jacobson and E.P. Muntz, Radiology 110, 667 (1974).

17 H. Bauser and W. Ronge, Health Phys. 34, 97 (1978).

18 R.M. Schaffert, in Electrophotography (Focal Press, London, 1975), p. 476.

19 H.E.J. Neugebauer, Appl. Opt. 3, 385 (1964).

20 D. Plewes and H.E. Johns, Med. Phys. 2, 61 (1975).

21 P.P. Fatouros and G.U.V. Rao, Med. Phys. 7, 331 (1980).

[22] H.E.J. Neugebauer, Appl. Opt. 4, 453 (1965).

[23] H.E.J. Neugebauer, Appl. Opt. 6, 943 (1967).

[24] C.C. Kao, J. Appl. Phys. 44, 1543 (1973).

[25] R.B. Crofoot and Y.C. Cheng, J. Appl. Phys. 50, 6583 (1979).

[26] Y.C. Cheng and G.C. Hartmann, J. Appl. Phys. 51, 2332 (1980).

[27] P.P. Fatouros, G.U.V. Rao and C.C. Kao, Med. Phys. 7, 331 (1980).

[28] A. Papoulis, Systems and Transforms with Applications in Optics, (McGraw-Hill, New York, 1968).

[29] I.S. Gradshteyn and I.M. Ryzhik, Table of Integrals, Series, and Products (Academic, New York, 1980).

[30] Handbook of Mathematical Functions, edited by M. Abramovitz and I.A. Stegun (Dover, New York, 1972).

[31] J.D. Jackson, Classical Electrodynamics (John Wiley & Sons, New York, 1962), p. 10.

CHAPTER 7

CHARGING CHARACTERISTICS OF GAS IONOGRAPHIC LATENT IMAGES

7.1 INTRODUCTION

In this chapter the charging characteristics of the ionographic latent images are discussed in terms of saturation characteristics of ionographic chambers. We apply the results of our study of collection efficiencies of parallel-plate ionization chambers, discussed in Chapter 4, and of the charging and discharging dynamics of the radiation induced foil electret, discussed in Chapter 5, to improve the understanding of the ionographic process.

Gas ionography,[1-5] sometimes referred to as Electron Radiography,[6-8] has been proposed as a possible alternative to emulsion film radiography. The basic principles of ionography both with air at normal pressure and with pressurized high atomic number gases [2,4,6,8] were discussed in Sec. 2.3. The technique has resolution capabilities similar to those of film, offers edge enhancement and independence of silver as a main advantage over film, but unfortunately has a low sensitivity, when compared to modern screen-film combinations.

In gas ionography, the x-ray photon absorption in a gas is used to generate free charge carriers which drift in an externally applied electric field and get trapped on a polymer surface to form a latent image of the object. This latent image is subsequently rendered visible with standard electrographic techniques.[9] The ionographic chamber resembles a parallel-plate ionization chamber, except that the measuring electrode is blocked by a thin dielectric foil. The charge carriers that drift in an electric field towards the measuring electrode get trapped on or near the dielectric surface thereby forming the latent image of the object, which is essentially a foil electret. We have recently performed

an extensive study of this radiation induced foil electret state[10-13] The results were presented in Chapter 5 and we now use some of them to improve the understanding of the physical properties of the ionographic latent image. Since the ionographic chamber used in our experiments utilizes air at atmospheric pressure as the absorbing medium, it has a much lower sensitivity than some previously described pressurized high atomic number gas ionographic chambers.[3] Nonetheless, the conclusions about the latent image formation process, obtained with our chamber, can be generalized to describe the more sophisticated chambers.

7.2 PRODUCTION (CHARGING) AND DEVELOPMENT (DISCHARGING) OF THE IONOGRAPHIC LATENT IMAGE

The latent ionographic image of the object is obtained by positioning the chamber, shown in Fig. 3.4, behind the object irradiated by x-rays. Some of the photons transmitted through the object interact either with the gas in the chamber sensitive volume producing energetic electrons, or with the polarizing electrode (photoemitter) creating photoelectrons, some of which are scattered back into the chamber sensitive volume. Both types of electrons ionize the gas in the chamber sensitive volume. The free charge carriers thus produced drift in the chamber effective electric field towards the appropriate electrodes. The charges that drift towards the measuring electrode get trapped on or near the surface of the polymer covering the electrode. The charged polymer foil therefore contains the latent image of the object and is essentially a stable electret with a surface charge distribution modulated by the photon

transmission through the object. Both positive and negative latent images can be produced, depending on the polarity of the external power supply.

During the latent image production, shown schematically in Fig. 7.1(a), the chamber effective electric field $\vec{E}_{eff}(t)$ is equal to the vector sum of $\vec{E}_a(0)$, the field produced in the air gap by the external power supply V_o, and $\vec{E}_\sigma(t)$, the field produced by the electret charges accumulated on the polymer foil

$$E_{eff}(t) = E_a(0) - E_\sigma(t) = \frac{V_o \varepsilon_p - p\sigma(t)/\varepsilon_o}{p\varepsilon_a + a\varepsilon_p} , \qquad (7.1)$$

where $\sigma(t)$ is the time (exposure) dependent electrect surface charge density, a and p the air gap and polymer thicknesses respectively, and ε_a and ε_p the dielectric constants of air and polymer respectively.

The latent image, produced with techniques discussed above, may be discharged by charge annihilation achieved through trapping, on the polymer surface, of charge carriers opposite to those forming the latent image. In the standard electrographic development technique discussed, in detail in Sec. 3.7, charged powder is used for this purpose to render the latent image visible. The latent image, however, may also be discharged in the ionographic chamber by simply grounding the polarizing electrode and continuing the irradiation of the object as indicated in Fig. 7.1(b). The effective field $\vec{E}_{eff}(t)$ in the air gap is now equal to the field $\vec{E}_\sigma(t)$ produced by the electret charges forming the latent image on the polymer foil. Since $\vec{E}_{eff}$ is now in the opposite direction from the effective field which was present during the formation of the latent image, charge carriers of opposite sign will drift towards the polymer foil, annihilate the charges forming the latent image, until the $\vec{E}_{eff}$ in the chamber finally

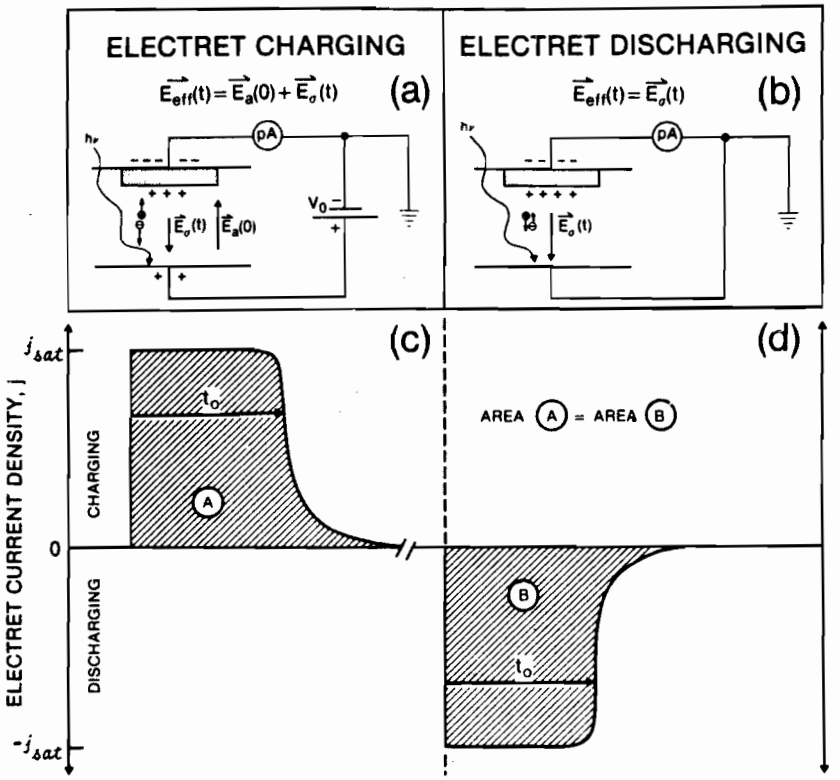

Figure 7.1 Time dependence for a typical latent image : (*a*) formation (charging), and (*b*) development (discharging) process; (c) typical current density profile measured during the charging process, and (*d*) typical current density profile measured during the discharging process.

becomes equal to zero and the latent image is completely discharged.

7.3 SATURATION CURVES OF IONOGRAPHIC CHAMBERS

The sensitivity of ionographic chambers depends on the charge carrier yield per incident photon as well as on the chamber collection efficiency. In air at normal pressure the charge density yield is 3.33×10^{-10} C/cm^2 per R per cm of air gap assuming that all primary electrons expand all their energy in air. This represents a relatively small charge yield and various methods have been proposed for its increase in ionographic chambers. Photoemission[1,14] from a high atomic number polarizing electrode, which may increase the sensitivity by more than an order of magnitude and a high atomic number pressurized gas[2-9,15,16] as the radiation sensitive medium, which may give a sensitivity increase of three orders of magnitude,[3] are two best known examples.

Furthermore, to maximize the sensitivity of a given ionographic chamber, no ions should be lost to recombination, i.e., saturation conditions should exist in the chamber during the latent image formation. In order to study the efficiency for charge carrier collection on the polymer foil during latent image formation, we converted our ionographic chamber into a standard parallel-plate ionization chamber by removing the polymer cover from the measuring electrode. Ion collection efficiencies were measured for various polarizing electrode materials and air gap thicknesses.

We have shown[13] in Chapter 4 that the full saturation curve, i.e., the collection efficiency f as a function of the effective electric field E_{eff} in an air filled parallel-plate ionization chamber may be expressed by a hyperbolic relationship:

$$\delta = j/j_{sat} = \tanh\ (E_{eff}/E^*)\ , \qquad (7.2)$$

where j is the measured ionization current density, j_{sat} the saturation current density and E^*, the extrapolated electric field, is the field at which the collection efficiency would equal to unity if the initial linear relationship between δ and E_{eff}, exhibited at small fields, held for all electric fields. The extrapolated field was found to be independent of beam energy but a function of both exposure rate $\dot{x}$ and air gap thickness a.

In Fig. 7.2, we show typical measured saturation curves with an air gap a of 1 cm for (a) our air-filled ionization chamber with an aluminum polarizing electrode and an exposure rate of 150 mR/s, (b) our air-filled ionization chamber with a lead polarizing electrode and an exposure rate of 150 mR/s, and (c) an ionization chamber filled with xenon gas at 10 atmospheres with an exposure rate of 25 mR/s. The measurements in Fig. 7.2 (c) are from Fenster et al.[3] The solid lines in Fig. 7.2 represent the saturation curves calculated from Eq. (7.2) using the appropriate E^* obtained by extrapolating the initial linear portion of the saturation curve to $\delta = 1$. It is evident that Eq. (7.2) holds not only for air-filled ionization chambers at normal pressure; it also covers the saturation characteristics resulting from polarizing electrode photoemission and from high atomic number pressurized gases provided that the appropriate E^* is applied. The main characteristics of Fig. 7.2 are summarized in Table 7.1 from where we conclude that both the saturation current density j_{sat} and the extrapolated electric field E^* in a parallel-plate ionization chamber depend strongly on the polarizing electrode material and on the atomic number and density of the radiation sensitive medium, in addition to depending on the exposure rate and air gap thickness .

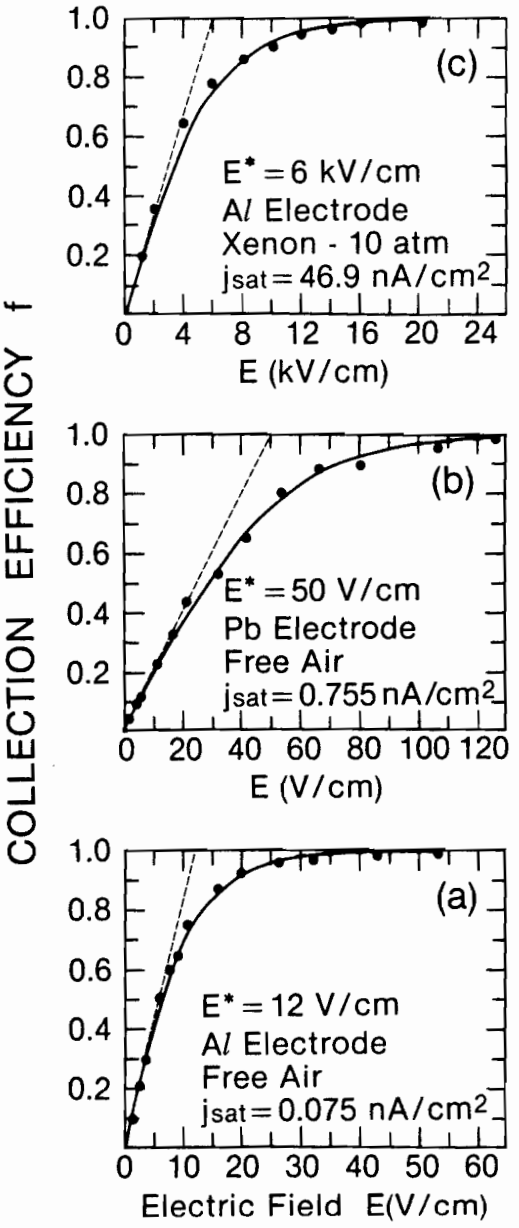

Figure 7.2 Saturation curves for various ionographic chambers with an air gap a of 1 cm. (a) Air-filled ionographic chamber with an aluminum polarizing electrode and an exposure rate of 150 mR/s, (b) air-filled ionographic chamber with a lead polarizing electrode and an exposure rate of 150 mR/s, and (c) an ionographic chamber[3] filled with xenon at 10 atmospheres and an exposure rate of 25 mR/s.

Table 7.1 Characteristics of various Ionographic Chambers

	Electrode Material	Sensitive Medium	Exposure Rate(mR/s)	Pressure (atm)	E^* (V/cm)	$j_{sat}/\dot{x}$ ($nA/cm^2/mR/s$)	Sensitivity
(a)	aluminum	air	150	1	12	5×10^{-4}	1
(b)	lead	air	150	1	50	5×10^{-3}	10
(c)[3]	aluminum	xenon	25	10	6000	2	4000

7.4 SATURATION CURRENT DENSITIES IN IONOGRAPHIC CHAMBERS

In the ionographic chamber sensitive volume, the free charge carriers are produced by electrons originating through direct interactions of photons with gas molecules and by photoelectrons produced in the polarizing electrode and backscattered into the chamber sensitive volume. The efficiency ε for photoelectron production defined as the number of backscattered photoelectrons per incident photon [17,18] depends on the photon energy and on the atomic number of the polarizing electrode Z. The range a_r of these photoelectrons in the gas depends on photon energy and on the gas density. Some values for both ε and a_r are available in the literature.[19]

The saturation current density j_{sat} is a very important parameter of an ionographic chamber since it is directly proportional to the chamber sensitivity. It is a function of the x-ray exposure rate $\dot{x}$, air gap thickness a, atomic number of both the polarizing electrode and the gas, as well as of the density of the gas. In Fig. 7.3 we plot the measured j_{sat} vs a for our ionographic chamber with various polarizing electrode materials ranging from aluminum to lead. For a given material, j_{sat} increases linearly with a for large a; for small a, however, the linearity breaks down as discussed in Sec. 5.5. The j_{sat} vs a curve may be separated into two components; a linear function j_{sat}^{air} and an exponential function j_{sat}^{p}, both starting at the origin:

$$j_{sat}(a) = j_{sat}^{air} + j_{sat}^{p}(a) \ . \tag{7.3}$$

The linear function j_{sat}^{air} is the component of j_{sat} produced by the charge carriers originating from electrons released in the chamber

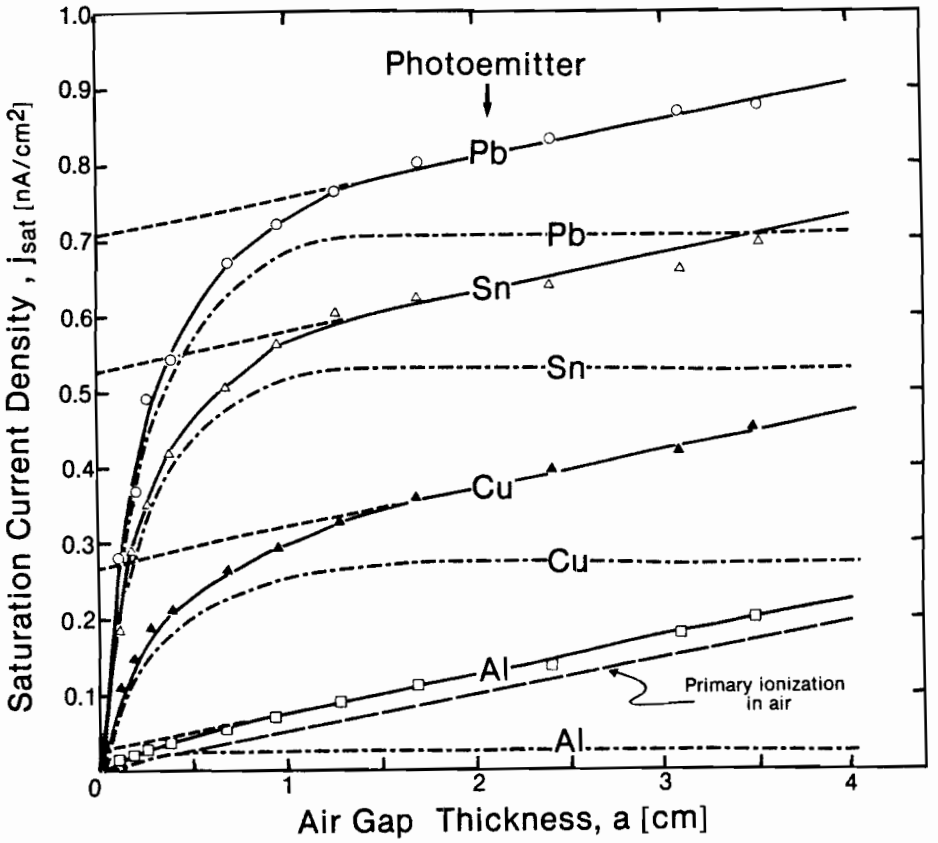

Figure 7.3 Saturation current density j_{sat} as a function of air gap a for various polarizing electrode materials. Exposure rate : 150 mR/s. The dashed line represents the primary ionization in air, the solid curves represent Eq. (7.4), and the dotted curves represent the contribution from the photoelectrons backscattered from electrode (see Sec. 5.5).

sensitive volume by direct interactions of photons with the gas molecules. It is independent of electrode material and linearly dependent upon the air gap a. The exponential component j^{p}_{sat} of j_{sat} represents the contribution of charge carriers produced by photoelectrons backscattered into the chamber sensitive volume from the polarizing electrode. These photoelectrons have a range[17,18] of about 1 cm for our experimental conditions. In Sec. 5.5, we used Eq. (4.12) which was subsequently presented as Eq. (7.2) to derive a general expression for the electret chamber saturation current density [Eq. (5.27)] which held for air at normal pressure. In Sec. 7.3 we showed that Eq. (7.2) holds not only for air-filled ionization chambers at normal pressure but it also represents the saturation curve resulting from polarizing electrode photoemission and from high atomic number pressurized gases. We can thus represent the saturation current density j_{sat} of the ionographic chamber (the ionographic chamber is essentially an electret chamber) as:

$$j_{sat}(a,Z,\rho,Z_g) = \dot{x}\,\{\kappa(\rho,Z_g) + \lambda'(\rho,Z_g)\varepsilon(Z,E_\nu) \times [1 - e^{-3a/a_r(E_\nu,\rho,Z_g)}]\}, \qquad (7.4)$$

where κ, λ', and a_r are functions of the density ρ and atomic number Z_g of the gas, and were given in Sec. 5.5 for normal air pressure; ε, the efficiency for production of backscattered photoelectrons[17,18] and E_ν, the photon energy, were also given in Sec. 5.5 .

7.5 EXTRAPOLATED ELECTRIC FIELD IN IONOGRAPHIC CHAMBERS

The extrapolated electric field E^*, introduced in Eq. (7.2), is a parameter in the saturation curve expression and depends on the configuration of the ionographic chamber, the x-ray exposure rate as well as on the pressure and atomic number of the chamber gas.

In Fig. 7.4 we show a plot of E^* vs a measured in our ionographic chamber for various polarizing electrode materials with an exposure rate of 150 mR/s. We notice that, similarly to the $j_{sat}(a)$ behavior, $E^*(a)$ is linear with a for large a; the linearity breaks down, however, for small a. $E^*(a)$ also has two components, both starting at 0 for $a = 0$; one, $E^*_{air}(a)$, is linear for all a and attributed to primary ionization in air, and the other, $E^*_p(a)$, exhibiting an exponential saturation behavior at approximately 3 a_r, is attributed to the photoemission from the polarizing electrode. The saturation value $E^*_p(\infty)$ is obtained by extrapolating the linear portion of E^* vs a curve to $a = 0$ as shown in Fig. 7.4. In Sec. 5.6 we derived a general expression for the extrapolated electric field E^*. We can apply the arguments discussed above for j_{sat} to E^* and thus express it as:

$$E^*(a,Z,\rho,Z_g) = k'(\rho,Z_g)a\dot{x}^{\frac{1}{2}} + m'(\rho,Z_g)$$

$$\times \varepsilon(Z,E_\nu)\dot{x}\,[1 - e^{-a/a_r(E_\nu,\rho,Z_g)}]\ , \qquad (7.5)$$

where k' and m' which, in general, are functions of the density ρ and atomic number Z_g of the gas were given in Sec. 5.6 for normal air pressure.

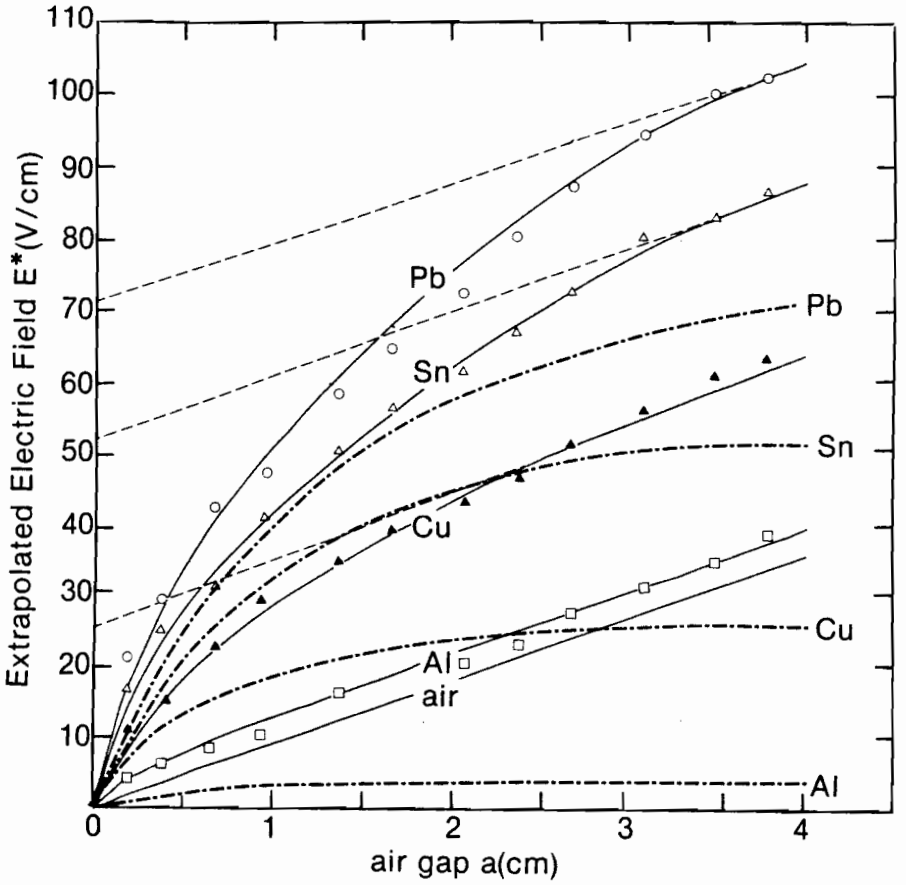

Figure 7.4 Extrapolated electric field E^* as a function of air gap a for various polarizing electrode materials. Exposure rate: 150 mR/s. The solid line represents the primary ionization in air, the solid curves represent Eq. (7.5), and the dotted curves represents the contribution from photoelectrons (see Sec. 5.6).

7.6 MAXIMUM CHARGE DENSITY IN THE LATENT IMAGE

Since the ionographic chamber is basically a parallel-plate ionization chamber we assume that saturation characteristics in both are essentially identical, with one important difference, however; in an ionization chamber the E_{eff} in Eq. (7.2) is constant, while in an ionographic chamber it is decreasing in time as given by Eq. (7.1). The conclusions about j_{sat} and E^* discussed in the previous two sections are thus valid for ionographic chambers as long as the appropriate $E_{eff}(t)$ is used. During the latent image formation in an ionographic chamber with relatively long exposure times (or high exposure rates) the two opposing electric fields, $E_a(0)$ and $E_\sigma(\infty)$, eventually become equal in magnitude, i.e., $E_{eff}(\infty) = 0$ close to the polymer surface. The charge carriers produced by radiation no longer drift in an electric field and therefore recombine, so that no additional charge deposition onto the polymer surface is possible. As shown in Sec. 5.3, by substituting $E_{eff} = 0$ in Eq. (7.1) we get the following relationship for the maximum surface charge density σ_{max}:

$$\sigma_{max} = \sigma(\infty) = \varepsilon_o \varepsilon_p V_o / p = C_e V_o \ , \tag{7.6}$$

but we have found that an equation resembling a Schottky[21] or Poole-Frenkel[22] process of the form:

$$\sigma_{max} = 2\, C_e \nu_B^{\frac{1}{2}} \left[(V_o + \nu_B)^{\frac{1}{2}} - \nu_B^{\frac{1}{2}} \right] \ , \tag{7.7}$$

fits the measured data better.

In Fig. 7.5 we show for two thicknesses of Mylar the maximum surface charge density as a function of voltage V_o applied to the ionographic chamber. The solid curves, which represent Eq. (7.7) with ν_B of 2500 Volts and appropriate C_e, are in excellent agreement with the measured data.

Equation (7.7) thus sets the physical limit on the surface charge distribution forming the latent image. This limit is proportional to the polymer foil dielectric constant ε_p and inversely proportional to the polymer thickness p. Its dependence on V_o is given in general by Eq. (7.7) which, for $V_o \ll \nu_B$, transforms into Eq. (7.6), indicating a linear relationship between σ_{max} and V_o for small V_o. Thus, when sophisticated ionographic chambers with a high charge carrier yield per incident photon are designed, consideration should be given to the charge density limit as given by Eq. (7.7). Moreover, the exposure of the object should be terminated long before the limit in σ_{max} is reached in order to keep the charge density variations in the latent image representative of variations in photon transmissions through different parts of the object. If the exposure is too long, the result will be a foil electret charged uniformly to its maximum value and the latent image will lose all information about the object.

7.7 CURRENT DENSITY DURING LATENT IMAGE PRODUCTION

The current density j that is measured in the external circuit during the irradiation of the object is attributed to charges moving onto the measuring electrode to compensate for the increasing number of oppositely charged carriers trapped on the polymer surface forming the latent image. Assuming that at $t = 0$ the saturation conditions are met in the ionographic chamber, this current density is initially equal to the

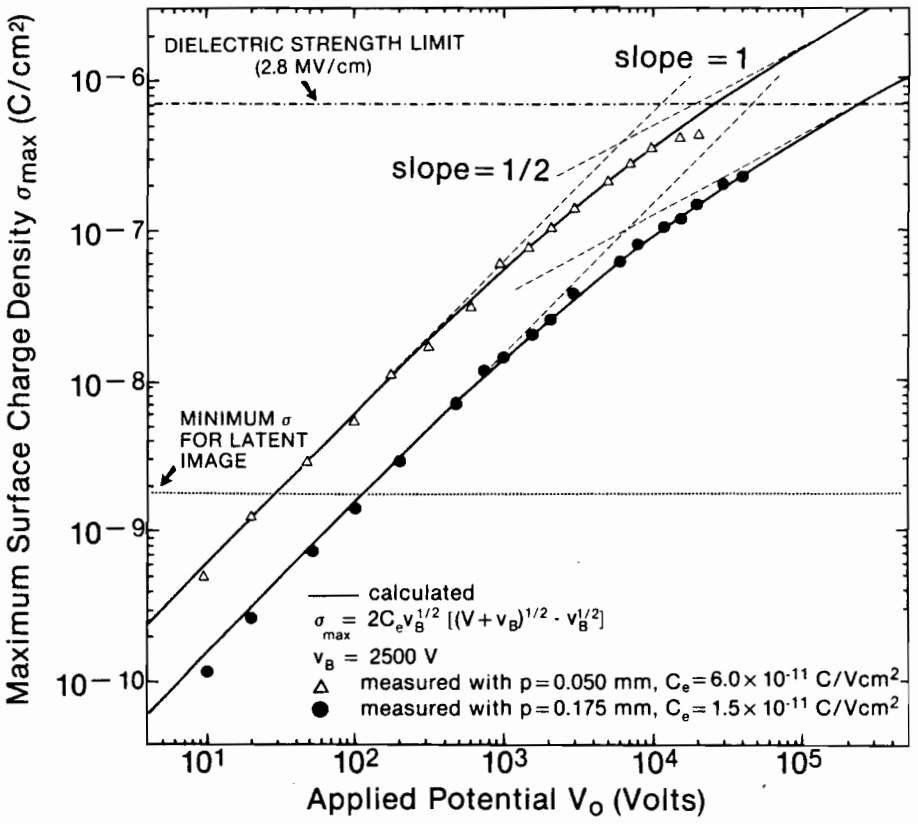

Figure 7.5 Dependence of the maximum surface charge dnesity σ_{max} in the latent image upon the externally applied voltage V_o for two thicknesses of Mylar.

ionization current density which would be measured in a standard ionization chamber under identical conditions. As shown in Eq. (7.1), however, the effective field in the ionographic chamber is steadily decreasing with time as $E_\sigma(t)$ increases, eventually causing non-saturation conditions in the chamber sensitive volume, before becoming equal to zero. As discussed in Sec. 5.4, by combining Eq. (7.1) with Eq. (7.2) and noting that $j = d\sigma/dt$ we get the following relationship for j as a function of time:

$$j = j_{sat} \exp[(t_o - t)/\tau]\{1 + \exp 2(t_o - t)/\tau\}^{-\frac{1}{2}}, \tag{7.8}$$

where τ, the electret relaxation time, is:

$$\tau = \varepsilon_o(a\varepsilon_p + p\varepsilon_a)\, E^*/pj_{sat} \tag{7.9}$$

and t_o, the electret characteristic polarization time, is:

$$t_o = \tau \ln \sinh E_a(0)/E^*. \tag{7.10}$$

In a similar fashion the effective electric field $E_{eff}(t)$ in the ionographic chamber can be written as:

$$E_{eff}(t) = E^* \operatorname{arc\,sinh}[\, e^{(t_o - t)/\tau}\,]\,. \tag{7.11}$$

A typical current density profile as given by Eq. (7.8) is shown schematically in Fig. 7.1 (c). By definition t_o, which is given by Eq. (7.10), is equal to the time in which the current density j reaches a value of $(1/\sqrt{2})j_{sat}$. The area under the $j\ (t)$ curve of course is equal to σ_{max} as given by Eq. (7.7). A typical current density profile obtained

during the discharge of a latent image is shown in Fig. 7.1 (*d*). It is equal in magnitude but opposite in sign to the charging profile given by Eq. (7.8) and shown in Fig. 7.1 (c). The areas under the two profiles are equal , i.e., charge conservation is upheld.

7.8 PRACTICAL ASPECTS OF GAS IONOGRAPHY IMAGING

In the electrostatic imaging the aim is to optimize the image quality by maximizing the charge collected in the latent image on the polymer foil with a minimal exposure to the object. It was shown that a minimum charge density σ_{max} of 10-20 nC/cm^2 is required in the latent image for subsequent successful development with presently known electrographic development techniques. The exposures required to attain these charge densities in air filled ionographic chambers at normal pressure are on the order of Roentgens. As shown in Table 7.1 a considerable improvement in sensitivity can be gained when a high atomic number metal is employed as the polarizing electrode and a high atomic number pressurized gas is used as the radiation sensitive volume.

As discussed above, the potential V_o applied to the ionographic chamber is also an important parameter. To prevent loss of charge carriers to recombination, it has to be sufficiently high to maintain saturation conditions in the chamber during the x-ray exposure of the object. Furthermore, it should be sufficiently high so that during the x-ray exposure the change density in the latent image does not reach the limit σ_{max} as given by Eq. (7.7). As discussed above, this would degrade the latent image eventually resulting in a fully charged uniform foil electret.

We estimate the applied field $E_a(0)$ for given ionographic chamber parameters as follows: the time at a given exposure rate to achieve

σ_{max} in the latent image is: $t_{min} = \sigma_{min}/j_{sat}$, where j_{sat} is the saturation current density. The current density during the exposure will remain equal to j_{sat} until the effective field $E_{eff}(t)$ in the air gap given by Eq. (7.1) falls below $3E^*$, where E^* is the extrapolated electric field introduced in Eq. (7.2).

The electret characteristic polarization time t_o given by Eq. (7.10) can also calculated from Eq. (7.11), substituting $3E^*$ for E_{eff} and t_{min} for t, to get:

$$t_o = 2.3\ \tau + t_{min}\ . \tag{7.12}$$

A substitution of Eq. (7.12) into Eq. (7.10) gives the minimum required external electric field $E_a(0)$, satisfying the above conditions, as:

$$E_a(0) = E^*\ arc\ sinh\ \{\ 10\ exp[\ p\sigma_{min}/\varepsilon_o E^*(a\varepsilon_p + p\varepsilon_a)]\ \}. \tag{7.13}$$

In Fig. 7.6 we show developed images of a bar phantom obtained with our simple ionographic chamber with air gap a of 0.2 cm, and x-ray exposure rate $\dot{x}$ of 150 mR/s and an applied voltage V_o of 900 Volts; (*a*) with a lead polarizing electrode and an exposure time of 37 s, (*b*)same as (*a*) but with opposite polarity, (c) with an aluminum polarizing electrode and an exposure time of 74 s, and (*d*) with a lead polarizing electrode and an exposure time of 15 minutes. The image with the lead polarizing electrode is obviously better than the one with the aluminum electrode, substantiating Eq. (7.4) which shows that the saturation current density in an ionographic chamber strongly depends on the atomic

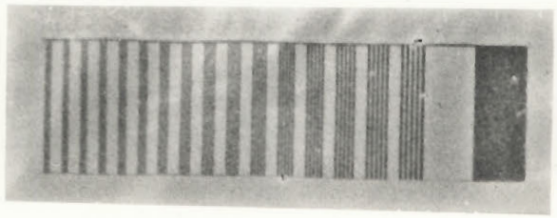

(a)

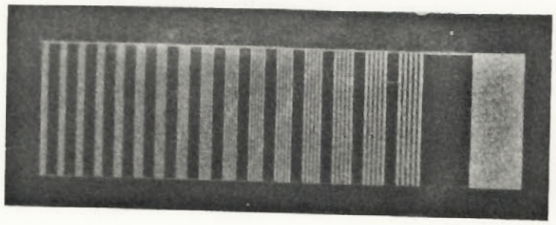

(b)

(c)

(d)

Figure 7.6 Developed latent images of a bar phantom obtained with our ionographic chamber with an air gap a of 0.2 cm, an x-ray exposure rate $\dot{x}$ of 150 mR/s and an applied voltage V_o of 900 Volts: (a) and (b) lead polarizing electrode and exposure time of 37 s, (c) aluminum polarizing electrode and exposure time of 75 s, and (d) lead polarizing electrode and exposure time of 15 minutes.

number of the polarizing electrode. A comparison between Fig. 7.6 (*b*) and 7.6 (*d*) clearly indicates that there is an optimum exposure and that an increase beyond this optimum not only unnecessarily increases the dose to the object; it also degrades the image quality, eventually resulting in a uniform foil electret with the surface charge density determined by Eq. (7.7).

Substituting the values a = 0.2 cm, p = 0.0125 cm, ε_p = 3, and E^* = 21 V/cm (Fig. 7.4) into Eq. (7.13), we calculated a value of 3600 V/cm for the minimum applied field $E_a(0)$ required for optimum charge collection in the chamber to reach a σ_{min} of 15 nC/cm^2 in the latent image shown in Fig. 7.6 (*b*). This corresponds to an applied voltage V_o of 720 Volts; thus the V_o of 900 Volts, that we had used, was above the required minimum. The exposure time t_{min} for the image in Fig. 7.6 (*b*) is calculated as follows: first, the electret characteristic polarization time t_o and the electret relaxation time τ are calculated using a value of 0.4 nA/cm^2 for j_{sat} and 3600 V/cm for $E_a(0)$ in Eqs. (7.9) and (7.10) respectively to get t_o = 37.5 s and τ = 0.22 s. Next, these values are substituted into Eq. (7.12) to yield t_{min} = 37 s, which is the time that was actually used in our experiment to get Fig. 7.6 (*b*).

7.9 CONCLUSION

The charging characteristics of ionographic latent images were discussed in terms of saturation characteristics of ionographic chambers. We showed that the charged latent images on the polymer produced in gas ionography are essentially electrets with surface charged

densities modulated by photon transmission through the object.

The maximum possible surface charge density that can reside on the latent image was calculated and found to depend on the polarizing voltage according to an expression resembling a Schottky or Poole-Frenkel process. It exhibits direct proportionality with the polarizing voltage V_o and then follows a $V^{\frac{1}{2}}$ dependence for voltages greater than the breakpoint voltage. The breakpoint voltage for two thicknesses of Mylar was found to be 2500 Volts.

It has been found that the hyperbolic dependence of chamber ionization current density on the effective electric field in the chamber sensitive volume not only applies for air ionization but also for high atomic number gases at elevated pressures. This dependence is used in conjunction with the laws of Gauss and Kirchoff in the derivation of the equations governing the charging and discharging dynamics of the latent image. It is found that both the saturation current density and the extrapolated electric field consist of a component which is linear with air gap thickness and is produced by primary photon interactions in the chamber sensitive volume, and of another component which exhibits an exponential saturation and is attributed to photoelectrons backscattered from the polarizing electrode into the chamber sensitive volume.

A discussion on the effect of different polarizing electrode materials is given and it is suggested that an order of magnitude increase in sensitivity can be achieved in ionographic chambers by changing the aluminum polarizing electrode to lead.

The minimum applied electric field needed for an optimized charge collection in the ionographic chamber is calculated and given as a function of the extrapolated field. The optimum exposure for the latent

image is also calculated for latent image production and it is shown that exposures below this optimum give insufficient charge densities for electrographic development, while exposures above it will slowly degrade the image and eventually result in a uniform foil electret charged to its maximum theoretical value with no relevance to the object exposed.

We will apply some of the charging and discharging properties of the ionographic latent image presented here to perform radiographic subtraction in subsequent chapters.

7.10 REFERENCES

1 K.H. Reiss, Z. Angew. Phys. 19, 1(1965).

2 H.E. Johns, A. Fenster, D. Plewes, J.W. Boag and P.N. Jeffrey, Brit. J. Rad. 47, 519(1974).

3 A. Fenster, D. Plewes and H.E. Johns, Med. Phys. 1, 1(1974).

4 D. Plewes and H.E. Johns, Med. Phys. 7, 315(1980).

5 B.M. Moores, J.A. Ramsden and D.L. Asbury, Phys. Med. Biol. 25, 893(1980).

6 E.P. Muntz, A. Proudian and P.B. Scott, U.S. Patent Number 3 774 029(1973).

7 A. Proudian, R.L. Carangi, G. Jacobson and E.P. Muntz, Radiology 110, 667(1974).

8 E.P. Muntz, H. Meyers, E. Wilkinson and G. Jacobson, Radiology 125, 517(1977).

9 R.M. Schaffert, in Electrophotography, (Focal, London, 1975), p. 557.

10 B.G. Fallone and E.B. Podgorsak, Phys. Rev. B 27, 2615(1983).

11 B.G. Fallone and E.B. Podgorsak, Phys. Rev. B 27, 5062(1983).

12 B.G. Fallone and E.B. Podgorsak, Phys. Rev. (in press).

13 B.G. Fallone and E.B. Podgorsak, Med. Phys. 10, 191(1983).

14 K.H. Reiss and G. Lange, Phys. Med. Biol., 18, 695(1973).

15 J.W. Boag, R.J. Barish and W.W. Seelentag, Med. Phys. 2, 245(1975).

16 W.W. Seelentag, J.W. Boag and R.J. Barish, Med. Phys. 3, 384(1975).

17 K.W. Dolan, J. Appl. Phys. 46, 2456(1975).

18 C.A. Aeby and G.A. Whan, IEEE, Trans. Nucl. Sci., NS-28, 4177(1981).

19 A.T. Nelms, Nat. Bur. Stand. (U.S.) Circ. 577(1965).

CHAPTER 8

RADIOGRAPHIC IMAGE SUBTRACTION IN GAS IONOGRAPHY

8.1 INTRODUCTION

We will now study the feasibility of radiographic image subtraction based on the ionographic imaging principles we discussed in the previous chapter.

Interest in subtraction radiography has increased in recent years mainly through the advent of digital subtraction angiography[1] which is based on computer manipulation of digitized video images. Presently, all major manufacturers of radiographic equipment are involved in development of digital radiographic subtraction systems. As an alternative to the expensive digital system, we investigated a simple on-line non-computerized method for subtraction radiography using electrostatic imaging techniques.

Various electrophotographic processes have been proposed as alternatives to emulsion film radiography. The best known is xeroradiography[3], which is based on x-ray induced charge cancellation on a pre-polarized photoconductive plate to form an electrostatic latent image of the object. It has gained widespread use in mammography[4] and is commercially available from the Xerox Corporation. Another well known technique is referred to as electroradiography[5,6] or gas ionography[7,10] and employs x-ray photon absorption in air in an electric field to generate free charge carriers which subsequently form the latent electrostatic image of the object. Efficiency is increased by employing a high atomic number polarizing electrode[5,6] and a high atomic number pressurized gas[7,10] as the radiation sensitive medium.

As discussed in Chapter 7, the latent image which is formed on a polymer film in the imaging chamber is essentially a stable foil electret. We have recently performed an extensive study[11,13] (which we have discussed in Chapter 5) of the physical properties of this

radiation-induced electret and will use some of the results to perform electrostatic image subtraction. The latent image (electret) can be discharged with electrographic toners, a technique used to developed the latent electrostatic image,[14] which we have discussed in Sec. 3.7. It can, however, also be discharged by continued irradiation of the chamber with the electrodes at polarities opposite to those used to form the initial latent image. The remaining latent image represents the subtraction of the discharging from the charging process and can subsequently be visualized with standard electrographic toner techniques.

8.2 IMAGE SUBTRACTION IN GAS IONOGRAPHY

The latent ionographic image of an object is obtained by positioning the chamber, shown in Fig. 3.4, behind the object irradiated by x-rays. Because of the low chamber sensitivity, typical exposures to achieve the charge densities required for the latent image development are on the order of 1 R. Thus, our chamber could not be utilized in a clinical environment; it served well, however, in the investigation of the electrostatic image subtraction technique. The air in the chamber sensitive volume is ionized by electrons produced by direct interactions of photons with air molecules and by photoelectrons which are produced by x-rays in the polarizing electrode and backscattered into the chamber sensitive volume. The free charge carriers drift in the effective electric field towards the appropriate electrode. The charges that drift towards the measuring electrode, get trapped on the surface of the polymer thereby forming the latent image of the object which is essentially a stable foil electret with the surface charge distribution modulated by the photon transmission through the object. Both positive and negative latent images can

be produced, depending on the polarity of the external power supply.

Once the latent image has been formed, the discharging process can be initiated by reversing the external field, so that opposite charge carriers to those that formed the latent image, drift towards the polymer and cause depletion of the existing electret charge layer through annihilation. In principle, equal radiation exposures of identical objects for the charging and discharging process in sequence should result first in formation of the latent image and then in its complete cancellation.

The process of charge cancellation in the primary latent image will now be applied to the electrostatic image subtraction. Two exposures, one in the electret charging mode and the other in the electret discharging mode, are performed on two objects which are essentially identical but differ in a certain detail, which is of particular interest. The final latent image represents only the difference in the two objects, as the identical parts of the object are completely cancelled.

Figure 8.1 illustrates the technique with developed ionographic images of a lead wire phantom. Part (*a*) shows the primary (mask) image of the object taken at one polarity and part (c) shows the image, taken with opposite polarity, of the same object with a superposition of the object of interest. In practice part (c) would correspond to an image obtained after contrast medium is injected into the region of interest. This region is not at all visible in part (*a*) and only poorly visible in part (c) because of the extra and redundant information carried in the primary image. In Figs. 8.1 (*d*) - 8.1 (*f*) we show the results of the analog subtraction of image (c) from image (*a*) under various exposure and electric field conditions. The heavy black lines represent the object of interest, while the remnant of the primary image is shown in the

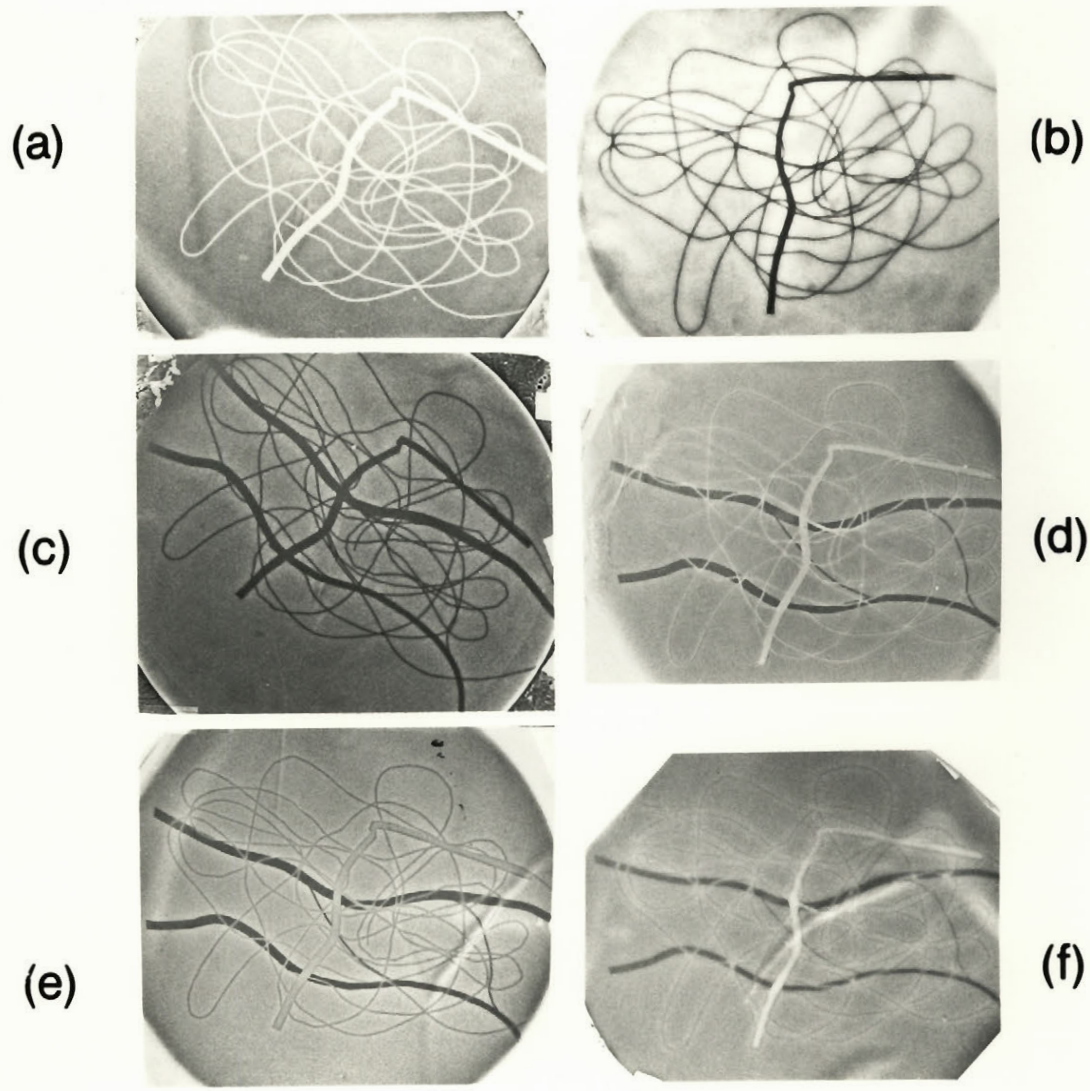

Figure 8.1 Electrostatic image subtraction achieved on a lead-wire phantom with an external potential of 2000 V across a 2 mm air gap and a 0.05 mm thick layer of white polypropylene: (*a*) primary (mask) image at one polarity; (*b*) primary image at polarity opposite to that in (*a*); (*c*) primary image as in (*b*) but with region of interest superimposed; (*d*) - (*f*) results of electrostatic image subtraction of (*c*) from (*a*) for various exposures, with the dark lines representing the region of interest.

background, indicating that the process of image subtraction worked, but was not fully successful. Image (*e*) was obtained with equal first and second exposures and opposite polarities, image (*d*) with about 20% lower second exposure than the first, and opposite polarities, and image (*f*) with equal first and second exposures but shorted electrodes during the second exposure. In the latter example, the latent image following the first exposure provides the effective electric field in the chamber during the second exposure. The two hairlines connecting the thicker lead wires in the object of interest are clearly visible in all subtracted images, while they were not at all distinguishable from the primary image in part (*c*). Figure 8.1 (*b*) represents the primary image taken with opposite polarity from image in Fig. 8.1 (*a*).

The consecutive irradiation of almost identical objects with similar exposures but at opposite ionographic chamber polarities thus results in a latent image which accentuates the minor difference between the two objects and at least partially cancels the identical part in both of them.

8.3 CONCLUSION

An analog radiographic image subtraction technique, based on electrostatic charging and discharging of latent images is presented. The object is exposed twice: the first exposure is taken at one chamber polarity and yields the primary (mask) latent image, and the second exposure is taken with opposite polarity after a contrast medium has been injected into the region of interest. The resulting latent image is subsequently developed with standard electrographic toner techniques and represents the object of

interest. Instead of an injection of a contrast medium preceeding the second exposure, one can envisage taking the two exposures at different kVp chosen so as to accentuate the photon absorption in the region of interest.

Electrostatic imaging has been investigated during the last two decades as a possible replacement for film radiography, so far without much commercial success, mainly because of its relatively low sensitivity compared to modern screen-film combinations. Electrostatic image subtraction, however, with consecutive latent image charging and discharging simply cannot be directly challenged by film. We believe that Fig. 8.1 clearly demonstrates the feasibility of radiographic image subtraction utilizing analog electrostatic techniques.

8.4 REFERENCES

1 Digital Radiography : A Focus on Clinical Utility, edited by R.R. Price, F.D. Rollo, W.G. Monahan and A.E. James (Grune and Stratton, New York, 1982).

2 L.A. Couvillon Jr. and L.M. Brenkus, Diagnostic Imaging 4, 3(1982).

3 J.W. Boag, Phys. Med. Biol. 8, 3(1973).

4 J.N. Wolfe, Xeroradiography of the Breast, (C.C. Thomas, Springfield, 1972).

5 K.H. Reiss, Z. Angew, Phys. 19, 1(1965).

6 K.H. Reiss and G. Lange, Phys. Med. Biol., 18, 695(1973).

7 E.P. Muntz, A. Proudian and P.B. Scott, U.S. Patent No. 3 774 029(1973).

8 E.P. Muntz, H. Meyers, E. Wilkinson and G. Jacobson, Radiology 125, 517(1977).

9 H.E. Johns, A. Fenster, D. Plewes, J.W. Boag and P.N. Jeffrey, Brit. J. Radiol. 47, 519(1974).

10 D. Plewes and H.E. Johns, Med. Phys. 7, 315(1980).

11 B.G. Fallone and E.B. Podgorsak, Med. Phys. 10, 191(1983).

12 B.G. Fallone and E.B. Podgorsak, Phys. Rev. B 27, 2615(1983).

13 B.G. Fallone and E.B. Podgorsak, Phys. Rev. B 27, 5062(1983).

14 R.M. Schaffert in Electrophotography, (Focal Press, London, 1975), p. 557.

CHAPTER 9

IMAGE SUBTRACTION BY SOLID STATE ELECTRORADIOGRAPHY

9.1 INTRODUCTION

In the previous chapter, we presented an analog radiographic image subtraction technique based on electrostatic charging and discharging of ionographic latent images.[1] These latent images as previously discussed, are essentially foil electrets with surface charge densities modulated by the x-ray transmission through the object. The object is exposed twice: the first exposure is taken at one chamber polarity and yields the primary (mask) latent image, and the second exposure is taken with opposite polarity after a contrast medium has been injected into the region of interest. The resulting latent image is subsequently developed with standard electrographic toner techniques[2] and represents the region of interest.

The feasibility of electrostatic image subtraction with gas ionography has thus been clearly shown; the problem, however, is the relatively low sensitivity of ionographic chambers. Only when pressurized high atomic number gases are used as the radiation sensitive medium one achieves sensitivities comparable to those of modern screen-film combinations. Engineering difficulties, however, make the high pressure ionographic equipment impractical and cumbersome to use, and attempts have been made to improve the charge yield per incident photon by employing liquids,[3] high purity ionic solids[4] or photoconductors[5,6] as the radiation sensitive medium. Of these, electrostatic chambers utilizing photoconductors have the largest sensitivities which are, however, still an order of magnitude below the sensitivity of modern screen-film combinations.

Photoconductors have been used to produce latent images either

in the charge accumulation mode or in the charge cancellation mode. The configuration of the former mode resembles the standard gas ionography technique with the photoconductor-dielectric foil combination placed into an electric field during the irradiation of the object.[5] In the latter configuration, a uniform charge layer on the photoconductor is locally discharged by charge carriers produced during the irradiation of the object. This technique, referred to as xeroradiography, has gained wide-spread use in mammography[6] and is commercially available from the Xerox corporation.

In this chapter, we describe an analog radiographic image subtraction technique in an imaging chamber utilizing a selenium photoconductor as the radiation sensitive medium. The technique first employs the charge accumulation mode to produce the primary (mask) latent image. After the contrast medium is injected into the region of interest, the charge cancellation mode is applied to subtract, electrostatically, the identical parts of the object, with the resulting latent image representing the region of interest.

9.2 SOLID STATE ELECTRORADIOGRAPHIC SUBTRACTION

The electrostatic imaging cassette utilizing a photoconductor as the radiation sensitive medium is shown schematically in Fig. 3.5. As discussed in Sec. 3.6, a rough vacuum is used to press the dielectric paper uniformly over the photoconductor. This is especially important in image subtraction studies when the polarity of electrodes is changed between the two x-ray exposures of the object.

The latent electrostatic image of an object is obtained by

positioning the cassette behind the object irradiated by x-rays. In the charge accumulation mode the charge carriers (electrons and holes) produced by photon interactions in the photoconductor drift in the externally applied electric field towards the appropriate electrode. The charges that drift towards the dielectric get trapped on the photoconductor-dielectric interface thereby forming a latent image, which as previously discussed, is essentially an electret with the surface charge density modulated by the photon transmission through the object. Both positive and negative latent images can be produced depending on the polarity of the external power supply. The latent image charges are subsequently transferred onto the dielectric through Paschen discharge and then made visible with standard electrophotographic toner techniques.[2] (See Secs. 3.6 and 3.7). The minimum charge density of about 15 nC/cm^2 required for subsequent electrographic toner visualization is achieved with exposures of ~50 mR.

In Fig. 9.1, we show some images of high resolution bar phantoms taken with this technique. A resolution of at least 150 line pairs/inch can be perceived with exposures of 80-100 mR.

The latent image can also be discharged without removing the paper from the photoconductor, through a charge cancellation mode. The electrodes are connected to an external voltage with polarities opposite to those in the first exposure. During the discharging process the electric field points in such a direction that charge carriers opposite to those, that formed the latent image in the charge accumulation mode, drift towards the dielectric and cause the depletion of the existing latent image charge layer through annihilation.

Thus, if the second exposure (discharging process) is taken

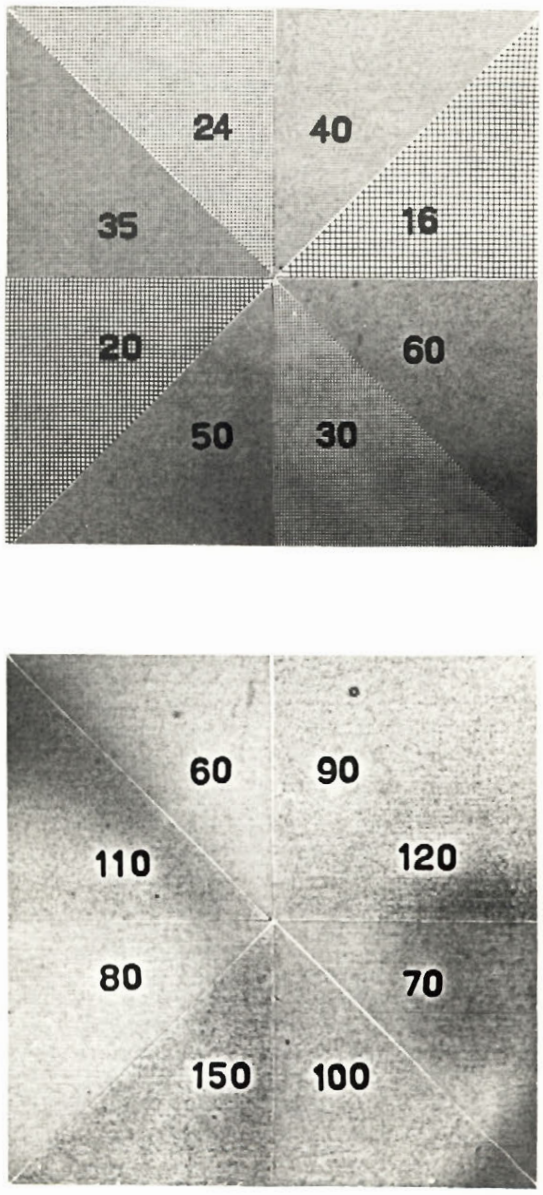

Figure 9.1 Images taken with the solid state electrostatic cassette shown in Fig. 3.5 of bar phantoms with spatial resolution of up to (*a*) 60 line pairs/inch and (*b*) 150 line pairs/inch, with a chamber voltage of 1500 Volts.

either after a contrast medium is injected into the region of interest or with an x-ray beam of different quality, the resultant latent image represents the region of interest alone. A successive application of the charge accumulation mode at one chamber polarity and the charge cancellation mode at an opposite polarity is thus used to perform radiographic image subtraction to enchance the region of interest.

A knowledge of the relative electron and hole mobilities in the photoconductor and the amount of charge accumulated in the original exposure will determine the cancellation exposure required to annihilate the original charged latent image. Information in literature on electron and hole drift mobilities and lifetimes is rather scarce and inconsistent. The easiest method to determine the cancellation exposure is with several trial runs till the optimum subtraction is achieved.

The electrostatic subtraction technique achieved with the chamber shown in Fig. 3.5 is illustrated in Fig. 9.2 with various images of a lead wire phantom. Part (*a*) shows separately an image of the region of interest we wish to enchance by the subtraction procedure. Part (*b*) shows the primary (mask) image of the object obtained with a particular chamber polarity, and part (*c*) shows the image of the region of interest superimposed on the same object but taken with a chamber polarity opposite to that of part (*b*). Part (c) corresponds to an image obtained after contrast medium is injected into the region of interest. It is obvious that the region of interest Fig. 9.2 (*a*) is barely distinguishable from the primary image in Fig. 9.2 (c). Results of an analog electrostatic subtraction of image (c) from image (*b*) are shown in Fig. 9.2 (*d*). As discussed above, the subtraction is achieved by two successive exposures: the first to obtain the latent image (*b*) at a given polarity, and the

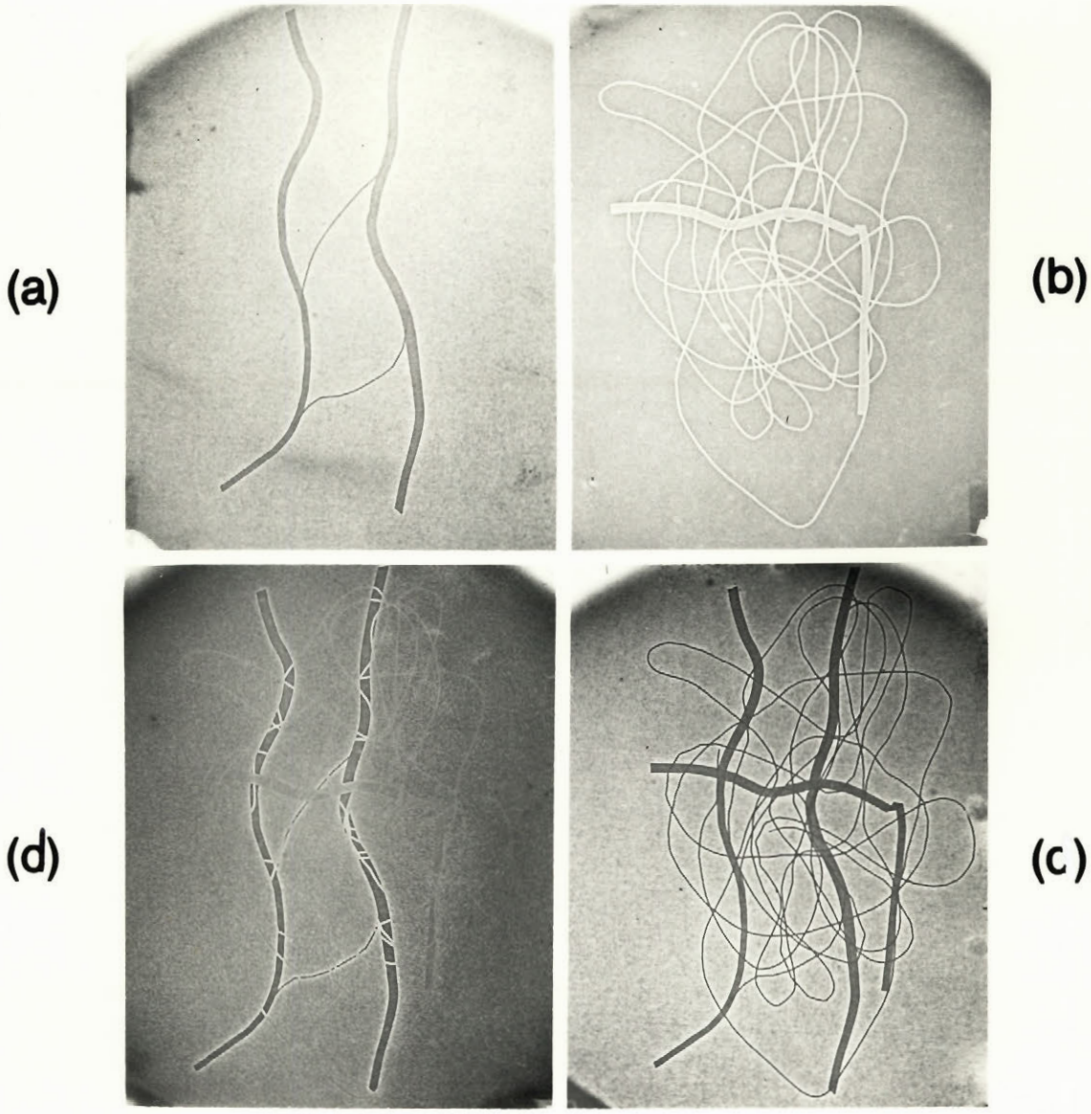

Figure 9.2 Electrostatic image subtraction achieved on a lead-wire phantom with a chamber voltage of 1500 volts: (*a*) image of the region of interest, (*b*) primary (mask) image of the object at a given polarity, (c) image of the object with the region of interest superimposed, taken at polarity opposite to that in (*b*), and (*d*) result of electrostatic subtraction of image (c) from image (*b*), representing the region of interest.

second to add to the latent image (c) with an opposite polarity. The identical parts of latent image (*b*) and (c) cancel out, and only the region of interest remains clearly visible as shown in Fig. 9.2 (*d*), where the heavy black lines represent the object of interest. The two hairlines connecting the thicker lead wires in the object of interest are now clearly visible while they were not at all distinguishable from the primary image in Fig. 9.2 (c).

To compare the electrostatic analog technique with computerized digital methods, we performed the same subtraction experiment on a commercially available digital angiography unit.[7] Results are shown in Fig. 9.3, where parts (*a*) and (*b*) represent the digital and electrostatic method, respectively. Both images show a remnant of the primary image in the background indicating that the subtraction process has not been perfectly successful. In the electrostatic image, which as shown in Fig. 9.3, has a lower background than the digital one, this remnant may be attributed to edge enhancement processes[8] in the latent image. Since our lead wire phantom does not represent a good approximation to a clinical situation, because of a very drastic difference in density and atomic number of lead vs air, we conclude that the background in a clinical situation would be much less noticeable.

Another example of this electrostatic analog subtraction technique is shown in Fig. 9.4. Part (*a*) shows the mask image taken at one polarity. In part (*b*) we show the object with a contrast medium at its centre taken with opposite polarity. When the two exposures are taken successively the result is a latent image shown in part (c) representing the addition of images (*a*) and (*b*). A circular bar pattern overwhich the contrast medium had placed to prevent photon transmission during

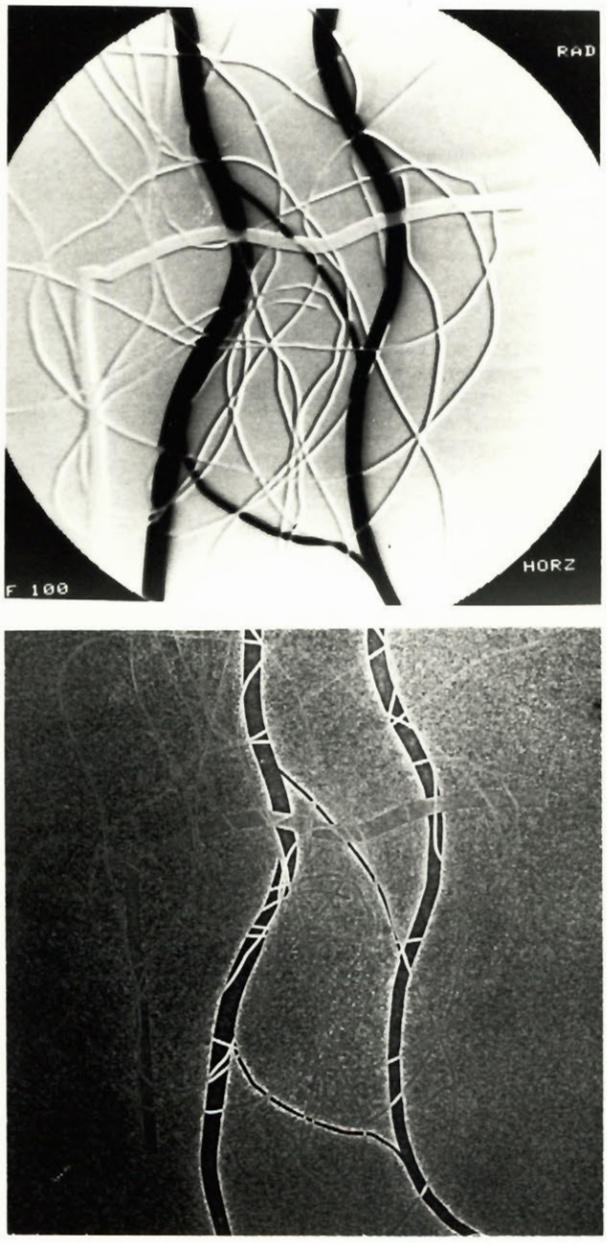

Figure 9.3 Radiographic image subtraction on a lead wire phantom: (*a*) with computerized digital techniques, and (*b*) with electrostatic analog techniques.

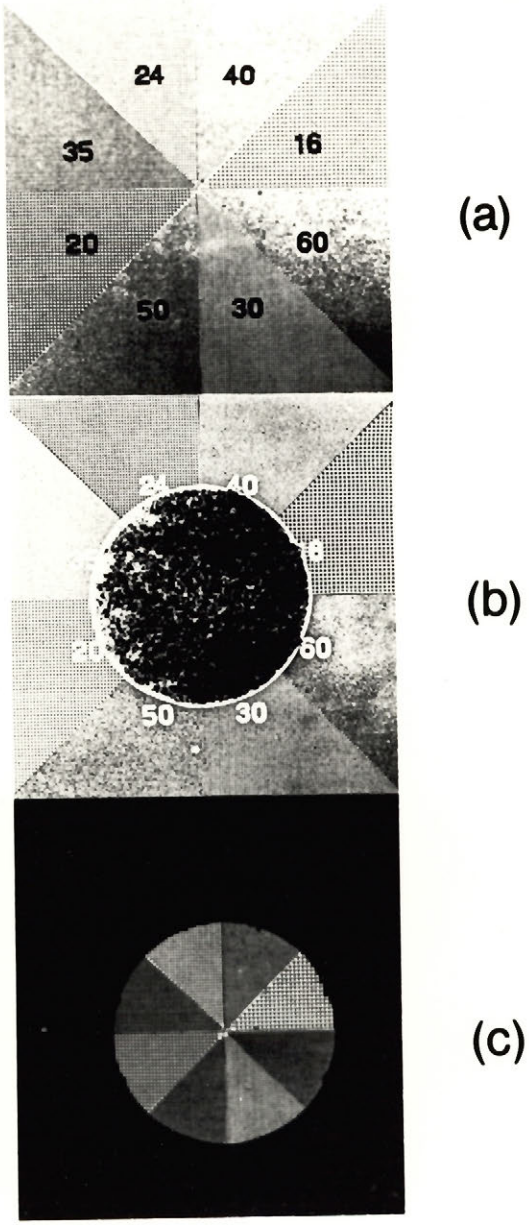

Figure 9.4 Electrostatic image subtraction achieved on a bar phantom with a chamber voltage of 1500 Volts: (*a*) mask image of the bar phantom at a given polarity, (*b*) image of the bar phantom with a circular medium at its centre, and (*c*) result of electrostatic subtraction of image (*b*) from (*a*) representing the circular region of interest.

the second exposure remains. The rest of the bar phantom cannot be visualized since the latent image representing it was charged during the first exposure and completely discharged during the second one.

Although motion artifacts may be a problem in the electrostatic subtraction technique it does offer a possible simple high quality imaging alternative to other types of subtraction radiography techniques.

9.3 CONCLUSION

An analog radiographic image subtraction technique, based on electrostatic charging and discharging of latent images, is presented. A selenium photoconductor is used as the radiation sensitive medium. The object is exposed twice: the first exposure is taken at one chamber polarity and yields the primary (mask) latent image, and the second exposure is taken with opposite polarity after a contrast medium has been injected into the region of interest. The resulting latent image is subsequently developed with standard electrographic toner techniques and represents the region of interest. A comparison with digital subtraction methods shows that the electrostatic technique gives a similar image quality, clearly demonstrating the feasibility of the radiographic image subtraction utilizing analog electrostatic techniques.

9.4 REFERENCES

1 B.G. Fallone and E.B. Podgorsak (unpublished)

2 R.M. Schaffert, in Electrophotography, (Focal, London, 1975) p. 557.

3 A. Fenster and H.E. Johns, Med. Phys. 1, 262(1974).

4 L.A. DeWerd and P.R. Moran, Med. Phys. 5, 23(1978).

5 I. Brodie, R.A. Gutcheck and J.B. Mooney, Proc. SPIE Appl. Opt. Instrum. Med. V, 233, 65(1980).

6 J.W. Boag, Phys. Med. Biol. 18, 3(1973).

7 DF100, Diasonics Inc.,Milpitas, California.

8 D. Plewes and H.E. Johns, Med. Phys. 7, 315(1980).

CHAPTER 10

CONCLUSION

10.1 SUMMARY

Charge transport in the production of ionographic latent image was discussed in terms of saturation characteristics of ionographic chambers. The charged latent image in gas ionography and solid state electroradiography was shown to be an electret with a surface charge density modulated by the photon transmission through the object.

The study of the polarization and depolarization phenomena of the radiation-induced foil electret and of the ionographic latent image, required an accurate knowledge of the full saturation curve of a parallel-plate ionization chamber. Since presently available analytical expressions are suitable only for the near saturation region, a new empirical expression which has the form: $\eta = \tanh(E/E^*)$ and describes the whole saturation curve, has been developed. The extrapolated field E^* is the value of the electric field E at which the extrapolated initial slope of the saturation curve intersects the collection efficiency value η of unity. E^* is independent of the photon beam energy but is a function of both exposure rate and the air gap thickness of the chamber. It can also be calculated numerically or graphically from a single current density j measurement for a given electric field and air gap thickness. In contrast to the currently known expressions which hold only in the near saturation region, the hyperbolic tangent relationship between η and E is in excellent agreement with measurements in the whole collection efficiency range from 0 to 1 for x-ray sources with effective energies from 20 keV to 150 keV and cobalt-60 gamma rays.

The standard parallel-plate ionization chamber used in radiation dosimetry can be transformed into a chamber that produces electrets

or ionographic latent images by blocking the collecting electrode with a thin polymer film. This new isothermal technique for producing stable foil electrets offers certain advantages over the other presently known electret production methods. Some of these advantages are simplicity, uniformity of charge deposition and excellent control of the exact surface charge density produced in the foil.

The dynamics of the charging and discharging of the electret was studied and an excellent agreement obtained between the measured and theoretical polarization and depolarization current density profiles and surface charge densities. The theoretical calculation was based on the hyperbolic relationship between current density and the effective electric field in a standard parallel-plate ionization chamber, discussed above, with the collecting electrode blocked by a polymer progressively acquiring a surface charge. It was shown that the maximum electret surface charge density depends upon the polarizing voltage according to an expression resembling a Schottky or Poole-Frenkel process, first exhibiting direct proportionality with the polarizing voltage V and then following a $V^{\frac{1}{2}}$ dependence for voltages greater than the breakpoint voltage (2500 V for Mylar). Electret surface charge densities close to $10^{-6}C/cm^2$ were attained with an applied potential of a few kV and a typical dielectric foil thickness of 100 μm. The characteristic electret polarization or depolarization time depends on the externally applied field, on the x-ray exposure rate and on electret chamber parameters, such as polymer and air gap thickness, polarizing electrode material, etc., The influence of these parameters on the chamber saturation current density and on the extrapolated electric field was discussed in detail. Both the saturation current density and extrapolated field consist of two

components. One, which is linear with the air gap thickness,is produced by primary photon interactions in the chamber sensitive air volume. The other, exhibiting an exponential saturation, is attributed to photoelectrons backscattered from the polarizing electrode into the chamber sensitive volume.

The theoretical calculations expressing the dynamics of the radiation induced foil electret discussed above utilized Gauss' law to approximate the effective electric field in the electret chamber. Since this law describes the field only at the polymer-air interface, a more detailed calculation of the electrostatic field and potential at any point inside the chamber was presented. Essentially, the theory of linear optical systems was used to solve the Laplace's equation in frequency space through a two dimensional Fourier transform. In this calculation, the electric field was related through the transfer function to a two dimensional delta point charge on the surface of the polymer. To perform the inverse Fourier transform and thus calculate the solution of the Laplace's equation in distance space, the transfer function was simplified by a condition that the air gap separating the electret from the polarizing electrode in the chamber is much larger than the thickness of the polymer. The limitations of the approximation were examined, the general solutions for the near, intermediate and far regions given, and the domain of convergence for off-axis solutions was discussed. The potential calculated on the chamber axis near the electret surface was found to equal the potential obtained from Gauss' law. With polarizing electrode removed, the axial solutions for large distances from the electret surface were equal to those calculated from a dipole layer model of the electret.

The practical calculations describing the charging and discharging characteristics of the ionographic latent images, which are foil electrets with a surface charge distribution proportional to the x-ray photons transmitted through the object, were derived from Gauss' law rather than from the solutions to Laplace's equation discussed above. The derivation was thus much simpler, yet the results still agreed extremely well with the measured charging and discharging properties of the electret and the ionographic latent image. It was also shown that the hyperbolic dependence of chamber ionization current density on the effective electric field in the chamber sensitive volume not only applied for air ionization but also for high atomic number Z_g gases at elevated pressures. Thus the theoretical calculations describing the charging and discharging characteristics of the ionographic latent image when air is the radiation sensitive medium in the chamber, are directly applicable to any gas ionographic chamber where a high Z_g gas at elevated pressures is used. A discussion of the effect of different polarizing electrode materials upon the ionographic latent image was given and it was shown that up to an order of magnitude increase in sensitivity can be achieved in ionographic chambers by changing the aluminum polarizing electrode to lead. It was also shown that exposures greater than those required for optimum visualization by electrographic development degrade the image. The result of very high exposures is an ionographic latent image with a uniform surface charge distribution.

The feasibility of radiographic image subtraction based on the charging and discharging properties of the ionographic latent image was demonstrated. Firstly, latent image charging at one polarity corresponds to the production of the primary image. Secondly, latent image

discharging was achieved with an opposite chamber polarity, so that opposite charge carriers to those that formed the primary latent image drifted towards the polymer and caused cancellation of identical parts of the image to create the final latent image representing the region of interest.

In gas ionography, only when high Z_g gases at elevated pressures are used as the radiation sensitive medium does one achieve sensitivities that are comparable to screen-film combinations. Engineering difficulties, however, make such ionographic equipment cumbersome and expensive. The much simpler method of utilizing a commercially available selenium photoconductor as the radiation sensitive medium was presented. Although, sensitivity of this system is still about an order of magnitude below that of screen-film combinations, image subtraction, as discussed for gas iongraphy, can also be achieved with this system. The image quality of the final subtracted image was compared to that resulting from digital subtractions techniques and was considered excellent. Although, motion artifacts cannot be corrected in the two analog electrostatic radiographic techniques given above, the techniques represent simple alternatives to other subtraction radiography methods.

10.2 SUGGESTIONS FOR FUTURE WORK

The hyperbolic expression presented to describe the full saturation curve fits the experimental data very well for parallel-plate ionization chambers. However, the fitting of the data measured with cylindrical ionization chambers to this expression should be investigated since this would be of considerable interest to radiation

dosimetry. The saturation curves from particles (e.g., electrons, alphas) and from pulsed x-ray beams should also be measured and fitted to the expression.

Although the charging and discharging dynamics of the radiation induced foil electret was well explained,we did find slight discrepancies between calculated and measured data for very high externally applied fields. Most probably, there is a stronger penetration of charge carriers into the polymer at these fields and the effect could be accounted for to further refine the theory.

There are some interesting applications of the radiation induced foil electret presented in the thesis. An important one is the use of this electret as a long term radiation monitoring device or ion collecting device around high voltage lines. Once charged, the electret would lose its charge only if the sensitive air volume under the electric field produced by the electret is under irradiation. The electret would be read by a complete discharge in the manner discussed in Chapter 5. The ratio of the charge measured before and after the monitoring activity is proportional to the amount of exposure received or amount of ions received.

The calculation presented in Chapter 6 solved the Laplace's equation. The next step would be to introduce mobile charge carriers into the air gap and solve the Poisson's equation instead.

An attempt could be made to improve the sensitivity of the solid state electrostatic cassette. An option would be to change the aluminium substrate to lead so that a greater number of radiation induced photoelectrons are backscattered in the selenium layer thus producing a greater number of charge carriers. The sensitive medium

could be changed to a higher atomic number photoconductor, e.g., $CdTe$. Research into the digitization of the charged latent image and subsequent computer image analysis would be an exiting medical physics study.

APPENDIX

A set of computer listings to calculate Eqs. (6.37) and (6.38) are given in the following pages. Programs CALP and CALPO calculate Eq. (6.37), while CALCU and CALCO calculate Eq. (6.38) for the grounded electrode at a finite distance a and at infinity, respectively.

```
      PROGRAM CALP
      REAL*8 C,N1(105),N2(105)
      REAL*8 SM,SF,ST,S(33),S2,S4,FAC(33)
      DATA R/.1/
C  CALCULATION OF THE POTENTIAL WITH THE GROUNDED
C  ELECTRODE AT A DISTANCE A
      WRITE(5,108)
108   FORMAT(' UNIT 5=TT,6=LP ')
      READ(5,109)IU
109   FORMAT(I1)
1     FORMAT(F5.1)
2     FORMAT(E11.4)
101   FORMAT(' Y= ')
102   FORMAT(' SMALL R = ')
200   FORMAT(' P (CM) = ')
201   FORMAT(E11.4)
      FAC(1)=1
      DO 1000 I=2,33
1000  FAC(I)=FAC(I-1)*I
      S(1)=3.
      DO 4000 N=2,33
4000  S(N)=S(N-1)*(2.*N+1.)*(2.*N)/(N*(N+1.))
2000  WRITE(5,102)
      READ(5,1)R1
      WRITE(5,555)
555   FORMAT(' R=',E14.5)
      READ(5,256)R
256   FORMAT(E14.5)
      WRITE(5,101)
      READ(5,2)Y
      WRITE(5,110)
110   FORMAT(' AIR GAP = ')
      READ(5,2)A
      C=.5*R**2/(3.*8.85E-14)
      Z=(R1/R)**2
      Y1=1./(Y+2.*A)**2
      Y3=1./Y**2
      S1=-(R**2/(4.*(Y+2.*A)**2))
      S3=-(R**2/(4.*Y**2))
      ST=(Y3-Y1)*C
      WRITE(IU,2222)R
2222  FORMAT(' R=',E14.5)
      WRITE(IU,223)A,Y,R1,P
223   FORMAT(' AIR GAP(C)=',F5.1,'Y=',E11.4,'SM R=',F5.1,'P=',E11.4)
      WRITE(IU,222)ST
222   FORMAT(' M=0',5X,' ST (V/CM) = ',E14.5)
      WRITE(IU,565)Y3
565   FORMAT(' 1/Y**2 = ',E15.6)
      M=1
5     N1(1)=-1.*M
      N2(1)=-1.*M-1.
      SF=1.+N1(1)*N2(1)*Z
      IF(M.EQ.1)GO TO 11
      DO 10 N=2,M
      N1(N)=(-M+N-1)*N1(N-1)
      N2(N)=(-M-2+N)*N2(N-1)
10    SF=SF+(((N1(N)/FAC(N))*N2(N))/FAC(N))*Z**N
11    S2=S1**M*Y1
      SP=S3**M
      S4=SP*Y3
      SM=S(M)*SF*(S4-S2)*C
      ST=ST+SM
      SS=SP*S(M)
      WRITE(IU,22)M,SS,SF,ST
      M=M+1
      IF(M.GE.31) GO TO 2000
      GO TO 5
22    FORMAT(' M=',I3,3X,' SS=',E15.5,' SF=',E14.5,' ST=',E14.5)
20    STOP
      END
```

```
      PROGRAM CALP0
      REAL*8 C,N1(105),N2(105)
      REAL*8 SM,SF,ST,S(33),S2,S4,FAC(33)
      DATA R/1./
C  CALCULATION OF THE POTNETIAL WITH THE GROUNDED
C  ELECTRODE AT INFINITY
      WRITE(5,108)
108   FORMAT(' UNIT 5=TT,6=LP ')
      READ(5,109)IU
109   FORMAT(I1)
1     FORMAT(F5.1)
2     FORMAT(E11.4)
101   FORMAT(' Y= ')
102   FORMAT(' SMALL R = ')
200   FORMAT(' P (CM) = ')
201   FORMAT(E11.4)
      FAC(1)=1
      DO 1000 I=2,33
1000  FAC(I)=FAC(I-1)*I
      S(1)=3.
      DO 4000 N=2,33
4000  S(N)=S(N-1)*(2.*N+1.)*(2.*N)/(N*(N+1.))
2000  WRITE(5,102)
      READ(5,1)R1
      WRITE(5,555)
555   FORMAT(' R=')
      READ(5,256)R
256   FORMAT(E14.5)
      WRITE(5,101)
      READ(5,2)Y
      C=.5*R**2/(3.*8.85E-14)
      Z=(R1/R)**2
      Y1=0.
      Y3=1./Y**2
      S1=0.
      S3=-(R**2/(4.*Y**2))
      ST=(Y3-Y1)*C
      WRITE(IU,223)A,Y,R1,P
223   FORMAT(' AIR GAP(C)=',F5.1,'Y=',E11.4,'SM R=',F5.1,'P=',E11.4)
      WRITE(IU,222)ST
222   FORMAT(' M=0',5X,' ST (V/CM) = ',E14.5)
      YY3=Y3*C
      WRITE(IU,565)YY3
565   FORMAT(' 1/Y**2 = ',E15.6)
      M=1
5     N1(1)=-1.*M
      N2(1)=-1.*M-1.
      SF=1.+N1(1)*N2(1)*Z
      IF(M.EQ.1)GO TO 11
      DO 10 N=2,M
      N1(N)=(-M+N-1)*N1(N-1)
      N2(N)=(-M-2+N)*N2(N-1)
10    SF=SF+(((N1(N)/FAC(N))*N2(N))/FAC(N))*Z**N
11    S2=S1**M*Y1
      SP=S3**M
      S4=SP*Y3
      SM=S(M)*SF*(S4-S2)*C
      ST=ST+SM
      SS=SP*S(M)
      WRITE(IU,22)M,SS,SF,ST
      M=M+1
      IF(M.GE.31) GO TO 2000
      GO TO 5
22    FORMAT(' M=',I3,3X,' SS=',E15.5,' SF=',E14.5,' ST=',E14.5)
20    STOP
      END
```

```
      PROGRAM CALCU
      REAL*8 C,N1(105),N2(105)
      REAL*8 SM,SF,ST,S(33),S2,S4,FAC(33)
      DATA R/.1/
C CALCULATION OF THE FIELD WITH THE GROUNDED
C  ELECTRODE AT A DISTANCE A
      WRITE(5,108)
108   FORMAT(' UNIT 5=TT,6=LP ')
      READ(5,109)IU
109   FORMAT(I1)
1     FORMAT(F5.1)
2     FORMAT(E11.4)
101   FORMAT(' Y= ')
102   FORMAT(' SMALL R = ')
200   FORMAT(' P (CM) = ')
201   FORMAT(E11.4)
      FAC(1)=1
      DO 1000 I=2,33
1000  FAC(I)=FAC(I-1)*I
      S(1)=12.
      DO 4000 N=2,33
4000  S(N)=S(N-1)*(2*N+2)*(2*N+1)/(N*(N+1))
2000  WRITE(5,102)
      READ(5,1)R1
      WRITE(5,555)
555   FORMAT(' R=',E14.5)
      READ(5,256)R
256   FORMAT(E14.5)
      WRITE(5,101)
      READ(5,2)Y
      WRITE(5,110)
110   FORMAT(' AIR GAP = ')
      READ(5,2)A
      C=.5*R**2/(3.*8.85E-14)
      C=-C
      Z=(R1/R)**2
      Y1=1./(Y+2*A)**3
      Y3=1./Y**3
      S1=-(R**2/(4.*(Y+2.*A)**2))
      S3=-(R**2/(4.*Y**2))
      ST=(Y3-Y1)*C*2.
      WRITE(IU,2222)R
2222  FORMAT(' R=',E14.5)
      WRITE(IU,223)A,Y,R1,P
223   FORMAT(' AIR GAP(C)=',F5.1,'Y=',E11.4,'SM R=',F5.1,'P=',E11.4)
      WRITE(IU,222)ST
222   FORMAT(' M=0',5X,' ST (V/CM) = ',E14.5)
      WRITE(IU,565)Y3
565   FORMAT(' 1/Y**2 = ',E15.6)
      M=1
5     N1(1)=-1.*M
      N2(1)=-1.*M-1.
      SF=1.+N1(1)*N2(1)*Z
      IF(M.EQ.1)GO TO 11
      DO 10 N=2,M
      N1(N)=(-M+N-1)*N1(N-1)
      N2(N)=(-M-2+N)*N2(N-1)
10.   SF=SF+(((N1(N)/FAC(N))*N2(N))/FAC(N))*Z**N
11    S2=S1**M*Y1
      SP=S3**M
      S4=SP*Y3
      SM=S(M)*SF*(S4-S2)*C
      ST=ST+SM
      SS=SP*S(M)
      WRITE(IU,22)M,SS,SF,ST
      M=M+1
      IF(M.GE.31) GO TO 2000
      GO TO 5
22    FORMAT(' M=',I3,3X,' SS=',E15.5,' SF=',E14.5,' ST=',E14.5)
20    STOP
      END
```

```
      PROGRAM CALC0
      REAL*8 C,N1(105),N2(105)
      REAL*8 SM,SF,ST,S(33),S2,S4,FAC(33)
      DATA R/.1/
C  CALCULATION OF THE ELECTRIC FIELD  WITH THE GROUNDED
C  ELECTRODE AT INFINITY
      WRITE(5,108)
108   FORMAT(' UNIT 5=TT,6=LP ')
      READ(5,109)IU
109   FORMAT(I1)
1     FORMAT(F5.1)
2     FORMAT(E11.4)
101   FORMAT(' Y= ')
102   FORMAT(' SMALL R = ')
200   FORMAT(' P (CM) = ')
201   FORMAT(E11.4)
      FAC(1)=1
      DO 1000 I=2,33
1000  FAC(I)=FAC(I-1)*I
      S(1)=12.
      DO 4000 N=2,33
4000  S(N)=S(N-1)*(2*N+2)*(2*N+1)/(N*(N+1))
2000  WRITE(5,102)
      READ(5,1)R1
      WRITE(5,555)
555   FORMAT(' R=',E14.5)
      READ(5,256)R
256   FORMAT(E14.5)
      WRITE(5,101)
      READ(5,2)Y
      C=.5*R**2/(3.*8.85E-14)
      C=-1*C
      Z=(R1/R)**2
      Y1=0.
      Y3=1./Y**3
      S1=0.
      S3=-(R**2/(4.*Y**2))
      ST=(Y3-Y1)*C*2.
      WRITE(IU,2222)R
2222  FORMAT(' R=',E14.5)
      WRITE(IU,223)A,Y,R1,P
223   FORMAT(' AIR GAP(C)=',F5.1,'Y=',E11.4,'SM R=',F5.1,'P=',E11.4)
      WRITE(IU,222)ST
222   FORMAT(' M=0',5X,' ST (V/CM) = ',E14.5)
      WRITE(IU,565)Y3
565   FORMAT(' 1/Y**2 = ',E15.6)
      M=1
5     N1(1)=-1.*M
      N2(1)=-1.*M-1.
      SF=1.+N1(1)*N2(1)*Z
      IF(M.EQ.1)GO TO 11
      DO 10 N=2,M
      N1(N)=(-M+N-1)*N1(N-1)
      N2(N)=(-M-2+N)*N2(N-1)
10    SF=SF+(((N1(N)/FAC(N))*N2(N))/FAC(N))*Z**N
11    S2=S1**M*Y1
      SP=S3**M
      S4=SP*Y3
      SM=S(M)*SF*(S4-S2)*C
      ST=ST+SM
      SS=SP*S(M)
      WRITE(IU,22)M,SS,SF,ST
      M=M+1
      IF(M.GE.31) GO TO 2000
      GO TO 5
22    FORMAT(' M=',I3,3X,' SS=',E15.5,' SF=',E14.5,' ST=',E14.5)
20    STOP
      END
```

LIST OF FIGURES

tion of image (a) and (b) representing the circular region of interest.

LIST OF TABLES

LIST OF SYMBOLS

A	amplitude; electrode area
$A_{in}(x)$	sinusoidal input radiation signal
$A_{out}(x)$	sinusoidal output radiation signal
a	air gap thickness
a_r	range of photoelectrons
A_i	function of ω determined by boundary conditions
B_i	function of ω determined by boundary conditions
C	proportionality constant
CTF	Contrast Transfer Function
C_e	capacitance of a parallel plate dielectric capacitor; electret specific capacitance
D	optical density
D(z)	dipole layer moment
d	electrode separation
$d\alpha$	area element of $\sigma(x,y)$
E	electric field
E^*	extrapolated electric field
$E(r,z)$	electric field in cylindrical coordinates
$\overline{E}_a$	electric field at the polymer-air interface
$\vec{E}_a(0)$	field produced in the air gap by external supply
$E^*_{air}(a)$	extrapolated field due to primary ionizations in air
E_b	bias electric field in powder box
$\vec{E}_{eff}(t)$	effective electric field in air gap
E'_{eff}	effective electric field in the polymer

$\overline{E}_i$	Fourier Transform of the normal component of the electric field
$E_p^*(a)$	extrapolated electric field attributed to photoemission from the polarizing electrode
E_ν	energy of x-ray beam
$\vec{E}_\sigma(t)$	time dependent electric field produced by the electric charges accumulated on the foil
E_1	constant with dimensions of electric field
e	charge per ion; elementary charge
F	hypergeometric function
F_δ	electric force due to free charge
F_g	gravitational force
F_s	frictional force due to motion through a gas
$\overline{F}_E(\omega)$	Transfer Function relating charge distributions $\overline{\sigma}(\omega)$ with the electric field $E_a(\omega,z)$
$\overline{F}_V(\omega)$	Transfer Function relating the charge distributions $\sigma(\omega)$ with the potential $\overline{V}_a(\omega,z)$
δ	charge collection efficiency
δ_d	collection efficiency due to diffusion loss
δ_i	collection efficiency due to initial recombination
δ_v	collection efficiency due to volume recombination
$J_o(\omega r), J_1(\omega R)$	Bessel functions
j	current density
j_{sat}	saturated current density
j_{sat}^{air}	linear component of j_{sat} produced by the charge carriers originating from primary interactions with air
j_{sat}^{p}	exponential component produced by photoelectrons backscattered into sensitive medium

k	universal ionization chamber constant
k'	measured constant used in determining E^*
k_1, k_2	ion mobilities
LSF	Line Spread Function
m	characteristic of a gas in ionization chambers; measured value used in determining E^*
m'	measured constant used in determining E^*
$M(\nu)$	Modulation Transfer Factor
MTF	Modulation Transfer Function
N_e	equivalent pass band
n	characteristic of a gas used in ionization chambers
$O(\nu)$	Optical Transfer Function
$PSF(x,y)$	Point Spread Function
p	thickness of polymer
p_o	gas pressure
Q	charge of powder particle
q	ionization rate
r	charge liberated per unit volume per pulse
R	radius of x-ray aperture; recombination
r	cylindrical coordinate; radius of spherical powder particle; correlation coefficient
R	x-ray exposure
R_o	characteristic of a selenium plate
S	area of dipole layer distribution
$S(\nu)$	square wave response
s	thickness of selenium film
s_F	slope of function F vs the recursive integer

s_T	slope of relation T vs recursive integer
t	characteristic of a gas used in ionization chambers
T	recursive relation
t	time
t_{min}	minimum time of exposure required to produce σ_{min}
t_o	characteristic time
u	constant used in charge transfer expression; constant used in collection efficiency (pulsed beam)
V	collection voltage
$V(r,z)$	potential in cylindrical coordinates
$\overline{V}$	Fourier Transform of V
V_a	potential in air gap
V_c	potential produced by surface charge
V_d	air gap voltage between selenium and insulator
Vg	grid potential in the corona-charging apparatus
V_o	external power supply
V_p	potential in the polymer
v	velocity of powder particle
ν	constant used in charge transfer expression
ν_B	breakpoint voltage between linear and quadratic region
ν_o	spatial frequency at which the MTF is 0.5
V	residual voltage after x-ray exposure
V_o	initial voltage on the selenium plate
w	constant used in charge transfer expression
$\dot{x}$	exposure rate

Z	atomic number of polarizing electrode
Z_g	atomic number of gas
z	axial distance
α	adjustable parameter
β	parameter used in the electret charging formalism
γ	slope of optical density vs ℓog exposure curve
Γ_o	characteristic of a gas in ionization chambers
δ	slope of the E^* vs a plot; delta function
$\Delta D/D$	image contrast
$\Delta_1\sigma_t$	charge density transfered to the dielectric
ε	efficiency for production of backscattered electrons
ε_c	constant equal to $(s/\varepsilon_s + p/\varepsilon_p)$
ε_o	permittivity of free space
ε_p	dielectric constant of polymer
ε_Q	dielectric constant of powder particle
ε_s	dielectric constant of selenium film
ζ	characteristic of a gas in ionization chambers
η	viscosity of a gas
κ	constant equalling 3.33×10^{-10} (As/cm^3R)
λ,λ'	proportionality constants determining j_{sat}
ν	spatial frequency
ρ	density of powder particle; density of a gas
$\rho_1(x)$	charge density of positive ions at x from +ve electrode
$\rho_2(x)$	charge density of negative ions at x from +ve electrode

σ	surface charge density
σ_{max}	maximum electret surface charge density
σ_{min}	minimum surface charge density required for visualization of latent image
$\sigma(t)$	electret surface charge density
$\overline{\sigma}(\omega)$	Fourier Transform of the spatial charge distribution
τ	electret relaxation time
$\phi(\nu)$	linear phase displacement between the input and the output signals
$\omega, \omega_x, \omega_y$	spatial frequency

BIBLIOGRAPHY

page

Abramovitz, M.; see Handbook of Mathematical Functions

Aeby, C.A. and Whan, G.A.; IEEE Trans. Nucl. Sci., NS-28, 4177(1981), 94,206,208

Ahrens, C.R.; see Rossi, R.P.

Ames, A.E.; see Biad, G.R.

Andrews, J.R.; see Huntley, D.J.

Arnold, B.A. and Bjarnagard, B.E.; Med. Phys. 6, 500(1969) 15

Arnold, B.A., Eisenberg H., and Bjarngard, B.E. Radiology 121, 473(1976). 15,16

Arnold, B.A., Webster, E.W. and Kalisher, L. Radiology 129, 179(1978) 11,15

Arnold, B.; in The Physics of Medical Imaging: Recording System Measurements and Techniques, edited by A.G. Haus (Am.Inst. Phys. New York, 1979). 9,10

Asano, Y. and Suzuki, T.; Jpn. J. Appl. Phys. 2, 1139(1972) 112

Asbury, D.L.; see Moores, B.M.

Atomic Energy of Canada, Theratron-780. 52

Attix, F.H.; see Boag, J.W.

Azzarelli, T.; see Muntz, E.P.

Barish, R.J.; see Boag, J.W.

Barish, R.J.; see Seelentag, W.W.

Barnes, J.E.; see Jaeger, S.S.

Bauser, H. and Ronge W.; Health Phys. 34, 97(1978) 120,159

Bayer, B.; see Hamilton, J.F.

page

Bencomo, J.; see Haus A.G.

Berg, W.F.; see Lewis, R.B.

Bertan Associates, Model 205A 50P and/or Keithley, 245 H.V. Supply. 53

Biad, G.R., Jones, R.C. and Ames, A.E. Appl. Opt. 8, 2389(1969) 9

Bixby, W.E.; see Schaffert, R.M.

Bjarngard, B.E.; see Arnold, B.A.

Boag, J.W.; Br. J. Radiology 23, 601(1950). 85

Boag, J.W. "Ionization Chambers", in Radiation Dosimetry, edited by F.H. Attix and W.C. Roesch (Academic Press, New York, 1966), Vol. 2. 82,86

Boag, J.W.; Phys. Med. Biol. 8, 3(1973). 18,24,223

Boag, J.W.; Phys. Med. Biol. 18, 3(1973). 69,231,232

Boag, J.W., Barish, R.J. and Seelentag, W.W.; Med. Phys. 2, 245(1975). 19,202

Boag, J.W. and Wilson, T.; Br. J. Appl. Phys. 3, 222(1952) 82,86

Boag, J.W.; see Johns, H.E.

Boag, J.W.; see Seelentag, W.W.

Böhm, J.; Phys. Med. Biol. 21, 754(1976). 84

Brenkus, L.M.; see Couvillon J.C., L.A.

Broadhurst, M.G. and Davis, G.I.; Piezo-and Pyroelectric Properties in *ELECTRETS*, Topics of Applied Physics Vol. 33, edited by G.M. Sessler (Springer-Verlag, Berlin, 1980). 112

Brodie, I., Gutchek, R.A. and Mooney, J.B.; Proc.Soc. Photo-Optical Instrumentation Engineers 233, 65(1980). 23,29,231,232

page

Brodie, I. and Gutchek, R.A.; Med. Phys. 9, 79(1982) 32,34

Brodie, I. and Mooney, J.B.; Annual Meeting of IEEE Industrial Applications Society, Toronto, Canada (1978). 23

Burgess, A.E.; Med. Phys. 5, 199(1978). 15

Cacak, R.K.; see Jaeger, S.S.

Cameron, J.R.; see Mistretta, C.A.

Campos, M., Mascarenhas S. and Ferreira, G.L.; Phys. Rev. Lett. 27, 14 2(1971). 112

Capp, M.P.; see Nudelman, S.

Capp, M.P.; see Ovitt, T.W.

Carangi, R.L.; see Proudian, A.P.

Carlson, C.F.; U.S. Patent No. 2 588 699(1952). 113,158

Castellanos, A. Pereiras R. and Garcia, A.; Arch. Soc. Estud. Clin. (Habana) 31, 523(1937). 36

Cheng, Y.C. and Hartmann, G.C.; J. Appl. Phys. 51, 2332(1980) 160

Cheng, Y.C.; see Crofoot, R.B.

Christenson, P.C., Ovitt, T.W., Fisher, H.D.; et al., AJR 135, 1145(1980). 37

Chudleigh, P.W.; J. Appl. Phys. 47, 4475(1976). 113,158

Cleare, H.M.; in Med. X-Ray Photo-Opt. Sys. Eval. edited by Weaver, Wagner and Goodenough (Dept. of HEW, 1975) - p. 184. 9

Coltman, J.W.; J. Opt. Soc. Amer. 44, 468(1954). 14

Coulam, C.M.; see Mistretta, C.A.

Couvillon Jr., L.A. and Brenkus, L.M.; Diagnostic Imaging 4, 3(1982). 223

page

Cowart, R.W.; see Hays A.G.

Crofoot, R.B. and Cheng, Y.C.; J. Appl. Phys. 50, 6583(1979). 160

Crummy, A.B.; see Mistretta, C.A.

Cunningham, J.R.; see Johns, H.E.

Davis, G.I.; see Broadhurst, M.G.

Day, J.L.; see Stanton, L.

des Plantes, R.G.; Fortsch. Geb. Roentgenstr. 52, 69(1935). 36

DeWerd, L.A. and Moran, P.R.; Soc. Photo-Optical Instrumentation Engineers 96, 158(1976). 18,22,23

DeWerd, L.A. and Moran, P.R.; Med. Phys. 5, 23(1978). 18,22,23,231

DF100, Diasonics Inc., Milpitas, California. 237

Digital Radiography: A Focus on Clinical Utility, edited by Price, R.R., Rollo, F.D., Monahan W.G. and James A.E. (Grune and Stratton, New York, 1982). 223

Direct Torr Vacuum Pump 58

Dixon, R.L. and Ekstrand, K.E.; Med. Phys. 3, 340(1976). 9

Dodd, G.D.; Cancer 47, 1766(1981). 29

Dodd, G.D.; see Haus, A.G.

Doi, K. and Rossman, K.; Proc. Soc. Photo-Optical Instrumentation Engineers 56, 45(1975). 15

Dolan, K.W.; J. Appl. Phys. 46, 2456(1975). 94,139,206,208

Eguchi, M.; Philos. Mag. 49, 179(1925). 112,158

Eisenberg, H.; see Arnold, B.A.

Ekstrand, K.E.; see Dixon, R.L.

page

ELECTRETS, Topics in Applied Physics, Vol. 33, edited by G.M. Sessler (Springer-Verlag, Berlin, 1980). 111,158

Erickson, J.J.; see Mistretta, C.A.

Fallone, B.G. and Podgorsak, E.B.; Phys. Rev. B 27, 2615(1983). 4,114,158,199,223

Fallone, B.G. and Podgorsak, E.B.; Phys. Rev. B 27, 5062(1983). 4,114,159,199,223

Fallone, B.G. and Podgorsak, E.B.; Med. Phys. 10, 191(1983). 4,121,159,199,202,223

Fallone, B.G. and Podgorsak, E.B.; J. Appl. Phys., scheduled for August 1983, (in press). 4,158

Fallone, B.G. and Podgorsak, E.B.; Phys. Rev. B (in press). 4,111,114,159,199

Fallone, B.G. and Podgorsak, E.B.; IEEE Trans. Electrical Insulation, (in press). 4,111

Fallone, B.G. and Podgorsak, E.B.; IEEE Trans. Electrical Insulation, (in press). 4,223,231

Fallone, B.G. and Podgorsak, E.B.; Submitted to Medical Physics in May of 1983. 4,198,223,231

Fallone, B.G. and Podgorsak, E.B.; Submitted to Medical Physics in May of 1983. 4,223

Fallone, B.G. and Podgorsak, E.B.; Submitted to Medical Physics in May of 1983. 4,231

Fatourous, P.P.; in The Physics of Medical Imaging: Recording System, Measurements and Techniques, edited by A.G. Haus (Am. Inst. Phys., N.Y.,1979). 18,29

page

Fatouros, P.P.; Med. Phys. 9, 819(1982). 24,31

Fatouros, P.P. and Rao, G.U.V.; Med. Phys. 6, 1(1979). 25

Fatouros, P.P. and Rao, G.U.V.; Med. Phys. 7, 1(1980). 159

Fatouros, P.P. and Rao, G.U.V.; Med. Phys. 7, 331(1980). 18,27,160

Fatouros, P.P.; see Rao, G.U.V.

Fenster, A. and Johns, H.E.; Med. Phys. 1, 262(1974). 18,21,231

Fenster, A., Ostler, D. and Johns, H.E.; J. Appl. Photo. Engineering, 3, 18(1977). 72,73

Fenster, A., Plewes, D. and Johns, H.E.; Med. Phys. 1, 1(1974). 18,198,202,203,204,205

Fenster, A.; see Johns, H.E.

Ferreira, G.L.; see Campos M.

Fewell, T.R. and Weaver, K.E.; in Med. X-Ray Photo-Opt.Syst. Eval., edited by Weaver, Wagner and Goodenough, (Dept. of HEW, 1975) 9

Fisher, H.D.; see Christenson, P.C.

Fisher, H.D.; see Nudelman, S.

Fisher, H.D.; see Ovitt, T.W.

Fridkin, V.M. and Zheludev, I.S.; in Photoelectrets and the Electrophotographic Process (consultants Bureau, New York, 1960). 112,158

Garcia, A.; see Castellanos, A.

General Electric, Maximar 100. 51

Gillan, G.D.; see Pearce, J.G.

Goodenough, D.J.; see Cleare, H.M.

Goodenough, D.J.; see Fewell, T.R.

page

Gradshteyn, I.S. and Ryzlik, I.M.; Table of Integrals, Series, and Products (Academic, New York, 1980). 174

Greening, J.R.; Phys. Med. Biol. 9, 143(1964). 86

Grosche, G.; see Peschmann, K.R.

Gross, B.; in *ELECTRETS*, Topics in Applied Physics, Vol. 33, edited by G.M. Sessler (Springer-Verlag, Berlin, 1980) 131

Gross, B., Sessler, G.M. and West, J.E., J. Appl. Phys. 45, 111(1975). 113,158

Gross, B., Sessler, G.M. and West, J.E.; J. Appl. Phys. 47, 968(1976). 113,158

Gutchek, R.A.; see Brodie, I.

Handbook of Mathematical Functions, edited by M. Abramovitz and I.A. Stegun (Dover, New York, 1972). 176

Hartman, G.C.; see Cheng, Y.C.

Hauffe, K.; see Lewis, R.B.

Haus, A.G., Cowart, R.W., Dodd, R.W. and Bencomo, J.; Radiology 128, 775(1978). 29

Haus, A.G., Dodd, G.D. and Paulus, R.D.; Proc. Soc. Photo-Opt. Instrumentation Engineers 173, 120(1979). 29,30

Haus, A.G.; see Arnold, B.A.

Haus, A.G.; see Fatouros, P.P.

Haus, A.G.; see Sanerson, G.K.

Haus, A.G.; see Shaw, R.

Haus, A.G.; see Stanton, L.

Hamilton, J.F. and Bayer, B.; J. Opt. Soc. Amer. 55, 528(1965) 9

page

Hayford, R.E.; The Principles of Xeroradiographic Process, (Xerox, Pasadena, Calif., 1971). 18

Hendee, W.R.; Medical Radiation Physics (Year Book, Chicago, 1970). 7

Hendee, W.R.; see Jaeger, S.S.

Hendee, W.R.; see Rossi, R.P.

Henisch, H.K.; in Rectifying Semi-conductor Contacts (Oxford U.P., New York, 1957), p. 214. 121

Hewlett-Packard, 700 4B x-y Recorder 56

Hillman, B.J., Ovitt, T.W., Nudelman, S, et al., Radiology 139, 277(1981). 38,40

Hobbs, B.B.; see Taylor, K.W.

Honk, T.; see Kruger, R.

Hughes, I.J.; see Taylor, K.W.

Huntley, D.J. and Andrews, J.R.; Can. J. Phys. 46, 147(1968). 22

Jackson, J.D.; Classical Electrodynamics (John Wiley & Sons, New York, 1962). 180

Jacobson, G.; see Muntz, E.P.

Jacobson, G.; see Proudian, A.

Jaeger, S.S., Cacak, R.K., Barnes, J.E. and Hendee, W.R.; Radiology 128, 212(1978). 18

James Jr., A.E.; see Mistretta, C.A.

James Jr., A.E.; see Price, R.R.

James Jr., A.E.; see Rao, G.V.

James, A.E.; see Digital Radiography: A Focus on Clinical Utility

Jeffery, P.N.; see Johns, H.E.

page

Johns, H.E. and Cunningham, J.R.; The Physics of Radiology (C.C. Thomas, Springfield, 1983). 7,13,25,26,27,32,35,52,139

Johns, H.E., Fenster, A, Plewes, D., Boag, J.W. and Jeffrey, P.N.; Brit. J. Rad. 47, 519(1974). 18,20,198,202,223

Jones, R.C.; see Biad, G.R.

Johns, H.E.; see Fenster, A.

Johns, H.E.; see Plewes, D.

Kaegi, E.; see Muntz, E.P.

Kalister, L.; see Arnold, B.A.

Kao, C.C.; J. Appl. Phys. 44, 1543(1973).

Kao, C.C.; see Fatouros, P.P.

Kara-Michailova, E. and Lea, D.E.; Proc. Cambridge Philos. Soc. 36, 101(1940). 84

Keithley, 616 Digital Electrometer. 53

Kelcz, F.; Med. Phys. 3, 159(1976). 37

Kelcz, F.; see Mistretta, C.A.

Kelcz, F.; see Ort, M.G.

Kruger, R., Mistretta, C., Honk, T., et al., Invest. Radiol. 14, 279(1979). 37

Kruger, R., Mistretta, C., Honk, T., et al., Radiology 130, 49(1979). 37

Lange, G.; see Reiss, K.H.

Langevin, P.; Le Radium (Paris) 10, 113(1913). 84

Lawrence, D.J.; Med. Radiography and Photo. 53, 2(1977). 15

Lea, D.E.; see Kara-Michailova, E.

page

Lewis, R.B. and Stark, H.M.; in Current Problems in Electrophotography edited by W.F. Berg and K. Hauffe (de Gruyter, Berlin, 1972). 72

Lewis, J.; see Muntz, E.P.

Lightfoot, D.A.; see Stanton L.

Loeb, L.B.; in Basic Processes of Gaseous Electronics (Univ. of Calif. Press, Berkeley, 1955). 60,61,63,64

Mascarenhas, S.; see Campos, M.

Massey, J.B.; see Meredith, W.J.

McLeisch, B.P.; see Taylor, K.W.

McMaster, R.M.; see Schaffert, R.M.

Meredith, W.J. and Massey, J.B.; Fundamental Physics of Radiology (John Wright and Sons, Bristol, 1972). 7

Meyers, H.; see Muntz, E.P.

Mie, G.; Ann. Phys. 13, 857(1904). 82,84

Milne, E.; see Pearce, J.G.

Mistretta, C.A. and Crummy, A.B.; in Physical Basis of Medical Imaging, edited by C.M. Coulam, J.J. Erickson, F.D. Rollo and A.E. James (Appleton-Century-Crofts, New York, 1981). 37

Mistretta, C.A., Crummy, A.B. and Strother, C.M.; Radiology 139, 273(1981). 37

Mistretta, C.A., Ort, M.G., Cameron, J.R., Crummy, A.B. and Moran, P.R., Invest. Radiol. 8, 43(1973). 36,37

Mistretta, C.A., Ort, M.G., Kelcz, F., et al., Invest. Radiol. 8, 402(1973). 37

page

Mistretta, C.A.; see Kruger, R.

Mistretta, C.A.; see Ort, M.G.

Monahan, W.G.; see Digital Radiography A Focus on Clinical Utility

Monahan, W.G.; see Price, R.R.

Mooney, J.B.; see Brodie, I.

Moores, B.M., Ramsden, J.A. and Asbury, D.L.; Phys. Med. Biol. 25, 893(1980). 198,202

Moran, P.R.; see DeWerd, L.A.

Moran, P.R.; see Mistretta, C.A.

Moran, P.R.; see Podgorsak, E.P.

Moriuchi, Y.; Res. Electrotechn. Lab No. 736 (Tokyo, Japan, 1973). 84

Morsell, A.L.; see Muntz, E.P.

Muntz, E.P., Proudian, A. and Scott, P.B.; US Patent Number 3 774 029(1973). 18,198,202,223

Muntz, E.P., Meyers, H., Wilkinson, E. and Jacobson, G. Radiology 125, 517(1977).

Muntz, E.P., Lewis, J., Azzarelli, T., Welkowsky, M., Morsell, A.L., Kaegi, E. and Jacobson, C.; Proc. Photo-Optical Instrumentation Engineers 56, 208(1975). 18,20

Muntz, E.P.; see Proudian, A.P.

Muntz, E.P.; see Wagner, R.F.

Nadjakov, G.; Compt. Rend. 204, 1865(1937). 112

Nelms, A.T.; Nat. Bur. Stand. (U.S.) Circ. 577(1965). 94,206

Nudelman, S., Capp, M.P., Fisher, H.D. et al., Proc.Soc.Photo-Opt. Instrumentation Engineers 164, 138(1978). 37

page

Nudelman, S.; see Hillman, B.J.

Neugebauer, N.E.J.; Appl. Opt. 3, 385(1964). 25,159

Neugebauer, N.E.J.; Appl. Opt. 4, 453(1965). 25,159

Neugebauer, N.E.J.; Appl. Opt. 6, 943(1967). 25,159

Ort, M.G., Mistretta, C.A. and Kelcz,; Opt. Eng. 12, 169(1973). 37

Ort, M.G.; see Mistretta, C.A.

Osterman, F.A.; see Zeman, G.H.

Ostler, D.; see Fenster, A.

Ovitt, T.W., Capp, M.P., Fisher, H.D., et al., Proc. Soc. Photo-Opt. Instrumentation Engineers, 167, 61(1978). 37

Ovitt, T.W.; see Christenson, P.C.

Ovitt, T.W.; see Hillman, B.J.

Papoulis, A.; Systems and Transforms with Applications in Optics, (McGraw-Hill, New York, 1968). 167

Paulus, R.D.; see Haus, A.G.

Pearce, J.G., Gillan, G.D., Roeck, W.W. and Milne, E.; Proc. Soc. Optical Instrumentation Engineers 173, 105(1979). 11

Pereiras, R.; see Castellanos, A.

Peschmann, K.R. and Grosche, G.; Med. Phys. 1, 202(1977). 20

The Physics of Medical Imaging: Recording System Measurements and Techniques, edited by A.G. Haus (Am. Inst. Phys., New York 1979). 7

Plewes, D. and Johns, H.E.; Med. Phys. 2, 61(1975). 159

Plewes, D. and Johns, H.E.; Phys. Med. Biol. 23, 1000(1978). 21,25

page

Plewes, D. and Johns, H.E.; Med. Phys. 7, 315(1980). 18,32,33,116,159,198,202,223,237

Plewes, D.; see Fenster, A.

Plewes, D.; see Johns, H.E.

Podgorsak, E.P.; Radiation and Impurity Induced Thermally Activated Charge Transport in Calcium Fluoride, Ph. D. thesis, University of Wisconsin 1973). 22

Podgorsak, E.B. and Moran, P.R.; Phys. Rev. B: 8, 3405(1973). 22,112

Podgorsak, E.B. and Moran, P.R.; Science 179, 380(1973). 22

Podgorsak, E.B.; see Fallone, B.G.

Price, R.R., Rollo, F.D., Monahan, W.G. and James Jr., A.E.; in Digital Radiography: A Focus on Clinical Utility, edited by R.R. Price, F.D. Rollo, W.G. Monahan and A.E. James Jr., (Grune and Stratton, New York, 1982). 38,39

Proudian, A.P., Carangi, R.L., Jacobson, G. and Muntz, E.P.; Radiology 110, 667(1974). 18,24,116,159,198,202

Proudian, A.P.; see Muntz, E.P.

Ramsden, J.A.; see Moores, B.M.

Rao, G.U.V.; Amer. J. Roentgenol. 111, 628(1971). 14

Rao, G.U.V. and Fatouros, P.; Med. Phys. 5, 205(1978). 15,17

Rao, G.U.V. and Fatouros, P., James, A.E.; Invest. Radiol. 13, 460(1978). 11

Rao, G.U.V.; see Fatouros, P.

Rao, G.U.V.; see Zeman, G.H.

Reiss, K.H., Angew, Z; Phys. 19, 1(1965). 18,198,202,223

page

Reiss, K.H. and Lange, G.; Phys. Med. Biol., 18, 695(1973). 18,202,223

Robb, G.P. and Steinberg, I.; AJR 41, 1(1939). 36

Roeck, W.W.; see Pearce, J.G.

Roesch, W.C.; see Boag, J.W.

Rollo, F.D.; see Digital Radiography; A Focus on Clinical Utility

Rollo, F.D.; see Mistretta, C.A.

Rollo, F.D.; see Price, R.R.

Ronge, W.; see Bauser, H.

Rossi, R.P., Hendee, W.R. and Ahrens, C.R.; Radiology 121, 465(1976). 11

Rossman, K.; Radiology 93, 257(1969). 14

Rossman, K.; see Doi, K.

Rutherford, E.; see Thomson, J.J.

Ryzlik, I.M.; see Gradshteyn, I.S.

Sanerson, G.K.; in The Physics of Medical Imaging Recording System, Measurements and Techniques, edited by A.G. Haus (Am. Inst. Phys., N.Y. 1979). 14

Schaffert, R.M.; in Electrophotography, (Focal, London, 1975). 18,19,24,60,64,66,68,69,113,115,158,159,198,202,224,231

Schaffert, R.M., McMaster, R.M. and Bixby, W.E.; U.S. Patent 2 666 144(1954). 24

Scott, P.B.; see Muntz, E.P.

Seelentag, W.W., Boag, J.W. and Barish, R.J.; Med. Phys. 3, 384(1976). 19,202

page

Seelentag, W.W., Boag, J.W. and Barish, R.J.; Med. Phys. 3, 384(1976). 19,202

Seelentag, W.W.; see Boag, J.W.

Sessler, G.M. and West, J.E.; J. Appl. Phys. 43, 922(1972). 113,158

Sessler, G.M. and West,; J. Electrostatics 1, 111(1975). 113,158

Sessler, G.M.; see *ELECTRETS*, Topics in Applied Physics, Vol. 33.

Sessler, G.M.; see Broadhurst, M.G.

Sessler, G.M.; see Gross, B.

Shaw, R.; in The Physics of Medical Imaging; Recording System and Measurement and Techniques, edited by A.G. Haus (Am. Inst. Phys., N.Y., 1979). 18,27,29

Shaw, R.; Proc. Soc. Photo-Opt. Instrumentation Engineers 70, 359(1975) 27,28

Siemens, Stabilipan II. 52

Stanton, L.; in The Physics of Medical Imaging: Recording System, Measurements and Techniques, edited by A.G. Haus (Am. Inst. Phys., N.Y. 1979). 18,25

Stanton, L., Villafana, T., Day, J.L., Lightfoot, D.A. and Stanton, R.E. Radiology 132, 455(1979). 18,25

Stanton, R.E.; see Stanton, L.

Stark, H.M.; see Lewis, R.B.

Stegun, I.A.; see Handbook of Mathematical Functions

Steinberg, I.; see Robb, G.R.

Stevels, A.N.; Medica Mundi 20, 12(1975). 9

Strother, C.M.; see Mistretta, C.A.

Suzuki, T.; see Asano, Y.

page

Takagi, K., Tasai, K. and Tsukatani,; Fujitsu Sci. Tech. J., 1, 227(1965) 60,62,67

Tasai, K.; see Takagi, K.

Taylor, K.W., McLeish, B.P., Hobbs, B.B. and Hughes, I.J.; Proc. Soc. Photo-Optical Instrumentation Engineers 173, 306(1979). 11,12

Ter-Pogossian, M.M.; The Physical Aspects of Diagnostic Radiology (Harper and Row, New York, 1967). 7,9

Thomson, J.J. and Rutherford, E.; Philos. Mag. 42, 392(1896) 82

Townsend, J.S.; Electricity in Gases (Oxford University Press, London, 1915). 82

Tsukatani, K.; see Takagi, K.

Versatec, Electrographic paper. 58

Villafana, T.; see Stanton, L.

Vodenicharov, C.M. and Vodenicharova, M.B.; Phys. Stat. Sol. (a) 57, 58(1980). 121

Vodenicharova, M.B.; see Vodenicharov, C.M.

Wagner, R.F. and Muntz, E.P.; Proc. Soc. Photo-Opt. Instrumentation Engineers 173, 162(1979). 29,30

Wagner, R., Weaver, K.E.; Radiology 118, 183(1976). 11

Wagner,; see Cleare, H.M.

Wagner,; see Fewell, T.R.

Weaver, K.E.; see Wagner, R.

Webster, E.W.; see Arnold, B.A.

Welkowsky, M.; see Muntz, E.P.

West, J.E.; see Gross, B.